



Pilkington Library

Author/Filing Title WILLIAMS, S.L.

Accession/Copy No. G40129764

Vol. No. Class Mark

LOAN COPY

26 JUN 1998

25 JUN 1999

14 JAN 2000

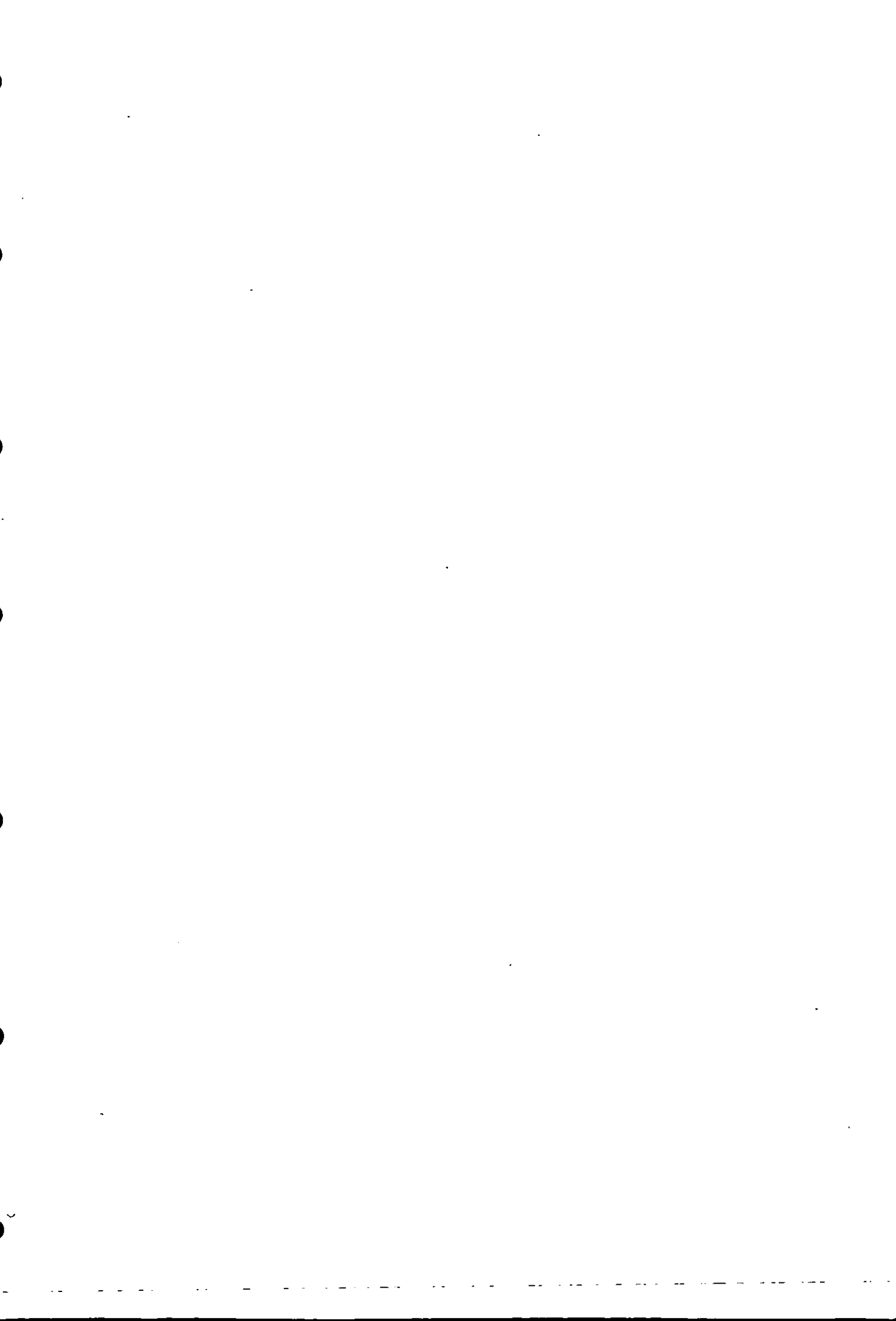
22 MAY 2000

FOR REFERENCE ONLY

0401297640



**BADMINTON PRESS
18 THE HAFCROFT
SYSTEM
LEICESTER, LE7 1LD
ENGLAND
TEL: 0116 260 2917
FAX: 0116 269 6639**



Photochemistry and Photophysics of Anthracenes on Silica Gel

By

Siân Lowri Williams


BSc, GRSC

A Doctoral Thesis Submitted in Partial Fulfilment of the Requirements
for the Award of

Doctor of Philosophy of Loughborough University

September 27th 1996

(c) Siân Lowri Williams 1996

	Loughborough University
	May 97
Class	
Acc No	040129764

99100105

To My Mother and Late Father, Hazel and Michael Williams

With Love.

Acknowledgements.

I would like to thank my supervisor Professor Frank Wilkinson for his encouragement and support throughout this project.

Thanks are also due to the following :- Dr. Dave Worrall for useful discussions and suggestions; Mr. John Spray for his glass blowing skills, without whom this project would have been impossible; Mr. Anthony Tredgett, Miss Fabienne Delepine and Mrs. Sonia Wilson for their assistance in the preparation of some of the samples; Prof. Dieter Oelkrug and Alfred Tompert of the Institut für Physikalische und Theoretische Chemie der Universität Tübingen for useful discussions; Dr. Luis Filipe Vieira Ferreira and Miss Anabela Oliveira of the Centro de Química Física Molecular, Universidade Técnica de Lisboa, in Portugal for their hospitality and useful discussions.

I would also like to acknowledge EPSRC for financial support.

Thanks to my family for their help and support throughout my time at Loughborough. A special thank you to my mum, sister and brother, Hazel, Ceri and David Williams.

Thanks also to the Loughborough Photochemistry research group past and present, Dave Worrall, David Mandley, Jon Hobley, Richard James, Phil Szekeres, Andres Olea, Marek Sikorski, Miquel Mir, Darren Greenhill, Garry Sturley, Lis Jansen, Anita Jones, Robin Vincent and Jill Crossley.

In addition I am grateful for the support from many old friends including : Jo Beddoe, Kirsty Speak, Jane Williams, Pauline Campbell, Rehana Sidat, Rhonda Mitchell, Martina Whitley and Justine Blomeley.

A very special thanks again to Dave Worrall for his great support, for keeping his patience when I was losing mine and for his love.

Table of Contents

Abstract	i
1. Introduction and theory	1
1.1. Basic photochemistry	1
1.1.1. Spin multiplicity	4
1.1.2. Molecular transitions	5
1.1.3. Spin-orbit coupling	10
1.2. Intermolecular processes	11
1.2.1. Energy transfer	11
1.2.1.1. Radiative energy transfer	11
1.2.1.2. Collisional exchange mechanism	12
1.2.1.3. Coulombic (induced dipole) mechanism	14
1.2.2. Electron transfer	16
1.2.2.1. Marcus theory	16
1.3. Flash photolysis	19
1.4. Lasers	19
1.4.1. Q-switching	25
1.4.2. Non-linear effects	27
1.5. Reflectance photochemistry	27
1.5.1. Kubelka-Munk theory	30
2. Photochemistry on surfaces	33
2.1. Nature of silica gel	33
2.2. Nature of gamma-alumina	34
2.3. Nature of zeolites	34
2.4. Properties of molecules adsorbed on surfaces	36
2.4.1. Pore size effects on molecules adsorbed on silica gel	37
2.4.2. Effect of pretreatment temperature on the mobility of the adsorbed molecule	38
2.4.3. Surface reactions	38
2.4.4. Surface kinetics	40
2.4.5. Energy transfer on surfaces	42
2.4.6. Electron transfer on surfaces	43
2.5. Summary	44

3. Experimental	45
3.1. Sample preparation	45
3.2. Anthracene adsorbed on silica gel at various anthracene loadings	46
3.3. Anthracene adsorbed on silica gel with radical cation quencher	46
3.4. Anthracene derivatives adsorbed on silica gel	46
3.5. Materials	46
3.6. Ground state absorption spectra	47
3.7. Fluorescence emission spectra	47
3.8. Laser flash photolysis	47
3.8.a. Time resolved transient absorption measurements	47
3.8.b. Time resolved transient emission measurements	51
3.9. Data analysis	51
3.9.1. Further data treatment	53
4. Fitting of kinetic data in heterogeneous media	56
4.1. Dispersive kinetic model	56
4.2. Fractal and two-dimensional model	56
4.2.1. Delayed fluorescence	57
4.2.2. Radical cation decay following electron transfer from electron donor	62
4.3. Geminate recombination of radical cations with their electrons	64
5. Results and discussion	66
5.1. Anthracene	66
5.1.1. Ground state absorption spectra	66
5.1.2. Fluorescence emission spectra	70
5.1.3. Transient absorption spectra	72
5.1.3.1. Kinetic analysis	76
5.1.3.1a. Triplet state kinetics	76
5.1.3.1b. Radical cation decay kinetics	81
5.1.4. Transient emission spectra	85
5.1.5. Conclusions	88

5.2. Anthracene and co-adsorbed electron donor	89
5.2.1. N,N,N',N'-tetramethyl-1,4-phenylenediamine and anthracene	91
5.2.1.1. Transient absorption spectra	91
5.2.1.2. Electron transfer kinetics	91
5.2.2. Azulene and anthracene	101
5.2.2.1. Transient absorption spectra	103
5.2.2.2. Electron transfer kinetics	103
5.2.3. Triphenylamine and anthracene	107
5.2.3.1. Transient absorption spectra	109
5.2.3.2. Electron transfer kinetics	109
5.2.4. N,N-dimethylaniline and anthracene	115
5.2.4.1. Transient absorption spectra	115
5.2.4.2. Electron transfer kinetics	118
5.2.5. Anthracene and azulene sublimed onto silica gel	121
5.3. Summary of the electron transfer data	123
5.3.1. Exciplex emission behaviour	126
5.3.2. 2,3-didecyloxyanthracene and triphenylamine	126
5.3.3. Other electron donors studied	127
5.3.4. Conclusions	131
6. Anthracene derivatives	132
6.1. Ground state absorption spectra	132
6.2. Fluorescence emission spectra	135
6.3. Transient absorption spectra	135
6.4. Transient emission spectra	150
6.5. Conclusions	153
7. Conclusions and suggestions for further work	155
8. References	158

Abstract.

Studies have been carried out investigating the photochemical and photophysical properties of anthracene adsorbed on silica gel. The photochemistry and photophysics of anthracene in solution are well reported and known, hence its choice as a probe for the silica gel surface. UV-visible absorption and fluorescence spectra of anthracene adsorbed on silica gel reveal aggregate formation at very low loadings (1% of a monolayer) indicating preferential adsorption occurs at some surface sites. Laser flash photolysis at 355 nm produces both the triplet and radical cation of anthracene, their production was found to be mono- and multi-photonic respectively. The decays of both these transients were complex and the rates increased with increasing loading. Analysis of the triplet state decay has been carried out by studying the delayed fluorescence which arises from triplet triplet annihilation. Fractal and two-dimensional models have been used to describe this bimolecular decay.

The coadsorption of anthracene and an electron donor having an oxidation potential below 1.09 V on silica gel causes electron transfer to occur from the electron donor to the anthracene radical cation produced following laser flash photolysis at 355 nm. Studies using a selection of electron donors with varying reduction potentials were carried out. The electron donor transfers an electron to the anthracene radical cation, thus greatly accelerating its rate of decay; for electron donors such as triphenylamine, N,N-dimethylaniline and N,N,N',N'-tetramethyl-1,4-phenylenediamine the rise of the donor radical cation is observed as the anthracene cation decays. These systems were studied using fluorescence measurements and laser flash photolysis to study any fluorescence quenching and the rate of decay of both the anthracene triplet and radical cation.

A selection of anthracene derivatives adsorbed onto silica gel were also briefly studied to see the effect of substituent group and its position. Symmetrically substituted dialkoxyanthracenes and 9-cyanoanthracene were used. The transient absorption spectra of the 2,3- and 2,6-dialkoxyderivatives and 9-cyanoanthracene revealed spectral similarities with that of unsubstituted anthracene. The spectra of 9,10- and 1,5-didecyloxyanthracene showed significant differences in the radical cation spectra to those obtained for unsubstituted anthracene.

Chapter 1

Introduction

1. Introduction and Theory.

1.1. Basic Photochemistry.

Photochemistry is a term used to describe the study of chemical reactions initiated by the absorption of light. Absorption of electromagnetic radiation of the appropriate wavelength, usually ultra violet (UV) or visible, may cause a molecule to form an excited state which may then fragment.

The Stark-Einstein law states "a molecule undergoing photochemical change does so through the absorption of a single quantum of light". The energy of this quantum of light will be equal to the excitation energy of each of the excited molecules and is given by equation 1.1 :-

$$\epsilon = h\nu \quad (1.1)$$

where h is Planck's constant, (6.63×10^{-34} J s molecule⁻¹) and ν is the frequency of radiation. A more useful or common way of expressing this equation is using molar excitation energy (E) and wavelength, (λ) instead of frequency :-

$$E = Nh\nu = \frac{Nhc}{\lambda} \quad (1.2)$$

where N is Avogadro's number and c is the velocity of light (2.998×10^8 m s⁻¹).

The Beer Lambert law (equation 1.3) can be used to describe the fraction of light absorbed by a solution of a low concentration (homogeneous absorbing system) of absorber at a given wavelength

$$A = \log_{10} \frac{I_0}{I_t} = \epsilon cl \quad (1.3)$$

where I_0 represents the intensity of monochromatic light at the front of a cell of length l , containing a solution of a single absorbing species of concentration c and I_t is the intensity of light transmitted through the cell of material. The molar absorption coefficient, ϵ , is constant for a given wavelength and has units of dm³ mol⁻¹ cm⁻¹ if l is in cm and c is in mol dm⁻³. ϵ is closely connected with the transition probability, a large probability being associated with large ϵ .

The absorption of a photon of light causes the molecule to become excited or 'energy-rich'. The energy of the absorbed photon dictates the nature of excitation. UV (10 nm - 400 nm) and visible (400 nm - 800 nm) light generally excite valence electrons and can cause various types of photochemical reactions; lower energy photons may excite vibrational and rotational transitions.

The positions of electrons in molecules can be described using molecular orbitals which are made from combining atomic orbitals. The orbitals produced are polycentric and filled starting with the orbital with the lowest energy. Each orbital may hold a maximum of two electrons whose spins must be paired (Pauli's exclusion principle). The orbitals can be bonding (σ or π), non-bonding (n) and anti-bonding (σ^* or π^*) which are of lower, equal and higher energy respectively than the atomic orbitals from which they are constructed (shown for molecular oxygen in Figure 1.1). σ and σ^* orbitals are symmetric about the internuclear axis (with high electron density for bonding orbitals along the molecular axis), π orbitals are formed if $2p_x$ or $2p_y$ orbitals are mixed (zero electron density along the molecular axis) and n orbitals if non-bonding valence shell electrons are present.

The relative energies of these orbitals are shown in Figure 1.2, and transitions induced between these levels by the absorption of a photon lead to excited states. The most common transitions seen in organic compounds are $n \rightarrow \pi^*$, $\pi \rightarrow \pi^*$, $n \rightarrow \sigma^*$, $\sigma \rightarrow \sigma^*$. A transition from n to π^* or from π to π^* would produce a 1 or $3(n, \pi^*)$ or 1 or $3(\pi, \pi^*)$ state respectively, where the 1 and 3 denote either a singlet or triplet state which will be discussed in the next section 1.1.1.

Wavefunctions ($\psi_{x,y,z}$) are often used to represent the spatial properties, momentum and energy of states. The modulus of the square of the wavefunction can be used to define the electron probability density and then the probability of finding electrons in given configurations is equal to multiplying ψ_{xyz}^2 by the volume concerned (dx dy dz). Wavefunctions describe the energy state and can be separated into electronic and vibrational components denoted by ϕ and χ respectively.

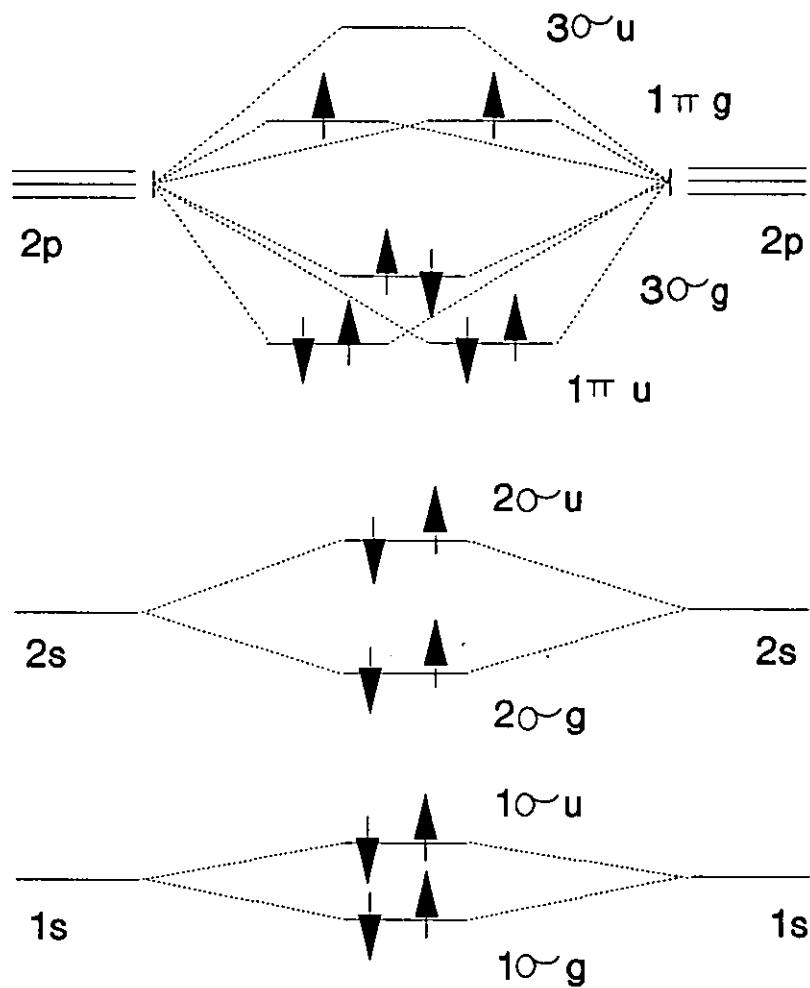


Figure 1.1 : The molecular orbitals of oxygen and the atomic orbitals from which they are constructed.

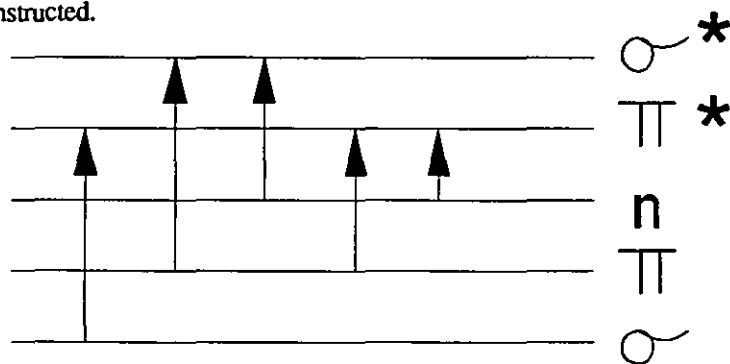


Figure 1.2 : The relative energies of the n , π , and σ molecular orbitals.

1.1.1. Spin Multiplicity.

Each electron in a molecule has a spin quantum number of $1/2$, which can take two orientations depending on the electron's alignment with respect to a specified axis corresponding to $m_s = 1/2$ and $m_s = -1/2$. The total spin angular momentum for a molecule is S , which is the vector sum of all the contributions from each electron, and for spin paired electrons will be equal to zero, while electrons with parallel spins give $S = 1$ ($1/2 + 1/2$). The spin multiplicity is given by $M_s = 2S+1$, therefore $M_s = 1$ for a singlet and 3 for a triplet state. The symbol used for a singlet ground state is S_0 and excited singlets become S_1, S_2, S_3 , etc. with the subscript denoting increasing energy. Triplet states follow the same pattern with T_1 the lowest triplet state and T_2, T_3, T_4 increasing in energy.

If two electrons occupy the same orbital they must have paired spins i.e. $m_s = +1/2$ and $-1/2$ (Pauli's exclusion principle). Therefore as most molecules in their ground state contain an even number of electrons, the electrons will be spin paired and therefore the ground states will be singlet states. Hund's rule states electrons tend to occupy degenerate orbitals singly and with their spins parallel - thus keeping the repulsion between electrons to a minimum. Consequently triplet states have lower energies than their corresponding singlet states. Promotion of an electron from the ground state can give rise either to an excited singlet (spin orientation is preserved $S=0, M_s=1$) or an excited triplet (spin orientation is inverted $S=1, M_s=3$) as shown in Figure 1.3.

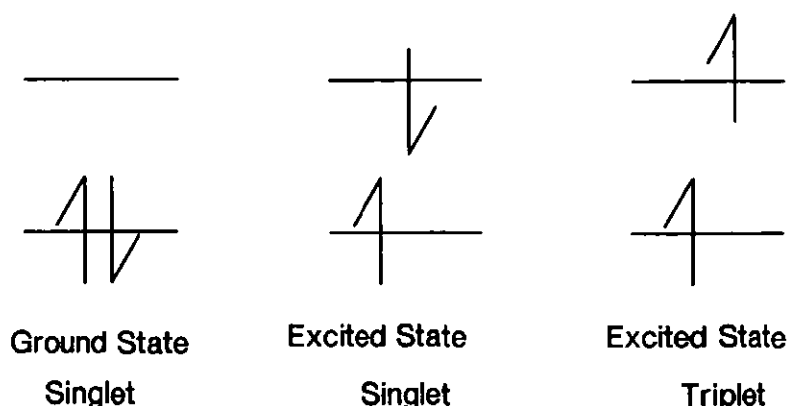


Figure 1.3 : Schematic diagram of singlet and triplet excited states.

1.1.2. Molecular Transitions.

The Franck Condon principle states that during an electronic transition (absorption or emission) the position and motion of all nuclei remain almost unchanged. Consequently vibrational lines in a progression are not all observed to be of the same intensity, the intensity of a transition is determined by the probability of finding a nucleus at a given internuclear distance in a given vibrational level v , i.e. χ_v^2 , where χ_v is the wavefunction describing the position of the nuclei in a vibrational level v . For each vibrational level (v) there are $v+1$ maxima, and the transition is most likely to occur from a v'' maximum in the lower state vertically upwards to the v' level in the upper state having the best overlap as shown in Figure 1.4. The most intense transition here is from $v'' = 0$ to $v' = 2$.

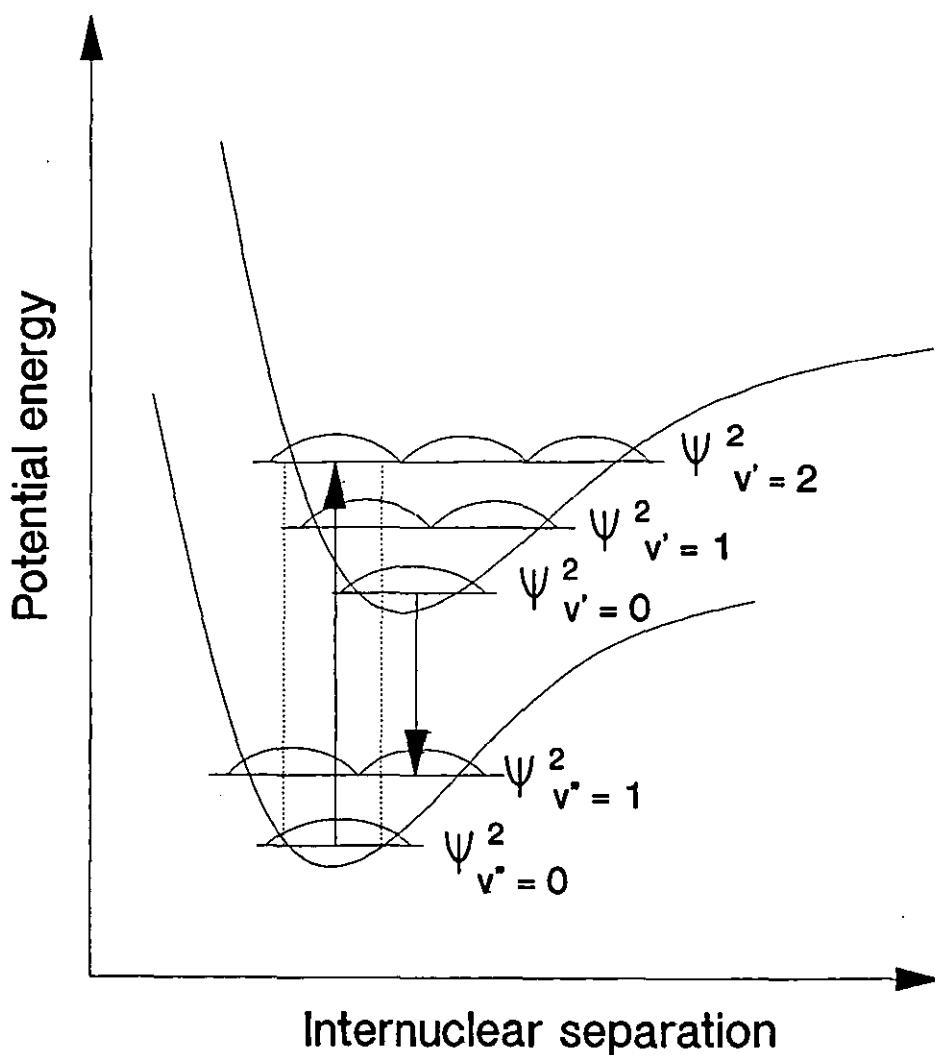


Figure 1.4 : Potential Energy versus Internuclear Separation for an electronic transition between two levels.

The quantum yield (ϕ) of a process can be used to express the efficiency of conversion of the incident radiation to product and is given by equations 1.4 and 1.5 :-

$$\phi = \frac{\text{number of product molecules formed}}{\text{number of quanta absorbed}} \quad (1.4)$$

or generally expressed as :-

$$\phi = \frac{\text{rate of a process}}{\text{rate of absorption of photons}} \quad (1.5)$$

There are a number of pathways available for the dissipation of energy and deactivation of the excited state. The transitions can be described as radiative or radiationless and can be spin allowed (spin is preserved) or spin forbidden (spin inversion occurs). A selection rule for molecular transitions is $\Delta S = 0$. Spin "forbidden" transitions can occur and are often observed as weak transitions. The intensity of a spin "forbidden" transition is dependent on the degree of spin-orbit coupling which is discussed below in section 1.1.3.

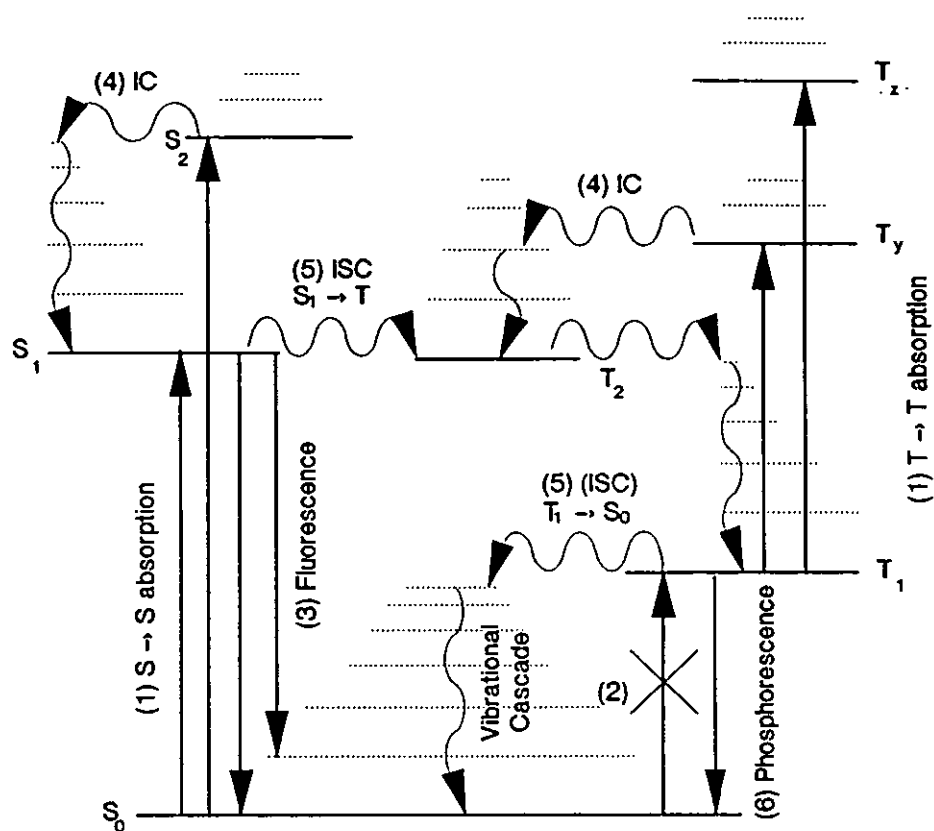
The Jablonski diagram (Figure 1.5) can be used to show the electronic excited states and transitions between the states of molecules. The rate constants relating to the more important transitions are also shown. Radiative transitions are shown by solid vertical lines and radiationless transitions are denoted by horizontal wavy lines, the vertical wavy lines representing vibrational relaxation. The principle transitions are described in more detail below.

1. ($S_0 + h\nu \rightarrow S_1$) and ($T_1 + h\nu \rightarrow T_2$)

Singlet to singlet and triplet to triplet absorptions preserve spin orientation and are therefore spin allowed, and consequently correspond to strong transitions.

2. ($S_0 + h\nu \rightarrow T_1$)

Singlet to triplet absorption requires spin flip and is spin forbidden, consequently such transitions are of low intensity.



where IC = Internal Conversion

ISC = Intersystem Crossing

Transition	Description	Rate Constant
(1) $A + h\nu \rightarrow {}^1A^*$	S-S absorption	I_a
(2) $A + h\nu \rightarrow {}^3A^*$	S - T absorption	I_a
(3) ${}^1A^* \rightarrow {}^1A + h\nu_f$	Fluorescence	k_f
(4) ${}^1A^* \rightarrow {}^1A$	Internal Conversion	k_{ic}
(5) ${}^1A^* \rightarrow {}^3A^*$	Intersystem Crossing	k_{isc}
(5) ${}^3A^* \rightarrow {}^1A$	Intersystem Crossing	k_{isc}
(6) ${}^3A^* \rightarrow {}^1A + h\nu_p$	Phosphorescence	k_p

Figure 1.5 : A Jablonski Diagram illustrating the possible deactivation pathways of an excited molecule, with the more important relaxation pathways and their rates summarised beneath.

3. ($S_1 \rightarrow S_0 + h\nu$) Fluorescence

Fluorescence is a spin allowed radiative transition resulting in emission between states of like multiplicity, the most common of which is singlet singlet emission. Fluorescence usually occurs from the lowest vibrational level in the S_1 state, to a vibrational level in the S_0 state. Higher excited singlet states such as the S_2 generally undergo internal conversion rapidly giving the S_1 state. Kasha's rule states that "the emitting electronic level of a given multiplicity is the lowest excited level of that multiplicity". There are exceptions, and some thioketones^{1, 2} and azulene^{3, 4, 5} undergo fluorescence from the S_2 state due to the large energy gap between their S_1 and S_2 states. Fluorescence describes radiative transitions between states of like multiplicity, so T_2 to T_1 emission would also be classed as fluorescence. The fluorescence lifetime is usually of the order of a few nanoseconds, and is discussed below.

4. ($S_1 \rightarrow S_0 + \text{heat}$) and ($T_2 \rightarrow T_1 + \text{heat}$) Internal Conversion

This is an allowed radiationless decay process between states of same spin multiplicity. The rate will depend on the energy separation between the initial and final electronic states e.g. S_1 to S_2 or T_2 to T_1 occurs rapidly whereas the S_1 to S_0 process is relatively slow.

5. ($S_1 \rightarrow T_1 + \text{heat}$) and ($T_1 \rightarrow S_0 + \text{heat}$) Intersystem Crossing

These are forbidden radiationless transitions between excited states of different spin multiplicities and are referred to as intersystem crossing. The three most important transitions are S_1 to T_n , T_1 to S_0 and T_1 to S_1 . The latter gives rise to the process termed E-type delayed fluorescence and is thermally activated intersystem crossing from T_1 to S_1 . Efficient intersystem crossing can occur via spin orbit coupling the mechanism of which is explained below in section 1.1.3. The presence of heavy atoms enhance intersystem crossing quantum yields due to the enhancement of the spin orbit coupling mechanism.

6. ($T_1 \rightarrow S_0 + h\nu$) Phosphorescence

Triplet to singlet emission, i.e. phosphorescence is a spin forbidden radiative transition of lower energy than fluorescence. Its spin forbidden nature results in the radiative lifetimes for phosphorescence being long (see below) which allows diffusional quenching of the triplet states by solvent molecules and other triplets to compete with phosphorescence. Consequently phosphorescence measurements are often carried out at low temperatures with the samples of

interest frozen in a glass. This slows down the rate of diffusion so the phosphorescence can be more readily observed.

The radiative or natural lifetime of a species τ_r^0 - either fluorescence or phosphorescence - can be defined by equation 1.6 :-

$$\tau_r^0 = \frac{1}{k_r} \quad (1.6)$$

where k_r is the radiative rate coefficient - also referred to as the Einstein coefficient for spontaneous emission. Typical radiative lifetimes for both fluorescence and phosphorescence are shown in Table 1.1.

Transition	Typical radiative lifetimes
$\tau_r (S_1 = {}^1(\pi, \pi^*))$	10^{-9} s
$\tau_r (S_1 = {}^1(n, \pi^*))$	10^{-6} s
$\tau_r (T_1 = {}^3(n, \pi^*))$	10^{-2} s
$\tau_r (T_1 = {}^3(\pi, \pi^*))$	10 s

Table 1.1 :- Typical radiative lifetimes of fluorescence and phosphorescence

The measured fluorescence or phosphorescence lifetime will generally be shorter than the radiative lifetime due to additional contributions to the decay of the excited state via, for example, internal conversion or intersystem crossing, so the singlet and triplet lifetimes are given by equations 1.7 and 1.8 :-

$$\tau_f = \frac{1}{(k_f + k_{isc} + k_{ic})} \quad (1.7)$$

or

$$\tau_p = \frac{1}{(k_p + k_{isc})} \quad (1.8)$$

and the quantum yields of fluorescence or phosphorescence can be given by :-

$$\phi_f = \frac{k_f}{(k_f + k_{isc} + k_{ic})} \quad (1.9)$$

$$\phi_p = \frac{k_p}{(k_p + k_{isc})} \phi_T \quad (1.10)$$

where ϕ_T is the triplet quantum yield.

1.1.3. Spin orbit coupling.

So called "forbidden" transitions can occur because pure singlet and pure triplet states do not exist. Singlets have some triplet character and triplets have some singlet character due to coupling between spin and orbital angular momentum so :-

$$\begin{aligned} \psi_T &= \psi_T^0 + \lambda_x \psi_S \\ \psi_S &= \psi_S^0 + \lambda_y \psi_T \end{aligned}$$

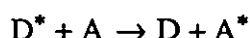
where ψ_S and ψ_T are the wavefunctions describing singlet and triplet states respectively and the superscript 0 denotes pure states, λ_x and λ_y are fractions much less than 1.

This coupling arises because an electron experiences a magnetic field due to the motion of the nucleus, this field resulting in some mixing of spatial and spin components - spin orbit coupling. The magnetic field is often strong enough to cause spin flipping of the electron, and so to conserve total angular momentum (spin and orbital) this results in the electron changing orbitals - this is illustrated by the differences in the triplet lifetimes shown earlier in Table 1.1. Decay from the triplet (n, π^*) excited state to the ground state involves both spin flip and a change in orbital configuration, whereas relaxation to the ground state from the excited (π, π^*) triplet requires just spin flip. Consequently compensation for spin flip from the change in orbital configuration results in the radiative lifetime of the former triplet being shorter than that of the latter. Since spin-orbit coupling depends on interactions with the nucleus, atoms with high atomic numbers give more spin-orbit coupling, the higher the charge the greater the coupling. Xenon, iodides and bromides are often used to enhance spin forbidden transitions either as intramolecular (substituents) or intermolecular quenching agents.

1.2. Intermolecular processes.

1.2.1. Energy transfer.

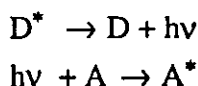
Energy transfer conserves energy and occurs from a vibrational level of a particular excited electronic state of a molecule to an isoenergetic vibrational level of an electronic state in another molecule, small mismatches in energy being dispersed by rotational and translational movement or motions in the solvent. The transfer of energy from an electronically excited donor (D^*) to an acceptor (A) is often referred to as quenching of D^* by A and can be summarised as :-



where D is the ground state of the donor and A^* is the electronically excited acceptor. Two types of energy transfer can occur, either radiative, described often as "trivial" energy transfer, or non-radiative. There are two possible mechanisms for non-radiative energy transfer between two weakly interacting molecules; these are collisional and coulombic.

1.2.1.1. Radiative energy transfer.

Radiative energy transfer involves the emission of light from the donor molecule followed by the absorption of the emitted photon by the acceptor :-



Obviously the emission spectrum of the donor must overlap with the absorption spectrum of the acceptor for this process to occur. The emission from the donor is spontaneous and is not influenced by the presence of the acceptor. Consequently the molecules do not need to be in close proximity.

1.2.1.2. Collisional (Exchange) Mechanism.

As the name suggests the process involves the exchange of electrons and requires overlap of the electronic charge clouds of the interacting molecules. The mechanism of exchange is shown in Figure 1.6, where the exchanging electrons are represented by hollow circles. The electron initially on the excited donor (D^*) jumps to the acceptor (A) and simultaneously an electron hops from the acceptor (A) to the excited donor (D^*). This exchange of electrons is usually a concerted mechanism.

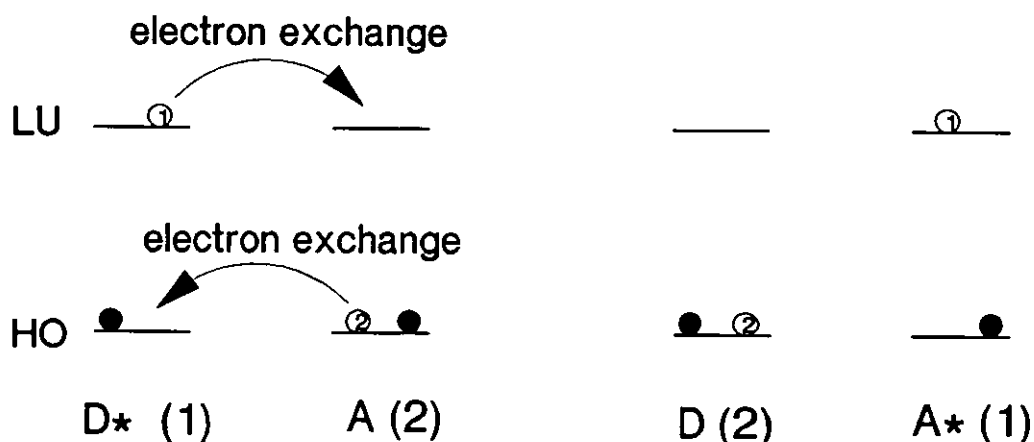


Figure 1.6: Schematic representation of exchange energy transfer

Concerted electron transfer will occur if both HOMO (Highest Occupied Molecular Orbital) to HOMO and LUMO (Lowest Unoccupied Molecular Orbital) to LUMO transitions are favourable. Electrons may also occasionally exchange in a stepwise manner via charge transfer exchange or via a bonded intermediate. The differences in these two mechanisms can be seen in Figure 1.7. The charge transfer mechanism involves a radical ion pair formed following electron transfer from the LUMO of the donor to the LUMO of the acceptor. A bonded intermediate (such as a diradical or zwitterion) is formed when electron transfer from the HOMO of the acceptor to the HOMO of the donor is the first step.

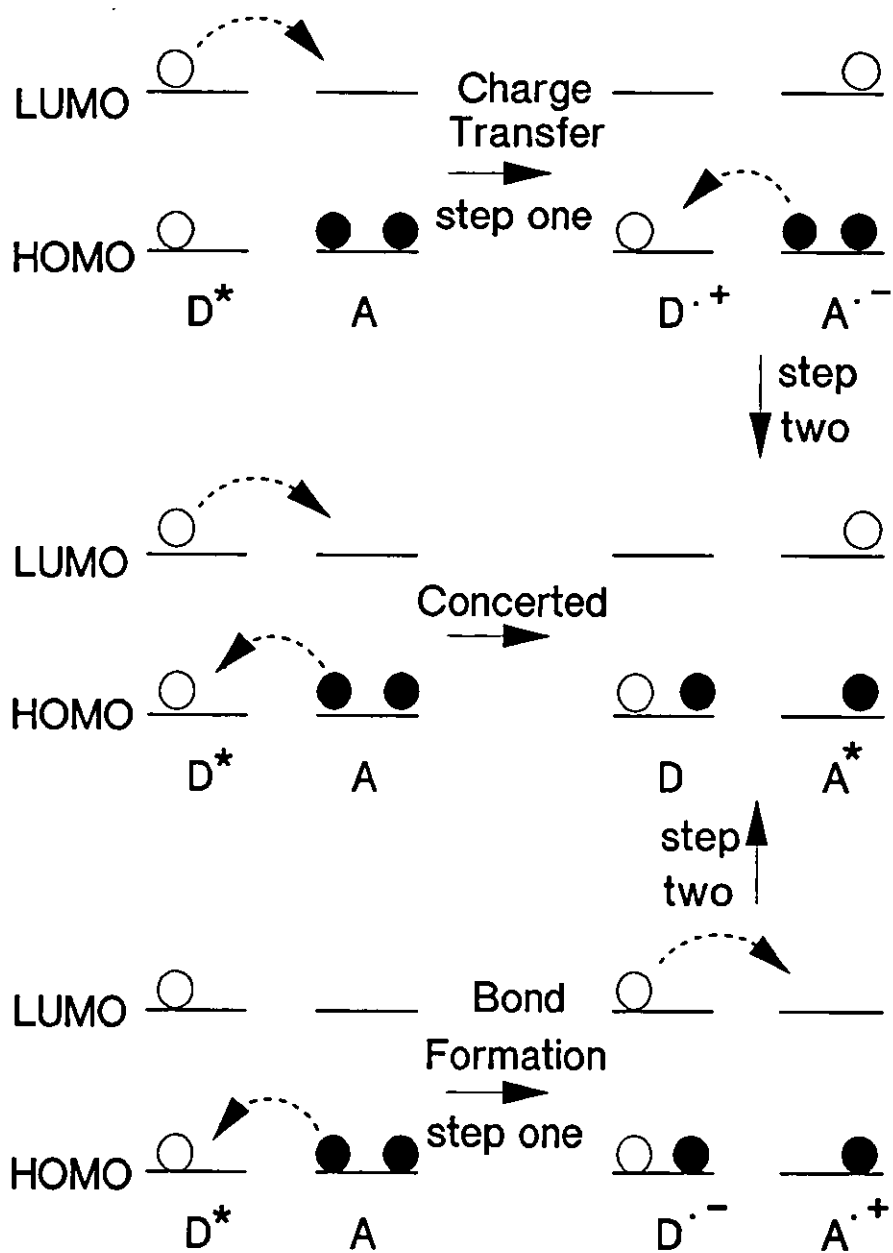


Figure 1.7: Schematic representation of the three possible sequences of events in exchange energy transfer

The equation derived by Dexter⁶ used to describe the rate of electron exchange i.e. the rate of energy transfer is (equation 1.11):-

$$k_{ET}(\text{exchange}) = KJ \exp(-2R_{DA}/L) \quad (1.11)$$

where K is related to the specific orbital interactions, J is the normalised spectral overlap integral (if the spectra overlap anywhere $J=1$) and R_{DA} is the donor-acceptor separation relative to their Van der Waal's radii, L. The rate of energy transfer will fall off exponentially as the separation between donor and acceptor increases, so this mechanism only operates over a small separation range (0-15Å). Triplet-triplet energy transfer proceeds almost exclusively via the collisional mechanism due to the low value of ϵ_a for the S_0 to T_n transition. The collisional mechanism is not dependent on the absorption characteristics (ϵ_a) of the acceptor whereas the coulombic mechanism is sensitive to the value of ϵ_a for the acceptor transition (explained below). A special case of the exchange mechanism is triplet triplet annihilation where both donor and acceptor are in their triplet excited states and following electron transfer give one higher excited state molecule and a ground state molecule. The highly excited state is often the S_1 excited singlet and its subsequent decay gives rise to P-type delayed fluorescence.

1.2.1.3. Coulombic (induced dipole) mechanism.

The exchange mechanism depends on the electronic interactions of the charge clouds between the donor and acceptor molecules whereas the coulombic mechanism depends on the electrostatic interactions. Coulombic resonance interaction occurs via the electromagnetic field and unlike the exchange mechanism does not require physical contact of the interacting partners. The mechanism involves the induction of a dipole oscillation in the acceptor (A) by the donor (D^*). There is no exchange of electrons (represented by circles) from the donor to the acceptor molecule or vice versa (Figure 1.8). The orbital motion of electron 1 causes perturbation in the orbital oscillations of electron 2. If resonance occurs the two transitions occur simultaneously, with electron 2 being excited and electron 1 relaxing.

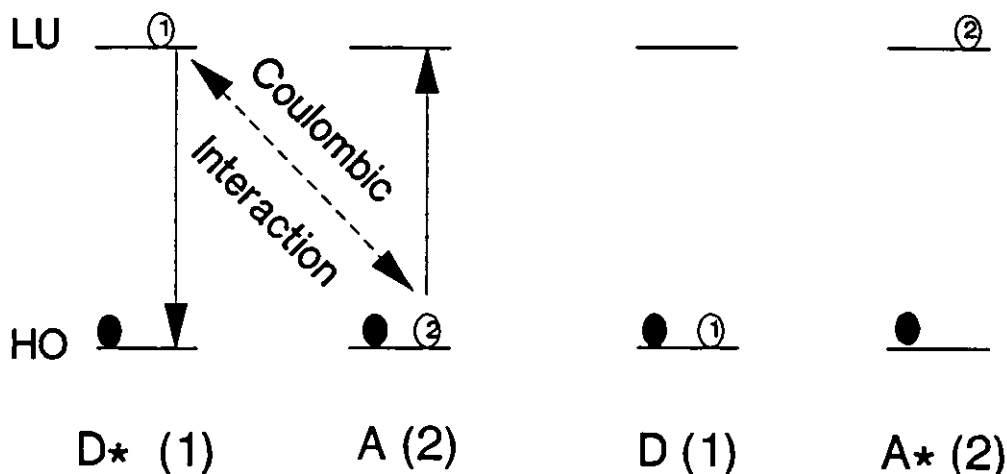


Figure 1.8: Schematic representation of coulombic energy transfer

The rate of energy transfer can be described by the Forster⁷ equation :-

$$k_{ET}(\text{Coulombic}) = k \frac{\kappa^2 k_D^0}{R_{DA}^6} J(\epsilon_A) \quad (1.12)$$

where k is a constant determined by experimental conditions such as refractive index of the solvent and concentration, and κ^2 takes account of the fact that the interaction between two oscillating dipoles depends on the orientation of the dipoles in space. The term $J(\epsilon_A)$ is similar to the spectral overlap integral except that now it is dependent on the absorption characteristics of the acceptor. The rate of energy transfer decreases as separation increases at a rate of $1/R_{DA}^6$ and operates up to separation distances of 50\AA . Fluorescence quenching (singlet-singlet energy transfer) is an example of the coulombic mechanism, singlet-singlet transitions are strongly allowed and usually have large ϵ_A values, making the coulombic mechanism more likely to dominate over the exchange mechanism.

1.2.2. Electron transfer.

An electronically excited state molecule can be expected to be both a better electron donor and electron acceptor than its ground state. This can be explained by the increased energy of the promoted electron and the resulting reduction in ionization potential; the increased electron affinity of the molecule is due to the "hole" left behind when the electron was promoted. Thus redox reactions are more likely to occur in the excited state than the ground state. Rehm and Weller studied fluorescence quenching via exciplex formation of many aromatic compounds by amines in hexane⁸. The overall free energy change for electron transfer (ΔG_{et}^0) in J mol^{-1} can be determined from the redox potentials of the reactants and is given by equation 1.13 :-

$$\Delta G_{et}^0 = F(E_D^{ox} - E_A^{red}) + \Delta\omega \quad (1.13)$$

where F is the Faraday constant ($9.6485 \times 10^4 \text{ C mol}^{-1}$), and E_D^{ox} and E_A^{red} are the oxidation and reduction potentials of the electron donor and acceptor respectively, expressed in volts. $\Delta\omega$ relates to the energy required to form the encounter complex and any solvent reorganisation needed.

1.2.2.1. Marcus theory.

For electron transfer to occur the reactants must be sufficiently close to form an encounter pair. The next step is electron transfer and subsequent reorganisation of the surrounding solvent molecules, thus forming the product. Potential energy surfaces for both the reactant encounter pair and the product can conveniently be described by simple quadratic curves, shown in Figure 1.9. Electronic transitions occur much faster than nuclear reorganisation and thus are governed by Franck Condon restraints. Consequently electron transfer will occur at the intersection of the curves relating to the encounter pair and product. The nuclear configuration remains constant during electron transfer and only the position of the electron changes. An interaction between the reactant and product curves is required to ensure the reaction proceeds on to give the products, and not proceed along the encounter pair curve. However Marcus theory ignores this interaction, which must be sufficiently weak to ensure only small errors are introduced due to its neglect.

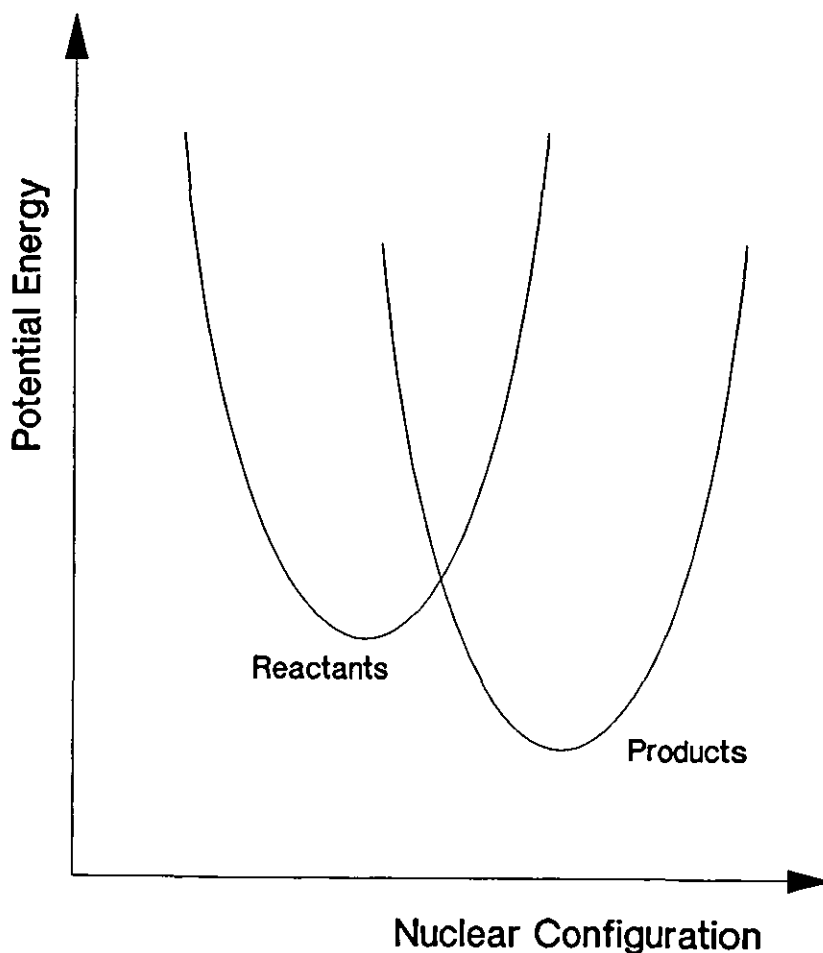
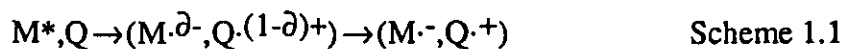


Figure 1.9: Schematic potential energy curves representing reactants and products in the Marcus theory of electron transfer

Marcus theory proposes that the intersection point on the curves can be viewed as an encounter pair which places part of the transferring electron on the reductant and part on the oxidant, shown in Scheme 1.1.



where ∂ represents the fraction of charge transferred in the encounter complex.

The bimolecular rate coefficient k_r for electron transfer in solution can be expressed as :-

$$k_r = Z \exp (-\Delta G^*/RT) \quad (1.14)$$

where Z is the bimolecular solution phase collision frequency and ΔG^* is the free energy of activation and is given by equation :-

$$\Delta G^* = W_r + \frac{\lambda}{4} \left(1 + \frac{\Delta G'}{\lambda} \right)^2 \quad (1.15)$$

where λ is the solvent reorganisation energy, $\Delta G'$ is the free energy for electron transfer and W_r is the Coulomb energy of attraction or repulsion experienced by the reactants as they are brought together in the encounter pair.

Equation 1.15 predicts unusual behaviour as the free energy of electron transfer ($\Delta G'$) becomes large and negative. The quadratic dependence of ΔG^* on $\Delta G'$ means that as $\Delta G'$ decreases from slightly positive to slightly negative the free energy of activation for electron transfer should decrease. Large negative free energies of electron transfer (greater than λ) cause increases in the value of ΔG^* and therefore a predicted reduction in k_r , the rate of electron transfer. Once the value of $-\Delta G'$ is greater than λ the theory breaks down, and this region is often referred to as the "inverted region".

1.3. Flash photolysis.

Flash photolysis is a powerful technique employed for studying rapid reactions, triplet states, isomerisation reactions, etc. and was initially developed by Norrish and Porter in the 1950s⁹. A pulse of exciting light from a laser or flashlamp (positioned at right angles to the analysing beam) is used to generate a transient species which can be monitored by measuring the changes in the amount of analysing light transmitted. Initially measurements were made on the millisecond timescale, but now with the emergence of short pulse lasers experiments are often carried out using nanosecond, picosecond and even femtosecond timescales. The transient changes in concentration of reactants, products or most frequently the intermediates themselves are monitored as a function of time. The decay or production of the transient absorption or emission at one particular wavelength is monitored or the absorption or emission spectrum of the transient is recorded at given times after the exciting pulse. A basic requirement of transmission flash photolysis is that the sample will transmit some analysing light; for solution or gas phase experiments this is usually the case, but many technological photochemical applications involve opaque materials which will not transmit much if any analysing light. In the 1980s Wilkinson et al¹⁰ described an alternative method for the collection of analysing light from a highly scattering or opaque sample. The diffusely reflected analysing light is monitored as a function of time; this requires a small change in the sample geometry used for transmission. The diffusely reflected analysing light yields information about the transients produced, in the same way as transmitted light. Laser flash photolysis and its data analysis will be discussed later in sections 3.8 and 3.9.

1.4. Lasers.

The name laser is an acronym for Light Amplification by the Stimulated Emission of Radiation. A laser consists of a lasing material (solid, liquid or gas) in a tuned optical cavity with mirrors at either end - one of which is partially transparent. Laser radiation is coherent (the light waves are all in phase in both time and space), highly monochromatic and collimated. For laser action to occur we require light amplification by stimulated emission and a resonant optical cavity both of which shall be discussed below. For a more comprehensive discussion of laser operation see references^{11,12,13}.

Stimulated emission occurs when a photon encounters a molecule in an excited state and the incident photon energy is equal to the energy difference between two levels in the excited molecule, causing the emission of another photon and regeneration of the ground state. The important features of the stimulated emitted photon is that the photon is of the same energy, travels in phase and in the same direction as the incident photon, giving a coherent beam.

Consider two energy levels, u (upper) and l (lower), with energies ϵ_u and ϵ_l and populations of N_u and N_l . Normally the distribution of population of molecules among their various energy states will be biased towards the ground state (N_l) according to the Boltzmann equation (equation 1.16).

$$\frac{N_u}{N_l} = \exp\left[\frac{-(\epsilon_u - \epsilon_l)}{kT}\right] \quad (1.16)$$

The absorption of a photon of energy equal to the difference between ϵ_u and ϵ_l (equation 1.17) will result in the promotion of an electron from the lower to the upper level.

$$v = \epsilon_u - \epsilon_l / h \quad (1.17)$$

This excited electron will relax back to its ground state through a relaxation pathway, either by spontaneous or stimulated emission (Figure 1.10)

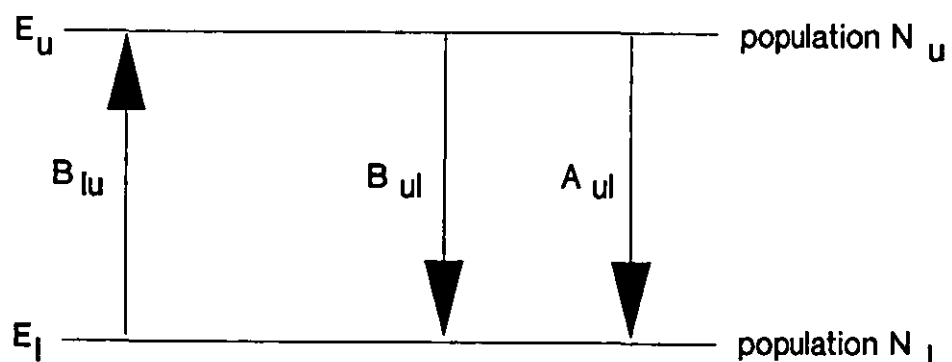


Figure 1.10: Diagram showing stimulated absorption and stimulated and spontaneous emission between two states. Here B_{ul} and B_{lu} are the Einstein B coefficients for stimulated absorption or emission, and A_{ul} is the Einstein A coefficient for spontaneous emission.

Spontaneously emitted light is incoherent due to a random creation of photons resulting in waves of random phase. If a photon of the required energy approaches a medium containing atoms in both the upper and lower states absorption or stimulated emission will occur. Normally both are equally probable, the dominant process depending on the relative numbers of atoms in the upper and lower states. A larger population in the upper level results in stimulated emission dominating, while if there are more in lower, absorption dominates. Population inversions are difficult in two level systems because the incident photon may cause either absorption or stimulated emission. Three and four level systems can achieve inversions much more easily and consequently are used in laser systems.

The Ruby laser (crystalline aluminium oxide doped with chromium) is an example of a 3-level system. Figure 1.11 shows the simplified system, state C is populated by optical pumping which rapidly decays via a radiationless transition to populate B, building up a population inversion. The transitions C to B must be rapid and B to X relatively slow so the population of B increases at the expense of C, and for laser action to occur the population of B must exceed the ground state population (X). 3-level systems are not run in continuous mode due to the difficulty in maintaining a population inversion.

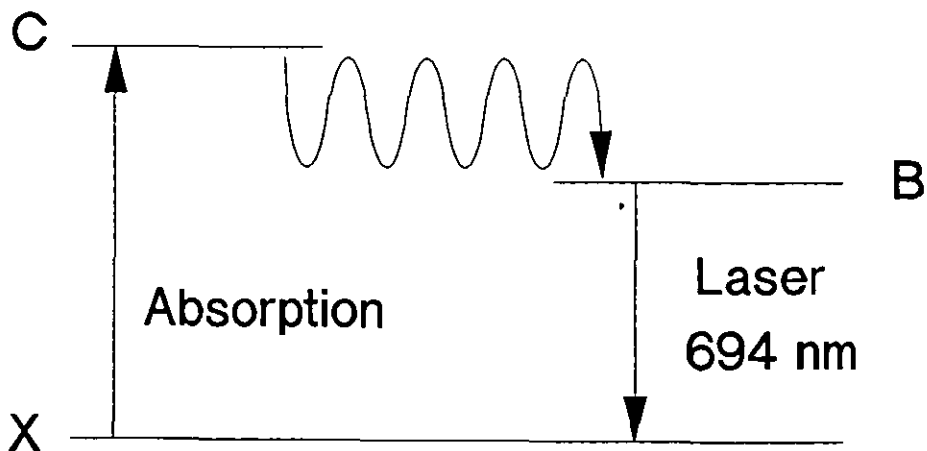


Figure 1.11: Schematic representation of a three level laser system

The Nd-YAG (neodymium yttrium-aluminium garnet) laser operates as a 4-level system and is illustrated in Figure 1.12. 4-level systems are potentially more efficient than 3-level due to the additional level (A), so the population of B no longer has to be greater than that of the ground state. Level A, to which the emission occurs, is initially unpopulated, so there is no need for large amounts of the ground state to be converted to C. State A must be rapidly depopulated if the laser is to be operated in continuous wave mode in order to maintain a population inversion with respect to B. Organic dye lasers such as those based on coumarin or rhodamine are a form of 4-level lasers. Here only two electronic levels are involved, but vibrational sub-levels within these states form the "B" and "A" levels required. Organic dye lasers are often pumped using other lasers, in place of the flashlamp used in the Nd-YAG system.

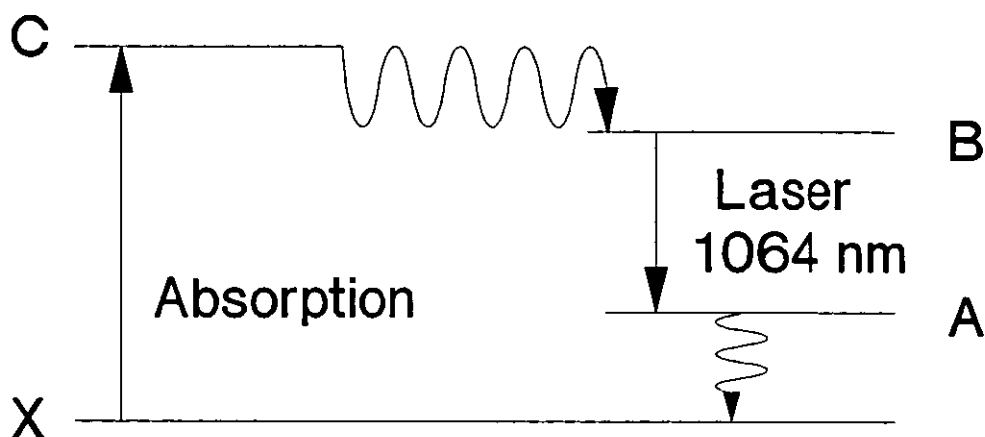


Figure 1.12 : Schematic representation of a four level laser system.

Population inversions are achieved by subjecting the lasing medium to intense excitation using two main techniques, optical pumping or by high-voltage discharge. Optical pumping techniques, where the lasing material is surrounded by a flash tube emitting light at frequency sufficient to excite the lasing material, are often used in solid state lasers. Electrical discharges are often used in gas lasers to cause ionisation and subsequent acceleration of charged particles in an electric field which then collide with particles of the lasing medium.

Once the population inversion is achieved, spontaneous emission from an excited molecule (M^*) releases a photon along the axis of the laser into a medium containing a high concentration of excited molecules. Stimulated emission dominates over stimulated absorption, and releases more photons to trigger yet more stimulated emission. Inverted populations in a laser medium within a resonant optical cavity amplify stimulated emitted photons in this way as they

pass back and forth between the mirrors. Daughter photons have the same energy and polarisation, pass in same direction and are in phase. Most lasers are multipass because unless the pumping is very intense the beam will not be very strong after just one pass of the laser cavity.

The Optical cavity must be resonant at the wavelength of radiation, must sustain laser action and improve the spatial and temporal coherence of any output beam. The fixed cavity length means maximum amplification is only achieved for light waves which exhibit nodes at the mirrors satisfying the so called standing wave condition :-

$$\lambda = \frac{2d}{n} \quad (1.18)$$

where d is the cavity length and n is the number of half wavelengths contained within length d. This places quite severe restrictions on the form of the wave and the frequencies of radiation, but a number of modes will satisfy this and these waves are called axial or longitudinal cavity modes - discussed briefly later.

With each pass through the cavity the intensity of the beam will increase, but the gain will decrease due to the reduction in the population inversion. Stimulated emission ceases when the initial population inversion has been destroyed, the duration of this stimulated emission determining the length of the pulse of radiation emitted through the partially transmitting end mirror. Continuous wave lasers must replace the excited species as fast as they are lost (by stimulated emission), to maintain the population inversion. Multiple passes within the cavity provide a considerable degree of collimation and hence a strongly directional and low divergence output beam.

The waves propagating through the laser cavity oscillate along the axis of the laser (axial or longitudinal modes) and slightly off axis (transverse modes).

Transverse modes.

The laser cavity is designed to amplify light travelling down the optical axis of the laser. A photon travelling at right angles to this axis may cause stimulated emission, but will not be amplified to form a laser beam because there will not be enough gain to overcome its losses. If a photon is only slightly off axis the wave

may be able to zigzag between mirrors enough times producing sufficient gain to overcome its losses, resulting in a complicated intensity distribution across the output mirror.

A laser may consist of a mix of different transverse modes, they are described in terms of TEM_{pq} and examples are given in Figure 1.13 where TEM stands for transverse electric and magnetic fields, p and q describe number of intensity minima across the laser beam in perpendicular directions. The modes are governed by the mirrors and apertures within the cavity. The ideal operating mode is TEM_{00} , which has a gaussian intensity profile across the beam and can be achieved by placing an iris in the cavity to cut out all off axis waves.

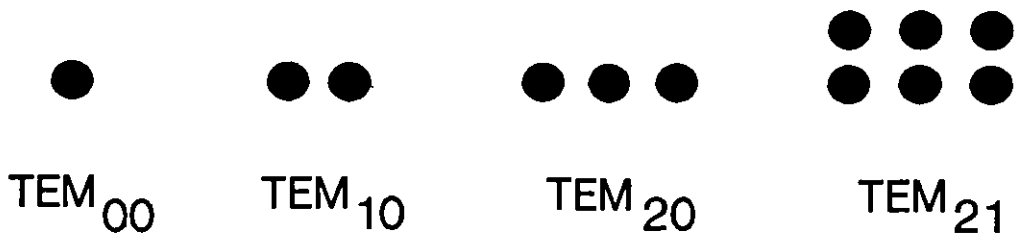


Figure 1.13: Laser output energy distributions corresponding to various transverse modes

Axial modes

Modes of oscillation along the length/axis of the cavity consist of a large number of frequencies given by :-

$$\nu = \frac{nc}{2d} \quad (1.19)$$

where n is the number of half-wavelengths contained in length d and c is the speed of light. The occurrence of more than one axial mode results in an increase in the output bandwidth. The quality of a laser can be defined by the mean frequency divided by the distribution width.

1.4.1. Q-switching.

Q-switching can be employed to increase the peak power of the laser and reduce pulse length. The quality factor of the laser cavity can also be expressed as :-

$$Q = \frac{2\pi\nu_0(\text{energy stored in mode})}{\text{energy lost per second from mode}} \quad (1.20)$$

The quality Q of a laser can suddenly be improved after allowing the population inversion to keep building up to well above its normal level by preventing laser action and then 'Q-switching' to suddenly depopulate it. This results in a very rapid increase in photon density inside the cavity, leading to a rapid reduction in the population inversion through stimulated emission producing a short intense pulse of radiation. This action is called 'Q-switching' because the system suddenly switches from high cavity loss (low Q) to low loss (high Q), all the energy accumulated in the inversion is released as a short (a few nanoseconds) and giant pulse.

Techniques of Q-switching

Different methods for preventing lasing action have been used by inserting a shutter of some sort which can be opened very rapidly (chemical, mechanical or optical) between the laser rod and the totally reflecting mirror in the cavity. One of the earliest Q-switches involved a rotating slit in the cavity, this was soon abandoned in favour of rotating one of the laser end mirrors so lasing could only occur when the mirror was very nearly perpendicular to the laser axis.

Passive Q-switching

Weak solutions of dyes that bleach at high light irradiances (saturable absorbers) have been used as Q-switches. The dye solution is placed in a 1mm cell in the laser cavity, up against the 100% reflecting mirror. When pumping starts the relatively low transmission of the dye cell means that the medium can be pumped to give a high degree of population inversion before the photon population begins to build up in the cavity. To be most effective the dye solution must rapidly bleach to give a high optical transmission during the initial photon build up (before a significant amount of the initial population inversion has been depopulated). Dye

solutions as Q-switches are simple and cheap, creating pulses of 10 - 20 nanoseconds, but there are a number of drawbacks. Dye solutions can degrade on use and operate better with circulation of the dye (between pulses) using a pump and reservoir. Problems can occur when there is incomplete bleaching of the dye, greatly reducing the final laser output.

Electro-optical Q-switching.

Several non-mechanical switching techniques may be used for Q-switching, and the most useful one is based on the Pockels effect. The Pockels effect occurs in uniaxial crystals which change their refractive index and thus rotate the plane of light when an electric field is applied. The Pockel cell sits between matched polarisers and acts as a switch, with no voltage across the cell the photons pass through it, so when a voltage is applied the population inversion builds up and rapidly depopulates when the voltage is removed.

Acousto-optic switching

The acousto-optic effect can be utilised to give a Q-switch which is a bit slower than those based on Pockels effect. When an acoustic wave travels through a medium such as silica, it causes local changes in the material density which gives rise to changes in the refractive index. As stated earlier it switches slowly, but it has a high repetition rate i.e. it is ready to use again faster.

Mode-locking

Pulses of even shorter duration can be obtained with mode-locking. In a free running multimode laser the different modes oscillating within the cavity have essentially random phases and amplitudes. The laser modes can be forced to oscillate with similar amplitudes and / or with their phases locked yielding a train of pulses whose individual components have durations on the timescale of ps. Mode-locking is achieved by modulating the gain of the laser with a period equivalent to the round trip time of the laser cavity¹⁴.

1.4.2. Non-linear effects.

The high intensity radiation emitted from lasers enables generation of other wavelengths of light in addition to the fundamental wavelength. The technique of second harmonic generation (frequency doubling) is a popular method of extending the normal frequency range of a laser, where half the original wavelength is produced. The incident radiation produces linear and non-linear polarisation effects within the doubling crystal. The applied field interacts with dipoles in the crystal causing oscillations, at low fluences the vibrations are small and the frequency of the radiation emitted, as a consequence of the vibrations, is equal to that of the incident beam. As the incident radiation ν increases in intensity so do the amplitudes of vibration and non-linearities occur, the strongest of which being the second harmonic i.e. 2ν . Liquids, gases and some solids cannot exhibit second harmonic generation, due to the material having a centre of symmetry which reduces non-linear effects to virtually zero. For efficient harmonic generation both the input beam and frequency doubled beam must travel with the same speed through the crystal, ensuring that the two beams retain the same phase relationship. This assures that the generated second harmonic radiation at any point in the crystal always adds coherently to the second harmonic radiation already present. Non-linear effects can also be applied to the mixing of two frequencies of light simultaneously incident on a crystal. Examples of the crystals used for doubling and tripling (frequency mixing) the fundamental frequency in a Nd-YAG laser are DCDA (deuterated caesium dihydrogen arsenate) and KDP (potassium dihydrogen phosphate) respectively.

1.5. Reflectance photochemistry.

Two types of reflectance can be identified for reflection of light from any surface; specular (mirror reflection from sample surface) which is at same angle to the normal as the incident beam and diffuse reflection which is random and non-directional. Specular reflection occurs to a certain extent at all surfaces which constitute boundaries of condensed phases and equations have been derived by Fresnel and Snell to describe specular reflection, refraction and polarization in non-absorbing media. Discussions of these equations can be found in the literature^{15, 16}, the work in this thesis is concerned with diffusely reflected light and not regular reflection so only the main equations will be shown here.

Snell's law of refraction states that for refraction at a boundary of two phases with refractive indices of n_1 and n_2 (equation 1.21) :-

$$n_1 \sin \theta_i = n_2 \sin \theta_t \quad (1.21)$$

where θ_i is the angle of the incident beam in the medium with a refractive index n_1 and θ_t is the angle of the beam following refraction at the boundary, both angles are measured with respect to the sample normal.

The regular reflection (R_{reg}) at such a boundary can be given by equation 1.22 :-

$$R_{reg} = \frac{1}{2} \left[\frac{\sin^2(\theta_i - \theta_t)}{\sin^2(\theta_i + \theta_t)} + \frac{\tan^2(\theta_i - \theta_t)}{\tan^2(\theta_i + \theta_t)} \right] \quad (1.22)$$

Diffusely reflected light is observed with matt samples and arises from penetration of a portion of incident beam into the interior of the sample. The interior of the sample consists of discrete particles which will scatter and partially absorb the incident light before it finally emerges at the surface following multiple scattering and absorption at many particle boundaries.

The Bouguer-Lambert equation (equation 1.23) can be used to predict the attenuation of the diffusely reflected light (I) as a function of penetration depth through an absorbing medium :-

$$I = I_0 \exp [-Kx] \quad (1.23)$$

where I_0 and I are the intensity of light entering and leaving the portion of sample of thickness x respectively and K is the absorption coefficient. This equation predicts that the intensity of reflected light decreases exponentially with increasing penetration depth into the sample, and is an important factor when considering transient concentrations as a function of penetration depth following laser flash photolysis.

The Lambert cosine law originates from the fact that when a white matt surface is irradiated with a constant intensity the surface appears uniformly light at all angles. Radiation (B) from a non-absorbing matt surface is given by equation 1.24 :-

$$B = \left(\frac{I_0}{\pi}\right) \cos \alpha \cos \theta \quad (1.24)$$

where I_0 is the incident radiation strength, α is the angle of incidence and θ is the angle of observation. This results in the reflected radiation being distributed symmetrically with respect to the surface normal, independent of the angle of incidence. The Lambert cosine law has been shown experimentally to hold for highly scattering samples and small values of α and θ .

Early theories for the origin of diffuse reflectance from a matt surface assumed that the combined specular reflections from a large number of particles, statistically distributed at all possible angles with respect to the macroscopic surface, were responsible for the scattering of incident radiation. This theory was later modified to assume that the diffusion of light occurs by multiple scattering by individual particles within the interior of the sample. Further investigations have suggested both regular and diffuse reflection are always present, and their relative proportions depending on nature of scattering medium under investigation. The situation is further complicated when an opaque sample also absorbs some of the radiation.

The Beer-Lambert law (section 1.1) can be used to define the dependence of absorbance on ground state absorber concentration for use in transparent systems. In the case of opaque or highly scattering samples one cannot use transmission spectroscopy and consequently the Beer-Lambert law is not applicable. The most widely used approach to the problem of describing the behaviour of light in diffusing media is that of a solution of simultaneous differential equations, which describe the diminution of light intensity within the sample due to scattering and absorption within the sample. The most widely applied theory relating "absorption" to concentration in opaque samples is that of Kubelka and Munk.

1.5.1. Kubelka Munk Theory.

Kubelka Munk theory considers light diffusely reflected from a layer of sample with infinite lateral extensions following irradiation with monochromatic light. The irradiated sample consists of randomly distributed, uniformly absorbing and scattering particles whose dimensions are far less than the layer thickness. If one considers two light fluxes I and J to be travelling in opposite directions through this sample and perpendicular to the irradiated sample surface, the reduction in the intensity of I and the generation of J in a thin slice of thickness dx can be given by two differential equations 1.25 and 1.26 :-

$$dI_{(x)} = -(K + S)I_{(x)} dx + SJ_{(x)} dx \quad (1.25)$$

$$dJ_{(x)} = +(K + S)J_{(x)} dx - SI_{(x)} dx \quad (1.26)$$

Figure 1.14 shows a schematic representation of a layer of sample consisting of absorbing and light scattering particles, following monochromatic irradiation with flux I_0 . Radiant fluxes $I_{(x)}$ and $J_{(x)}$ are travelling in the $+x$ and $-x$ directions respectively and at $x=0$ are denoted by I_0 and J_0 , where x is the penetration depth ($x=0$ is the illuminated surface) and D is the layer thickness.

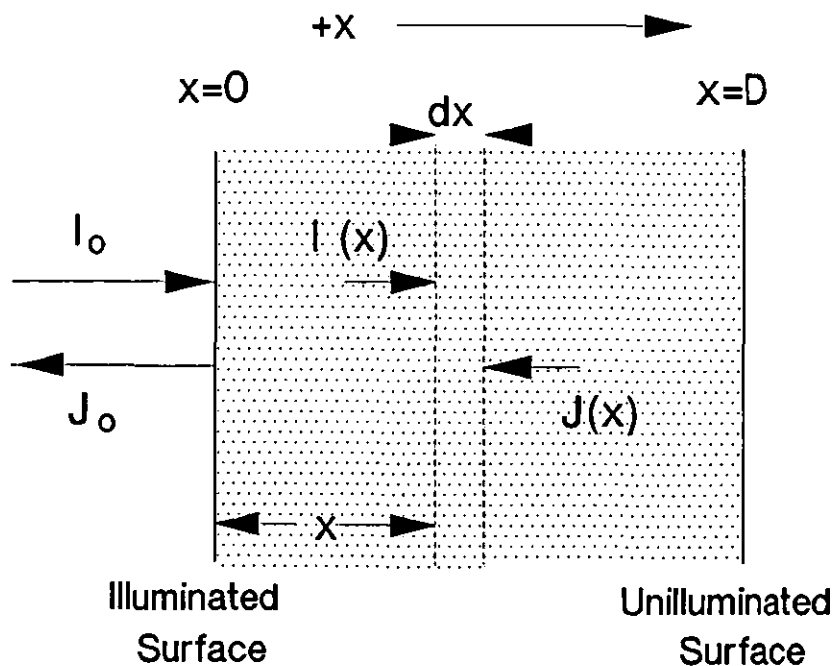


Figure 1.14: Schematic representation of a diffusely scattering layer showing the counterpropagating light fluxes and co-ordinate system

The two differential equations 1.25 and 1.26 can be solved for a layer so thick that any increase in D does not affect the observed sample reflectance, giving :-

$$I_{(x)} = I_{(0)} \exp(-bSx) \quad (1.27)$$

and

$$J_{(x)} = RI_{(0)} \exp(-bSx) \quad (1.28)$$

where

$$b = \frac{(K^2 + 2KS)^{1/2}}{S} = \left(\frac{1}{2R} - R \right)$$

K and S refer to the absorption and scattering coefficients respectively and R is the reflectance of an infinitely thick layer at the illuminated surface (x=0).

Division of equation 1.28 by equation 1.27 when x = 0, gives :-

$$R = \frac{J_0}{I_0} \quad (1.29)$$

When the layer is so thick that no light is transmitted through the sample, the reflectance R can be replaced by (R_∞), the reflectance of an optically thick sample. Further manipulation of equations 1.27 and 1.28 result in the more familiar form of the Kubelka Munk equation (equation 1.30) :-

$$F(R_\infty) = \frac{(1 - R_\infty)^2}{2R_\infty} = \frac{K}{S} \quad (1.30)$$

where F(R) is the Remission Function, a unitless quantity which for a uniform distribution of absorbers is a linear function of absorber concentration. K and S are the absorption and scattering coefficients respectively, both of which have units of reciprocal distance (usually cm^{-1}).

The absorption coefficient K can be expressed in equation 1.31 in terms of absorber concentration (C in units mol l^{-1}) and naperian absorption coefficient (ϵ with units $\text{l mol}^{-1}\text{cm}^{-1}$)

$$K = \omega\epsilon C \quad (1.31)$$

where ω is a geometric factor which allows for the angular distribution for diffusely reflected light, which for an ideal diffuser is equal to 2. Thus for an ideal diffuse reflector the Remission Function may also be written as equation 1.32 :-

$$F(R_{\infty}) = \frac{2\epsilon C}{S} \quad (1.32)$$

The scattering coefficient is not so easily quantified. The scattering coefficient is inversely proportional to average particle size i.e. as the particle size increases the scattering coefficient decreases. Kortum and Oelkrug¹⁷ were able to determine the scattering coefficients for glass filter powders with known particle dimensions at given wavenumbers. For weakly absorbing materials as the particles decrease in size the reflection from its irradiated surface becomes larger. This is due to the inability of the incident radiation to penetrate as deeply into the sample as for samples with larger particles.

Chapter 2

Photochemistry on Surfaces

2. Photochemistry on surfaces.

The photophysical and photochemical behaviour of adsorbates on solid substrates can provide valuable information regarding the interactions between the adsorbate and the substrate, the nature of the adsorption sites and mobility restrictions imposed on the probe by the surface. The substrate can be used to "hold" the adsorbed molecule possibly in a fixed orientation, in the form of physisorption or chemisorption. Physisorption arises when molecules are loosely held to the surface by for example hydrogen bonds, thus the molecular and electronic structure of the molecule should remain unchanged. Chemisorption involves the formation of a new bond between the molecule and the surface, there are two types of chemisorption - associative (the initial system remains intact) and dissociative (the molecule splits creating a completely different system). Recently much work has been carried out on the primary photochemical processes of molecules adsorbed on surfaces, such as silica gel, γ -alumina, zeolites, cellulose and dyed fabrics. A number of excellent reviews¹⁸⁻²¹ have been written detailing much of the work carried out to date. This thesis is concerned with the properties of anthracene adsorbed on silica gel, so the following review will concentrate on the photochemistry of aromatic molecules adsorbed on silica gel with relevant discussions of work carried out on zeolites and γ -alumina. A brief discussion of the nature of the surface of silica gel, alumina and zeolites will follow.

2.1. Nature of Silica gel.

Silica gel is a porous solid, consisting of siloxane and silanol moieties which strongly influence the reactivity of the silica. The pore size may vary considerably from micropores of <2 nm to macropores of >200 nm depending on the preparation conditions. The silanol functions are the principle sites for adsorption²²⁻²⁴ and can be described as isolated, geminal or vicinal and are as shown in Figure 2.1. Hydration of the silica gel surface has an appreciable effect on its adsorption properties. The water can be removed through heating. At temperatures below 400 K^{25,26} only the physisorbed water is removed from the surface. The silanol groups start to condense producing siloxane bridges and evolving water above 400 K, so the interactions between the surface and the adsorbed molecule are greatly dependent on the pretreatment temperature of the surface. There are on average between four and five^{26,27} silanol groups per nm^2 , with this number decreasing with increasing pretreatment temperature²⁸. The

distribution of silanol functions across the surface is not uniform^{29,30} and are believed to be concentrated in small surface areas.

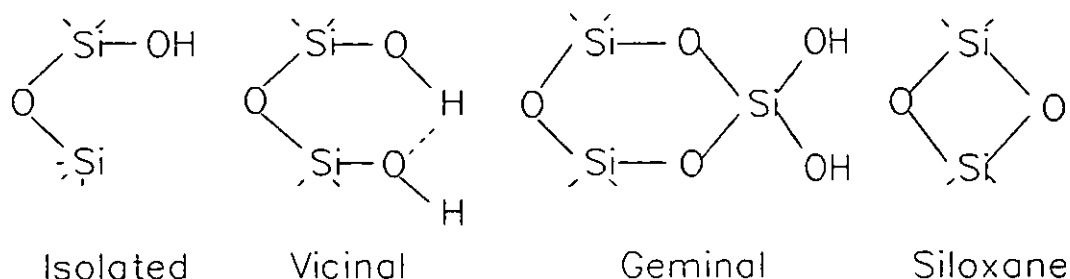


Figure 2.1 : Silanol functions present on the silica gel surface.

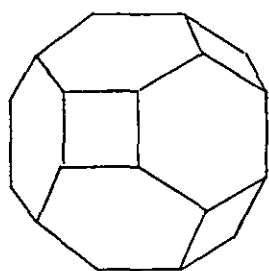
2.2. Nature of γ -Alumina.

Alumina occurs in various crystalline forms α -, η - and γ - phases, with γ -alumina being the least acidic. γ -Alumina, like silica gel is covered in hydroxyl groups and physisorbed water which can be removed through heating. There are a variety of adsorption sites on the alumina surface, their presence being highly dependent on the pretreatment temperature³¹. At low pretreatment temperatures (400 K) only the physisorbed water is removed leaving physisorption sites for the adsorption of molecules. There are a further two sites observed, at high pretreatment temperatures (above 1000 K) Lewis acid sites are formed where coordinatively unsaturated anions are exposed to the surface following condensation of the hydroxyl groups, and at intermediate temperatures a mixture of the physisorption and Lewis acid sites is observed, creating "charge transfer sites"³¹.

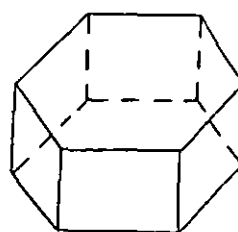
2.3. Nature of Zeolites^{18,20}.

Zeolites are crystalline aluminosilicates minerals and consist of $(\text{SiO}_4)^{4-}$ and $(\text{AlO}_4)^{5-}$ tetrahedra, linked by their corners, thus forming channels and cages of discrete sizes. As a consequence of the differences in charge between these tetrahedra, cations such as lithium, sodium, potassium, calcium or magnesium are incorporated into the zeolite cages and channels to balance the overall charge. Zeolites can be represented by the empirical formula $M_{2/n} \text{Al}_2\text{O}_3 (\text{SiO}_2)_x (\text{H}_2\text{O})_y$,

where M is a cation of valence n, and x and y are integer numbers. The basic building blocks in zeolites are the $(\text{SiO}_4)^{4-}$ and $(\text{AlO}_4)^{5-}$ tetrahedra which combine to form secondary building units such as sodalite cages and hexagonal prisms as shown in Figure 2.2. The most common zeolites used in photochemical studies are zeolites A, X and Y. Zeolite A consists of sodalite cages joined to other sodalite cages via their 4 sided faces, which form additional inner α -cages. The sodalite cages have small entry apertures of 2.6 Å and the entrances into the α -cages are 4 Å. Zeolites X and Y are again comprised of sodalite cages, and these are joined to one another by hexagonal prisms (on their 6 sided face), thus making the inner cage (supercage) of zeolites X and Y larger than the inner cage (α -cage) of zeolite A. The entry apertures of the supercages in zeolites X and Y are approximately 7 Å. The difference between zeolites X and Y is the ratio of silicon to aluminium resulting in differences in their acidity, ion exchange capacity and adsorption. Zeolite X generally has approximately 1.4 times more $(\text{SiO}_4)^{4-}$ tetrahedra than $(\text{AlO}_4)^{5-}$, and zeolite Y has approximately 2.5 times more $(\text{SiO}_4)^{4-}$ than $(\text{AlO}_4)^{5-}$ tetrahedra.



Sodalite Cage



Hexagonal Prism

Figure 2.2 : Structures of a sodalite cage and a hexagonal prism found in zeolites. The lines represent oxygen bridges and the intersections are Si or Al atoms.

2.4. Properties of molecules adsorbed on surfaces.

The nature of a surface determines the spectral properties of individual molecules, the mechanisms of their photochemical reactions and product distribution. Early work on the adsorption of molecules on surfaces was restricted to steady state absorption and fluorescence emission techniques until the advent of diffuse reflectance laser flash photolysis¹⁰. The initial diffuse reflectance laser flash photolysis studies were carried out studying aromatic hydrocarbons adsorbed on γ -alumina. The applicability of this technique was proved by comparison of the triplet-triplet absorption spectra observed on γ -alumina¹⁰ with those previously reported in solution. The triplet-triplet absorption spectra of naphthalene, biphenyl, pyrene, triphenylene and phenanthrene adsorbed on γ -alumina were recorded. The differences between the spectra of the adsorbed molecules on γ -alumina and those recorded in solution were assigned as arising from charge-transfer states formed on adsorption to the γ -alumina surface. Many molecules have been studied as probes on surfaces, for example arenes^{10,32-49} azaaromatics⁵⁰⁻⁵², conjugated aromatics⁵³⁻⁵⁵ ketones⁵⁶⁻⁶³ amines⁶⁴⁻⁶⁶ and dyes⁶⁷⁻⁷¹ such as acridine orange⁷⁰ and oxazine dyes⁶⁹.

Aromatic compounds are often chosen as probes for investigating surface properties as their properties in solution are well known and reported. Small shifts and the maintenance of the vibrational structure are observed in the fluorescence spectra of arenes adsorbed on silica gel in many studies, where only physisorbed water has been removed. This suggests that the adsorption process for aromatic hydrocarbons involves weak dispersion interactions. The physisorption of aromatics to silica gel is via "hydrogen" bonding through their π electron clouds and the silanol groups on the surface. Consequently the absorption and fluorescence emission spectra of aromatic hydrocarbons adsorbed on silica gel are very similar to those obtained in solution. The fluorescence and absorption spectra observed on silica gel³⁵⁻³⁸ are generally broader than those obtained in solution due to the interactions with the varied silanol environment. This behaviour was also observed by Leermakers et al³⁹ using a silica gel-solvent slurry.

Surface coverage plays an important role in the emission properties of a molecule. The formation of pyrene aggregates on silica gel^{35-37,40,41,72,73} is confirmed by the appearance of a broad excimer-like emission band in the fluorescence spectra and by the differences in excitation spectra when viewing the excitation spectra for the monomer and excimer. The excimer-like emission band arises following both

static (aggregation) and dynamic mechanisms. The aggregation can occur at extremely low surface coverages (1% of a monolayer) and has been shown using time-resolved emission^{35,40-45} to be a consequence of an inhomogeneous distribution of pyrene due to its adsorption at preferred sites. Time-resolved emission studies have also revealed the multi-exponential decay of both the monomer and excimer emission, arising from the inhomogeneous interactions with the surface. The coadsorption of long chain alcohols and polyalcohols^{35,41,72} render the surface more homogeneous by blocking silanol groups, thus reducing aggregation and encouraging mobility. The mobility of the arenes is increased due to the reduction in the interactions with the silanol groups and dynamic excimer formation can be seen using time-resolved studies to "grow" in. Similar studies have been carried out on γ -alumina^{31,72,74} controlled pore glasses^{72,75} and in zeolites⁷⁶⁻⁷⁸. Pyrene excimer emission and aggregation due to an inhomogeneous distribution of adsorbed pyrene was also observed as in the case of silica gel. Only at very high concentrations of anthracene⁷⁹ included in zeolites was excimer emission detected.

2.4.1. Pore size effects on molecules adsorbed on silica gel.

Work has been carried out studying the effect of silica gel pore size on excimer formation⁴³, oxygen quenching^{80,81} and radical decay⁸²⁻⁸⁴ of adsorbed molecules. Pyrene excimer formation was found to be more readily observed in porous glasses with small pore diameters⁴³. The pore sizes studied were 40 Å, 80 Å and 300 Å, the orientation forced on the molecules by the 40 Å pore glass enhancing pyrene excimer formation. Oxygen quenching on surfaces is dynamic and static in nature and the oxygen is both in the gas phase and adsorbed on the surface. Oxygen quenching experiments have been carried out comparing fluorescence quenching by oxygen on a non-porous silica gel with silica gel with a pore size of 60 Å. These experiments revealed a slower rate of oxygen quenching for the non-porous silica gel than those with silica gel with 60 Å pores⁸¹ and the quenching mechanism was assumed to be via surface diffusion of the oxygen. The quenching of triplet benzophenone on a homogeneous series of silica gels was studied by Turro et al⁸⁰. These experiments revealed an increase in the rate of triplet quenching with increasing pore size and assumed a predominantly Langmuir-Rideal (gas phase bombardment) mechanism of quenching. The stability of cation radicals produced by irradiation of molecules adsorbed on a series of silica gels of differing pore sizes was studied. Alkylphenothiazine⁸³ and N,N,N',N'-tetramethylbenzidine⁸⁴ cation radicals both gave a larger photoyield

and demonstrated a greater stability (longer lifetime) when substrates with small pores were used. The dimethylviologen radical cation is formed on irradiation of dimethylviologen chloride (at 320 nm) adsorbed on silica gel⁸². The stability of the dimethylviologen radical cation on silica gel is influenced by the proximity of its counter chloride. The chloride ion and methylviologen radical cation will be held relatively close together on silica gels with small pores and further apart on silica gels with larger pores. Consequently the methylviologen radical cations are more stable on silica gels with large pores than on those with smaller pores⁸².

2.4.2. Effect of pretreatment temperature on the mobility of the adsorbed molecule.

Molecules are physisorbed onto silica gel through interactions with the silanol groups. Consequently the mobility of arenes on silica gel is dependent on pretreatment temperature. The mobility of aromatics on the silica surface has been seen to decrease with increasing pretreatment temperature^{35,51,85}. This is due to the reduction in the number of silanol groups and formation of siloxane units. Siloxane units greatly restrict mobility on the surface. An increase in the pretreatment temperature of γ -alumina also shows this trend⁸⁶. The reduction in hydroxyl groups and the formation of Lewis acid sites on γ -alumina with increasing pretreatment temperature causes a decrease in mobility as pretreatment temperature is increased. This is due to the Lewis acid sites having stronger interactions with the adsorbed molecules than the hydroxyl groups do. Thus the molecules are held more strongly due to the increased number of Lewis acid sites. Diffuse reflectance laser flash photolysis experiments carried out studying the quenching of the pyrene triplet by ferrocene when adsorbed on γ -alumina⁸⁶ illustrate the reduction in the mobility of molecules with increasing pretreatment temperature.

2.4.3. Surface Reactions.

The mobility of molecules on surfaces is often probed by triplet-triplet annihilation^{50,51}, and dynamic excimer formation³⁵. Adsorption of a single species for the determination of diffusion rates is fairly simple as there is only one diffusion rate to be concerned with. An alternative method for the study of diffusion on surfaces involves the coadsorption of another molecule for energy^{31,86} or electron⁸⁶ transfer. The adsorption of different donor and acceptor molecules on a surface can complicate the calculation of the diffusion rates if both

the adsorbed molecules move. Often one of the molecules is fixed to the surface, thus only one diffusion rate needs to be accounted for.

The development of diffuse reflectance laser flash photolysis has enabled the study of transient spectra of molecules adsorbed on opaque surfaces. Numerous triplet-triplet absorption spectra and their similarities with solution measurements have been reported. In addition to triplet-triplet absorption¹⁰, features relating to aromatic radical cations are also often observed. The radical cations often show great stability on the surface, as compared with the radical cation in solution, due to the nature of the oxide surface. The detection of aromatic radical cations through photoionization on silica^{54,87-89} γ -alumina^{31,34,53,74,86,90} and in zeolites^{47,55,77-79,87,91-96} have been reported. The nature of production of the radical cation is dependent on the interactions between the molecule and the adsorption surface. The ionization potentials of arenes are between 7 and 8 eV in the gas phase so photoionization using laser light of, for example 355 nm (3.5 eV) would be expected to require two or more photons. Diffuse reflectance laser flash photolysis studies have shown that bi- or multi-photon production of aromatic radical cations tends to occur on silica gel and γ -alumina surfaces. Using laser dose studies the radical cation production of distyrylbenzenes⁵⁴ on both silica gel and γ -alumina, and pyrene^{34,86} on γ -alumina were shown to be bi- or multi-photon in nature. The production of radical cations in zeolites is more complicated due to the varied nature of the adsorption sites and presence of alkali metal cations such as sodium or copper. Pyrene^{91,93}, anthracene^{91,95}, naphthalene⁹⁵ and trans-stilbene⁹⁵ radical cations have been found using laser dose studies to be produced by both mono- and bi-photon mechanisms when included within zeolites. These mechanisms are explained on the basis of there being two adsorption sites in zeolites, one active and one nonactive. The active sites undergo charge transfer with the arene, thus reducing the energy required to remove the electron and produce the radical cation. Nonactive sites work in a similar fashion to those found on silica gel and alumina, in that the first photon creates an excited singlet state and the second photon is absorbed by the excited state and ionizes the arene. The mixed mono- and bi-photon production of the arene radical cations was proved using both oxygen quenching experiments and a laser dose study⁹¹. As the oxygen concentration was increased the singlet lifetime decreased. Thus the radical cation yield decreased as the interception and further excitation of the excited singlet became less likely i.e. the bi-photon mechanism of production decreased. The laser dose study was carried out at 300 Torr of oxygen - so the bi-photon production was kept to a minimum - and a linear dependence of radical

cation yield on laser intensity was observed. In copper exchanged zeolites the oxidising strength of the Cu^{2+} ion is sufficient to ionise anthracene⁷⁸ on addition to the zeolite, thus forming its radical cation and Cu^+ . Similar behaviour is observed in acid exchanged zeolites⁹⁶, the anthracene radical cation is formed immediately on addition to the zeolite. The presence of radical cations on a surface is obviously accompanied by either the production of electrons or radical anions. No evidence of trapped electrons or the corresponding radical anions have been reported on silica gel or γ -alumina following photoionization. The nature of the zeolite surface has enabled the observation of both trapped electrons and occasionally the corresponding radical anion. The trapped electron takes the form of an electron encased in sodium ion clusters^{89,91,94,95} in sodium exchanged zeolites. Either two, three or four sodium ions surround the electron, forming Na_2^+ , Na_3^{2+} and Na_4^{3+} clusters respectively. The number of sodium ions in the cluster is determined by the position of the adsorbed arene. NaA zeolites have small cages with narrow entrances, sodalite (2.6 Å) and α (4 Å) cages, both too small for arene molecules to enter. Thus the molecules are adsorbed solely on the external surface and the electron is trapped in a sodalite or α cage next to the arene cation. The clusters forming in the sodalite cages have been shown using oxygen quenching experiments⁹⁴ to be Na_4^{3+} and Na_2^+ , and those in the larger α -cage to be Na_3^{2+} clusters. In zeolites NaX and NaY the entry pores are large enough for the arene molecules to enter (7.4 Å) and only clusters of Na_4^{3+} are found⁹⁴. The sodium ion clusters all have broad absorption bands between 480 and 650 nm. Other ions such as copper⁷⁸ and lithium⁹¹ also show this electron trapping ability when used in place of the sodium ions in zeolites. The anion radical of pyrene has been observed to coexist with the pyrene radical cation in the supercages of caesium and potassium exchanged zeolites X and Y^{94,97}. Thus demonstrating both the acidic and basic nature of the zeolite surface.

2.4.4. Surface kinetics.

The rate of decay of excited states on surfaces are often very complex and do not conform to the simple rate laws often applied in solution measurements.

Fluorescence decay curves on surfaces are usually fitted with two or three exponential terms^{30,35-37,41,44,72,76,77} Ware et al⁹⁸⁻¹⁰⁰ provided an alternative method of analysis. Ware's analysis for single photon counting data requires excellent signal to noise and takes the form of a series of exponentials.

Triplet decay on surfaces is not usually measured directly due to the common occurrence of triplet-triplet annihilation. Triplet-triplet annihilation often gives rise to delayed fluorescence which can be used to monitor the rates of diffusion across the surface. Oelkrug et al have studied the mobility of azaaromatics^{50,51} on silica gel using delayed fluorescence decay rate measurements. The amount of delayed fluorescence observed decreased with increasing pretreatment temperature and increased with increasing azaaromatic concentration. On γ -alumina virtually no mobility of the azaaromatics was observed.

The models used to describe the silica gel surface were a two dimensional model⁵⁰ and a fractal model^{50,51}. The two dimensional model assumes a "flat" surface and was found to be a reliable model for silica gels with large pore diameters. The fractal nature of microporous silica gel has been reported¹⁰¹⁻¹⁰³ and the surface of microporous silica gels cannot be considered as two dimensional. A fractal dimensionality must be used, for highly dispersed silica gels the spectral dimension (d_s) has been calculated to be $4/3$ ^{104,105}. Bimolecular decay rate constants for the delayed fluorescence ranging from 4×10^{12} to $6 \times 10^{13} \text{ dm}^2 \text{ mol}^{-1} \text{ s}^{-1}$ were obtained for the azaaromatics on silica gels with pore sizes greater than 60 \AA using the two-dimensional model⁵¹. The rate constants for triplet-triplet annihilation of the azaaromatics on 60 \AA silica gel obtained from the fractal model⁵¹ were in the range 0.7×10^{12} to $3.4 \times 10^{12} \text{ dm}^2 \text{ mol}^{-1} \text{ s}^{-2/3}$.

The rate of decay of radical cations on oxide surfaces is generally via electron-radical cation recombination, regenerating the ground state. Oelkrug et al demonstrated this behaviour using distyryl benzenes adsorbed on silica gel and γ -alumina⁵⁴ by repetitive excitation at room temperature of the same sample area. The observed intensities and decays were reproducible indicating that the radicals decay mainly via electron cation recombination regenerating the ground state. This decay is usually complex, initially very fast followed by a slower long time component. Attempts have been made to fit radical cation decay traces.

Diphenylpolyenes¹⁰⁶ adsorbed on γ -alumina and distyrylbenzenes⁵⁴ on silica gel and γ -alumina have been shown to decay by geminate recombination at very low loadings ($7 \times 10^{-7} \text{ mol g}^{-1}$ and $3 \times 10^{-9} \text{ mol g}^{-1}$). The decay profile of the pyrene radical cation adsorbed on γ -alumina⁸⁶ has been fitted with the dispersive kinetic model of Alberly et al¹⁰⁷. This model has successfully been applied to describe the fluorescence decay of pyrene adsorbed on silica gel¹⁰⁸ and γ -alumina³¹. The dispersive kinetic model assumes a Gaussian distribution in the free energy of activation, or in the logarithm of the rate constant, and was applied to this data as a consequence of the distribution of adsorption sites on γ -alumina for the pyrene

radical cation. The rate of decay of the pyrene radical cation adsorbed on γ -alumina increases with increasing temperature⁸⁶, thus illustrating the temperature increases the rate of diffusion of the ions on the surface.

2.4.5. Energy transfer on surfaces.

Fluorescence quenching of the excited singlet states of molecules adsorbed on surfaces have received considerable attention. Steady state and time-resolved studies of singlet quenching by oxygen on surfaces^{81,108-111} have been carried out. Other compounds used for singlet quenching of arenes adsorbed on silica gel include 2-bromonaphthalene⁸⁵, nitromethane¹¹⁰, nitropropionic acid¹¹⁰ and N,N-diethylaniline⁶⁴. These experiments all demonstrate the mobility of molecules on adsorption to the silica gel surface.

Eremenko et al have reported exciplex formation at 510 nm between N,N-diethylaniline and the excited singlet of anthracene adsorbed on aerosil⁶⁴ (a non-porous silica gel). Quenching of the anthracene fluorescence was observed and exciplex formation was shown to be predominantly dynamic in nature. The concentration of N,N-diethylaniline used in these⁶⁴ experiments was a great deal higher than the anthracene surface coverage of 0.06% and was between 10-100% of N,N-diethylaniline. Time-resolved studies of the anthracene N,N-diethylaniline system revealed that as the anthracene singlet fluorescence intensity decreased the exciplex intensity increased.

Triplet-triplet energy transfer on surfaces has received some attention in order to estimate rate of diffusion on surfaces. Some of the earliest studies were carried out using the benzophenone naphthalene system, on both silica gel^{59,60} and microcrystalline cellulose⁶⁰. Energy transfer on silica gel was found to be comprised of both static and dynamic triplet-triplet energy transfer mechanisms^{59,60}. Triplet-triplet energy transfer between benzophenone and an oxazine dye on cellulose was also used to study the mobility of dyes on cellulose⁶⁹. Triplet-triplet energy transfer on cellulose in both of the above cases^{60,69} was found to be static in nature due to the lack of movement on the cellulose surface. Triplet energy transfer from eosin to anthracene has been reported on silica gel following laser excitation of the eosin at 532 nm^{106,112} or 560 nm¹¹³. The triplet-triplet energy transfer rate constant from eosin to anthracene was reported to be $9 \times 10^{13} \text{ dm}^2 \text{ mol}^{-1} \text{ s}^{-1}$ on a non-porous silica gel¹¹³. Triplet quenching of pyrene by ferrocene adsorbed on γ -alumina is dynamic in nature⁸⁶. The bimolecular rates of pyrene triplet quenching on γ -

alumina range from 3.31 to $2.2 \times 10^9 \text{ dm}^2 \text{ mol}^{-1} \text{ s}^{-1}$ with increasing pretreatment temperature.

2.4.6. Electron transfer on surfaces.

The pyrene radical cation adsorbed on γ -alumina is formed following laser excitation at 337.1 nm . Electron transfer between ferrocene and the pyrene radical cation adsorbed on γ -alumina has been observed⁸⁶. The pyrene radical cation rate of decay was fitted using the dispersive kinetic model of Albery¹⁰⁷. The observed rate constant from the Albery fit \bar{k}_{obs} was related to the total ferrocene concentration by :-

$$\bar{k}_{\text{obs}} = \bar{k}_0 + k'_q [\text{quencher}]$$

where \bar{k}_0 is the average rate constant in the absence of quencher and k'_q is the bimolecular quenching rate constant. This yielded a linear correlation between the observed rate of radical cation decay and ferrocene concentration in the range 0.2 to $1.08 \mu\text{mol g}^{-1}$. The bimolecular rate constant (k'_q) for the quenching of the pyrene radical cation on γ -alumina ranged from 3.39 to $2.35 \times 10^9 \text{ dm}^2 \text{ mol}^{-1} \text{ s}^{-1}$ with increasing pretreatment temperature ($130 - 350^\circ\text{C}$).

The formation of the methylviologen radical cation is readily observed following photoirradiation of methylviologen ions (MV^{2+}) adsorbed on silica gel¹¹⁴. The coadsorption of sodium chloride increases the radical cation yield, but also increases its rate of decay. Electron transfer was studied using a range of polychloroalkanes and methylviologen cation radicals coadsorbed on silica gel. The rate of decay of the methylviologen radical cation is influenced by the degree of chloro substitution and thus the electron affinity of the polychloroalkane¹¹⁴. The polychloroalkane with the most chloride groups is carbon tetrachloride, which yields the fastest reaction rate of $1.1 \times 10^5 \text{ dm}^2 \text{ mol}^{-1} \text{ s}^{-1}$, following analysis using the dispersive kinetic model, and the less chlorosubstituted dichloromethane yielded an electron transfer rate of $1.3 \times 10^4 \text{ dm}^2 \text{ mol}^{-1} \text{ s}^{-1}$.

Pyrene adsorbed on silica gel has been studied with the coadsorption of electron acceptors such as methyl viologen and tetranitromethane⁹⁷. Coadsorption of electron donors in the pyrene system encourages the formation of the pyrene radical cation. Coadsorption of methylviologen with pyrene on silica gel results in rapid dynamic quenching of the pyrene excited singlet state. Excitation of the methylviologen at 266 nm causes quenching of the pyrene excited singlet state and

formation of the pyrene radical cation following electron transfer from the methylviologen photoproducts.

A common reaction studied on surfaces is that of the recombination kinetics of radical ion pairs^{55,63,66,88,115-117}. These reactions do not require diffusion across the surface and consequently will not be discussed here.

2.5. Summary.

The work discussed above outlines the interactions observed between the surfaces of γ -alumina, silica gel and zeolites and adsorbed molecules. The nature of zeolites, γ -alumina and silica gel have been shown to stabilise a number of radical cations, mainly through specific adsorption sites. Molecules are often adsorbed preferentially at certain sites, due to the heterogeneous nature of the surface, giving rise to a distribution of sites with varying structures and energies. This is illustrated by many molecules showing pronounced aggregation effects at low surface coverages. Molecular movement on surfaces is often restricted due to the strength of interaction between the surface and the adsorbed molecules. Kinetics of excited state decay and bimolecular energy and electron transfer are often complex, due to heterogeneity of the surface adsorption sites.

Chapter 3

Experimental

3. Experimental.

3.1. Sample preparation.

3.1.a. Method A.

Silica gel was dried under vacuum at 5×10^{-5} mbar and 125°C for 6 hours and left at room temperature under vacuum for a further 12 hours. Solvents were dried by reflux over calcium hydride and the adsorbate added and dissolved. The silica gel vessel was re-pressurised with dry nitrogen and the solution added to the silica gel under dry nitrogen. The mixture was agitated at intervals and allowed to equilibrate for 3 hours. The solution was then decanted off and the sample finally dried under vacuum to 5×10^{-5} mbar, first on a rotary pump then an oil diffusion pump and then sealed into a 22 mm diameter x 10 mm pathlength glass or fused silica cuvette.

3.1.b. Method B.

Silica gel was dried under vacuum at 5×10^{-5} mbar and 125°C for 6 hours and left at room temperature under vacuum for a further 12 hours. Solvents were dried by reflux over calcium hydride and the adsorbate added and dissolved. The silica gel vessel was re-pressurised with dry nitrogen and the solution added to the silica gel under dry nitrogen. The mixture was agitated at intervals and allowed to equilibrate for 3 hours. The solvent was removed under vacuum to 5×10^{-5} mbar, first on a rotary pump then an oil diffusion pump, the sample was then sealed into a 22 mm diameter x 10 mm pathlength glass or quartz cuvette.

3.1.c. Method C.

The sample preparation chamber consists of a round bottomed flask with two arms attached. The azulene and anthracene were dissolved in n-hexane and added to one arm of the vessel, the solvent was then removed under vacuum. The vessel was re-pressurised and the silica gel then added to the other arm. The silica gel was dried under vacuum at 5×10^{-5} mbar and at 125°C for 6 hours whilst the arm containing the anthracene and azulene was placed in a dewar of liquid nitrogen to prevent sublimation. The silica was removed from the heat, the vessel sealed and the liquid nitrogen dewar removed. The vessel was then left under vacuum at room temperature for 20 hours with periodic agitation to allow sublimation of the

anthracene and azulene onto the silica gel. The vessel was then evacuated to a pressure of 5×10^{-5} mbar, and the sample was then sealed into a 22 mm diameter x 10 mm pathlength glass or quartz cuvette. The concentrations of azulene and anthracene on the surface were determined by washing of a portion of the sample which was not transferred to the cuvette.

3.2. Anthracene adsorbed on silica gel at various anthracene loadings.

Samples were prepared by method A, using Davisil grade 635 silica gel, n-hexane as solvent, and anthracene as the adsorbate. Anthracene concentrations were determined both by the analysis of the decanted solvent and by washing adsorbed anthracene off a portion of the sample which was not transferred to the cuvette, and were in the range $0.56 \mu\text{mol g}^{-1}$ to $40 \mu\text{mol g}^{-1}$ corresponding to less than 5% of a monolayer.

3.3. Anthracene adsorbed on silica gel with radical cation quencher.

Anthracene with radical cation quencher adsorbed on silica were prepared using method A, using Davisil grade 635. Samples of anthracene with azulene, naphthalene or triphenylamine as quencher were adsorbed to the surface from n-hexane. Acetonitrile was used as solvent for the adsorption of anthracene with triphenylamine, N,N,N',N'-tetramethyl-1,4-phenylenediamine, aniline or N,N-dimethylaniline onto the silica gel surface.

3.4. Anthracene Derivatives adsorbed on silica gel.

Dialkoxyanthracene derivatives were adsorbed onto silica gel (Davisil grade 635) from hexane and the samples were prepared according to method B.

3.5. Materials.

Silica gels.

The silica gels used were either purchased from Sigma (Sigma 100-200 mesh, 25 Å pore size) or Aldrich.

The following silica gels were purchased from Aldrich :-

Davisil grade 635, 60-100 mesh, 60 Å pore size, surface area $480 \text{ m}^2 \text{ g}^{-1}$; Davisil grade 645, 60-100 mesh, 150 Å pore size, surface area $300 \text{ m}^2 \text{ g}^{-1}$; Merck grade 10184, 70-230 mesh, 100 Å pore size, surface area $300 \text{ m}^2 \text{ g}^{-1}$.

Anthracene was purchased from Sigma and the following compounds used for electron transfer to the anthracene radical cation were purchased from Aldrich :- N,N,N',N'-tetramethyl-1,4-phenylenediamine; azulene; aniline; triphenylamine; and naphthalene.

The solvents used were n-hexane, methanol, ethanol and acetonitrile. These were all Spectrophotometric grade and were obtained from Aldrich.

The dialkoxyanthracene derivatives listed below were kindly donated by Dr. H. Bouas-Laurent :-

2,3-dimethoxyanthracene; 2,3-dihexadecyloxyanthracene; 2,3-didecyloxyanthracene; 2,6-didecyloxyanthracene; 1,5-didecyloxyanthracene; 9,10-didecyloxyanthracene.

9-Cyanoanthracene was purchased from Aldrich.

3.6. Ground state absorption spectra.

All diffuse reflectance ground state absorption spectra and radical cation decay spectra at delays greater than 30s were carried out using a Phillips PU-8800 UV-Visible spectrophotometer equipped with an integrating sphere. Solution absorption measurements were recorded either using the above Phillips PU-8800 spectrophotometer in transmission mode or a Hewlett Packard 8453 diode array spectrophotometer.

3.7. Fluorescence emission spectra.

All fluorescence emission spectra of the silica gel samples were performed using a Spex fluoromax with a front face surface attachment.

3.8. Laser flash photolysis.

3.8.a. Time resolved transient absorption measurements.

The equipment used for nanosecond laser flash photolysis in diffuse reflectance mode is identical to that used in transmission mode except for the geometry of collection of the analysing light as shown in Figures 3.1a and 3.1b.

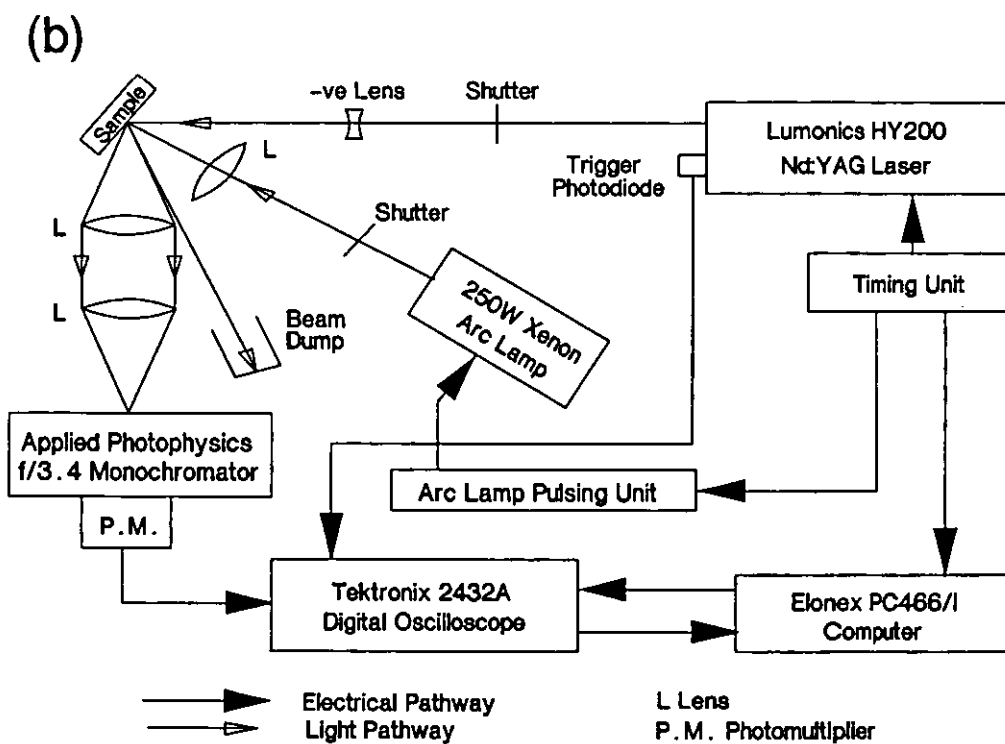
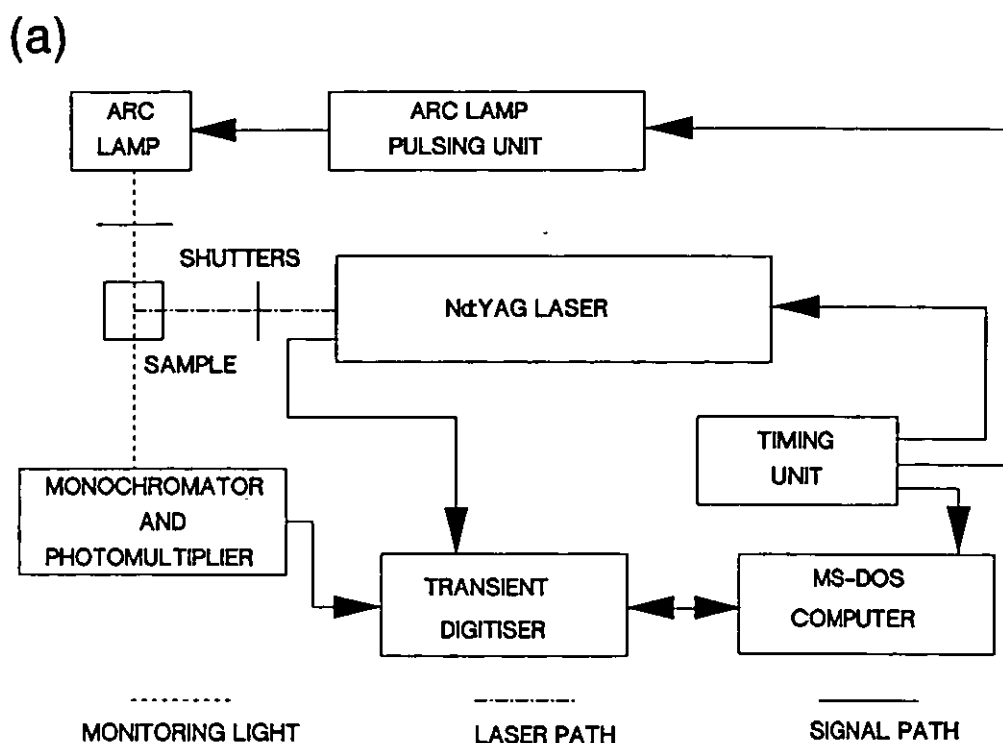
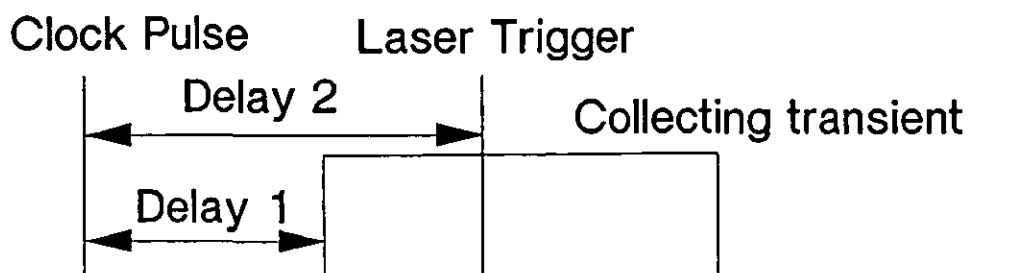


Figure 3.1: Schematic diagrams showing the apparatus used for (a) transmission laser flash photolysis (b) diffuse reflectance laser flash photolysis

The exciting source used was a Q-switched hyperYAG HY200 (Lumonics), providing wavelengths of 532 nm, 354.7 nm and 266 nm; the second, third and fourth harmonics of the fundamental wavelength 1064 nm. A 275W xenon arc lamp (Optical Radiation Corporation) was used as the analysing source with filters placed between the lamp and sample to cut off unwanted wavelengths. The analysing light was collected and focussed into an f3.4 grating monochromator (Applied photophysics) and photomultiplier tube (Hamamatsu R928). An accelerating voltage was applied to the photomultiplier tube using a Fluke 415B high voltage power supply, the signal from the photomultiplier was then transferred to a digital oscilloscope (Tektronix 2432A) and interfaced to the computer via an AT-GPIB interface card (National Instruments).

The sequence and timing of the events in this system are controlled by a home built analogue delay generator which sends out a clock pulse every 1.6 s, which triggers the computer and sets up two delays - one to trigger the opening of the shutters and one to fire the laser, the order of which is shown schematically in Figure 3.2. The computer enables the relevant shutters - ready to be triggered by the delay, and arms the oscilloscope. The signals from the delay generator then trigger the relevant shutters (i.e. the combination enabled earlier by the computer) and the laser. The 1064 nm from the laser is used to trigger the oscilloscope by leakage through the end cavity mirror and its detection using a photodiode. On receipt of this signal the oscilloscope triggers, digitises and transfers the data from the photomultiplier tube to the computer where it is first displayed on the screen and then saved. This whole cycle takes less than 1.6 seconds and is repeated on receiving the next clock pulse until the baseline, transient absorption, emission and topline are recorded. These 4 traces are then stored on the disk for analysis, described later in section 3.9. The 2432A Tektronix digital oscilloscope can only digitise at 1024 points per trace, so non-exponential decays spanning several decades would need to be recorded on a number of timebases. So for non-exponential decays spanning several decades an averaging transient recorder (EG&G model 9845-100) which can digitise up to 262,000 points per trace with 10ns resolution is used.



Computer triggered by the clock pulse
 Computer readies the shutters for the laser firing

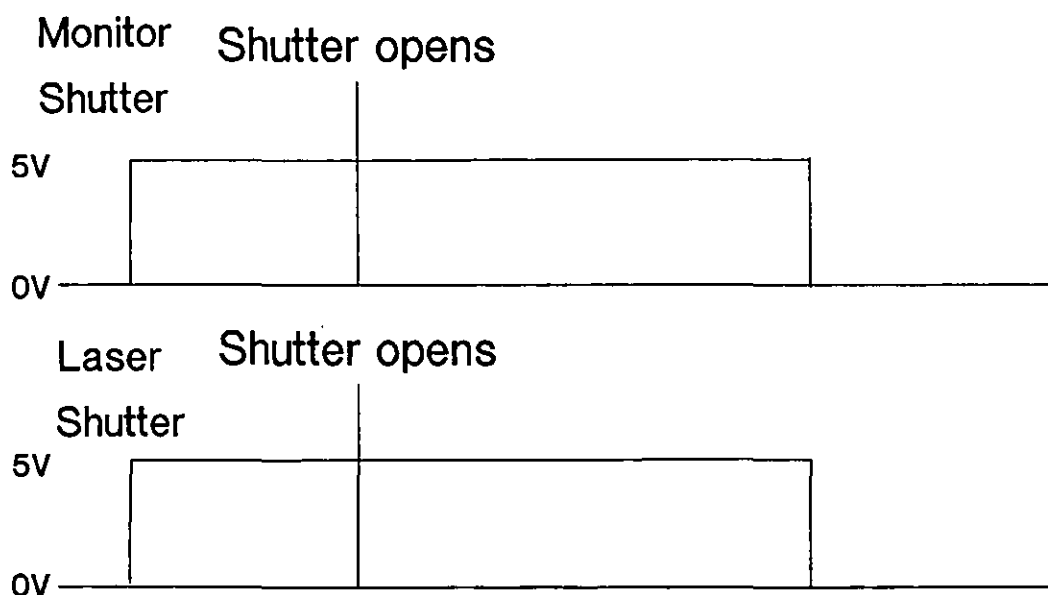


Figure 3.2: Sequence of events controlled by the timing unit in the collection of both transmission and diffuse reflectance transient data

3.8.b. Time resolved transient emission measurements.

Transient emission spectra were carried out using a gated Photodiode Array System (EG & G Princeton Applied Research). As above the Q-switched Lumonics hyperYAG HY200 was used as the excitation source at 354.7 nm. In this system the detector controller determines the timing of events, sending out a pulse to trigger the laser. The laser pulse is detected by a photodiode via a fibre optic cable positioned next to the laser output, and the signal from this photodiode triggers the gate pulse interface. The resulting gate pulse is amplified and applied to the microchannel plate, thus effectively "opening" the optical gate for the gate pulse duration allowing detection by the photodiode array. The emitted light from the sample is collected using a fibreoptic cable which transfers it to the spectrograph. Gate widths used were 100ns, the minimum gate delay from the laser pulse being 85ns determined by the insertion delay of the gate pulse interface. The system in detail consists of a detector interface (Model 1461), a gate pulse interface (Model 1303), a gate pulse amplifier (Model 1304) and an intensified detector (Model 1455B-700-HQ) with an 18 mm Blue specified intensifier, high quantum efficiency and 700 active elements. The spectrograph is a model 1235 digital triple grating spectrograph with two gratings:- one blazed at 300 nm, 147.5 g/mm and one at 500 nm, 150 g/mm.

Transient emission kinetic data were collected using the Q-switched hyperYAG HY200 (Lumonics), at 354.7 nm. The emission was collected and focussed into an f3.4 grating monochromator (Applied photophysics) and photomultiplier tube (Hamamatsu R928). An accelerating voltage was applied to the photomultiplier tube using a Fluke 415B high voltage power supply, the signal from the photomultiplier was then transferred to a digital oscilloscope (Tektronix 2432A) and interfaced to the computer via an AT-GPIB interface card (National Instruments). The sequence and timing of the events in this system are discussed in section 3.8.a, with traces being recorded for the laser emission and the top line.

3.9. Data Analysis.

Opaque and highly scattering samples require the analysis of changes in the intensity of diffusely reflected analysing light emerging from the sample. The intensity changes in the probing light can be used to obtain information regarding the excited state absorption and emission properties of molecules on surfaces. The corrected reflectance change yields kinetic data and also time resolved spectra by repeating the measurements at several different wavelengths.

Figure 3.3 shows the four traces recorded to obtain a corrected trace for the reflectance change ($\Delta R_{(t)}$) as a function of time. Where BL is the baseline (just arc lamp), TR the transient absorption before (pretrigger) and after laser excitation (both arc lamp and laser), EM the emission caused by laser excitation (just the laser) and TP the topline (neither arc lamp nor laser, to establish the zero settings).

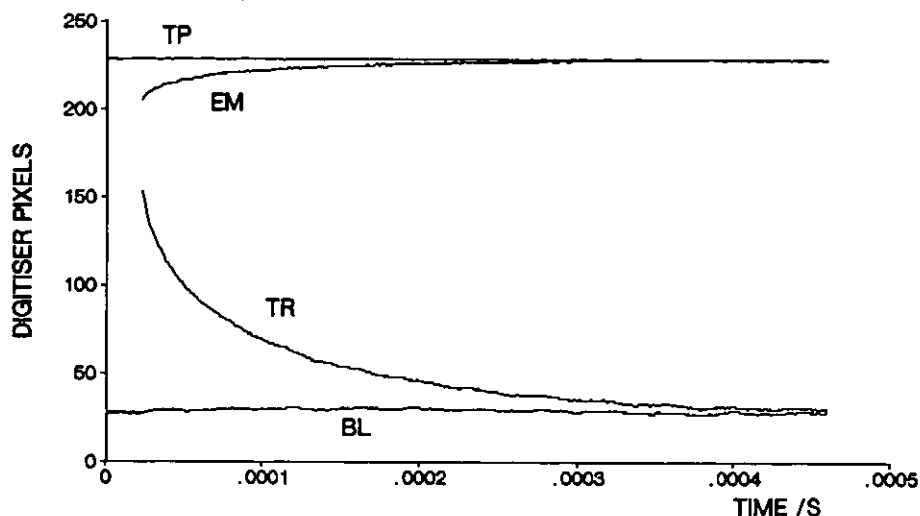


Figure 3.3: Experimental data collected from diffuse reflectance laser flash photolysis showing (BL) baseline (arc lamp only), (TR) transient (laser and arc lamp), (EM) emission (laser only), and (TP) top line (neither arc lamp nor laser)

First the transient absorption trace is corrected for emission by subtraction of the emission trace, then the topline is subtracted from the baseline to determine the range of the screen. The emission trace must remain on the screen otherwise no reliability can be placed on the data in the region where emission overload has occurred. Transient absorption is shown by a decrease in reflection and the change in reflectance can be calculated using equation 3.1 :-

$$\Delta R_{(t)} = \frac{(R_b - R_{(t)})}{R_b} \quad (3.1)$$

or alternatively expressed as :-

$$\% \text{ Reflectance change} = \frac{100(R_b - R_{(t)})}{R_b} \quad (3.2)$$

where R_b is the corrected sample reflectance before the laser pulse (BL - TP) and $R_{(t)}$ the corrected sample reflectance at time t after excitation (TR -EM). ΔR is the fractional change in reflectance and $100 \Delta R$ is often referred to as % absorption by the sample.

3.9.1. The further treatment of this data depends on the concentration profile of the transients produced as a function of penetration depth into the sample. The equations (3.3 and 3.4) describing the attenuation of the incident flux (described earlier in section 1.5) are given below :-

$$dI_{(x)} = -(K + S)I_{(x)} dx + SJ_{(x)} dx \quad (3.3)$$

$$dJ_{(x)} = +(K + S)J_{(x)} dx - SI_{(x)} dx \quad (3.4)$$

where I and J are the incident and reflected fluxes respectively and are considered perpendicular to the irradiated surface; K and S are the absorption and scattering coefficients. There are two limiting cases for the concentration profile as a function of penetration depth, they are shown schematically in Figure 3.4, curve 1 represents an exponential fall off, and curve 3 a plug :-

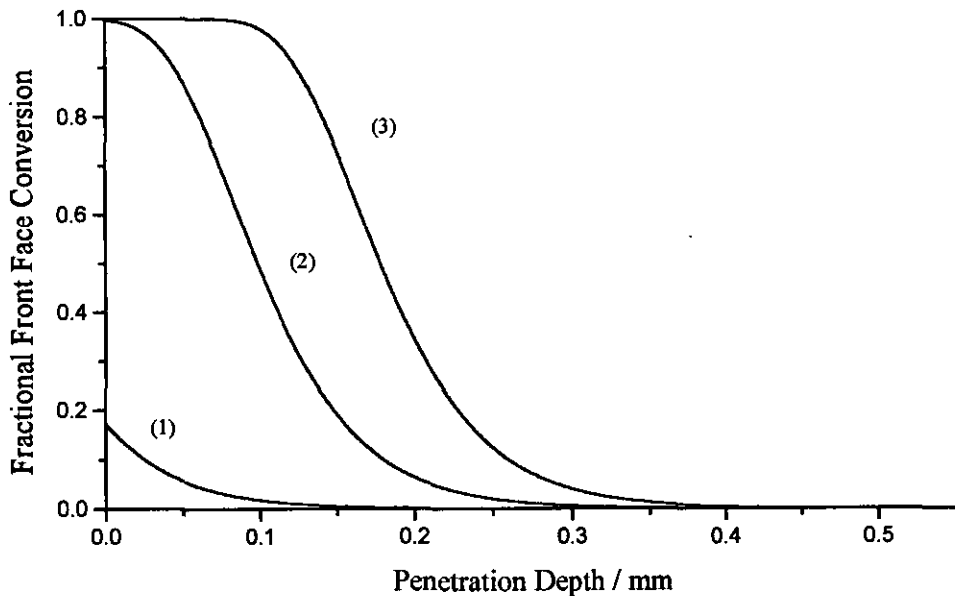


Figure 3.4: Diagram showing fractional conversion of ground state to transient as a function of sample depth with increasing laser irradiation showing (1) an exponential fall-off (2) an intermediate case and (3) a homogeneous plug of excited states

3.9.1a. Transient concentration falls off exponentially with increasing penetration depth.

This usually occurs for low laser fluences and samples with high molar absorption coefficients. The Kubelka Munk equation cannot be applied in this case as its main assumption is that the absorbing and scattering species are randomly distributed. Equations 3.3 and 3.4 were solved by Lin and Kan¹¹⁸ at the analysing

wavelength, where K (absorption coefficient = $\omega \epsilon C$) varies exponentially with x (penetration depth) following laser excitation to give equation 3.5 :-

$$R = R_B^* \frac{1 + \frac{\gamma}{\delta} u + \frac{\gamma(\gamma+1)u^2}{\delta(\delta+1)2!} + \dots}{1 + \frac{\gamma+1}{\delta} u + \frac{(\gamma+1)(\gamma+2)u^2}{\delta(\delta+1)2!} + \dots} \quad (3.5)$$

where R_B^* is the diffuse reflectance of the background in the absence of the exponentially decreasing absorber, and :-

$$\gamma = \frac{1}{(b^c R_B^*)}$$

$$\delta = \gamma + 1 - \frac{R_B^*}{b^c}$$

$$u = \frac{2K_T^*(0)}{b^c S}$$

where

$$b = \frac{1}{2} \left(\frac{1}{R} - R \right) = \frac{(K^2 + 2KS)^{1/2}}{S}$$

This series converges for values of u and has been shown¹¹⁹ to relate reflectance changes of less than 10% as a linear function of the number of absorbing species.

3.9.1 b. Transient concentration forms a plug of excited states close to the exposed surface.

Samples with low concentration of absorber with low molar absorption coefficient are most likely to produce a plug of excited states when a high laser fluence is used. The plug extends deeper into the sample than is probed by the analysing light and consequently there is a homogeneous distribution of transient absorbers which can be analysed using Kubelka Munk theory. If following laser excitation the transient decays back to the ground state the absorption coefficient K at any time t will be given by :-

$$K(t) = K_B + 2\epsilon_G(C_G - C_T) + 2\epsilon_T C_T \quad (3.6)$$

where K_B represents the substrate absorption coefficient, C the concentrations, ϵ the naperian molar absorption coefficient and the subscripts G and T the ground state and transient absorbers.

The change in remission function will be given by (equation 3.7) the difference between the remission function following laser excitation and the remission function prior to excitation :-

$$\Delta F(R) = \frac{(1 - R')^2}{2R'} - \frac{(1 - R)^2}{2R} = 2 \frac{(\epsilon_T - \epsilon_G)C_T}{S} \quad (3.7)$$

where R and R' are the observed reflectances before and after laser excitation respectively. $\Delta F(R)$ the change in remission function will be linearly dependent on the concentration of transient species at wavelengths where only the transient absorbs, elsewhere the spectra will be distorted by the ground state absorption.

These are the two extremes for the concentration profile, usually the profile is somewhere between an exponential fall off and a homogeneous plug. Analysis of data which is neither a plug nor an exponential fall off is very difficult and is to be avoided by adjusting the sample concentration or laser fluence to form one of the cases discussed above. A program based on the equations previously published in references¹¹⁹ and¹²⁰ was written by Dr. D.R. Worrall in Loughborough and used to calculate the transient concentration profile of any sample at the laser wavelength so the correct analysis method can be selected. The concentration profile program works as follows :-

1. The sample is divided up into a large number of thin slices, parallel to the sample surface and such that within each slice the concentration of ground state absorber is constant. Before laser excitation the concentration of ground state absorbers (A) in each slice is $A_i = A_0$. The transient is assumed not to absorb significantly at the exciting wavelength and the scattering coefficient is independent of wavelength, so the absorption coefficient in each slice is given by $K_{A,i}^e = 2\epsilon_A^e A_i$ where ϵ_A^e is the naperian molar absorption coefficient of the absorber at the excitation wavelength.
2. The laser pulse is divided into a number of portions Δt
3. The sample is then considered irradiated by a portion of the laser, and the concentration of transients determined by the light absorbed and a new set of ground state concentrations are determined such that $A_i + T_i = A_0$.
4. Using the new A_i the absorption coefficients K can be calculated for each slice.
5. The next portion is taken and steps 3 to 5 are repeated over and over until all the portions are accounted for.
6. Now all the A_i and T_i are known and the concentration profile can be generated.

Chapter 4

Data Analysis

4. Fitting of kinetic data in heterogeneous media.

The kinetic decays in homogeneous systems can usually be explained by simple first and second order kinetics, in heterogeneous media this is often not the case. Numerous models have been used to describe kinetics in heterogeneous systems including multiexponentials^{30,35,36,40,41,44,72,76,77}, the dispersive kinetic model of Albery^{31,63,66,86,92,94,97,107,108,114,116,121}, fractal and two-dimensional models⁵¹ and geminate recombination^{54,71,106}.

4.1. Dispersive kinetic model.

The dispersive kinetic model of Albery¹⁰⁷ provides an alternative to the multiexponential fits once used. It assumes a Gaussian distribution of activation energies and therefore a Gaussian distribution of the logarithm of the rate constant about some mean value \bar{k} , with a distribution width of γ .

$$\frac{C}{C_0} = \frac{\int_{-\infty}^{+\infty} \exp(-t^2) \exp[-\bar{k}t \exp(\gamma t)] dt}{\int_{-\infty}^{+\infty} \exp(-t^2) dt} \quad (4.1)$$

where C refers in this case to the concentration of transient and t to the time following laser excitation. This is the equation used to describe the data, the actual fitting of the data is achieved by using the transformations to the equation as described in the appendix of reference¹⁰⁷.

4.2. Fractal and two-dimensional model.

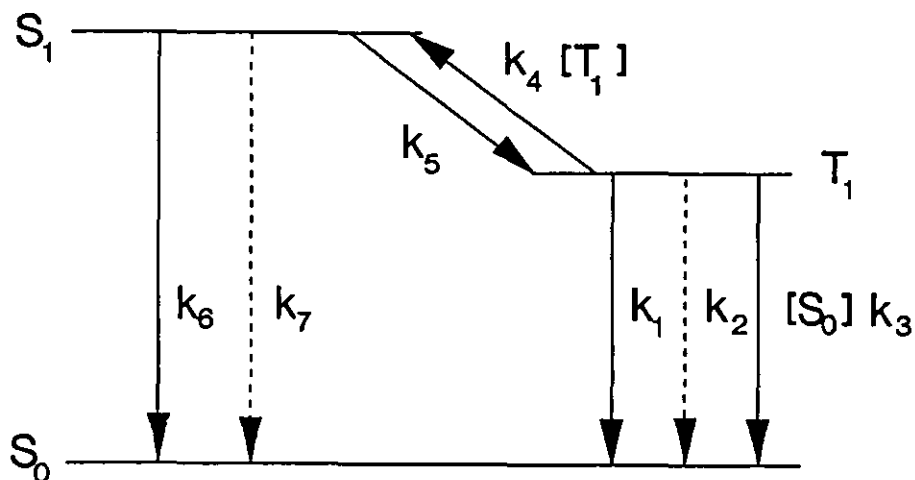
The fractal and 2-dimensional models were presented by Oelkrug et al⁵¹ to describe the bimolecular rate constants arising from triplet triplet annihilation of some aromatic N-heterocycles adsorbed on a range of silica gels. The two models are based on the translational mobility of molecules adsorbed on surfaces during bimolecular reactions. The two dimensional model assumes the molecules can only diffuse in two dimensions, i.e. the surface is flat. The surface of microporous silica gels are often described as fractals^{101,102}. The fractal model assumes the molecules diffuse across the surface of a random fractal with a spectral dimension (d_s) of 4/3. The spectral dimension of 4/3 was calculated by Alexander et al¹⁰⁴ and Leyfraz et al¹⁰⁵ for highly dispersed silicas.

The equations used for the data analysis of both delayed fluorescence and radical cation decay (following electron transfer) on 60 Å silica gel are derived below.

4.2.1. Delayed fluorescence.

The rate of decay of delayed fluorescence is dependent on the mobility of the anthracene triplet state on the silica gel surface. Therefore fitting this data can provide information regarding the nature of the surface in terms of adsorption and the distribution of adsorption sites.

The different pathways for the deactivation of the triplet state are shown in scheme 4.1, which is a simplified version of one used by Saltiel et al¹²². The derivations of the two models for the analysis of delayed fluorescence which are used later in section 5.1.3.1a. are based on this scheme and are described below.



Scheme 4.1: Photophysical deactivation pathways in excited state anthracenes

4.2.1a. The 2-dimensional model for delayed fluorescence analysis.

The derivation of the equation describing the two-dimensional model used in section 5.1.3.1a. for the analysis of the bimolecular triplet state decay of anthracene adsorbed on silica gel, and in the work of Oelkrug et al⁵¹ for the analysis of the bimolecular triplet state decay of acridine on silica gel, is shown below.

From scheme 4.1 the rate of decay of the excited triplet (equation 4.2) and singlet (4.3) states can be given by :-

$$-\frac{d[T_1]}{dt} = k_p [T_1] + k_3 [S_0][T_1] + 2k_4 [T_1]^2 - k_5 [S_1] \quad (4.2)$$

and

$$-\frac{d[S_1]}{dt} = k_f[S_1] - k_4[T_1]^2 \quad (4.3)$$

where :-

$$k_p = k_1 + k_2$$

$$k_f = k_5 + k_6 + k_7$$

$[S_1]$, $[S_0]$ and $[T_1]$ are the concentrations of the excited singlet state, the ground state and the excited triplet state respectively.

To gain an expression for the singlet concentration the steady state approximation is applied to $[S_1]$ in equation 4.3 which gives :-

$$[S_1] = \frac{k_4 [T_1]^2}{k_f} \quad (4.4)$$

Then substituting the expression for singlet concentration $[S_1]$ (equation 4.4) into equation 4.2 gives :-

$$-\frac{d[T_1]}{dt} = [T_1](k_p + k_3[S_0]) + 2k_4[T_1]^2 - \frac{k_5 k_4 [T_1]^2}{k_5 + k_6 + k_7} \quad (4.5)$$

The quantum yield of triplet formation is given by equation 4.6 :-

$$\phi_T = \frac{k_5}{k_5 + k_6 + k_7} \quad (4.6)$$

thus substitution of equation 4.6 into equation 4.5 gives :-

$$-\frac{d[T_1]}{dt} = [T_1](k_p + k_3[S_0]) + 2k_4[T_1]^2 - \phi_T k_4 [T_1]^2 \quad (4.7)$$

Which on rearrangement gives :-

$$-\frac{d[T_1]}{dt} = [T_1] (k_p + k_3[S_0]) + k_4 [T_1]^2 (2 - \phi_T) \quad (4.8)$$

Assuming that second order decay dominates, all uni-molecular terms in equation 4.8 can be ignored, giving :-

$$-\frac{d[T_1]}{dt} = k_4[T_1]^2(2 - \phi_T) \quad (4.9)$$

Integration of equation 4.9 gives :-

$$\int_0^t -\frac{d[T_1]}{[T_1]^2} dt = \int_0^t k_4(2 - \phi_T) dt \quad (4.10)$$

$$\frac{[T_1]^0}{[T_1]} = k_4(2 - \phi_T)t [T_1]^0 + 1 \quad (4.11)$$

The intensity of diffuse reflectance is proportional to the square of the triplet intensity i.e. $I_{DF} \propto [T]^2$ and therefore $[T] \propto \sqrt{I_{DF}}$, which when substituted into equation 4.11 results in the following expression (equation 4.12) being used to describe the bimolecular behaviour of molecules adsorbed on a two-dimensional surface :-

$$\sqrt{\frac{I_{DF}^0}{I_{DF}}} - 1 = (2 - \phi_T) k_4 [T_1]^0 t \quad (4.12)$$

Equation 4.12 is used later in section 5.1.3.1a. for the analysis of the delayed fluorescence decay of anthracene adsorbed on silica gel in terms of a two-dimensional model. A plot of $\sqrt{I_{DF}^0/I_{DF}} - 1$ versus t should yield a straight line if this model holds, i.e. if the diffusion across the silica gel surface is predominantly two-dimensional in nature.

4.2.1b. The Fractal Model for delayed fluorescence analysis.

The derivation of the equation describing the fractal-dimensional model used in section 5.1.3.1a. for the analysis of the bimolecular triplet state decay of anthracene adsorbed on silica gel, and in the work of Oelkrug et al⁵¹ for the analysis of the bimolecular triplet state decay of acridine on silica gel, is shown below.

In the case of the fractal model the bimolecular rate constants will be time dependent. The conventional bimolecular rate constants are replaced by time

dependent rate coefficients k_i^0 . Kopelman et al¹²³⁻¹²⁵ proposed a simple approximation for the time dependence on fractal surfaces of $k_i = k_i^0 t^{-h}$ where $h = 1 - d_s/2$ and for highly dispersed silicas $d_s = 4/3$ (see section 4.2) which results in :-

$$k_i = k_i^0 t^{-1/3} \quad (4.13)$$

so from scheme 4.1 in section 4.2.1 and equation 4.13, the rate of production of triplet and singlet are given below :-

$$\frac{d[T_1]}{dt} = -k_p[T_1] - k_3[S_0][T_1] - 2k_4^0[T_1]^2 t^{-1/3} + k_5[S_1] \quad (4.14)$$

and

$$\frac{d[S_1]}{dt} = -k_f[S_1] + k_4^0 t^{-1/3} [T_1]^2 \quad (4.15)$$

Applying the steady state approximation to $[S_1]$, in equation 4.15 the singlet concentration can be expressed as :-

$$[S_1] = \frac{k_4^0 t^{-1/3} [T_1]^2}{k_f} \quad (4.16)$$

The triplet quantum yield can be expressed by :-

$$\phi_T = \frac{k_5}{k_5 + k_6 + k_7} \quad (4.6)$$

where $k_5 + k_6 + k_7 = k_f$

Substituting equation (4.16) and equation (4.6) into equation (4.14) gives :-

$$\frac{d[T_1]}{dt} = -k_p[T_1] - k_3[S_0][T_1] - 2k_4^0[T_1]^2 t^{-1/3} + \phi_T k_4^0 t^{-1/3} [T_1]^2 \quad (4.17)$$

$$\frac{d[T_1]}{dt} = -[T_1](k_p + k_3[S_0]) + (k_4^0 t^{-1/3} [T_1]^2) (\phi_T - 2) \quad (4.18)$$

As in the case of the two-dimensional model one assumes bimolecular reactions dominate, consequently all unimolecular rate constants in equation 4.18 can be ignored producing :-

$$\frac{d[T_1]}{dt} = -k_4^0 t^{-1/3} [T_1]^2 (\phi_T - 2) \quad (4.19)$$

Integration of equation 4.19 between the limits of $t=0$ and $t=t$ gives :-

$$-\int_0^t \frac{d[T_1]}{[T_1]^2} = \int_0^t k_4^0 (2 - \phi_T) t^{-1/3} dt \quad (4.20)$$

$$\frac{1}{[T_1]} = \frac{3}{2} k_4^0 (2 - \phi_T) t^{2/3} + \frac{1}{[T_1]^0} \quad (4.21)$$

multiplying both sides of equation 4.21 by the initial triplet concentration $[T_1]^0$, gives :-

$$\frac{[T_1]^0}{[T_1]} = \frac{3}{2} k_4^0 [T_1]^0 (2 - \phi_T) t^{2/3} + 1 \quad (4.22)$$

The intensity of delayed fluorescence is proportional to the square of the triplet concentration, thus :-

$$\left(\frac{\sqrt{I_{DF}^0}}{\sqrt{I_{DF}}} = \frac{[T_1]^0}{[T_1]} \right) \quad (4.23)$$

Substituting equation 4.23 into 4.22 produces the equation used to express the rate of diffusion across a fractal surface :-

$$\sqrt{\frac{I_{DF}^0}{I_{DF}}} - 1 = \frac{3}{2} (2 - \phi_T) k_4^0 [T_1]^0 t^{2/3} \quad (4.24)$$

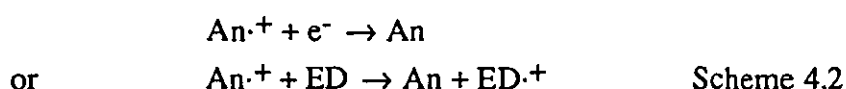
or alternatively equation 4.24 expressed in terms of t , gives :-

$$\left(\sqrt{\frac{I_{DF}^0}{I_{DF}}} - 1 \right)^{3/2} = \left(\frac{3}{2} (2 - \phi_T) k_4^0 [T_1]^0 \right)^{3/2} t \quad (4.25)$$

Equation 4.25 is used later in section 5.1.3.1a. for the analysis of the delayed fluorescence decay of anthracene adsorbed on silica gel in terms of a fractal-dimensional model. A plot of $\left(\sqrt{I_{DF}^0/I_{DF}} - 1\right)^{3/2}$ versus t should yield a straight line if this model holds, i.e. if the diffusion of the triplet across the silica gel surface is fractal-dimensional in nature.

4.2.2. Radical cation decay following electron transfer from an electron donor.

The possible deactivation mechanisms for radical cation decay in the presence of electron donor are shown in scheme 4.2 :-



4.2.2a. The two-dimensional model for radical cation decay analysis.

The derivation of the equation describing the two-dimensional model used in section 5.2.1.2. for the analysis of the bimolecular radical cation decay of anthracene adsorbed on silica gel with an electron donor, is shown below. The rate of decay of the anthracene radical cation ($\text{An}^{\cdot+}$) in the presence of an electron donor (ED) can be given by :-

$$-\frac{d[\text{An}^{\cdot+}]}{dt} = k_1[\text{An}^{\cdot+}][e^-] + k_2[\text{An}^{\cdot+}][\text{ED}] \quad (4.26)$$

if quenching by electron transfer is to dominate one can ignore the first term in equation 4.26, leaving :-

$$-\frac{d[\text{An}^{\cdot+}]}{dt} = k_2[\text{An}^{\cdot+}][\text{ED}] \quad (4.27)$$

Integration of equation 4.27 between the limits $t = 0$ and $t = t$ gives :-

$$\int_0^t -\frac{d[\text{An}^{\cdot+}]}{[\text{An}^{\cdot+}]} = \int_0^t k_2 [\text{ED}] dt \quad (4.28)$$

$$k_2 t [\text{ED}] + \log_e \frac{[\text{An}^{\cdot+}]}{[\text{An}^{\cdot+}]_0} = 0 \quad (4.29)$$

On rearrangement equation 4.29 gives :-

$$\log_e \frac{[An^{\cdot+}]^0}{[An^{\cdot+}]} = k_2 t [ED] \quad (4.30)$$

For low ΔR values (<10%) reflectance change is proportional to concentration and equation 4.30 can be expressed as :-

$$\log_e \frac{\Delta R^0}{\Delta R} = k_2 t [ED] \quad (4.31)$$

Equation 4.31 is used for fitting the data with the two-dimensional model. Thus a plot of $\log_e (\Delta R^0/\Delta R)$ should yield a linear plot with gradient equal to $k_2 [ED]$ if this model holds for the electron transfer reaction between an electron donor and the anthracene radical cation.

4.2.2b. The fractal-dimensional model for radical cation decay analysis.

The derivation of the equation describing the fractal-dimensional model used in section 5.2.1.2. for the analysis of the bimolecular radical cation decay of anthracene adsorbed on silica gel with an electron donor is shown below.

For the fractal analysis $k_i = k_i^0 t^{-1/3}$ which modifies the original equation (equation 4.26) for the rate of decay of the radical cation in the presence of an electron donor to :-

$$-\frac{d[An^{\cdot+}]}{dt} = k_1^0 t^{-1/3} [An^{\cdot+}] [e^-] + k_2^0 t^{-1/3} [An^{\cdot+}] [ED] \quad (4.32)$$

Again assuming the radical cation decay by electron transfer dominates the first term of equation (4.32) can be ignored, leaving:-

$$-\frac{d[An^{\cdot+}]}{dt} = k_2^0 t^{-1/3} [An^{\cdot+}] [ED] \quad (4.33)$$

Integration of equation 4.33 between $t = 0$ and $t = t$ gives :-

$$\int_0^t \frac{d[\text{An}^{\cdot+}]}{[\text{An}^{\cdot+}]} = -k_2^0 [\text{ED}] \int_0^t t^{-1/3} dt \quad (4.34)$$

$$\log_e \frac{[\text{An}^{\cdot+}]^0}{[\text{An}^{\cdot+}]} = \frac{3}{2} k_2^0 [\text{ED}] t^{2/3} \quad (4.35)$$

Equation 4.35 can be rearranged and expressed in terms of t and reflectance change instead of anthracene radical concentration :-

$$\left(\log_e \frac{\Delta R^0}{\Delta R} \right)^{3/2} = \left(\frac{3}{2} k_2^0 [\text{ED}] \right)^{3/2} t \quad (4.36)$$

so a plot of $\left(\log_e \frac{\Delta R^0}{\Delta R} \right)^{3/2}$ vs t should yield a straight line with gradient $3/2 (k_2^0 [\text{ED}])^{3/2}$

4.3 Geminate recombination of radical cations with their electrons.

Geminate recombination between radical cations and their electrons has been observed on various surfaces. The equation used for the rate of geminate pair recombination in three-dimensional systems is ^{126,127} :-

$$\frac{-dc}{dt} = kt^{-n} \quad (4.47)$$

where c is the pair concentration and $n=1$.

Integration of equation 4.47 gives :-

$$c = \text{constant } t - k \ln t \quad (4.48)$$

This equation (equation 4.48) cannot be valid as t tends towards zero or as t gets very large. Mozumder^{128,129} et al showed at long times the rate of recombination of the pair will be independent of the original separation distance and proposed the following equation :-

$$\frac{-dc}{dt} = k' t^{-3/2} \quad (4.49)$$

Which on integration gives :-

$$c = \frac{2k'}{\sqrt{t}} - \text{constant} \quad (4.50)$$

Obviously equation 4.50 cannot be used as t approaches 0 because it results in C_0 approaching infinity. Oelkrug et al⁵⁴ proposed the following approximation (equation 4.51) which can be used as t approaches zero and infinity :-

$$c = \frac{c_0}{(1 + a\sqrt{t})} \quad (4.51)$$

For an exponential fall off of transients and low reflectance change C and C_0 can be replaced by ΔR and ΔR_0 respectively for the fitting of the data giving :-

$$\frac{\Delta R_0}{\Delta R} = 1 + a\sqrt{t} \quad (4.52)$$

where ΔR and ΔR_0 is the reflectance change at time t and $t=0$. This equation is used later in section 5.1.3.1b to describe the initial rate of decay of the anthracene radical cation.

Chapter 5

Results

5. Results and Discussion.

5.1. Anthracene.

5.1.1. Ground State Absorption Spectra.

As discussed earlier in section 1.5 the ground state absorption spectra of highly scattering samples cannot be measured using transmission techniques and the diffusely reflected light is used to measure the absorption spectrum of a sample. Figure 5.1 shows a typical reflectance spectrum of anthracene on silica gel and its corresponding Kubelka Munk remission function (F(R)) spectrum. The advantage of plotting diffuse reflectance spectra as remission function is that the remission function is linearly dependent on concentration, as is absorbance for studies using transmission spectroscopy. At low surface loadings the peak positions and shapes of the remission function spectra are similar to those obtained in dilute methanol solution (Figure 5.2), the slight broadening of the spectrum being due to interactions between anthracene and the surface. The calculated molar absorption coefficient at 376 nm for low concentrations of anthracene adsorbed on silica is also similar ($5000 \text{ L mol}^{-1} \text{ cm}^{-1}$) to that found in methanol solution ($7000 \text{ L mol}^{-1} \text{ cm}^{-1}$). As the anthracene surface loading is increased the spectra show a broadening, a slight red shift (Figure 5.3) and there is a deviation from Kubelka Munk theory. The deviation from Kubelka Munk theory is illustrated (Figure 5.4) by the fact that there is no longer a linear relationship between concentration and F(R). If the anthracene loading is increased from 0.56 to $5.0 \mu\text{mol g}^{-1}$, Kubelka Munk theory predicts an F(R) of nine times the F(R) of the $0.56 \mu\text{mol g}^{-1}$ sample - this is not observed. The deviation from Kubelka Munk and distortion in the spectra at higher loadings can partly be explained by aggregation and the limits of the instrument :-

- (i) an F(R) of, for example, 10 means a reflectance of only 4% - of a similar magnitude to the stray light in the instrument which obviously introduces large errors.
- (ii) the spectrophotometer only has one monochromator which is placed before the sample so any fluorescence is collected with an efficiency equal to that of the diffusely reflected light and consequently the emitting samples can appear "whiter than white".
- (iii) aggregates will have different absorption spectra to their monomers, consequently a shift in the absorption spectra would be observed. The formation

of aggregates causes a reduction in the number of monomers and thus a reduction in the expected absorption.

Aggregation effects are also seen in the fluorescence spectra which will be discussed in the next section (5.1.2). Aggregation has been reported for acridine⁵⁰ and pyrene^{35,36,40,41} on silica gel at similar loadings.

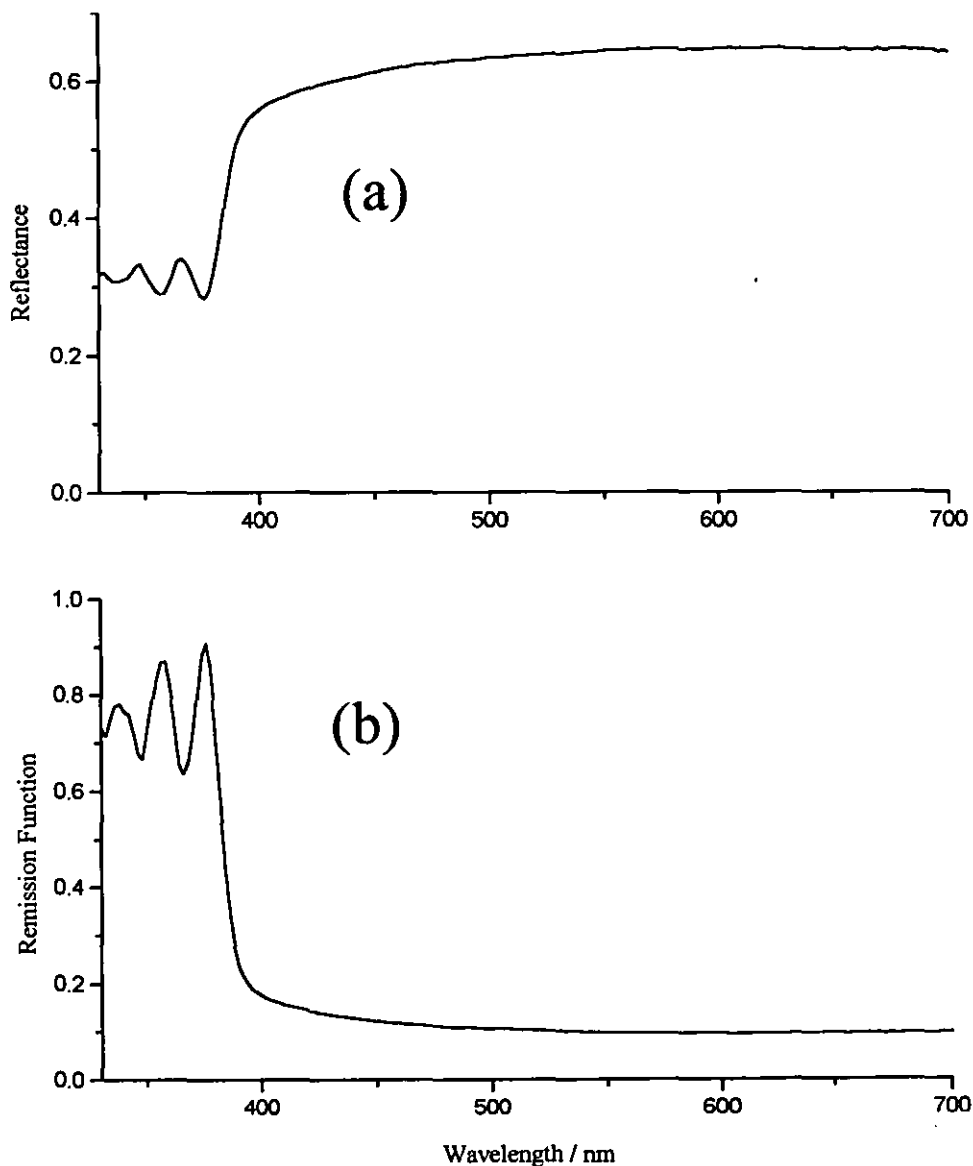


Figure 5.1 : The ground state diffuse reflectance absorption spectrum of anthracene at a loading of $0.6 \mu\text{mol g}^{-1}$ adsorbed on silica gel shown as (a) reflectance and (b) as its corresponding Kubelka Munk remission function (F(R)) spectrum.

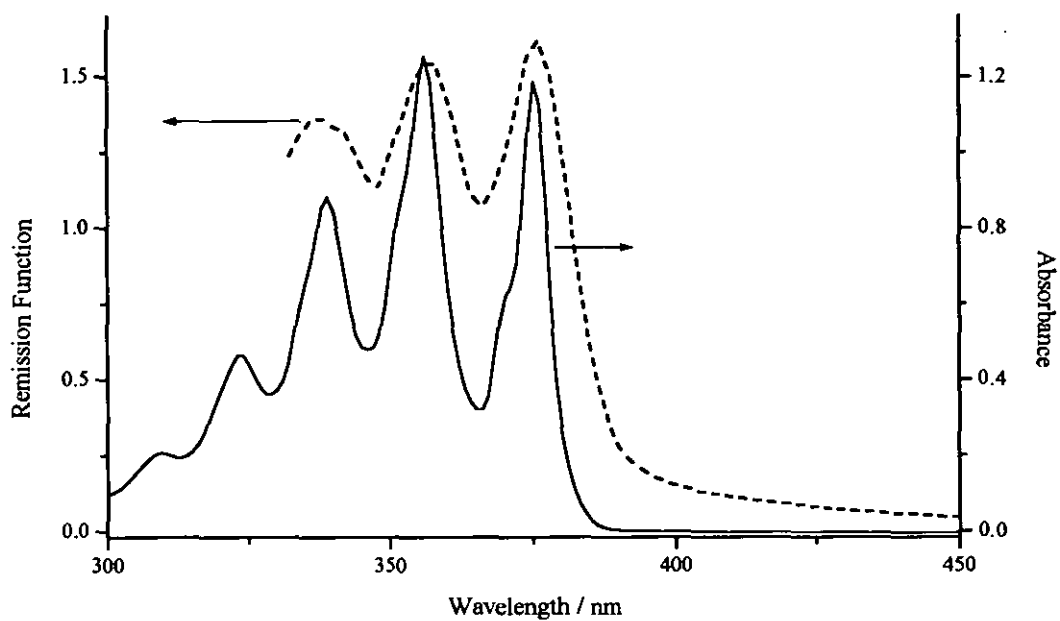


Figure 5.2 : A comparison between anthracene in methanol solution plotted as absorbance (solid line) and anthracene on silica gel plotted as remission function (broken line)

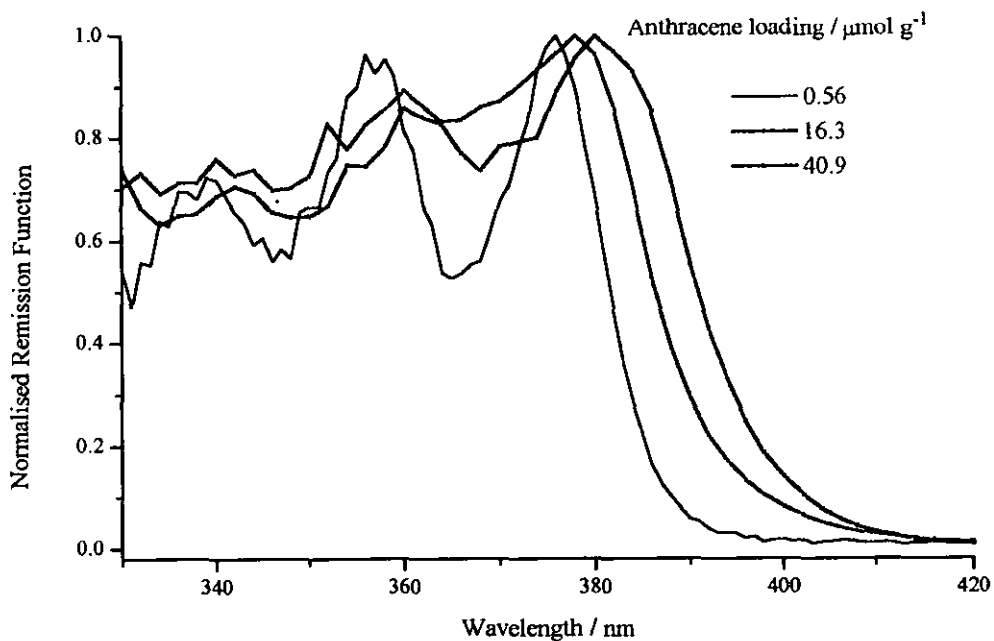


Figure 5.3 : Ground state diffuse reflectance spectra of anthracene adsorbed on silica gel plotted as normalised remission function as a function of anthracene concentration.

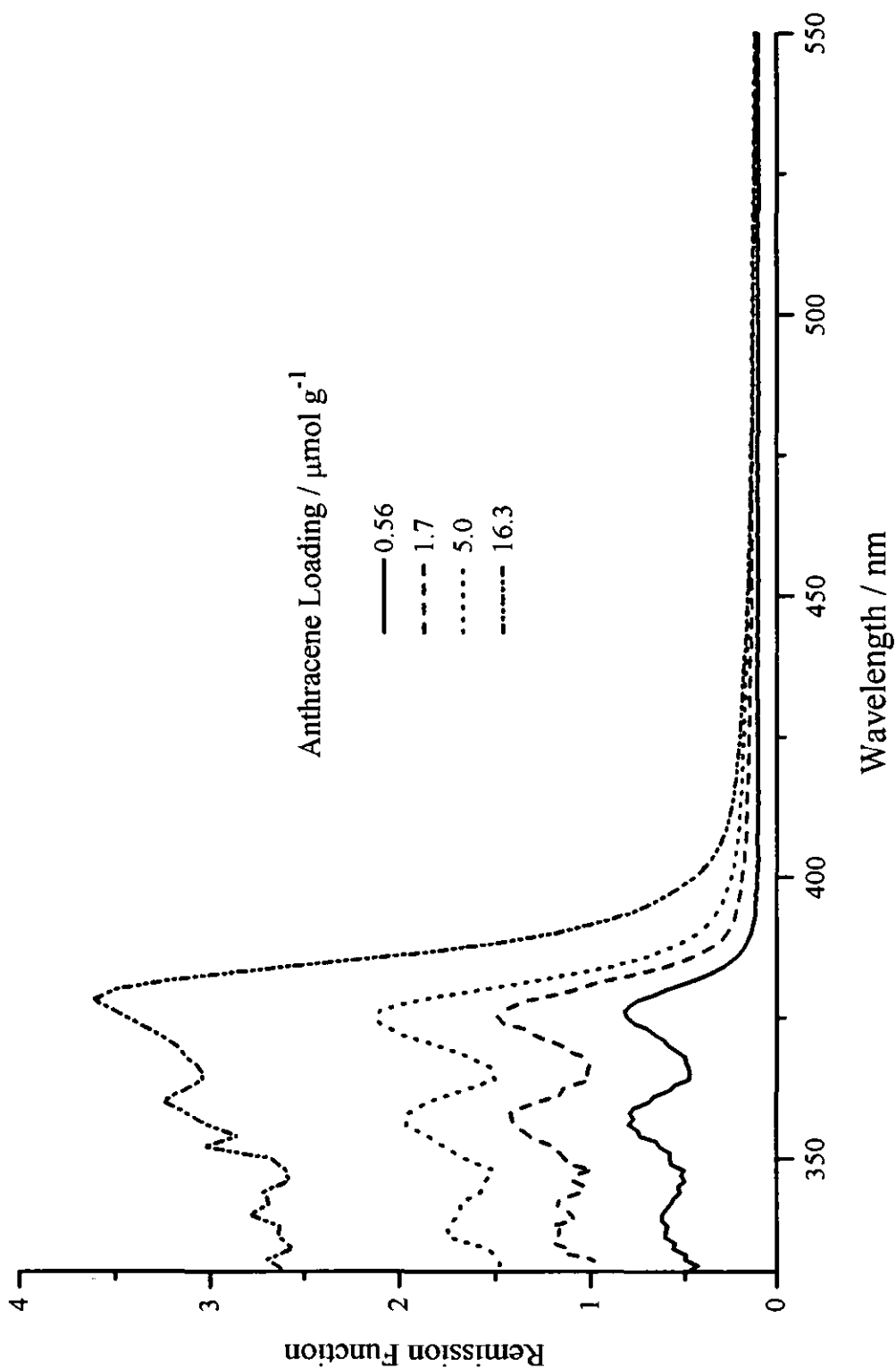


Figure 5.4 : Ground state diffuse reflectance spectra of anthracene adsorbed on silica gel plotted as remission function spectra as a function of anthracene concentration.

5.1.2. Fluorescence Emission Spectra.

A typical emission spectrum of anthracene on silica at a low surface loading ($0.56 \mu\text{mol g}^{-1}$) and a solution spectrum of anthracene in methanol following excitation at 350 nm are shown in Figure 5.5. The positions of the fluorescence peaks are the same, but the intensity of the anthracene peaks when adsorbed on silica gel are distorted by reabsorption (on the shorter wavelength edge) and reemission (shown by a broadening on the longer wavelength edge) effects. With increasing anthracene loading (Figure 5.6) the fluorescence intensity of the longer wavelength peaks (400 and 420 nm) increase relative to the shorter wavelength peak at 384 nm which decreases due to reabsorption where there is overlap with the absorption spectrum. The emission spectrum also narrows on the longer wavelength edge and can be explained by a decrease in penetration depth as the anthracene concentration is increased, thus reducing the effects of self-absorption and reemission. Above a loading of $16.3 \mu\text{mol g}^{-1}$ the emission intensities of all three peaks decrease. This cannot be explained by self-absorption and reemission effects alone and suggests the formation of non-emitting aggregates. The fluorescence intensity is dependent on the amount of light absorbed, and generally as the concentration of a compound is increased the amount of light absorbed increases. When aggregates are formed the amount of light absorbed by the monomer no longer increases with increasing concentration and also the aggregates may absorb the emitted and/or exciting light, consequently the fluorescence intensity decreases.

Typical fluorescence spectra of anthracene on silica following excitation at 390 nm as a function of anthracene concentration are shown in Figure 5.7. These spectra confirm the presence of aggregates by studying the 420 nm peak. Therefore the peak intensity at 420 nm initially increases with increasing loading due to the increasing absorption by monomeric anthracene. However above a loading of $5.0 \mu\text{mol g}^{-1}$ the emission intensity at 420 nm decreases as a result of reabsorption by the aggregates. Monitoring the emission intensity at 500 nm, where the aggregates do not absorb, also shows that the intensity increases with increasing loading, this time up to $16.3 \mu\text{mol g}^{-1}$ and then decreases. This is due to the reduction in absorption of the 390 nm exciting light by the monomer anthracene as a result of aggregate formation and an increase in the absorption of the exciting light by the aggregates.

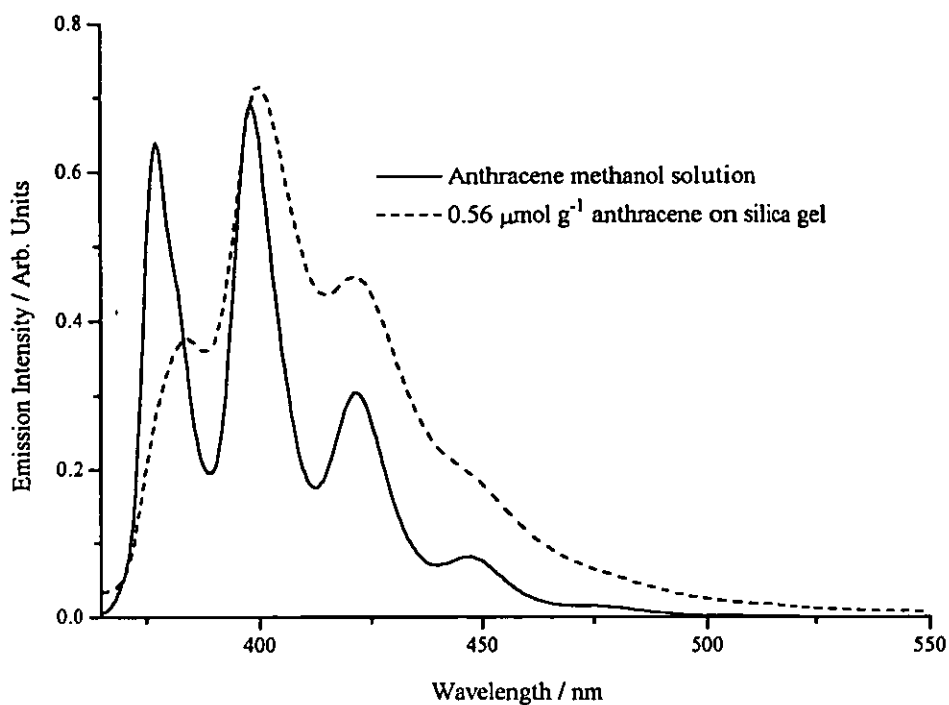


Figure 5.5 : Fluorescence emission spectra of anthracene in methanol solution and adsorbed on silica gel following excitation at 350 nm.

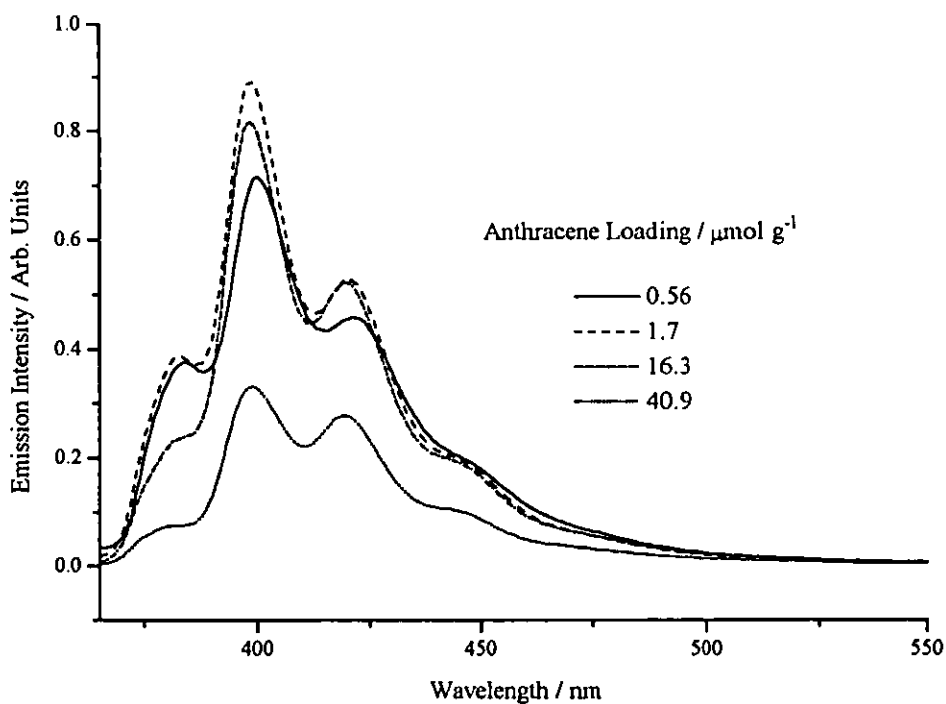


Figure 5.6 : Fluorescence emission spectra of anthracene adsorbed on silica gel plotted as a function of anthracene concentration following excitation at 355 nm.

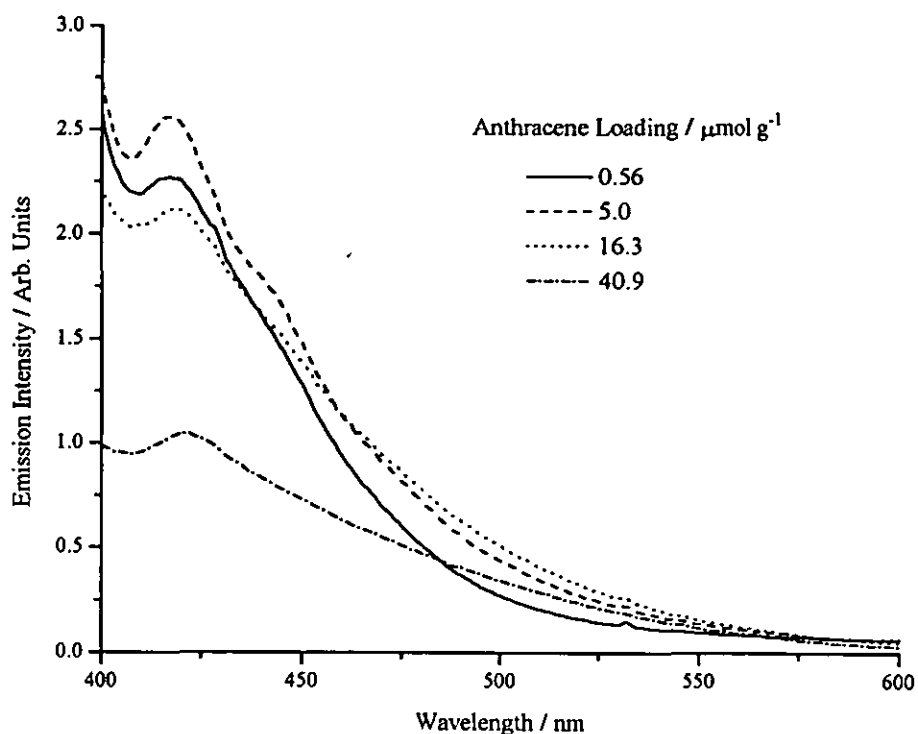


Figure 5.7 : Fluorescence emission spectra of anthracene adsorbed on silica gel following excitation at 390 nm as a function of anthracene concentration.

5.1.3. Transient Absorption Spectra.

A typical transient difference spectrum of anthracene adsorbed on silica gel at a loading of $1.7 \mu\text{mol g}^{-1}$ obtained following diffuse reflectance laser flash photolysis at 355 nm is shown in Figure 5.8. The characteristic triplet-triplet absorption peak at 420 nm, the radical cation peaking at 320, 420, and 715 nm and ground state depletion, illustrated by the negative reflectance change at 375 nm, are observed. The characteristics of the transient absorption spectra are independent of anthracene loading and the normalised spectra are superimposable. No transient absorption attributable to aggregates has been detected from any of the samples studied. The radical cation is not easily observed in solution and peaks are assigned as such due to the similarities with spectra obtained in solution¹³⁰⁻¹³³, in zeolites⁹¹ and in the vapour phase¹³⁴. The addition of a coadsorbed electron donor to the system (section 5.2) also supports this assignment, by the increase in the rate of decay of the anthracene radical cation with the concomitant rise of the donor radical cation.

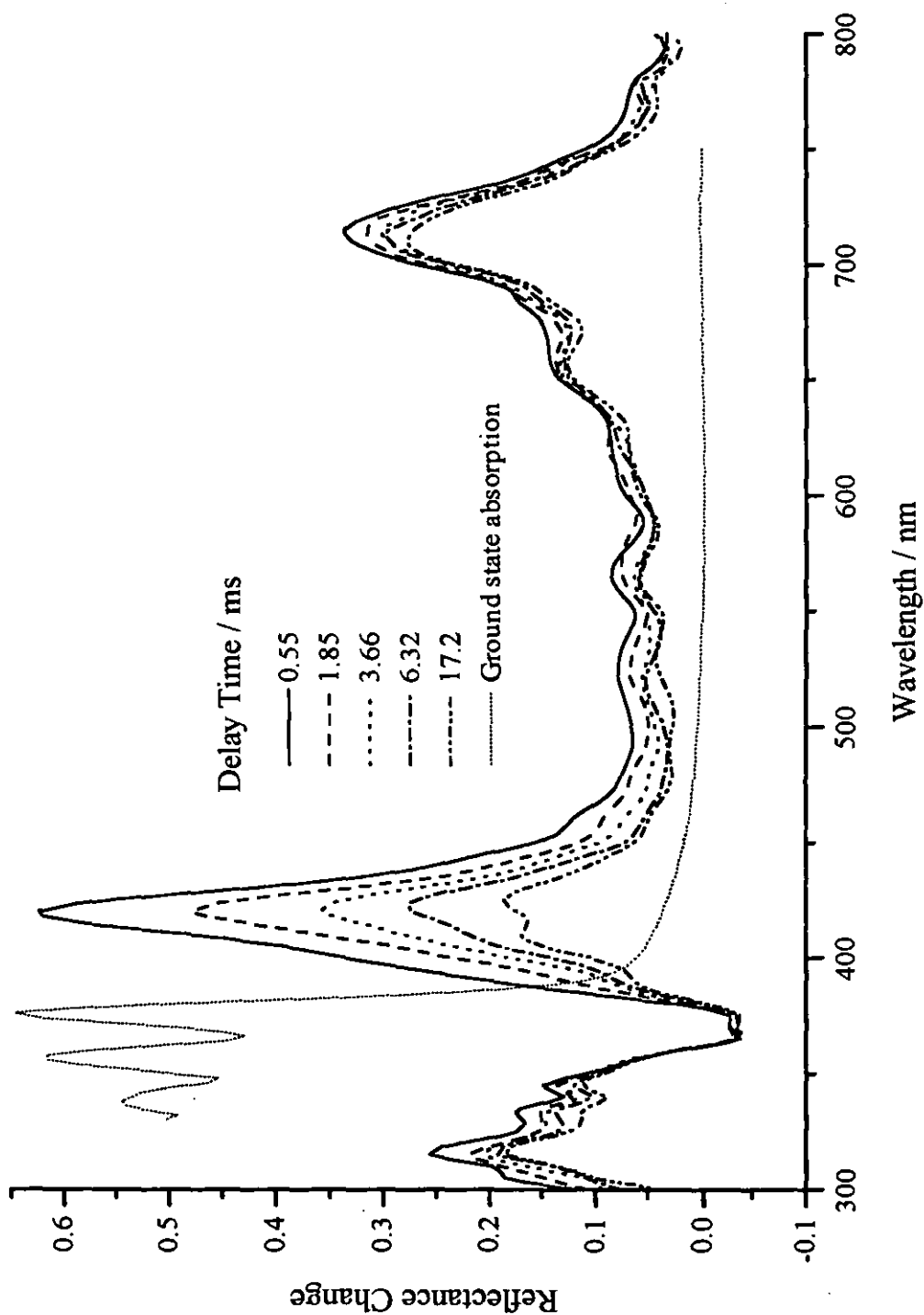


Figure 5.8 : Time-resolved transient spectrum showing reflectance change $(R_0 - R_t)/R_0$ of anthracene adsorbed on silica gel at a sample loading of $1.7 \mu\text{mol g}^{-1}$ following laser excitation at 355 nm. With the sample's ground state reflectance spectrum shown as a dotted line.

Production of both the radical cation and triplet occurs in less than 50 ns, the time resolution of the apparatus. Using the triplet-triplet absorption intensity dependence on laser fluence as a model for one-photon absorption the nature of radical cation production can be determined. Figure 5.9a shows the change in reflectance for the triplet and radical cation, at a loading of $3.4 \mu\text{mol g}^{-1}$, as a function of laser fluence, monitoring at 420 and 715 nm respectively. The triplet-triplet absorption increases rapidly and then saturates at higher laser fluences - typical of the profile expected and reported⁵⁴ for one-photon absorption. The radical cation absorption at low laser fluences is hardly present and rises slowly with increasing fluence forming a concave curve. A straight line could be drawn through these points at lower laser fluences, but this line would intercept the x axis before reaching zero. Experiments using a millisecond flashlamp in place of the laser have also been carried out and re-inforce the suggestion of the multiphotonic production of the anthracene radical cation on silica. Figure 5.9b shows the large signal observed for the triplet which is similar to that produced using laser excitation (Figure 5.9a), but the radical cation signal is absent when the millisecond flashlamp is used for excitation. This and the dependence on laser fluence demonstrate that there is a threshold intensity before the radical cation can be detected and a bi- or multi-photon mechanism is therefore assumed for the production of anthracene radical cation on silica gel. The bi- or multi-photon production of the anthracene radical cation on silica is not surprising as the laser energy (3.49 eV) is below the ionisation potential of anthracene (7.4 eV)¹³⁵. The production of pyrene radical cations on γ -alumina has been observed to be via a two-photon process⁸⁶ and Oelkrug et al⁵⁴ observed similar behaviour for the production of the radical cation of distyrylbenzenes adsorbed on silica. A more complicated mechanism for photoionisation of arenes occurs in/on zeolites^{91,95}; significant amounts of both mono- and bi-photon production is observed. The nature of the zeolite produces so called "active" and "nonactive" sites; at "active" sites mono-photon production of the radical cation occurs, at "non-active" sites the arene is first excited to its singlet and then photoionised to the radical cation in a two photon mechanism. The "active" sites are suggested to be where ground-state charge-transfer complexes form between the arene and the zeolite, thus increasing the ease of extraction of an electron.

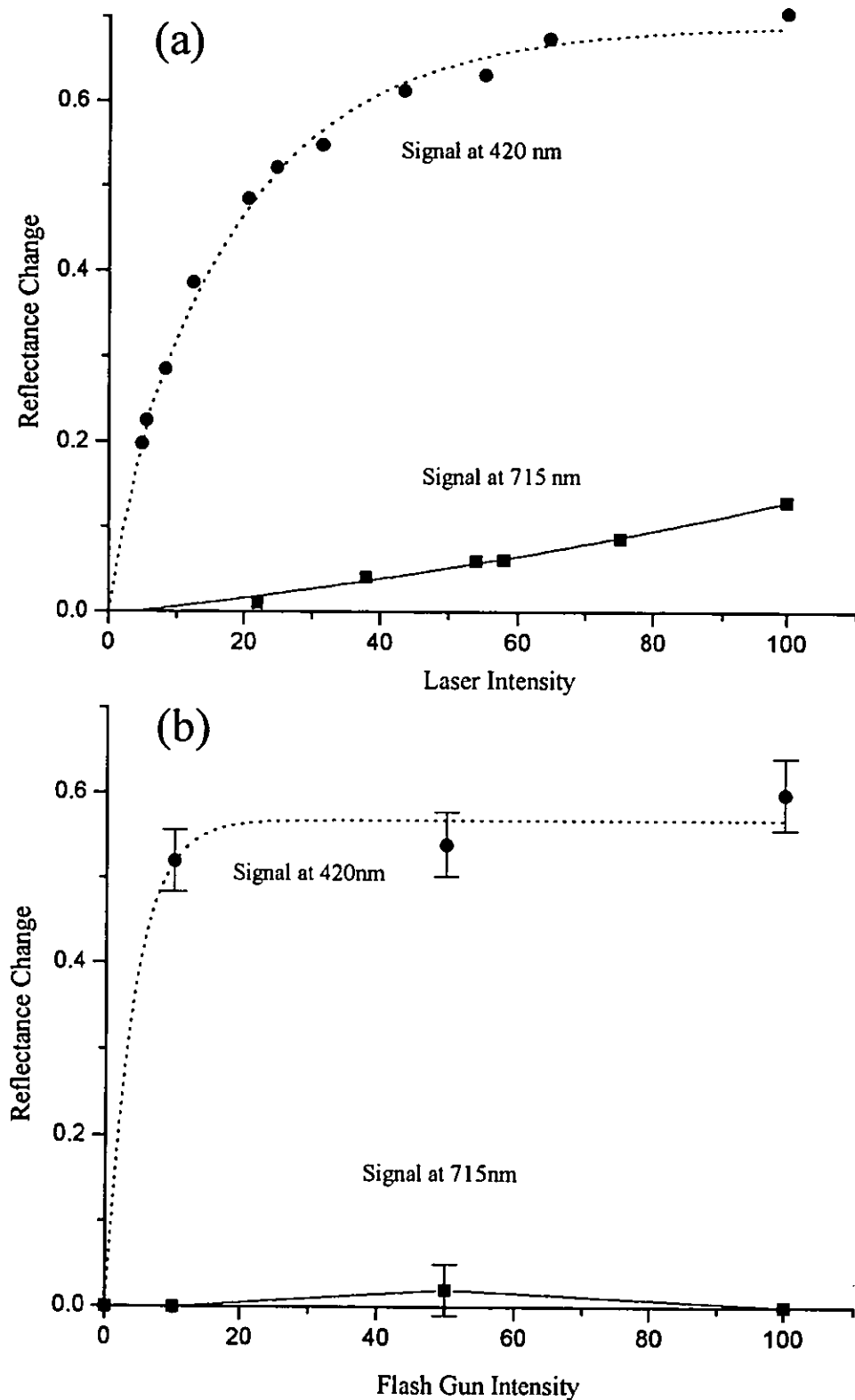


Figure 5.9 : Triplet and radical cation intensity plotted as a function of (a) relative laser intensity and (b) relative flash gun intensity.

5.1.3.1. Kinetic Analysis.

Since modelling has shown an exponential fall-off of transient concentration below the surface (see Figure 5.10), the reflectance change must be kept at or below 10% for kinetic analysis measurements. If this is the case a linear relationship is observed between the concentration of the transient and the reflectance change^{118,119}.

5.1.3.1a. Triplet State Kinetics.

The anthracene triplet lifetime in solution ranges from 0.7 ms to 3.3 ms in non-polar¹³⁶ and polar¹³⁷ solutions respectively. On silica gel, as in solution, the anthracene triplet decays to regenerate the ground state. The decay on silica gel is non-exponential with the first empirical half-lives decreasing from 6.7 ms to 22 μ s as loading increases from 0.56 to 40.9 μ mol g⁻¹. Figure 5.11 illustrates the decrease in triplet lifetime following laser excitation at 355 nm with an energy of 2.5 mJ cm⁻² as anthracene loading is increased. The triplet concentration profile has been modelled using the program described earlier in section 3.9.1. The triplet concentration was found to fall off exponentially, shown in Figure 5.10, for a sample loading of 3.4 μ mol g⁻¹ and a laser fluence of 2.5 mJ cm⁻². The modelled data is shown as points and is plotted along with an exponential decay (solid line). If (1-R) is kept below 0.1 this flash photolysis data can be analysed by assuming the reflectance change ΔR is directly proportional to the triplet concentration. Anthracene photophysics on silica gel is summarised in Scheme 4.1 on page 57. The triplet state decay comprises both first and second order components. The first order component of the decay arises from deactivation of the triplet excited state via interactions with the surface, similar to solvent interactions in solution. The bimolecular component can be attributed to triplet-triplet annihilation, also seen in solution, thus illustrating the mobility of the anthracene on the silica gel surface. The decay is also complicated by the additional absorption from the radical cation in this region, consequently direct analysis of the triplet decay is difficult.

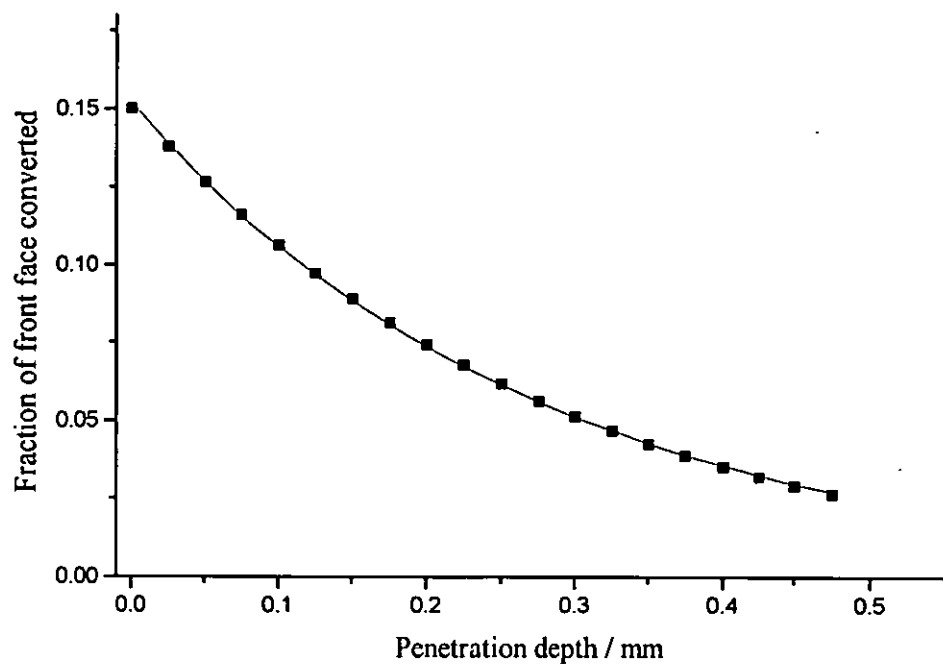


Figure 5.10 : Modelled transient concentration fall-off for anthracene adsorbed on silica (shown as points) at a loading of $3.4 \mu\text{mol g}^{-1}$ and a laser fluence of 2.5 mJ cm^{-2} fitted with an exponential decay (solid line).

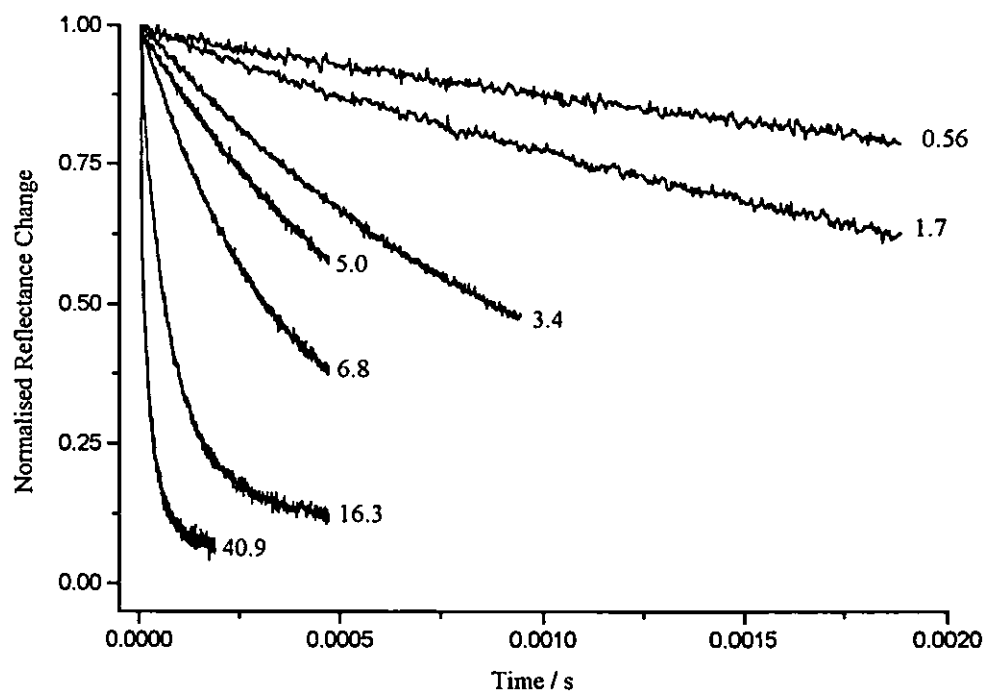
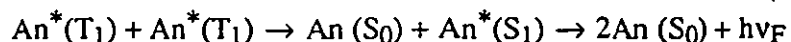


Figure 5.11 : Normalised triplet decay kinetics at 420 nm as a function anthracene concentration in $\mu\text{mol g}^{-1}$ on silica gel.

Indirect analysis of the triplet decay can be carried out by studying the delayed fluorescence produced by the triplet-triplet annihilation, illustrated in scheme 5.2.



Scheme 5.2.

The initial delayed fluorescence intensity as a function of laser fluence is shown in Figure 5.12 plotted along with the normalised square of the calculated front face triplet state concentration, calculated using the modelling program described in section 3.9.1. The observed delayed fluorescence intensity increases with increasing laser fluence and correlates well with the increase in the square of the front face triplet anthracene concentration calculated using the above modelling program. This suggests that the delayed fluorescence arises as a consequence of triplet-triplet annihilation. The intensity and rate of decay of delayed fluorescence both increase with increasing anthracene loading.

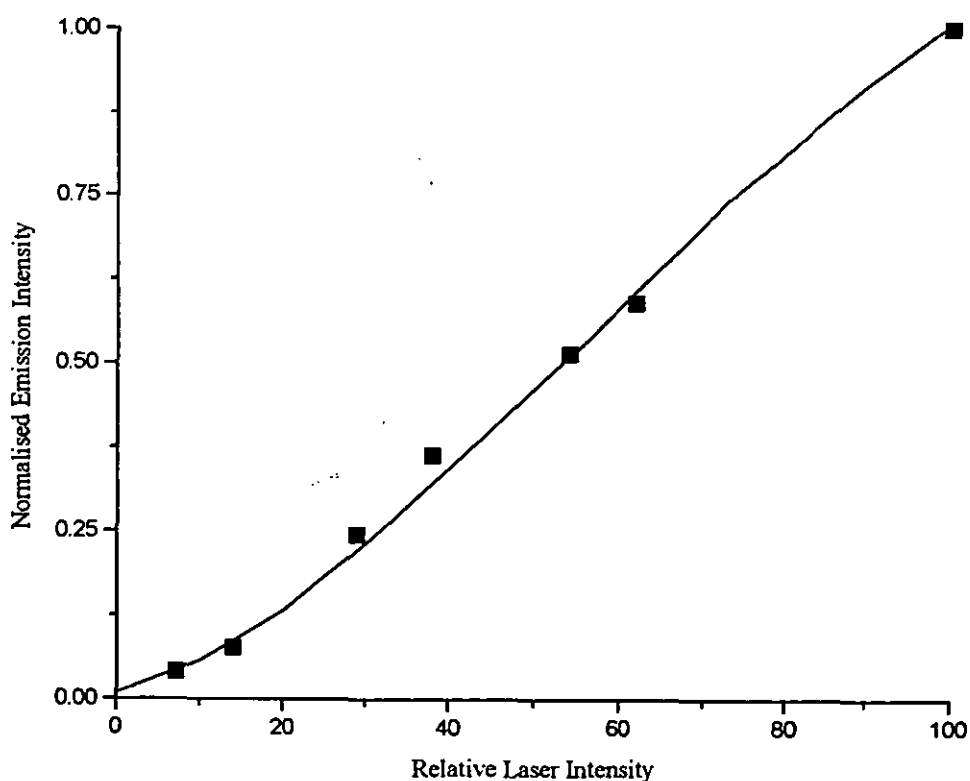


Figure 5.12 : Observed delayed fluorescence intensity (■) plotted as a function of relative laser intensity with the square of the modelled front face triplet concentration (solid line). These traces are normalised to 100% relative laser energy.

Fractal and two-dimensional models as described in section 4.2 can be used to describe bimolecular reactions on surfaces. The fractal model considers the surface as being a random fractal with spectral dimension $4/3$ ^{104,105} and the 2-dimensional model assumes a "flat" two-dimensional surface.

The equations used for the analysis of the delayed fluorescence are :-

$$\sqrt{\frac{I_{DF}^0}{I_{DF}}} - 1 = (2 - \phi_T) k_4 [T_1]^0 t \quad (5.1)$$

and

$$\left(\sqrt{\frac{I_{DF}^0}{I_{DF}}} - 1 \right)^{3/2} = \left(\frac{3}{2} (2 - \phi_T) k_4^0 [T_1]^0 \right)^{3/2} t \quad (5.2)$$

Equation 5.1 is the equation used for the 2-dimensional kinetic analysis and equation 5.2 for the fractal analysis.

A plot of either $(\sqrt{I_{DF}^0}/\sqrt{I_{DF}} - 1)$ or $(\sqrt{I_{DF}^0}/\sqrt{I_{DF}} - 1)^{3/2}$ vs t , where I_{DF} is the delayed fluorescence intensity, should yield a straight line at early times depending on whether fractal or two-dimensional kinetics dominate. Figures 5.13a and 5.13b. show plots of $(\sqrt{I_{DF}^0}/\sqrt{I_{DF}} - 1)$ and $(\sqrt{I_{DF}^0}/\sqrt{I_{DF}} - 1)^{3/2}$ vs t for anthracene adsorbed on silica gel at loadings of $1.7 \mu\text{mol g}^{-1}$ and $16.8 \mu\text{mol g}^{-1}$ respectively. Figure 5.13a reveals that at low anthracene loadings ($1.7 \mu\text{mol g}^{-1}$) the initial decay is predominantly by fractal-dimensional kinetics. As the anthracene loading is increased ($> 5.0 \mu\text{mol g}^{-1}$) two-dimensional kinetics dominate the decays, illustrated in Figure 5.13b which shows the more linear initial portion of the decay occurs when using the two-dimensional analysis for a loading of $16.8 \mu\text{mol g}^{-1}$. This behaviour can be explained by preferential adsorption of anthracene into the silica gel pores; once the pores are full the molecules must then be adsorbed onto the outer, two-dimensional surface. The preferential adsorption into the pores is not surprising as there will be a greater density of adsorption sites in the pores. Hence at lower loadings most of the anthracene molecules can be housed in the pores, as the loading increases and the sites in the pores become occupied and more and more molecules are adsorbed to the outer "flatter" surface. At longer times the decays become predominantly two-dimensional in nature for all loadings of anthracene. This indicates the triplets are annihilated within the pores faster than those on the outer surface, possibly due to "across pore" interactions.

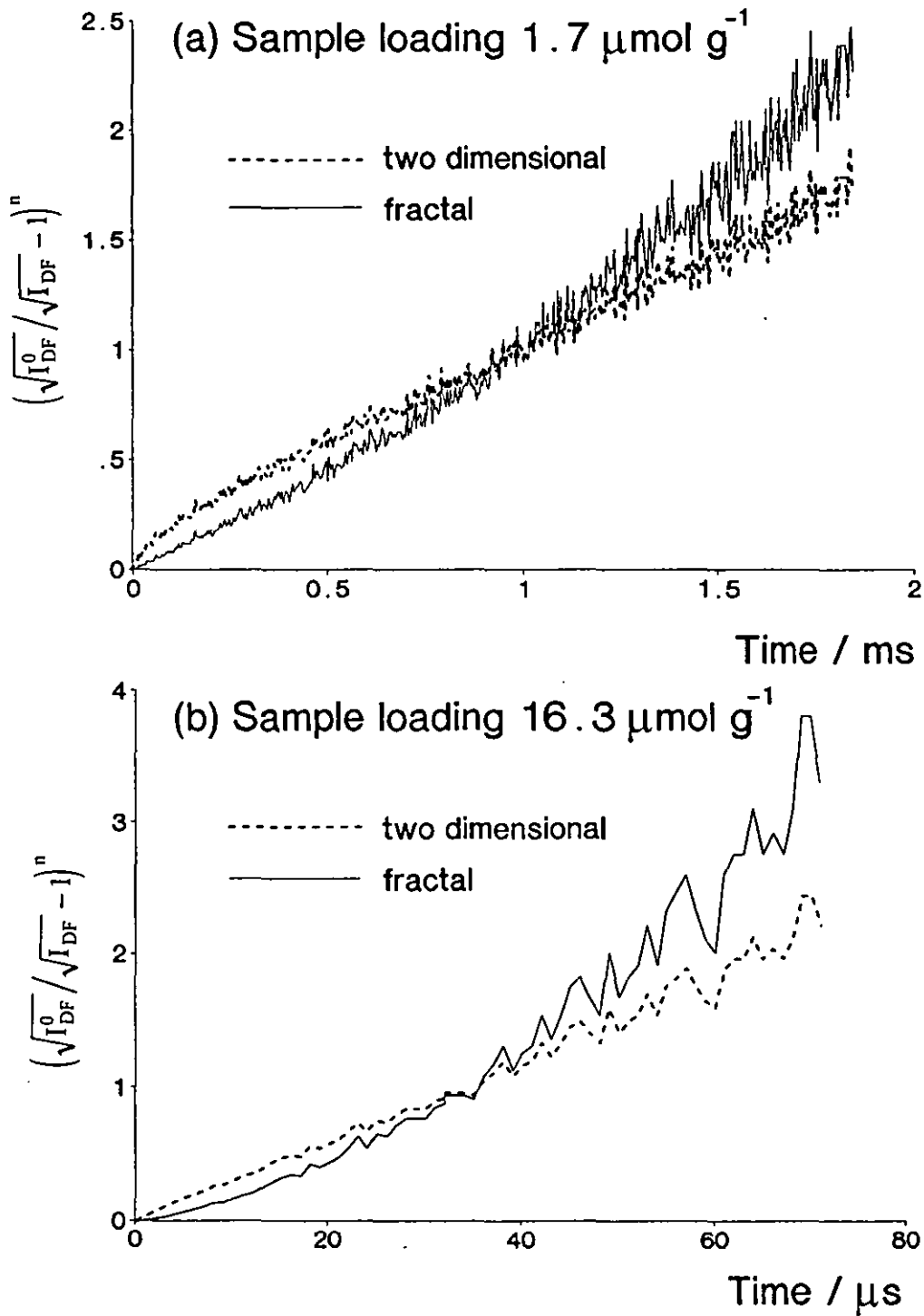


Figure 5.13 : Delayed fluorescence decay kinetics of (a) $1.7 \mu\text{mol g}^{-1}$ and (b) $16.3 \mu\text{mol g}^{-1}$ of anthracene adsorbed on silica gel plotted as $(\sqrt{I_{DF}^0} / \sqrt{I_{DF}} - 1)^n$ vs t where $n = 1$ for the two-dimensional model and $n = 3/2$ for the fractal model.

5.1.3.1b. Radical Cation Decay Kinetics.

The radical cation can live for hours (Figure 5.14) and decays by a complex mechanism, initially very fast then followed by a much slower long time component. The radical cation decays via electron-radical cation recombination, regenerating the ground state. Figure 5.15 shows that the radical cation rate of decay increases with increasing anthracene loading, as one might expect due to the higher number of radical cations formed per unit volume and consequently more electrons.

The process of electron radical cation recombination could be via geminate recombination i.e. the electron recombines with the anthracene it has just left, or the electron could diffuse around the surface until it finds a different radical cation to combine with. Equation 5.3 has been used to describe geminate recombination^{54,106,112} :-

$$\frac{C_0}{C} = (1 + a\sqrt{t}) \quad (5.3)$$

where a is a constant, C_0 and C are the transient concentration at time $t=0$ and t respectively. Equation 5.3 is derived earlier in section 4.3.

The model assumes that the separation between the radical cation and the electron is much smaller than the nearest distance between adsorbates. A plot of C_0/C vs \sqrt{t} at early times should be linear if geminate recombination is to be the major decay pathway. Figure 5.16 shows that as the anthracene concentration is increased from 0.56 to 40.9 $\mu\text{mol g}^{-1}$ the plots of C_0/C vs \sqrt{t} for radical cation decay at 715 nm become less and less linear. At lower loadings of anthracene ($<1.7 \mu\text{mol g}^{-1}$) the decay mechanism of the radical cation is predominantly by geminate recombination, but as the anthracene loading is increased geminate recombination plays little part in the decay pathway. As the anthracene concentration is increased the ion-electron separation distance becomes comparable with the ion-ion separation distance and the model is no longer valid. Oelkrug et al showed that geminate recombination is the major decay pathway for distyrylbenzenes adsorbed on silica gel and γ -alumina⁵⁴ at loadings between 0.7 $\mu\text{mol g}^{-1}$ and 0.003 $\mu\text{mol g}^{-1}$, which is consistent with the results for anthracene at low loadings.

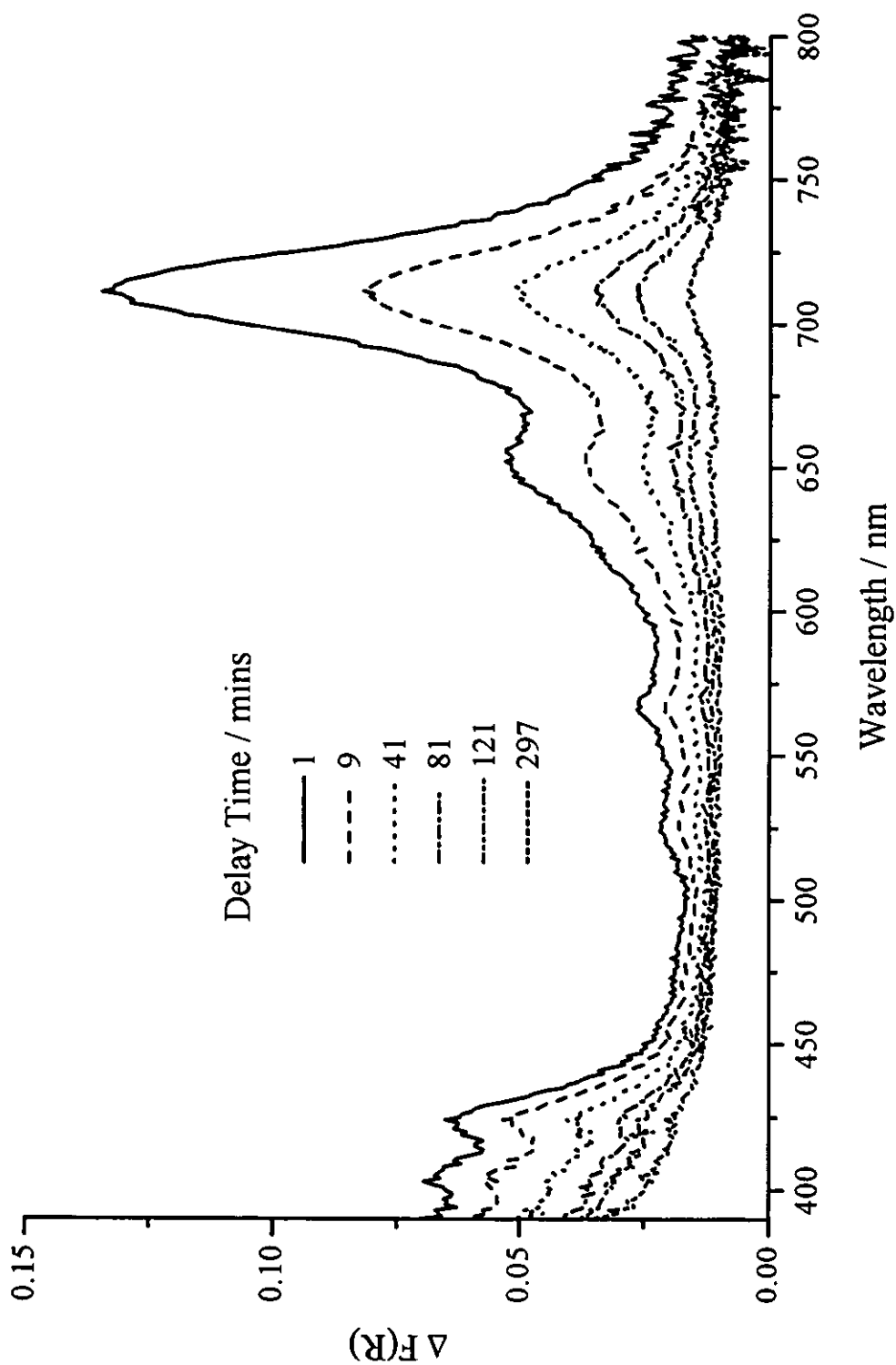


Figure 5.14 : Anthracene cation radical decay of a sample loading of $3.4 \mu\text{mol g}^{-1}$ following laser excitation of the same spot with 40 shots of 15 mJ cm^{-2} at 355 nm.

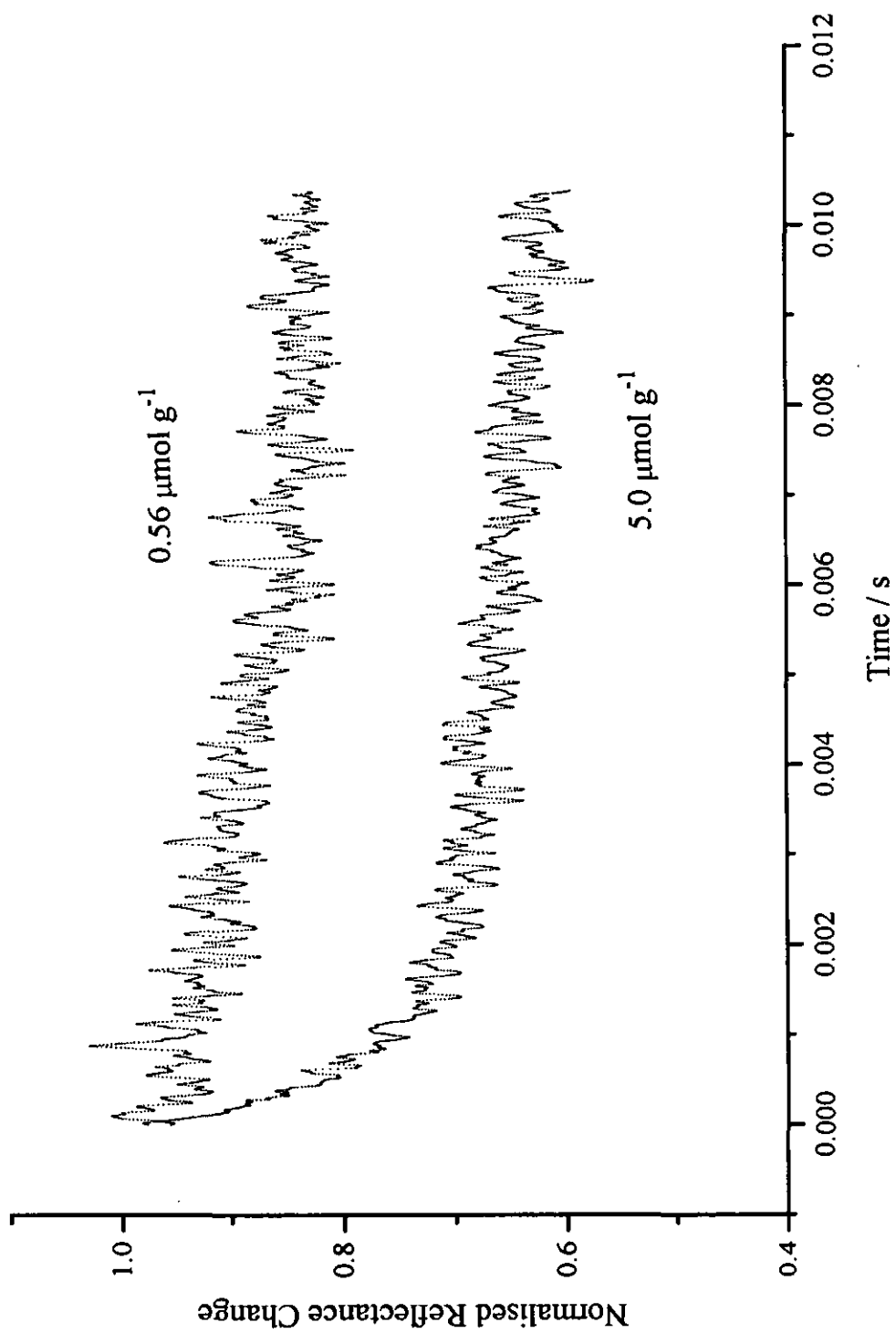
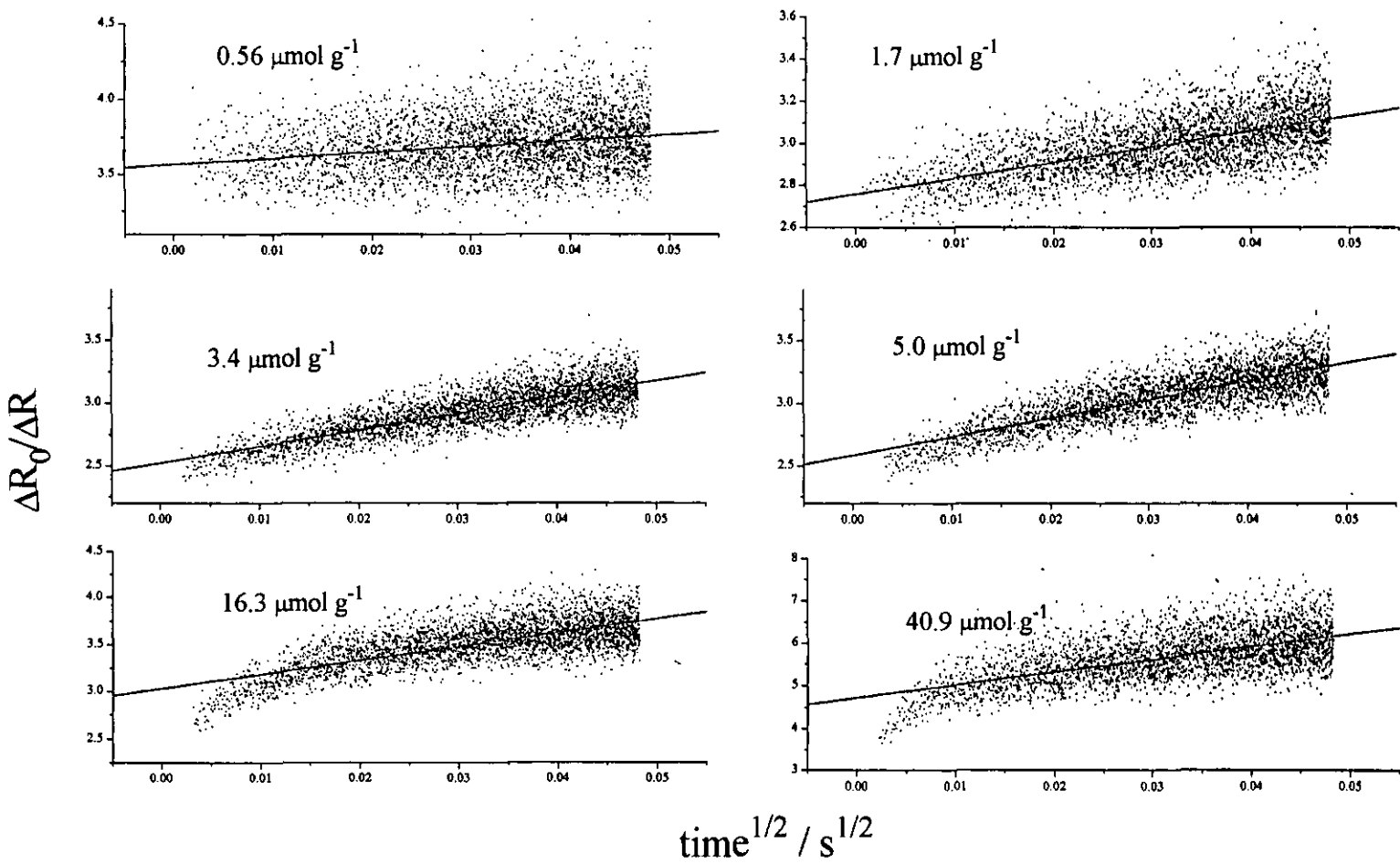


Figure 5.15 : Normalised anthracene radical cation decay shown as reflectance change following laser excitation at 355 nm as a function of anthracene concentration on silica gel.

Figure 5.16 : The initial part of the anthracene radical cation decay plotted as R_0/R versus \sqrt{t} as a function of anthracene loading.



5.1.4. Transient Emission Spectra.

Using nanosecond laser flash excitation at 355 nm the time resolved emission spectrum of anthracene on silica gel was obtained. The transient emission spectra were recorded 85 ns after the laser pulse using a 100 ns gate width. The transient emission spectrum (Figure 5.17) reveals a peak around 400 nm, a broad structureless peak centred at about 450 nm and a more structured peak at 530 nm. The 400 nm peak is a consequence of the delayed fluorescence which was discussed earlier in section 5.1.3.1a.

The other two emission peaks decay with different rates, with the 450 nm peak decaying with a lifetime of approximately 200 ns, much faster than the 530 nm peak. As anthracene concentration is increased the 450 nm peak increases in intensity relative to the 530 nm peak, suggesting that the 450 nm peak originates from the interaction of two or more anthracene molecules. Anthracene excimer fluorescence, previously observed in crystals and low temperature glasses¹³⁸ has very similar spectral properties to the 450 nm emission observed here. The spectral similarities with excimer fluorescence and the suggestion of bimolecular involvement lead to the assignment of the 450 nm peak as excimer fluorescence.

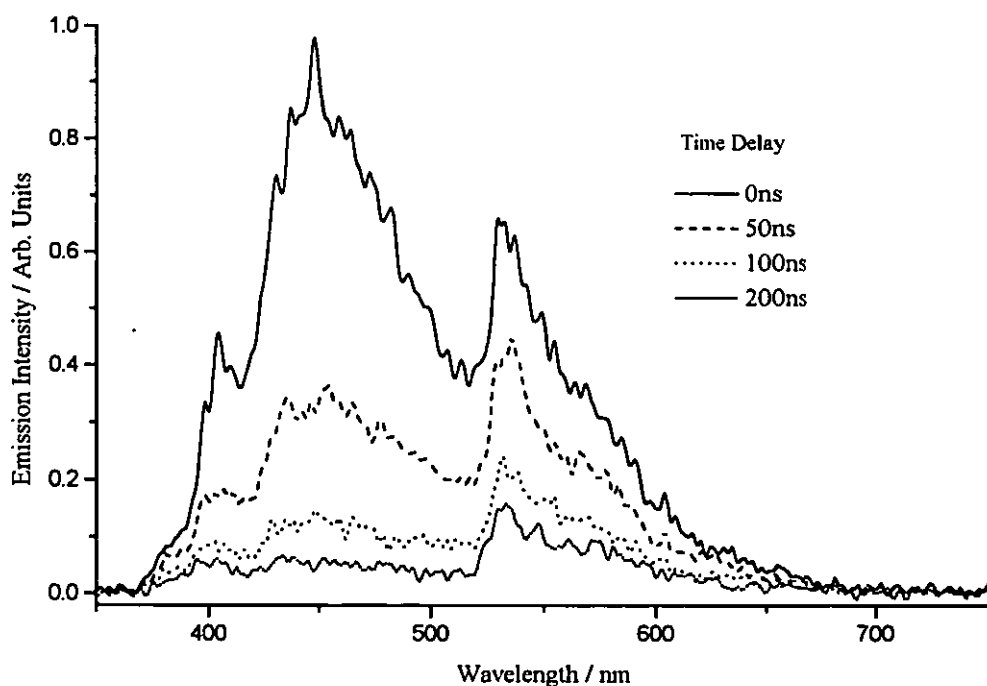


Figure 5.17 : Time-resolved transient emission spectrum of anthracene adsorbed on silica gel at a loading of $1.7 \mu\text{mol g}^{-1}$ following laser excitation at 355 nm, pulse energy 15 mJ cm^{-2} and a gate width of 100 ns.

The 530 nm peak is similar to an emission formed when anthracene is excited in a methanol glass at 77K, see Figure 5.18. Experiments have been carried out using ethanol, butanol, methanol, 2-propanol, 2-methylbutane and methylcyclohexane for forming the glass at 77K. The anthracene was dissolved in the appropriate solvent and cooled to 77K in a glass dewar using liquid nitrogen. The transient emission spectra were collected using a gated photodiode array, gated 85 ns after the laser pulse. The same area of the glass (still inside the glass dewar) was repeatedly excited at 355 nm and the emission intensity was measured as a function of laser irradiation, i.e. number of laser shots, shown in Figure 5.18. Each of the spectra were integrated over the same number of shots, the first integration after 20 shots gives a very small signal, the second integration after a further 20 shots gives a larger signal and the third integration yields an even larger emission signal. The emission intensity builds up depending on the length of laser irradiation, additional irradiation of the glass using a xenon arc lamp also causes a further increase in the emission intensity. The 530 nm emission was only observed when the alcoholic glasses were used. This suggests the emission from the methanol glass is formed by a monophotonic photochemical reaction between anthracene and the alcoholic hydroxyl groups in the glass. The 530 nm emission observed on silica gel does not show this build up on laser irradiation, so on silica gel this emission is not formed via a photochemical reaction. The emitting species is probably formed on adsorption of the anthracene to the surface, by interactions between a few highly active acidic sites on silica gel and anthracene. The protonated form of anthracene enclosed in a zeolite has been reported to emit at 545 nm⁹⁶. The emission spectrum of protonated anthracene in zeolites and the spectra in the alcoholic glasses imply that the emission at 530 nm is probably due to protonated anthracene, formed on adsorption of the anthracene to the silica surface.

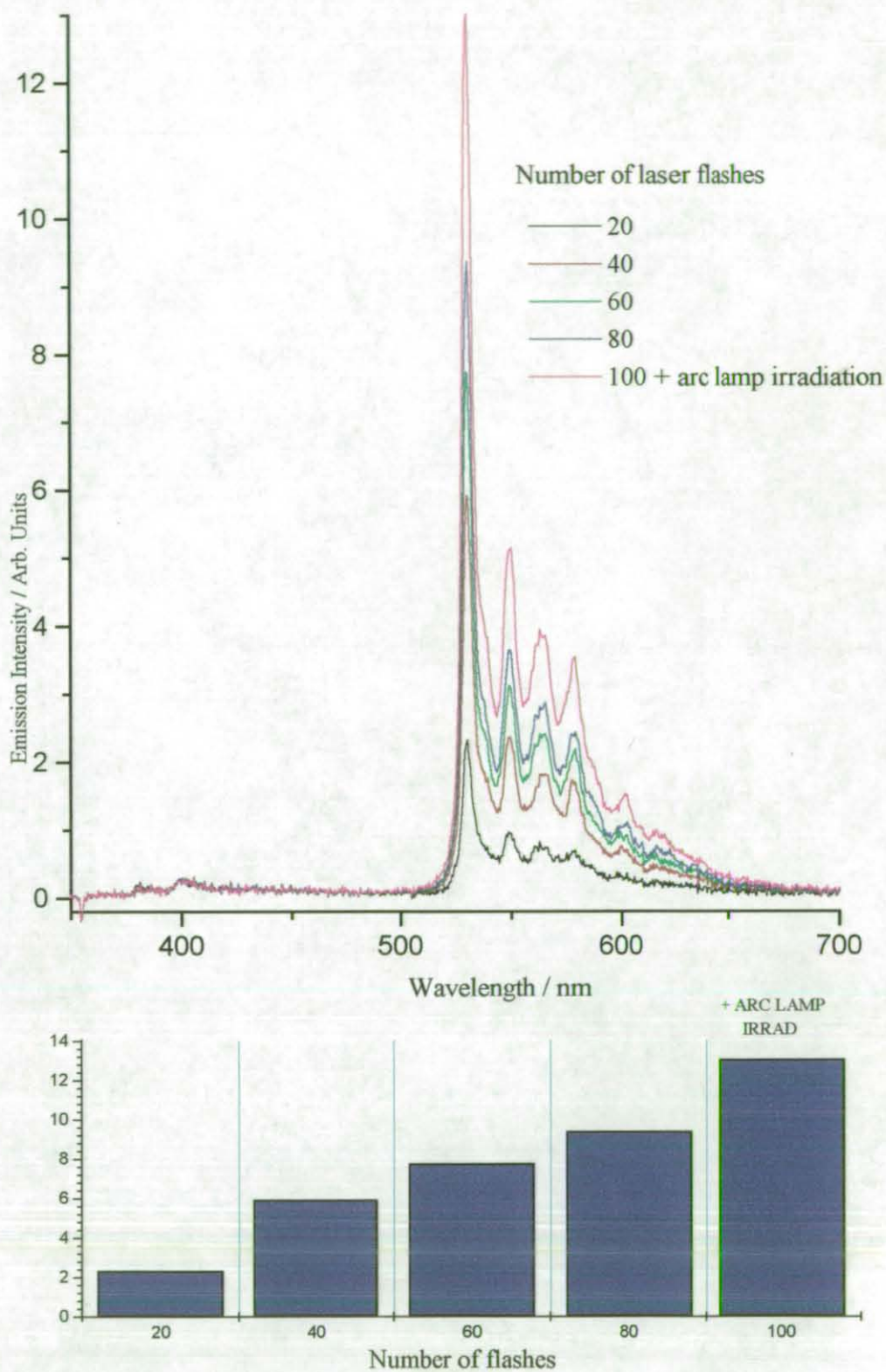


Figure 5.18 : Transient emission spectrum of anthracene in a methanol glass following laser excitation at 355 nm.

5.1.5. Conclusions

The study of anthracene adsorbed on silica gel as a function of anthracene concentration has demonstrated the formation of aggregates at relatively low loadings corresponding to coverages of only a few percent of a monolayer. The analysis of the decay of the delayed fluorescence displays the presence of two different regions for the adsorption of anthracene molecules. The different domains on porous silica gel are suggested to be due to adsorption within the pores and interconnecting channels, and adsorption over the outer, "flatter" surface.

The production of the anthracene radical cation on silica gel is multiphotonic in nature. The presence and long lifetime of the radical cation demonstrates the electron accepting ability of the silica gel. The radical cation decay is predominantly by electron-radical combination. At low loadings geminate recombination of the electron and radical cation is the dominant mechanism; in more concentrated samples the electron may combine with other cation radicals as the ion-ion separation approaches the ion-electron separation distance.

5.2. Anthracene and coadsorbed electron donor.

This work originated as a study of triplet-triplet energy transfer between anthracene and azulene adsorbed on silica gel. The kinetics of this reaction on silica gel are very difficult to analyse (see section 5.1.3.1) and the presence of azulene caused a rapid increase in the rate of decay of the anthracene radical cation. This observation prompted the study of other electron donors and their effects on the rate of decay of the anthracene radical cation.

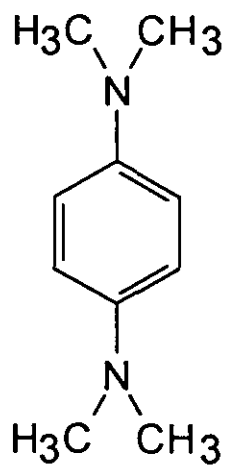
As shown earlier in section 5.1.3 both the triplet and cation radical are formed following laser excitation of anthracene on silica gel at 355 nm. The radical cation lives for hours and the addition of various electron donors can cause an increase in its rate of decay. Electron donors with oxidation potentials below the reduction potential of the anthracene radical cation (1.09V vs SCE) can quench it via an electron transfer mechanism (Scheme 5.3), as follows :-



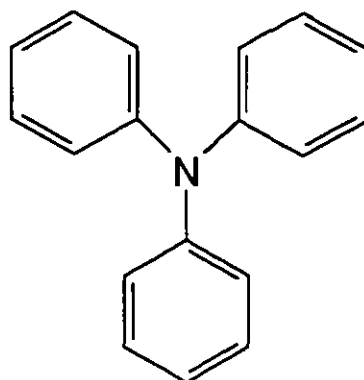
where An and An^{·+} represent anthracene and its radical cation respectively and ED and ED^{·+} represent the electron donor and its radical cation respectively. A number of compounds have been studied for possible electron transfer to the anthracene cation radical. The structures of these compounds are shown overleaf in Figure 5.19 and are listed below in Table 5.1 with their oxidation potentials.

Compound	E _{OX} / V (vs SCE)
N,N,N',N'-tetramethyl-1,4-phenylenediamine (TMPD)	0.32
N,N-dimethylaniline (DMA)	0.53
Azulene	0.71
Triphenylamine (TPA)	0.92
Aniline	0.98
Naphthalene	1.54

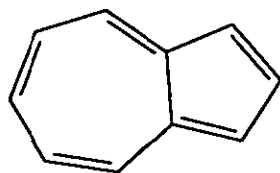
Table 5.1:- Oxidation potentials of electron donors, from reference¹³⁹



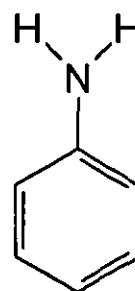
TMPD



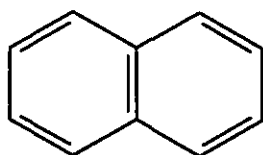
TPA



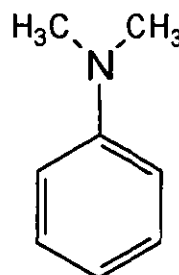
Azulene



Aniline



Naphthalene



N,N-dimethylaniline

Figure 5.19 : Structures of electron donors used.

Of the above naphthalene is the only compound that did not undergo electron transfer to the anthracene radical cation, due to its oxidation potential being above the reduction potential of the radical cation. In the cases of TMPD, TPA and DMA the anthracene radical cation decay is accompanied by the concomitant rise of the radical cation of the electron donor. Details of the electron transfer between anthracene and azulene, triphenylamine (TPA), N,N,N',N'-tetramethyl-1,4-phenylenediamine (TMPD) and N,N-dimethylaniline (DMA) are discussed below.

5.2.1. N,N,N',N'-tetramethyl-1,4-phenylenediamine and anthracene

TMPD and anthracene were coadsorbed from acetonitrile onto silica gel and studied as a function of TMPD concentration, in the range $0.7 \mu\text{mol g}^{-1}$ to $10 \mu\text{mol g}^{-1}$ with a loading of approximately $1 \mu\text{mol g}^{-1}$ of anthracene. This is the simplest of the electron donor systems studied, in that no additional quenching of the singlet or triplet is observed due to the TMPD presence.

5.2.1.1. Transient absorption spectra.

The anthracene triplet and radical cation are observed following laser excitation at 355 nm, the decay of the anthracene radical cation being accompanied by the concomitant rise of the previously reported TMPD radical cation¹³², at 560 and 610 nm (Figure 5.20). The characteristics of the transient spectra are independent of TMPD concentration, an increase in TMPD concentration only increases the rate of decay or formation of the transients observed. A sample of TMPD with no anthracene adsorbed on silica gel reveals no transients on laser excitation at 355 nm, so the TMPD radical cation is not formed by laser excitation alone.

5.2.1.2. Electron Transfer Kinetics.

The rate of decay of the anthracene radical cation at 715 nm without the electron donor present is negligible on these timescales (see section 5.1.3.1b.), consequently the observed decay is predominantly via electron transfer from the TMPD and can be fitted using kinetic models making this assumption (described briefly below and in detail in section 4). The anthracene radical cation decay is still complex and does not conform to a single exponential model. Various models can be used for describing kinetics in heterogeneous media, for example stretched exponentials, exponential series⁹⁸⁻¹⁰⁰, fractal and 2-dimensional^{51,140}, and dispersive kinetics^{97,111,114}.

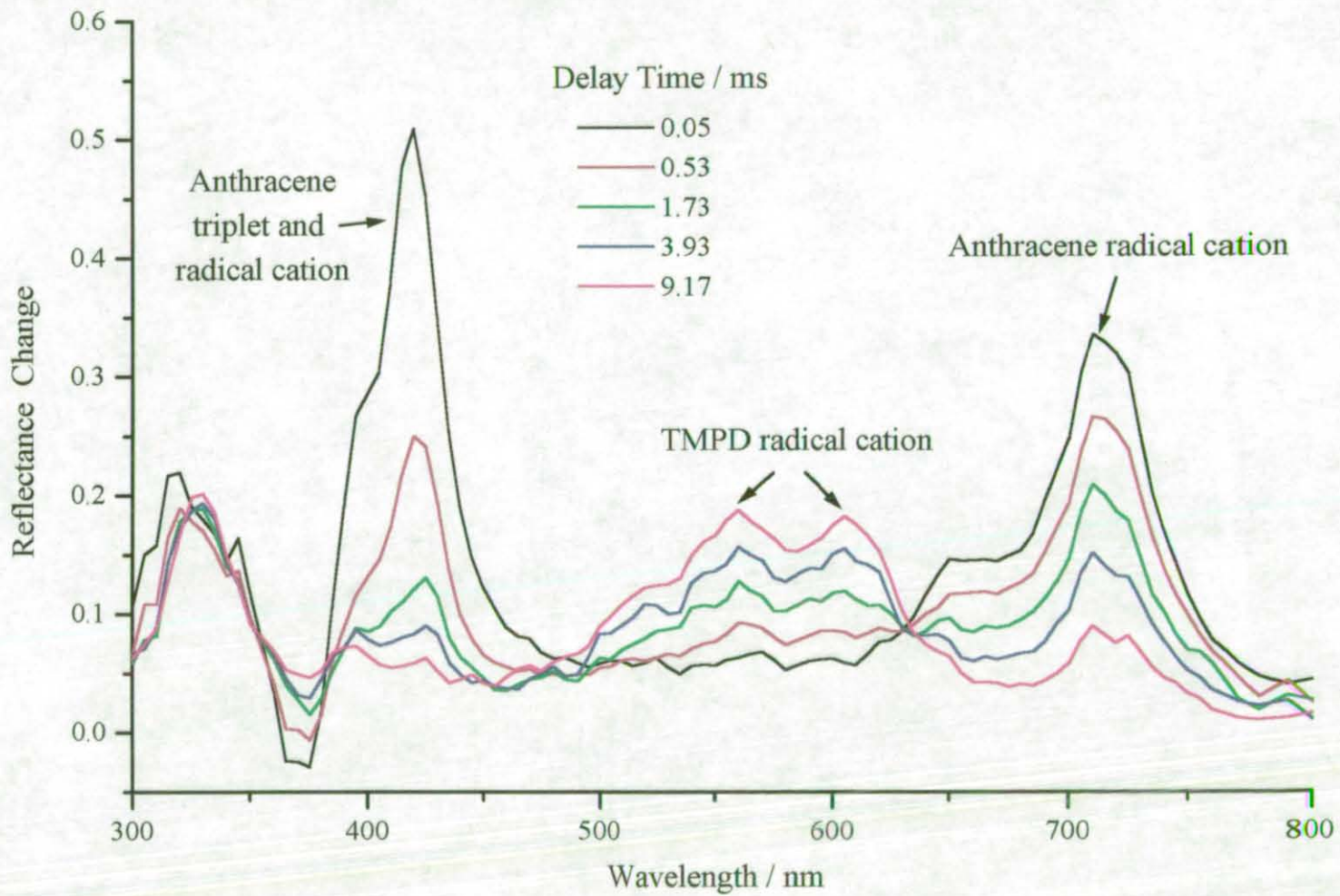


Figure 5.20 : Time-resolved transient difference absorption spectrum of anthracene coadsorbed with TMPD on silica gel at loadings of 0.7 and 1.7 $\mu\text{mol g}^{-1}$ respectively following laser excitation at 355 nm.

The models used here to fit the anthracene radical cation decay in the presence of an electron donor are the fractal and the two-dimensional model and the dispersive kinetic model of Albery et al¹⁰⁷. The equation relating to the latter is shown below :-

$$\frac{C}{C_0} = \frac{\int_{-\infty}^{+\infty} \exp(-t^2) \exp[-\bar{k}t \exp(\gamma t)] dt}{\int_{-\infty}^{+\infty} \exp(-t^2) dt} \quad (5.4)$$

where C_0 and C are the initial transient concentration and the concentration at time t respectively, γ is the width of the distribution and \bar{k} the mean rate constant. If ΔR is kept around 10%, ΔR is proportional to transient concentration and so for low reflectance changes C/C_0 can be replaced by $\Delta R/\Delta R_0$. This model assumes a gaussian distribution of activation energies for the decay process and therefore a logarithmic gaussian distribution of rate constants. A typical decay of the anthracene radical cation at 715 nm and its dispersive model fit are shown in Figures 5.21a & 5.21b as reflectance change vs time and \log_e time respectively. Table 5.2 shows the results of the fits obtained for constant anthracene concentration ($1 \mu\text{mol g}^{-1}$) with varying TMPD concentrations ($0.3 \mu\text{mol g}^{-1}$ to $10 \mu\text{mol g}^{-1}$).

TMPD conc. / $\mu\text{mol g}^{-1}$	\bar{k} / s^{-1}	sd	γ
0.3	468	80	1.85
1.7	1662	209	1.23
4.9	6638	309	1.10
6.2	7130	548	1.25
10.5	14383	913	1.24

Table 5.2:- Mean rate constant (\bar{k}), standard deviation (sd) and distribution width for the rate of electron transfer (γ) between TMPD and the anthracene radical cation.

γ is an indication of the heterogeneity of the surface and from Table 5.2 appears to be virtually independent of the electron donor concentration while \bar{k} increases linearly with increasing concentration. A plot of \bar{k} vs TMPD concentration is linear with a gradient of $1.4 \times 10^9 \text{ g mol}^{-1} \text{ s}^{-1}$ (Figure 5.22). If this plot can be described by the equation :-

$$\bar{k} = \bar{k}_0 + \bar{k}_{\text{TMPD}} [\text{TMPD}] \quad (5.5)$$

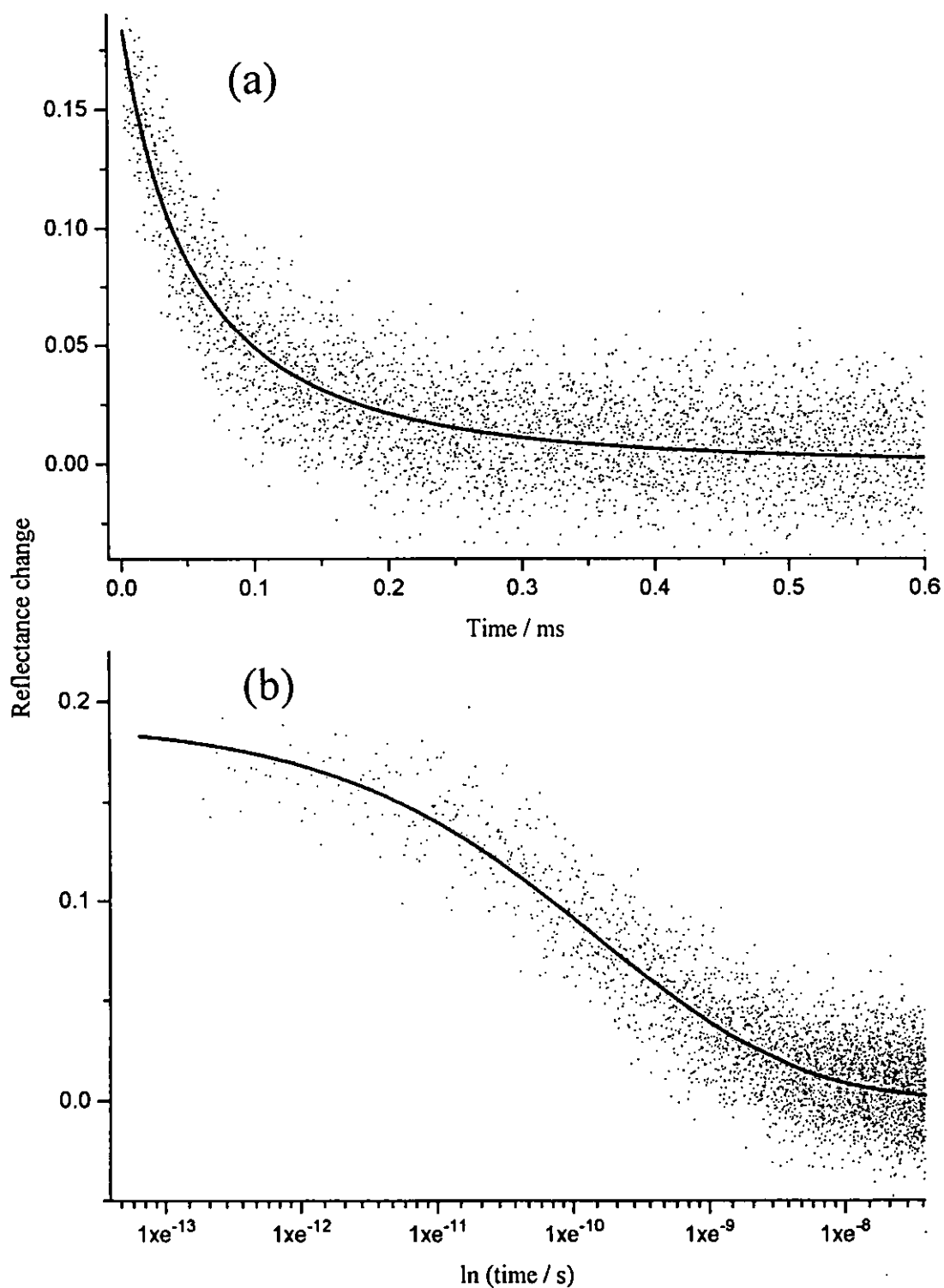


Figure 5.21 : Anthracene radical cation decay at 715 nm following laser excitation at 355 nm in the presence of coadsorbed TMPD ($1.7 \mu\text{mol g}^{-1}$) plotted as reflectance change versus (a) time and (b) \ln (time) both with the dispersive model fits shown by solid lines.

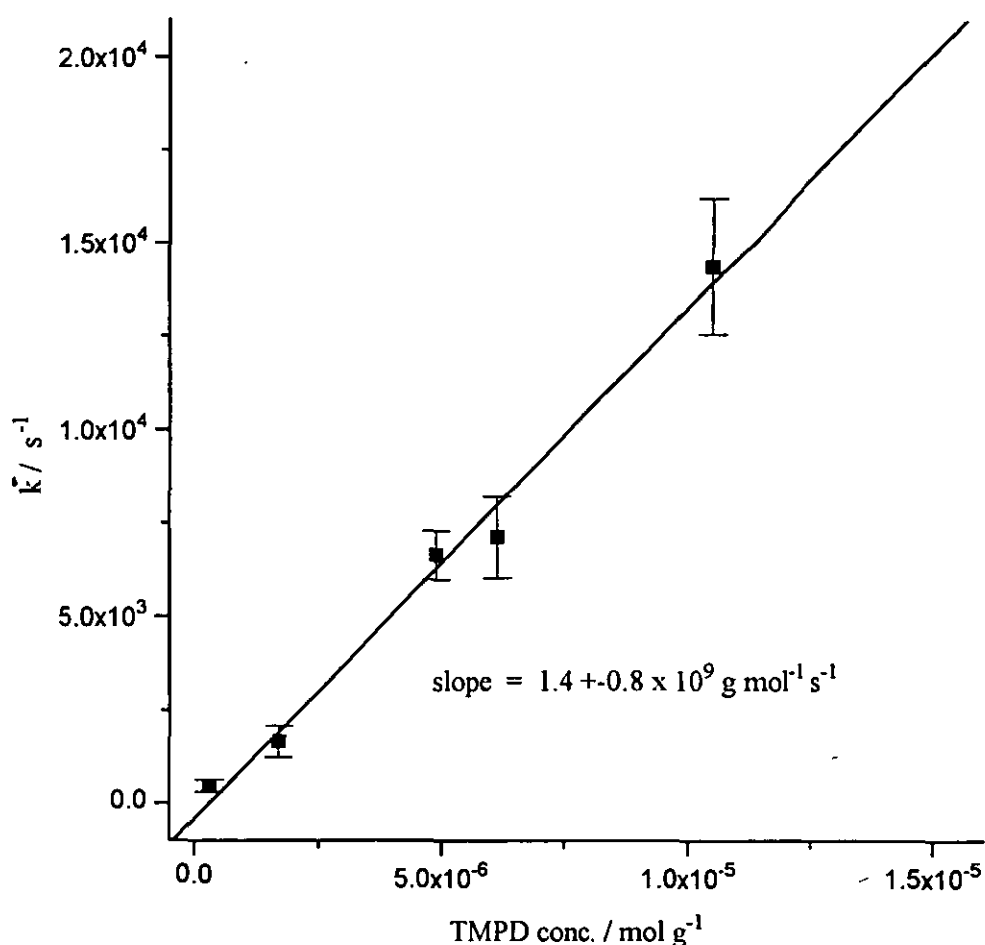


Figure 5.22 : The average rate constant (\bar{k}) obtained from the dispersive kinetic analysis for the rate of decay of the anthracene radical cation at 715 nm plotted versus TMPD concentration.

where \bar{k}_0 is the rate of decay of the anthracene radical cation without electron donor present and the intercept on the graph, and \bar{k}_{TMPD} is the gradient of the graph, then the gradient of this graph can be used as an estimate of the rate of electron transfer between TMPD and the anthracene radical cation and thus used for comparison of the rates of electron transfer of the other electron donor systems. \bar{k}_0 is zero (within experimental error) adding validity to the assumption that the decay is predominantly via electron transfer.

The increase in \bar{k} and similarity of the γ values can be shown by plotting reflectance change vs $\log_e(\text{time})$ as a function of electron donor concentration (Figure 5.23). The shape and width of the plots remain the same but shift along the x-axis with change in electron donor concentration.

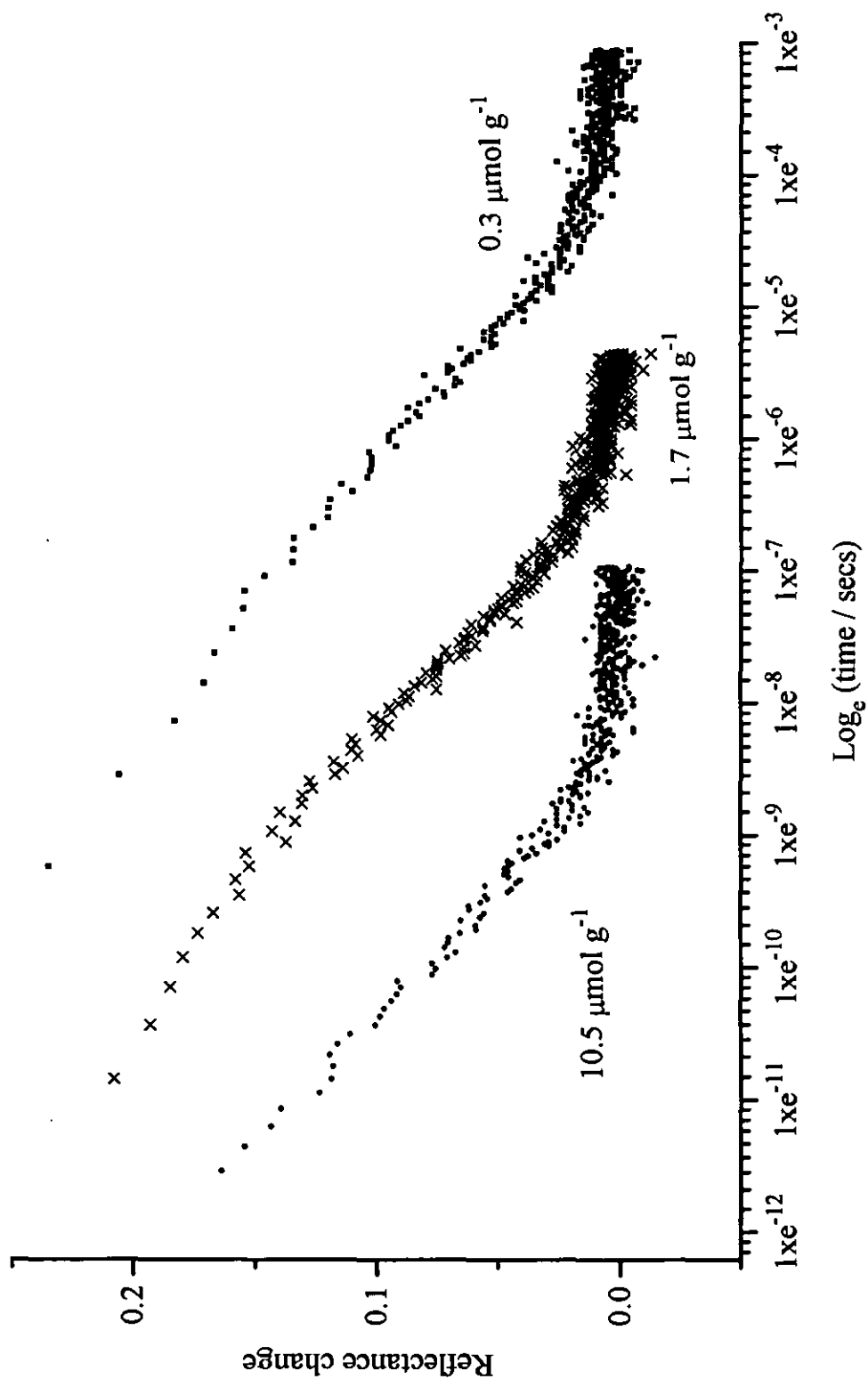


Figure 5.23 : Anthracene radical cation decay at 715 nm plotted as reflectance change versus \ln (time) as a function of TMPD concentration.

The fractal and two-dimensional models, as used to describe the delayed fluorescence data in section 5.1.3.1a and discussed in detail in section 4.2.1 can be modified and used to describe the anthracene radical cation decay. The derivations are described in section 4.2.2 so only a brief recap will be given here. The decay of the anthracene radical cation in the presence of an electron donor can be described by the following expression :-

$$-\frac{d[\text{An}^{\cdot+}]}{dt} = k_1[\text{An}^{\cdot+}][e^-] + k_2[\text{An}^{\cdot+}][\text{ED}] \quad (5.6)$$

If electron transfer dominates only the bimolecular rate constants of equation 5.6 are important, i.e. the k_2 term and the equation reduces to :-

$$-\frac{d[\text{An}^{\cdot+}]}{dt} = k_2[\text{An}^{\cdot+}][\text{ED}] \quad (5.7)$$

Integration and manipulation of equation (5.7) gives :-

$$\log_e \frac{\Delta R^0}{\Delta R} = k_2 t [\text{ED}] \quad (5.8)$$

This equation (equation 5.8) is used to describe the 2-dimensional model, when the reflectance change is low (< 10%). If this model holds a plot of $\log_e (\Delta R^0/\Delta R)$ vs t should yield a straight line with gradient of $k_2 [\text{ED}]$.

For the fractal analysis $k_1 = k_1^0 t^{-1/3}$ in the original equation (equation 5.6), so the decay of the anthracene radical cation in the presence of an electron donor is modified to give the following expression :-

$$-\frac{d[\text{An}^{\cdot+}]}{dt} = k_1 t^{-1/3} [\text{An}^{\cdot+}][e^-] + k_2 t^{-1/3} [\text{An}^{\cdot+}][\text{ED}] \quad (5.9)$$

If electron transfer dominates only the k_2 term is important in equation 5.9 and it reduces to :-

$$-\frac{d[\text{An}^{\cdot+}]}{dt} = k_2 t^{-1/3} [\text{An}^{\cdot+}][\text{ED}] \quad (5.10)$$

Integration and manipulation of equation 5.10 produces equation 5.11 which is used for describing the fractal nature of the radical cation decay in the presence of electron donors :-

$$\left(\log_e \frac{\Delta R^0}{\Delta R} \right)^{3/2} = \left(\frac{3}{2} k_2^0 [\text{ED}] \right)^{3/2} t \quad (5.11)$$

so a plot of $(\log_e [\Delta R]^0 / [\Delta R])^{3/2}$ vs t should yield a straight line at early times with gradient $(3/2 (k_2^0 [\text{ED}]))^{3/2}$

The analysis based on the fractal-dimensional model fits the initial decay well, the similar model based on the 2-dimensional rate constant does not provide such good fits as shown in Figure 5.24. The fractal-dimensional fits for the rate of decay of the anthracene radical cation are more linear than the 2-dimensional fits.

The data obtained using the fractal-dimensional analysis is shown in Table 5.3, as the slope of the initial part of the plot and its standard deviation.

TMPD conc. / $\mu\text{mol g}^{-1}$	slope	sd
0.3	363	4
1.7	3000	35
4.9	8440	233
6.2	8121	101
10.5	19760	756

Table 5.3:- Initial slope from the fractal dimensional analysis and its standard deviation for the rate electron transfer between TMPD and the anthracene radical cation, where

$$\text{Slope} = \left(\frac{3}{2} (k_2^0 [\text{ED}]) \right)^{3/2}$$

If the slope gained from the fractal-dimensional analysis is plotted to the power of $2/3$ vs TMPD concentration again a linear correlation between rate and donor concentration is obtained (Figure 5.25) with a gradient equal to $3/2k_2^0$. As with the dispersive kinetic model this gradient can be used as an estimate for the rate of electron transfer, for comparison with the gradients / rates obtained for the other electron donor systems.

A linear correlation between the TMPD concentration and the decay rates obtained from both the dispersive kinetic and fractal models is found, therefore either model can be used to gain an estimate of the rate of electron transfer.

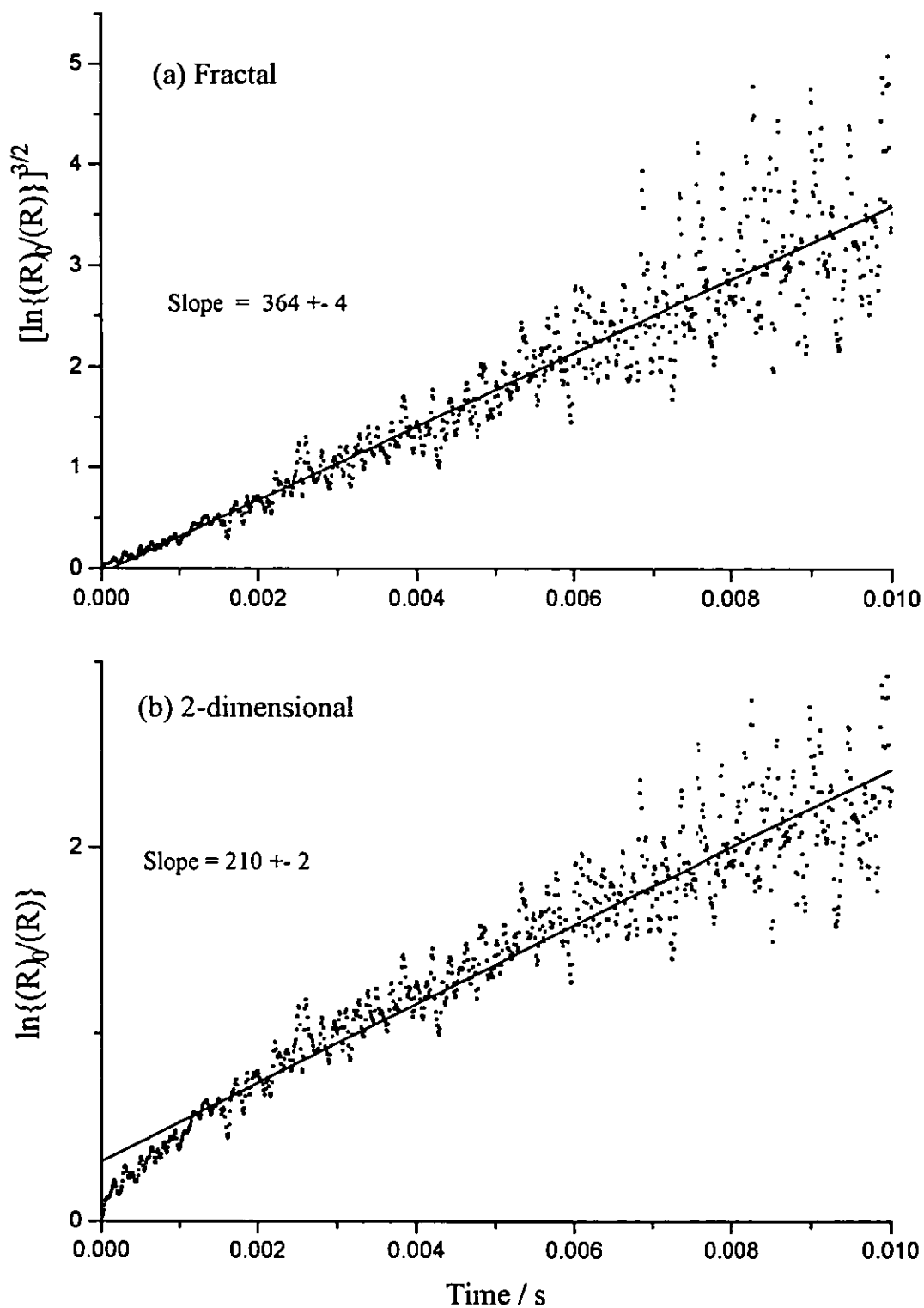


Figure 5.24 : Anthracene radical cation decay at 715 nm of a sample of anthracene ($1.1 \mu\text{mol g}^{-1}$) coadsorbed with TMPD ($0.3 \mu\text{mol g}^{-1}$) plotted according to (a) the fractal-dimensional model and (b) the two-dimensional model.

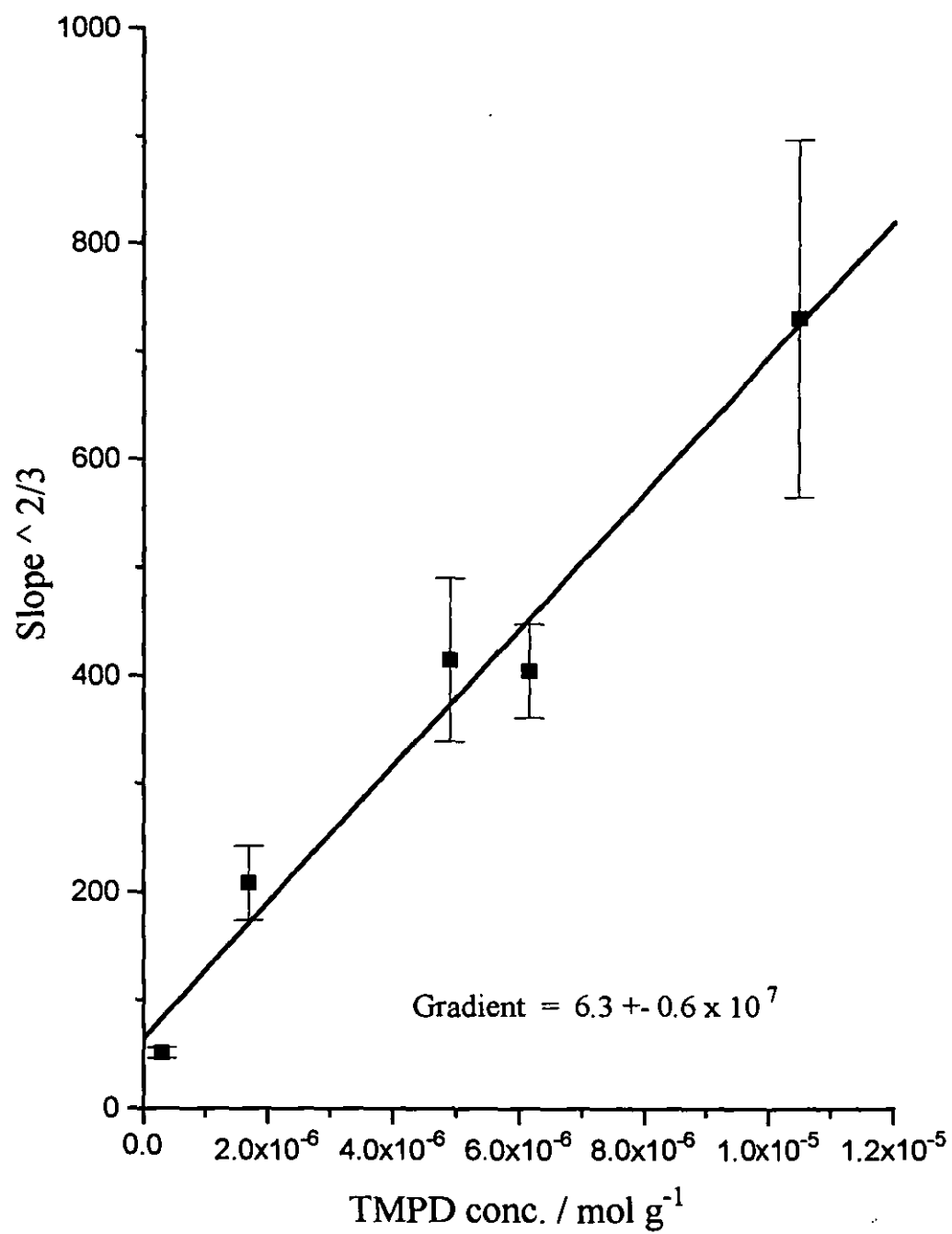


Figure 5.25 : A plot of the initial $(\text{slope})^{2/3}$ obtained from the fractal kinetic analysis of the anthracene radical cation decay at 715 nm plotted against TMPD concentration.

Dispersive kinetic model of Albery et al vs Fractal dimensional model.

These two models have both been used to describe the rate of decay of the anthracene radical cation in the presence of TMPD. The aim of using these kinetic models is to find a simple way to compare the rate of decay of the anthracene radical cation when using a variety of electron donors, not to calculate an exact rate of electron transfer. A model to characterise and compare the decay rates of different electron donors is required. The advantages of using the dispersive kinetic model over the fractal model are discussed below :-

1. The dispersive model of Albery et al is a continuous model, i.e. it is valid for the whole of the decay and not just a part of it.
2. The fractal model can only be used to describe the initial part of the decay, at later times the kinetics become more two-dimensional. This is because anthracene radical cations that are in the pores undergo electron transfer early on due to close proximity forced upon them and the electron donor by the small pores. Consequently the dispersive kinetic model will be used to compare the different rates of decay for the different electron donor systems.

5.2.2. Azulene and Anthracene.

Azulene and anthracene coadsorbed from hexane onto silica were studied as a function of azulene concentration in the range $0.76 \mu\text{mol g}^{-1}$ to $11 \mu\text{mol g}^{-1}$, with a loading of approximately $2 \mu\text{mol g}^{-1}$ of anthracene. As in the case of TMPD there is no excited singlet state quenching, but the excited triplet state anthracene is quenched by triplet-triplet energy transfer to the azulene, thus forming the azulene excited triplet state. The transient emission spectra recorded as a function of azulene concentration show evidence of exciplex formation between the excited singlet state of anthracene and azulene ground state. The excimer emission peak, observed with anthracene alone, decreases in intensity on coadsorption of azulene (Figure 5.26). The reduction in intensity of the excimer emission peak is accompanied by the appearance of another peak shifted to the blue of the excimer emission peak, shown in Figure 5.27 by normalising the transient emission spectra to the 530 nm peak. Quenching of the anthracene excited singlet state is not observed in the fluorescence spectra monitored as a function of azulene concentration. Small changes in fluorescence intensity would be very difficult to quantify due to the massive fluorescence background; whereas transient emission spectra are gated after the prompt fluorescence and therefore measured against an almost "zero" background.

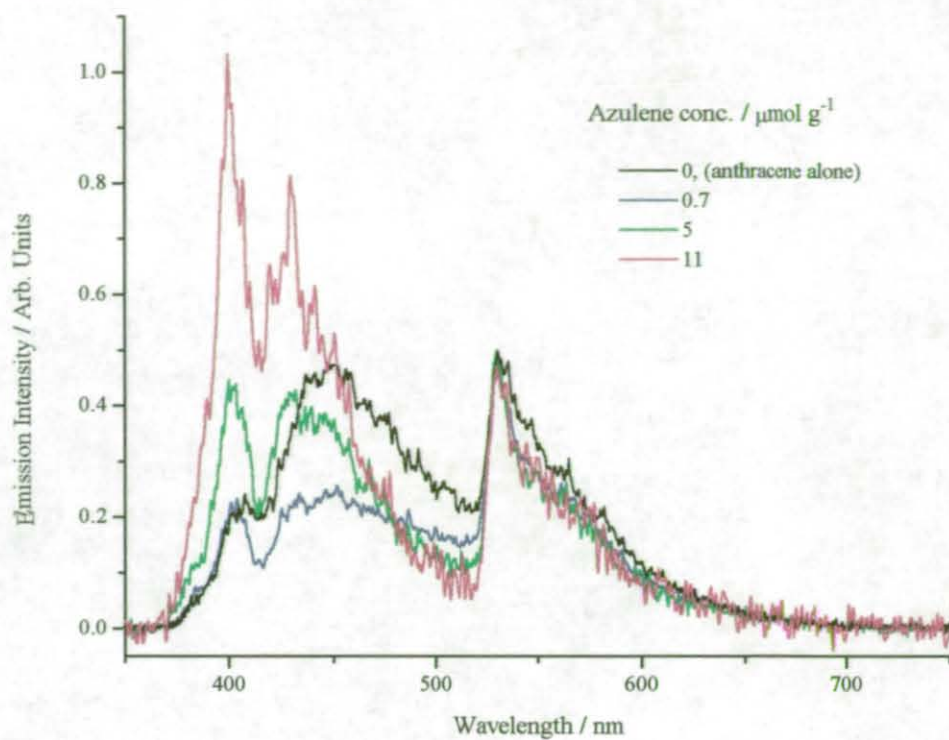


Figure 5.27 : Normalised transient emission spectra of anthracene coadsorbed with azulene.

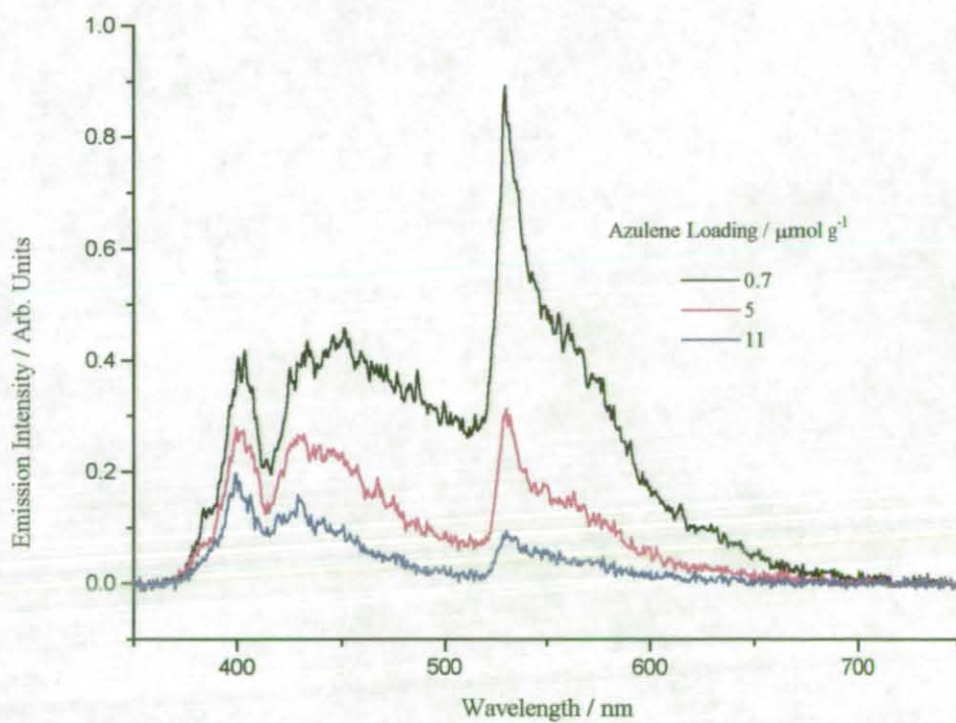


Figure 5.26 : Transient emission spectra of anthracene coadsorbed with azulene recorded 85 ns after laser excitation at 355 nm as a function of azulene loading.

5.2.2.1. Transient Absorption Spectra.

The anthracene excited triplet state and radical cation are observed following laser excitation, both of which have an increased rate of decay when azulene is present (Figure 5.28). Triplet-triplet energy transfer between anthracene (178 kJ mol^{-1}) and azulene (163 kJ mol^{-1})¹⁴¹ is responsible for the increased rate of decay of the anthracene triplet. The azulene triplet at 360 nm ¹⁴¹ is not detected due to its low molar absorption coefficient ($4000 \text{ L mol}^{-1} \text{ cm}^{-1}$), due to the anthracene ground state absorption complicating that region and also possibly to overlap with the anthracene triplet peak. The decay of the anthracene triplet at 420 nm has not been fitted with a kinetic model due to the mixed nature of its decay; with contributions from first order components, delayed fluorescence, triplet-triplet energy transfer and the superimposed radical cation decay.

The formation of the azulene radical cation following electron transfer to the anthracene cation is not observed. The azulene radical cation absorption peaks are expected to be found¹³² at 368 nm , which would be obscured by the anthracene ground state absorption, and at 480 nm and 830 nm . The latter two bands are very weak and also the 830 nm peak is outside our monitoring range.

5.2.2.2. Electron Transfer Kinetics.

As in the case of TMPD, the rate of decay of the anthracene radical cation at 715 nm in the presence of azulene is predominantly via electron transfer from the azulene. A typical decay trace (fitted using the dispersive kinetic model) of the anthracene radical cation at 715 nm is shown in Figures 5.29a and 5.29b as both reflectance change vs time and \log_e time.

Azulene conc. / $\mu\text{mol g}^{-1}$	\bar{k} / s^{-1}	sd	γ
0.76	4482	20	0.96
1.29	19270	3180	1.10
1.56	14830	250	0.84
2.98	33780	3500	1.45
5.30	66240	2700	0.57

Table 5.4:- Mean rate constant (\bar{k}), standard deviation (sd) and distribution width (γ) for the electron transfer between azulene and the anthracene radical cation.

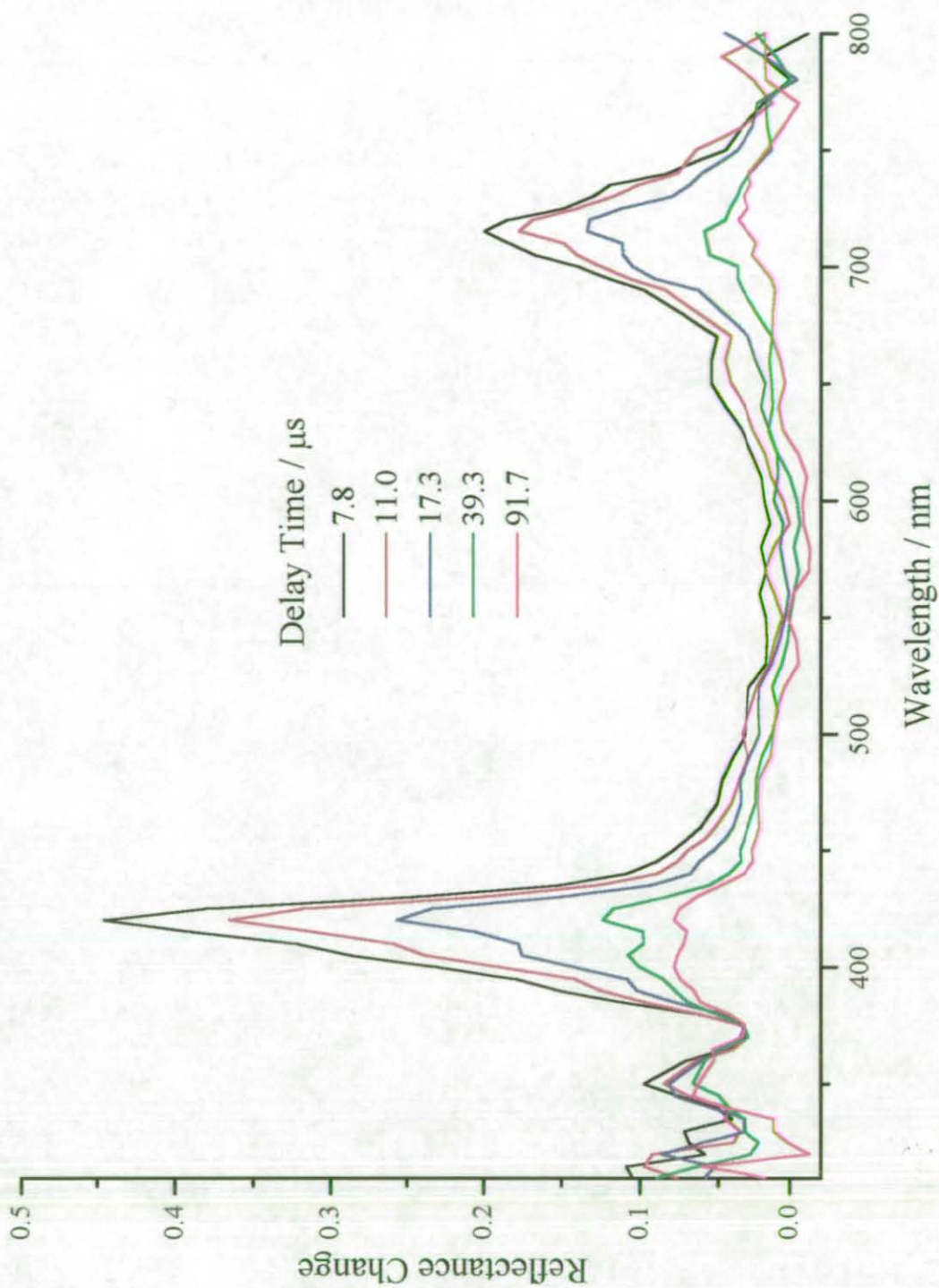


Figure 5.28 : Time-resolved transient difference absorption spectrum of anthracene coadsorbed with azulene on silica gel at loadings of 2.1 and 1.6 $\mu\text{mol g}^{-1}$ respectively following laser excitation at 355 nm.

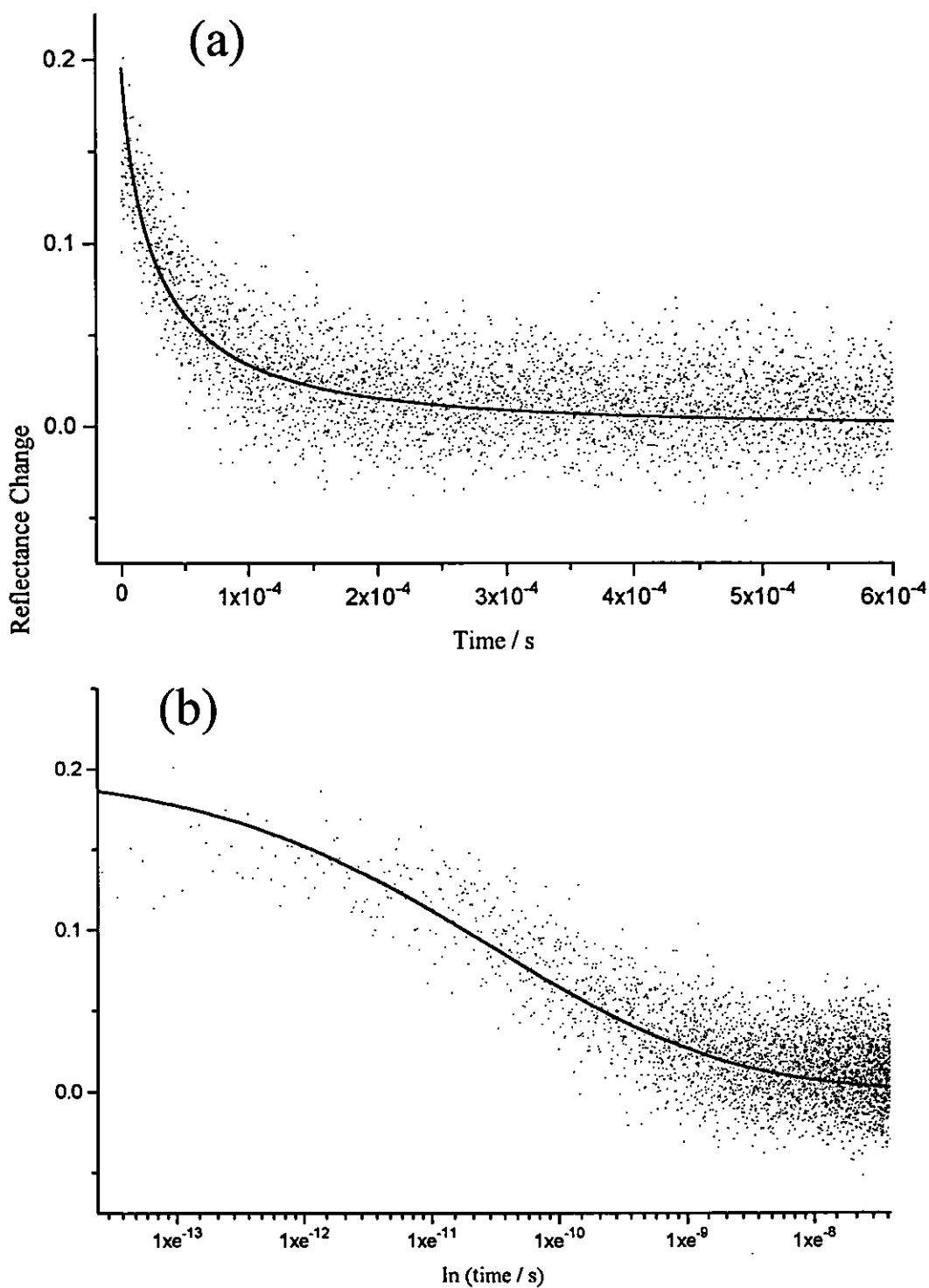


Figure 5.29 : Anthracene radical cation decay measured at 715 nm following laser excitation at 355 nm in the presence of azulene ($0.76 \mu\text{mol g}^{-1}$) plotted as reflectance change versus (a) time and (b) $\ln(\text{time})$ with the dispersive kinetic model fits shown by a solid line.

Table 5.4 shows the results (\bar{k} , its standard deviation (sd) and γ) of the dispersive kinetic model fits, obtained for constant anthracene concentration (approximately $2 \mu\text{mol g}^{-1}$) with varying azulene concentrations. γ again appears to be virtually independent of the electron donor concentration and similar but somewhat smaller than those found for TMPD and \bar{k} increases linearly with increasing concentration.

A linear correlation between the decay rates obtained from the dispersive kinetic model and azulene concentration is found and shown in Figure 5.30. The gradient of this graph, k_{AZ} is $1 \times 10^{10} \text{ g mol}^{-1} \text{ s}^{-1}$.

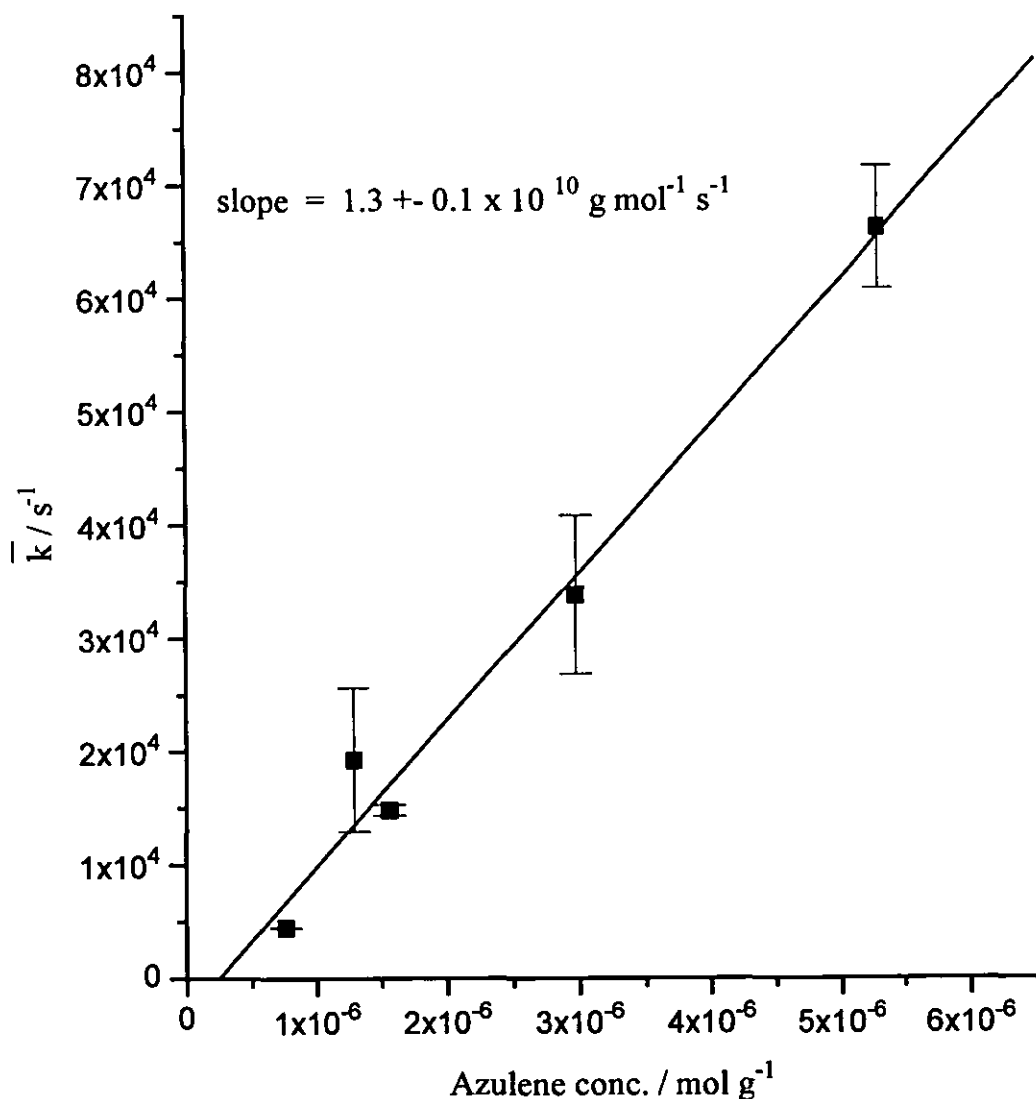


Figure 5.30 : The average rate constant (\bar{k}) obtained from the dispersive kinetic analysis for the rate of decay of the anthracene radical cation at 715 nm plotted versus azulene concentration.

5.2.3. Triphenylamine (TPA) and Anthracene.

Triphenylamine and anthracene were coadsorbed from both hexane and acetonitrile onto silica gel and studied as a function of TPA concentration. This system proved a little more complicated than the TMPD and azulene systems, discussed above. TPA quenches the anthracene singlet state as illustrated in Figure 5.31 where the fluorescence spectra are plotted as a function of TPA concentration. The fluorescence spectra were recorded exciting at 375 nm in order to excite the anthracene, but to avoid excitation of the TPA ground state. The transient emission spectra, recorded using a 100 ns gate width and 85 ns delay following laser excitation at 355 nm, reveal that the quenching of the anthracene singlet is accompanied by a red shift in the anthracene excimer emission peak illustrated in Figure 5.32. The intensity of this peak increases with increasing TPA concentration, as shown in Figure 5.33, and is thus assigned as emission from an exciplex formed between anthracene and TPA. Exciplex emission arising from the quenching of the excited singlet of aromatics by amines is often observed in solution¹⁴² and on the silica surface⁶⁴.

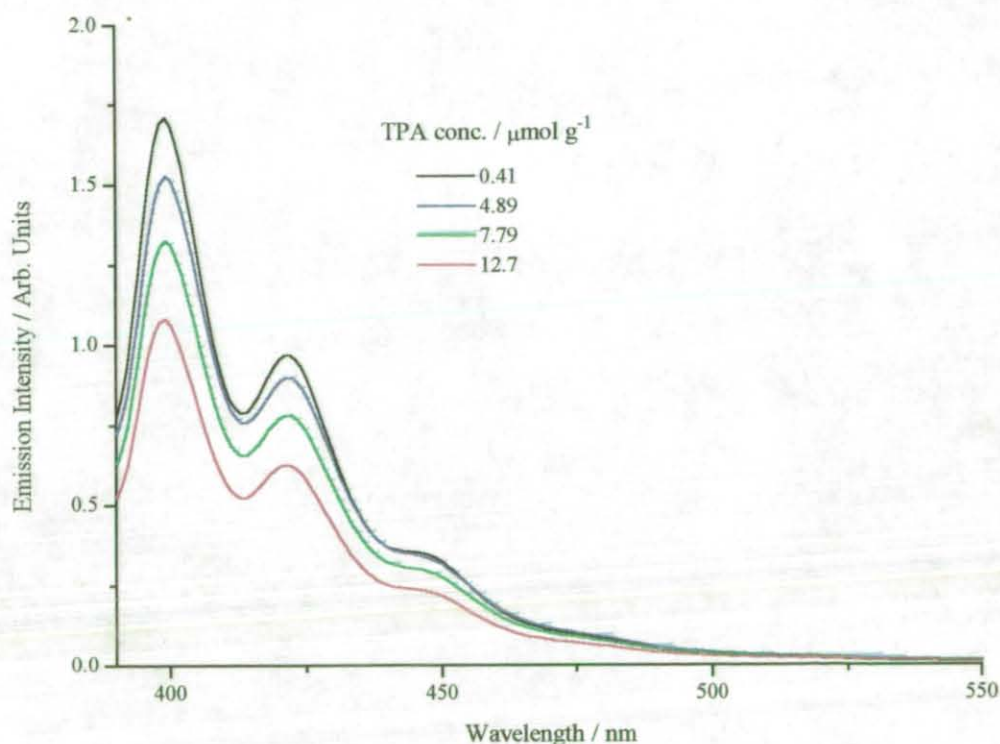


Figure 5.31 : Fluorescence emission spectra of anthracene coadsorbed with TPA on silica gel following excitation at 375 nm as a function of TPA concentration.

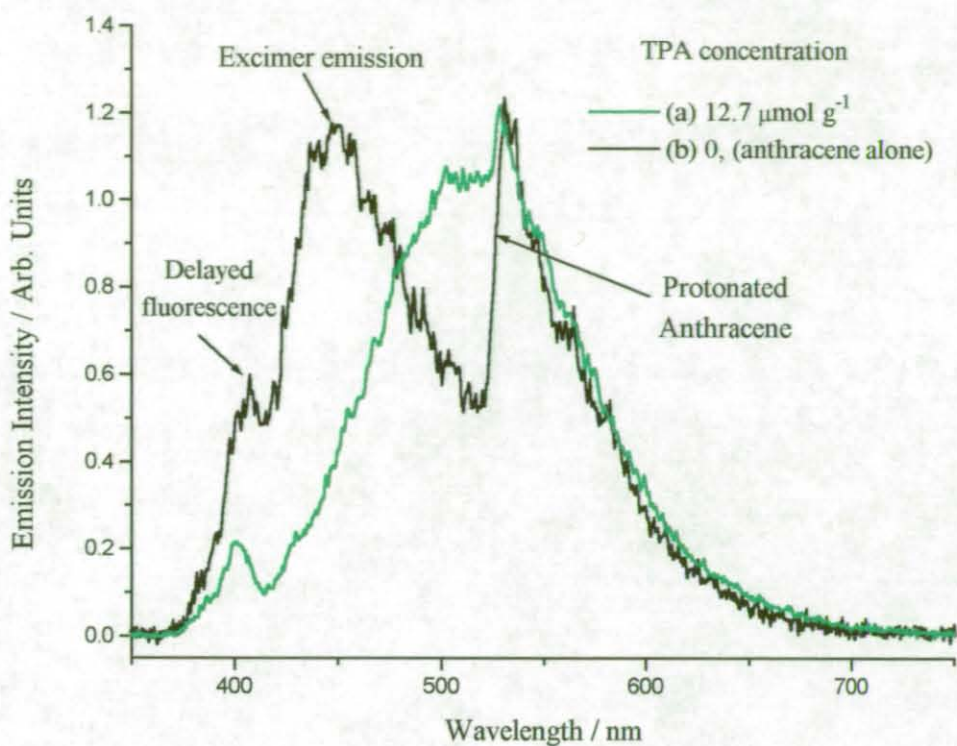


Figure 5.32 : Normalised transient emission spectra of (a) anthracene and (b) anthracene coadsorbed with TPA. The labels relate to the transient emission spectra.

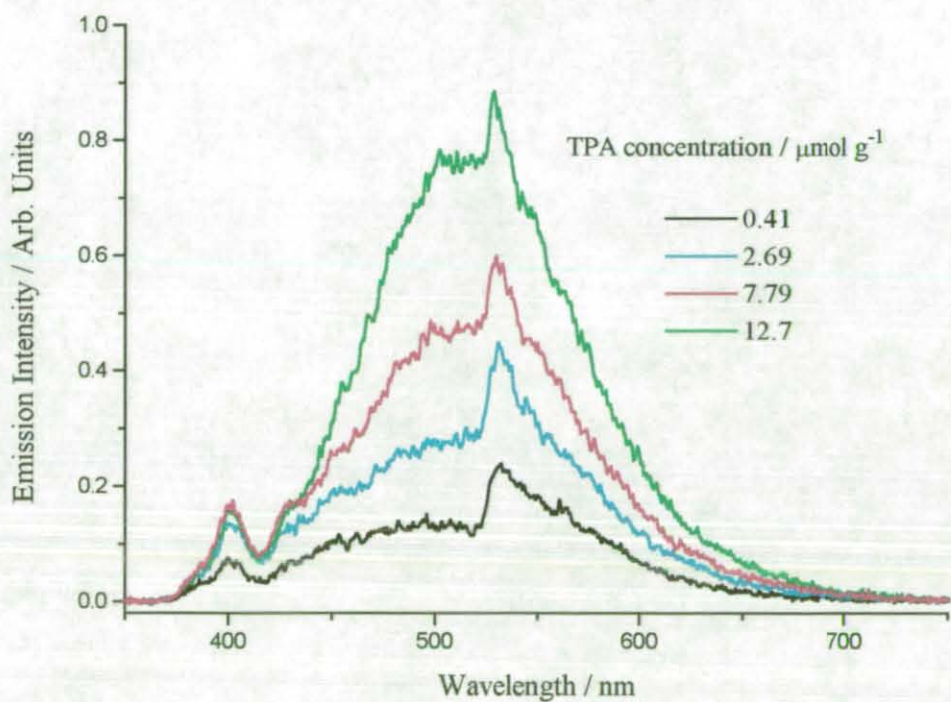


Figure 5.33 : Transient emission spectra of anthracene coadsorbed with TPA recorded 85 ns after laser excitation at 355 nm as a function of TPA loading.

5.2.3.1. Transient Absorption Spectra.

The anthracene triplet and radical cation are observed following laser excitation, and at low TPA concentrations ($2.2 \mu\text{mol g}^{-1}$) the decay of the radical cation is accompanied by a rise in the TPA radical cation peak at 650 nm, shown in Figure 5.34a. At higher TPA concentrations ($12.7 \mu\text{mol g}^{-1}$) the TPA radical cation appears to be produced by a different mechanism. The TPA radical cation peak rises within the laser pulse and does not follow the decay of the anthracene radical cation (Figure 5.34b). A sample of TPA with no anthracene coadsorbed on silica gel reveals a very small amount of TPA radical cation on laser excitation. The TPA radical cation is formed by electron transfer to the anthracene radical cation and rapid dissociation of the anthracene / TPA exciplex. The very rapid formation of the TPA radical cation, seen at both high and low loadings of TPA, can be assigned as electron transfer within the exciplex formed from the anthracene excited singlet state and TPA (discussed later in section 5.3.1). The rise in the TPA radical cation peak is absent at higher TPA concentrations. This could be due to the TPA radical cation decaying at the same rate as it is being formed, or possibly a more complex mechanism where the TPA clusters solvate the electron which can then recombine with the anthracene radical cation.

5.2.3.2. Electron Transfer Kinetics.

The rate of decay of the anthracene radical cation at 715 nm in the presence of low loadings of TPA is assumed to be predominantly via electron transfer from the TPA. A typical decay trace of the anthracene radical cation at 715 nm is shown in Figures 5.35a and 5.35b, fitted using the dispersive kinetic model and plotted as both reflectance change vs time and \log_e time. Table 5.5 shows the results of the fits obtained for the dispersive kinetic model for a constant anthracene concentration of around $2 \mu\text{mol g}^{-1}$ with varying TPA concentrations adsorbed on silica gel from hexane. These experiments were also carried out following adsorption from acetonitrile (in place of hexane) onto the silica gel, the results of which are shown in Table 5.6. In addition to varying the TPA concentration some experiments were performed where the rate of decay of the anthracene radical cation was monitored at an approximately constant TPA concentration as a function of anthracene concentration, shown in Table 5.7.

TPA (hexane) conc./ $\mu\text{mol g}^{-1}$	\bar{k} / s^{-1}	sd	γ
0.41	114	6	1.61
1.1	1928	63	1.59
2.2	617	27	1.44
2.69	728	17	1.29
4.89	2201	81	1.21
5.46	2785	183	1.48
7.79	6578	507	1.21
12.7	11627	588	1.32

Table 5.5:- Mean rate constant (\bar{k}), standard deviation (sd) and distribution width (γ) for the electron transfer between TPA and the anthracene radical cation, following adsorption from hexane.

TPA (acn) conc. / $\mu\text{mol g}^{-1}$	\bar{k} / s^{-1}	sd	γ
0.34	82	2	1.81
0.42	60	2	1.58
0.43	100	5	1.51
0.52	269	50	2.14
1.86	774	36	1.26
3.04	3234	94	1.14
4.85	7376	136	1.23

Table 5.6:- Mean rate constant (\bar{k}), standard deviation (sd) and distribution width (γ) for the electron transfer between TPA and the anthracene radical cation, following adsorption from acetonitrile.

Anthracene (acn) conc. / $\mu\text{mol g}^{-1}$	\bar{k} / s^{-1}	sd	γ
0.6	100	5	1.51
2.3	60	2	1.58

Table 5.7:- Mean rate constant (\bar{k}), standard deviation (sd) and distribution width (γ) for the electron transfer between TPA and the anthracene radical cation, as a function of anthracene loading following adsorption from acetonitrile.

From Table 5.7 it can be seen that the anthracene concentration has little or no effect on the rate of decay of its radical cation over this concentration range.

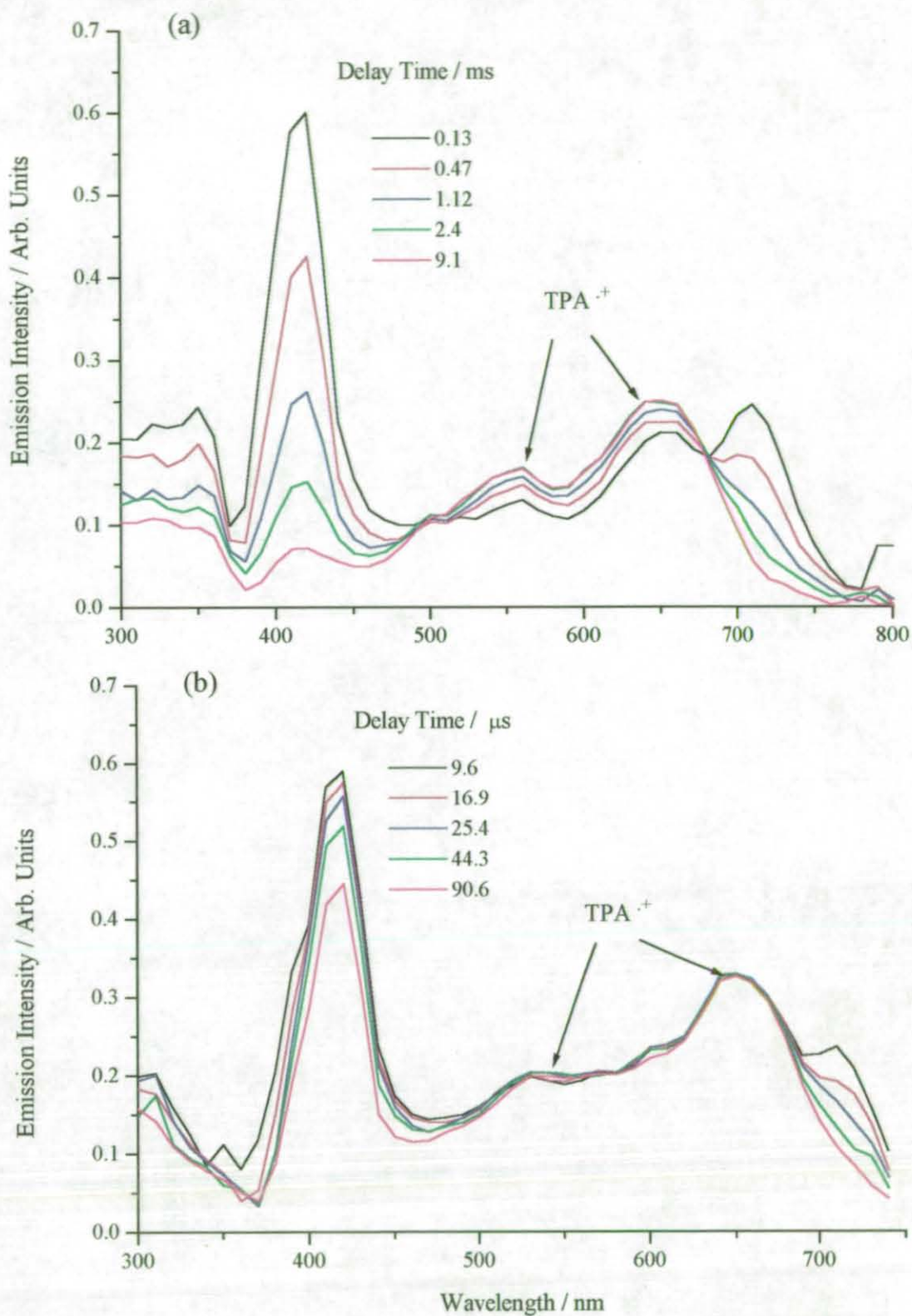


Figure 5.34 : Time-resolved transient difference absorption spectrum of anthracene ($2 \mu\text{mol g}^{-1}$) coadsorbed with TPA on silica gel at loadings of (a) $0.4 \mu\text{mol g}^{-1}$ and (b) $12.7 \mu\text{mol g}^{-1}$.

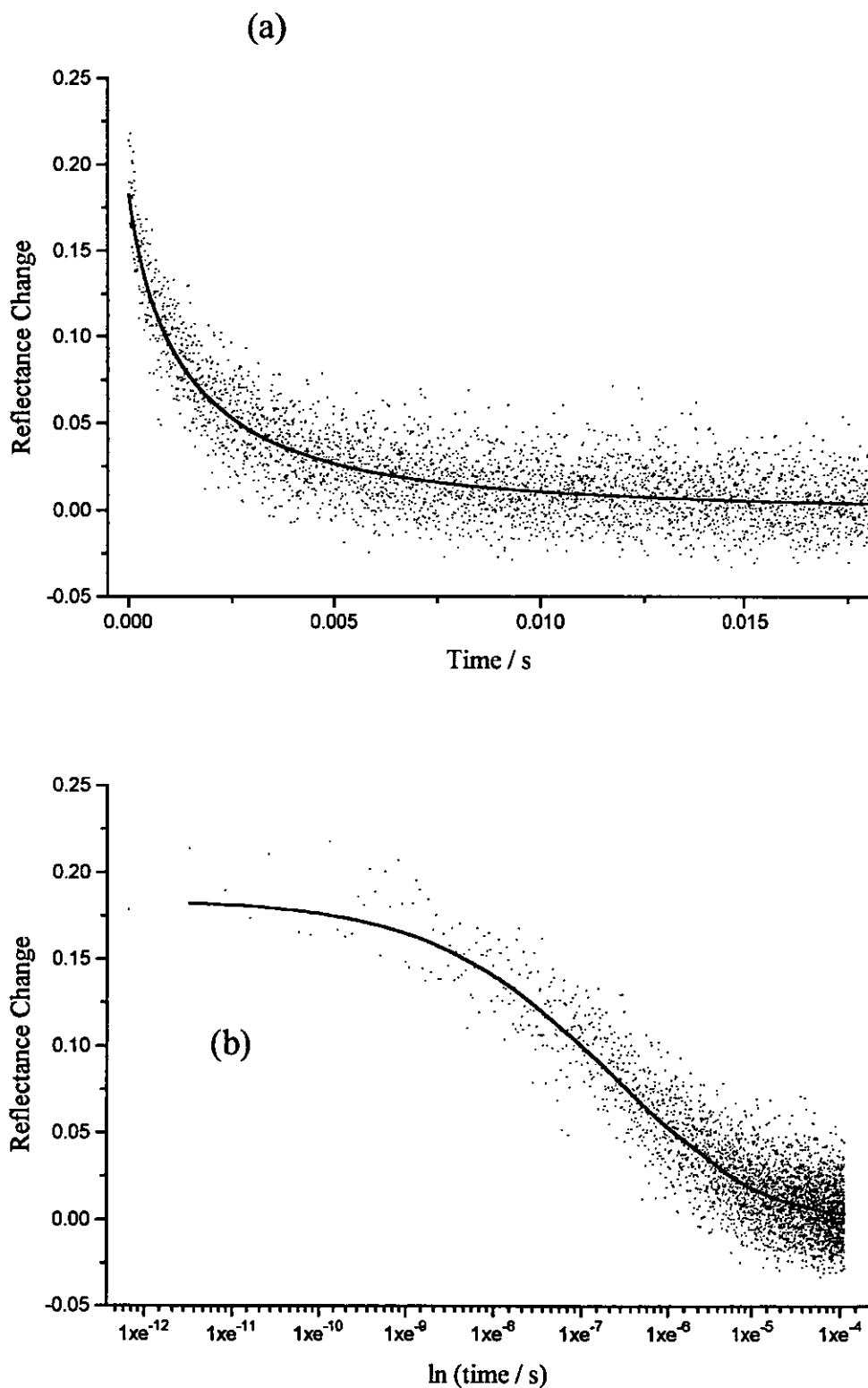


Figure 5.35 : Anthracene radical cation decay measured at 715 nm following laser excitation at 355 nm in the presence of TPA ($0.41 \mu\text{mol g}^{-1}$) plotted as reflectance change versus (a) time and (b) ln (time).

For both the hexane and the acetonitrile data, again γ appears to be independent of the electron donor concentration. \bar{k} initially increases linearly, but starts to curve upwards with increasing TPA concentration. Figures 5.36a and 5.36b show \bar{k} plotted as a function of TPA concentration adsorbed from a) hexane and b) acetonitrile. Here only the lower points are used to gain an estimate of the rate of electron transfer. The curvature on the plots of \bar{k} versus TPA concentration could be explained by one of two mechanisms. Firstly solvation of the electron by the TPA may occur thus preventing the electron from becoming trapped in the silica gel and facilitating the transfer back to the anthracene radical cation - this mechanism would explain why the rise on the TPA radical cation is not observed in transient absorption spectra at high TPA concentrations. The second and possibly more likely explanation is that the TPA is concentrated in clusters on the silica gel and the local concentration on the surface around the anthracene radical cation is much higher than the average surface concentration as shown in the plot. This clustering is evidenced by the formation of exciplexes between anthracene and TPA.

The estimates of the rates of electron transfer from TPA to the anthracene radical cation taken from the gradients of the graphs are $2.7 \pm 0.9 \times 10^8 \text{ g mol}^{-1} \text{ s}^{-1}$ and $4.6 \pm 0.8 \times 10^8 \text{ g mol}^{-1} \text{ s}^{-1}$ for the adsorption from hexane and acetonitrile respectively. The kinetics of electron transfer appear slightly faster when acetonitrile is used for adsorption onto the surface rather than hexane.

These experiments were carried out following adsorption from both hexane and acetonitrile since when acetonitrile is used as the solvent to adsorb the anthracene onto silica, the kinetics of triplet decay are faster, mainly due to increased triplet-triplet annihilation. Thus mobility on the surface is increased when acetonitrile is used as solvent, possibly due to the difficulty in removing the acetonitrile which may hydrogen bond to the silica surface. If hydrogen bonding of the acetonitrile to the silica surface occurs, it will block adsorption sites which would otherwise be occupied by anthracene. Thus the interactions between the adsorbed species and the surface would be reduced and their mobility increased.

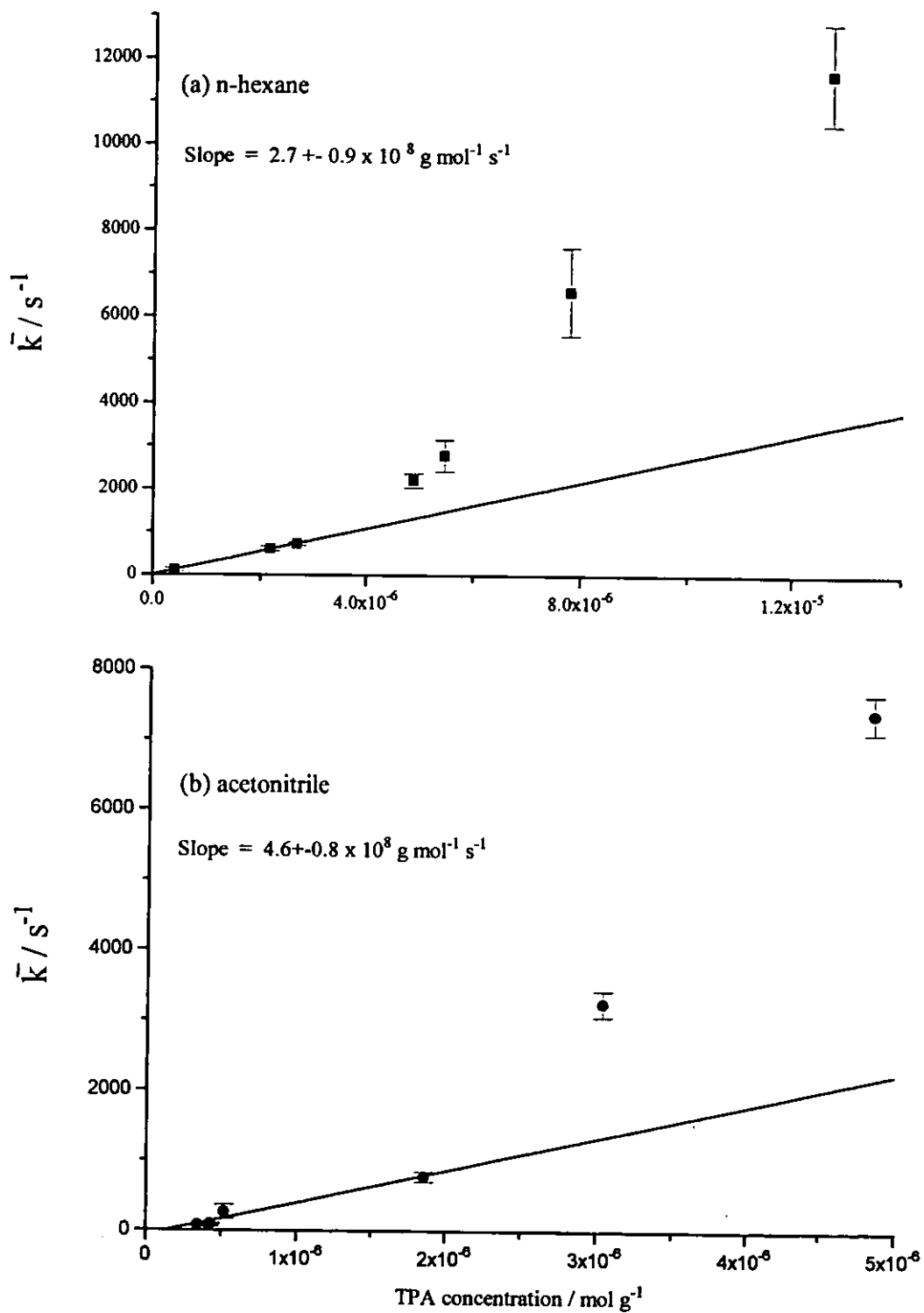


Figure 5.36 : The average rate constant (\bar{k}) obtained from the dispersive kinetic analysis for the rate of decay of the anthracene radical cation at 715 nm plotted versus TPA concentration following adsorption from (a) n-hexane and (b) acetonitrile onto silica gel.

5.2.4. N,N-Dimethylaniline (DMA) and Anthracene.

DMA and anthracene were coadsorbed from acetonitrile onto silica gel and studied as a function of DMA concentration, in the range $0.7 \mu\text{mol g}^{-1}$ to $19.3 \mu\text{mol g}^{-1}$ with an anthracene loading of approximately $2 \mu\text{mol g}^{-1}$. The transient emission spectra recorded as a function of DMA concentration show a decrease in the intensity of the anthracene excimer emission with increasing DMA concentration (Figure 5.37). This can be explained by the formation of an exciplex between the excited singlet state of anthracene and the ground state of DMA, thus inhibiting the formation of the anthracene excimer. Quenching of the anthracene excited singlet state emission is not observed in the fluorescence spectra monitored as a function of DMA concentration. Small changes in fluorescence intensity would be very difficult to quantify due to the massive fluorescence background, whereas transient emission spectra are gated after the prompt fluorescence and therefore measured against an almost "zero" background.

5.2.4.1. Transient Absorption Spectra.

The anthracene excited triplet state and radical cation are observed following laser excitation, and at low DMA concentrations ($0.7 \mu\text{mol g}^{-1}$) the decay of the radical cation is accompanied by a concomitant rise in the DMA radical cation at 460 nm, shown in Figure 5.38a. At higher DMA concentrations ($1.8 \mu\text{mol g}^{-1}$) the DMA radical cation appears to be produced by a different mechanism. The DMA radical cation rises within the laser pulse (Figure 5.38b) and does not follow the decay of the anthracene radical cation (as seen earlier with the TPA / anthracene system). The DMA radical cation is formed by electron transfer to the anthracene radical cation and rapid dissociation of the anthracene / DMA exciplex. The very rapid formation of the DMA radical cation, seen at both high and low loadings of TPA, can be assigned as electron transfer within the exciplex formed from the anthracene excited singlet state and DMA (discussed later in section 5.3.1). The rise in the DMA radical cation peak is absent at higher DMA concentrations. This could be due to the DMA radical cation decaying at the same rate as it is being formed, or possibly a more complex mechanism where the DMA clusters solvate the electron which can then recombine with the anthracene radical cation.

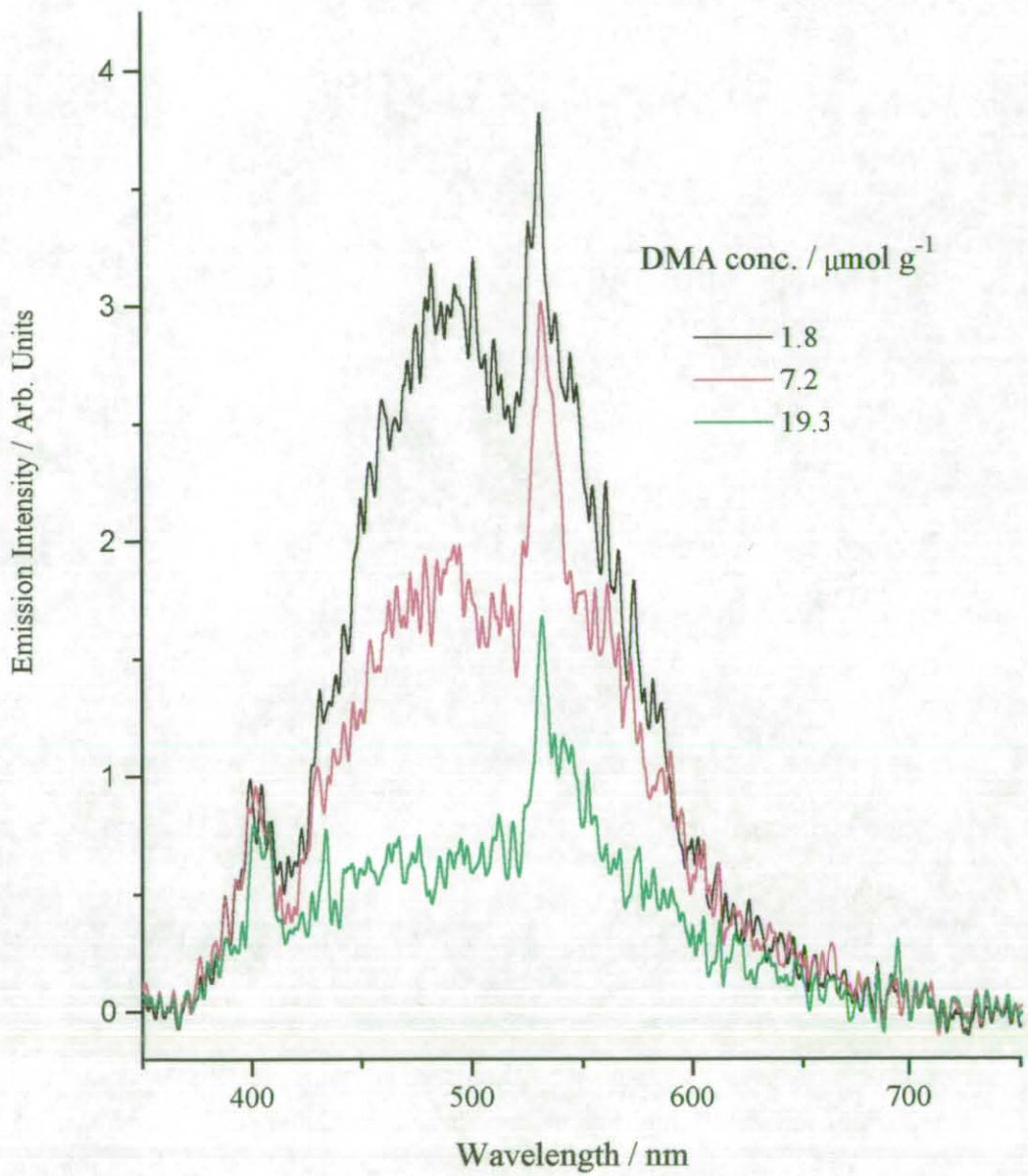


Figure 5.37 : Transient emission spectra of anthracene coadsorbed with DMA 85 ns after laser excitation at 355 nm, as a function of DMA concentration.

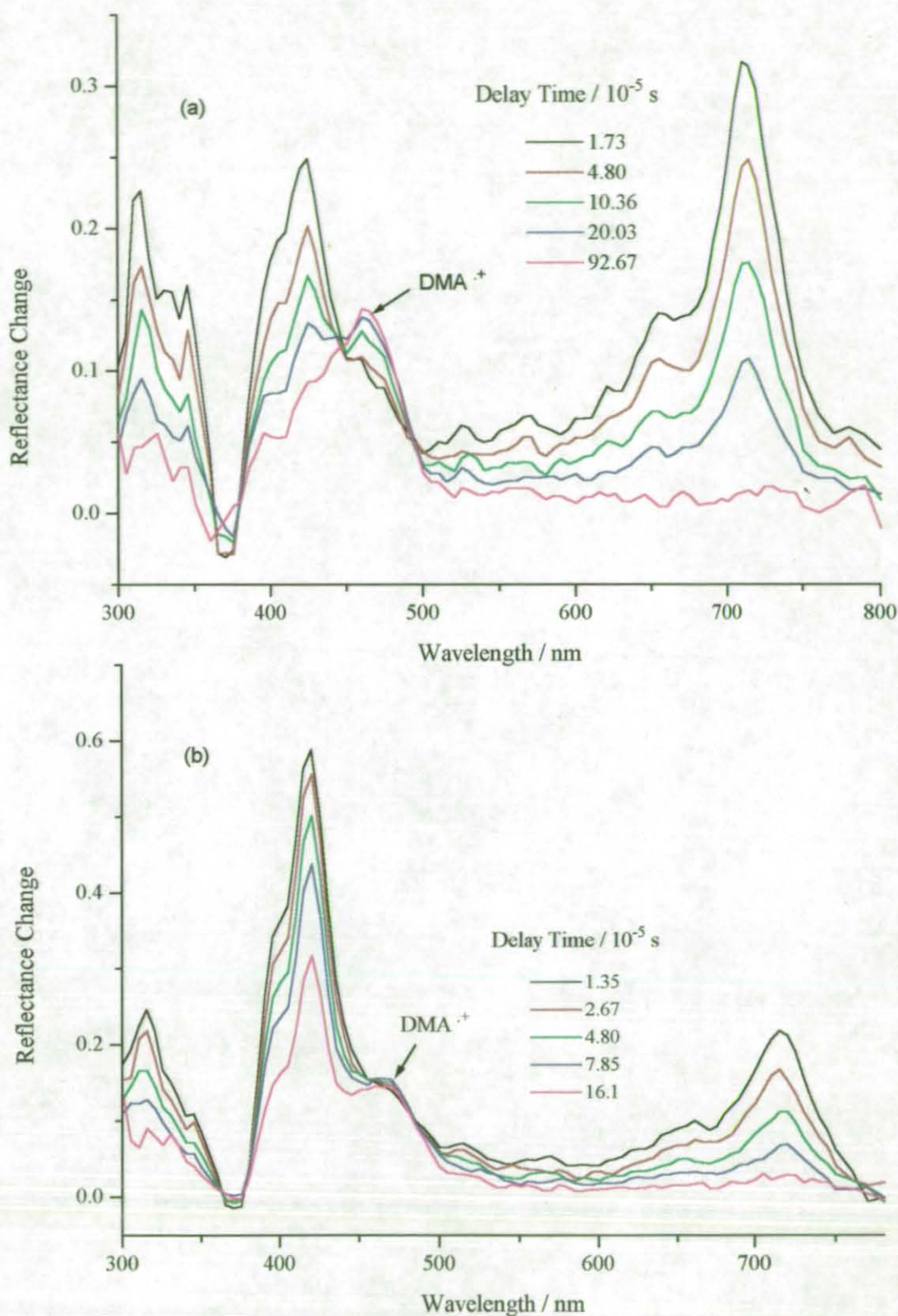


Figure 5.38 : Time-resolved transient difference absorption spectra of anthracene coadsorbed with DMA on silica gel following laser excitation at 355 nm, at DMA loadings of (a) $0.71 \mu\text{mol g}^{-1}$ and (b) $1.8 \mu\text{mol g}^{-1}$

5.2.4.2. Electron Transfer Kinetics.

The rate of decay of the anthracene radical cation at 715 nm in the presence of low loadings of DMA is assumed to be predominantly via electron transfer from the DMA. A typical decay trace of the anthracene radical cation at 715 nm is shown in Figures 5.39a and 5.39b fitted using the dispersive kinetic model as both reflectance change versus time and \log_e time. Table 5.8 shows the results of the fits obtained using for constant anthracene concentration (approximately 2 $\mu\text{mol g}^{-1}$) with varying DMA concentrations.

DMA conc. / $\mu\text{mol g}^{-1}$	\bar{k} / s^{-1}	sd	γ
0.71	7562	173	1.04
1.78	23347	2113	1.01
4.19	57397	612	0.88
7.22	156900	2722	1.10

Table 5.8:- Mean rate constant (\bar{k}), standard deviation (sd) and distribution width (γ) for the electron transfer between DMA and the anthracene radical cation.

Again γ appears to be independent of the electron donor concentration. \bar{k} initially increases linearly, but starts to curve upwards with increasing DMA concentration shown in Figure 5.40 where \bar{k} plotted as a function of DMA concentration. Here only the lower points are used to gain an estimate of the rate of electron transfer k_{DMA} , giving a value of $1.6 \times 10^{10} \text{ g mol}^{-1} \text{ s}^{-1}$. Here only the lower points are used to gain an estimate of the rate of electron transfer. The curvature on the plots of \bar{k} versus DMA concentration could be explained by either of the two mechanisms discussed previously for TPA. Firstly solvation of the electron by the DMA may occur by preventing the electron from becoming trapped in the silica gel thus facilitating the transfer back to the anthracene radical cation - this mechanism would explain why the rise on the DMA radical cation is not observed in transient absorption spectra at high DMA concentrations. The second and more likely explanation is that the DMA is concentrated in clusters on the silica gel and the local concentration on the surface around the anthracene radical cation is much higher than the average surface concentration calculated on the basis of surface loading. Clustering of anthracene on silica gel has been discussed earlier in sections 5.1.1 and 5.1.2, describing the aggregation of anthracene at concentrations well below a monolayer coverage.

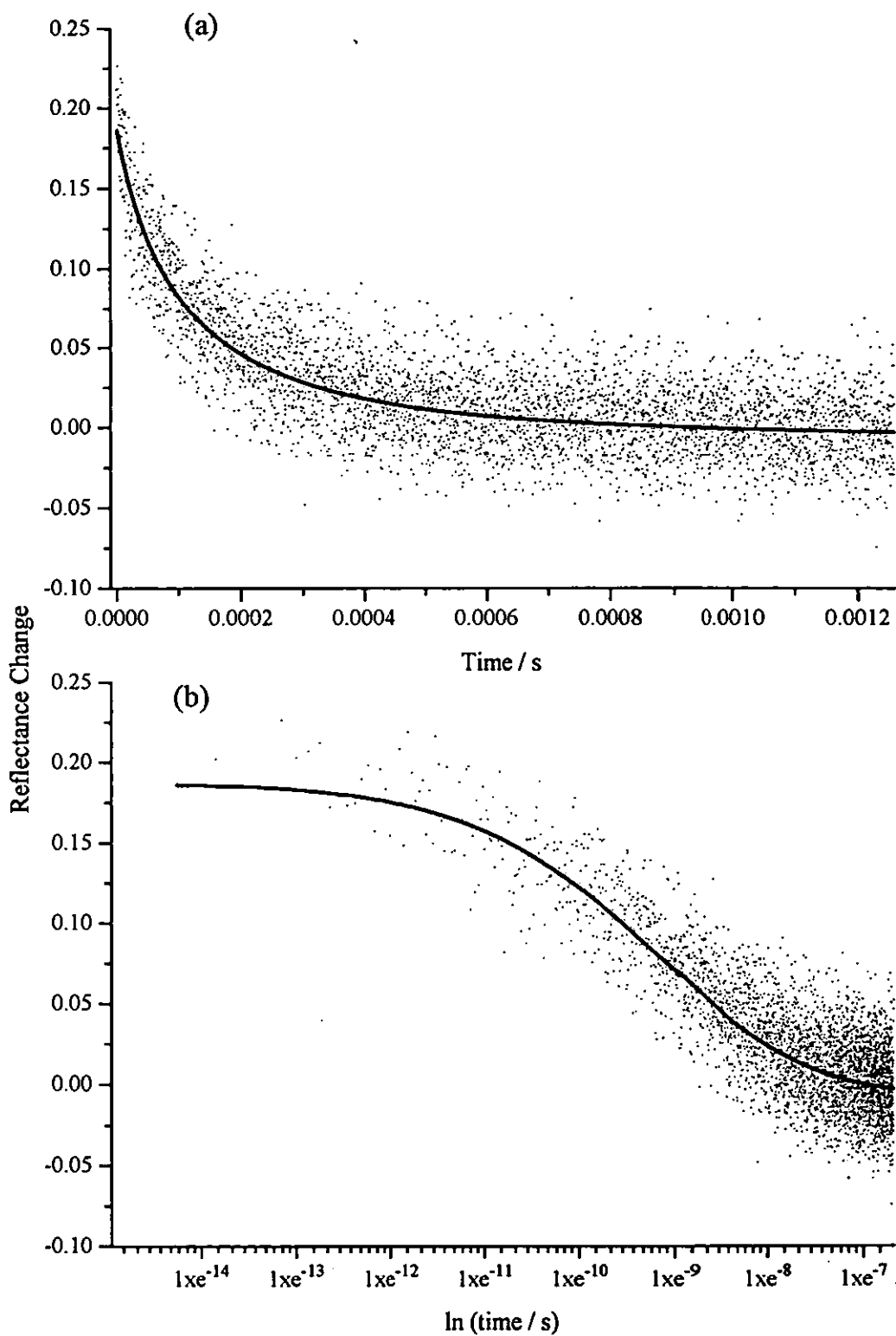


Figure 5.39 : Anthracene radical cation decay measured at 715 nm following laser excitation at 355 nm in the presence of DMA ($0.71 \mu\text{mol g}^{-1}$) plotted as reflectance change versus (a) time and (b) $\ln(\text{time})$

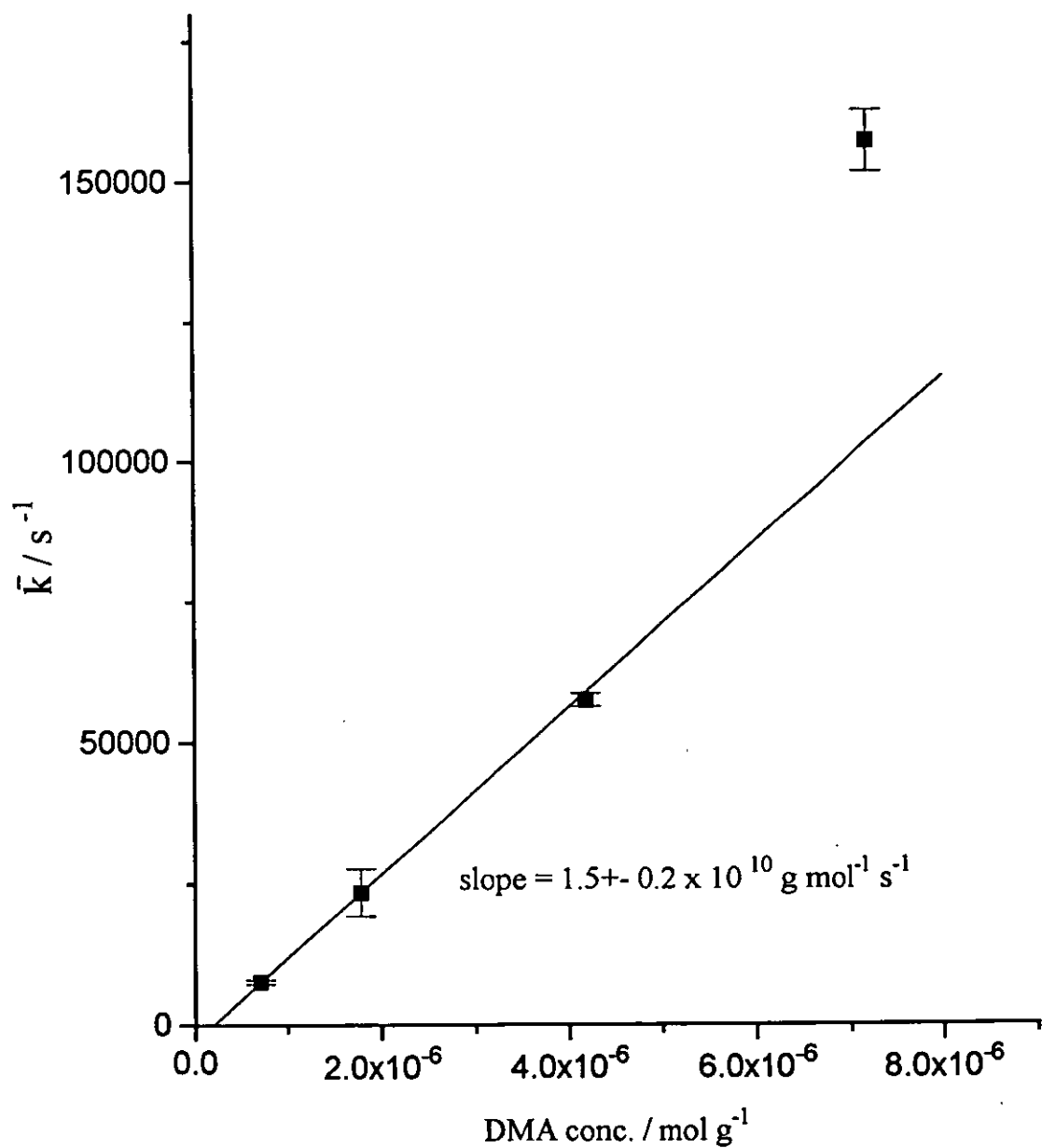


Figure 5.40 : The average rate constant \bar{k} obtained from the dispersive kinetic analysis for the rate of decay of the anthracene radical cation at 715 nm plotted versus DMA concentration.

5.2.5. Anthracene and azulene sublimed onto silica gel.

A limited number of experiments have been carried out adsorbing anthracene and azulene from the vapour phase onto silica gel. The sample preparation method is described in section 3.1 method C. These experiments have been performed in order to assess the extent to which residual solvent on the surface mediates the electron transfer process when adsorbing from solution phase. Co-adsorption of anthracene and azulene onto silica gel from the vapour phase results in electron transfer to the photoproducted anthracene radical cation from the azulene at surface loadings comparable with those used when adsorbing from solution phase. The anthracene radical cation decay at 715 nm has been fitted with the dispersive kinetic model and Table 5.9 shows the results of the fits obtained with varying azulene concentrations.

Azulene conc. / $\mu\text{mol g}^{-1}$	\bar{k} / s^{-1}	sd	γ
1.2	3924	90	0.93
3.0	38100	3400	1.39
5.1	330000	75000	1.13

Table 5.9 :- Mean rate constant (\bar{k}), standard deviation (sd) and distribution width (γ) for the electron transfer between azulene and the anthracene radical cation.

A plot of \bar{k} versus azulene concentration is shown in Figure 5.41, \bar{k} initially increases linearly but starts to curve upwards with increasing azulene concentration. The curvature of the plot at these concentrations, which if adsorbed from solution would still show a linear correlation between rate constant and concentration, suggests enhanced aggregation on adsorption from the gas phase. Here only the lower points are used to gain an estimate of the rate of electron transfer k_{AZ} , although the line of best fit has been made to intercept near zero due to the rate of anthracene radical cation decay being very slow in the absence of an electron donor. This gives a value of $1.3 \times 10^{10} \text{ g mol}^{-1} \text{ s}^{-1}$ for the electron transfer rate constant in the sublimed samples. This is identical, to within experimental error, to that observed when adsorbing from hexane solution, suggesting that any residual solvent left on the surface plays little role in determining the rate of electron transfer on the surface. The value of γ is also identical, within error, to those obtained when adsorbing from n-hexane, again suggesting that any residual solvent left on the surface has little effect on the surface properties.

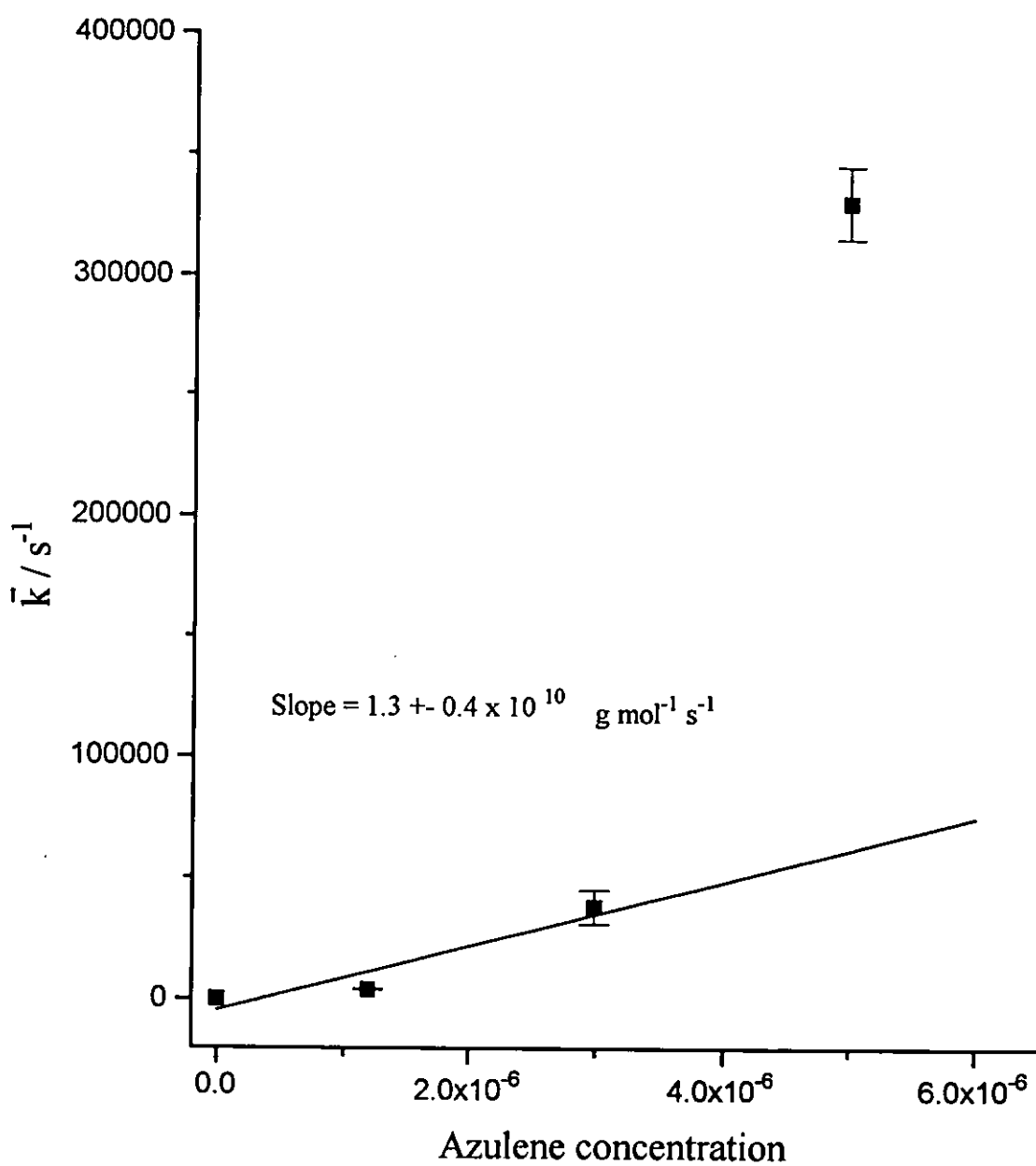


Figure 5.41 : The average rate constant \bar{k} obtained from the dispersive kinetic analysis for the rate of decay of the anthracene radical cation at 715 nm plotted versus azulene concentration sublimed onto silica gel.

5.3. Summary of the Electron Transfer Data.

A linear correlation between decay rates and electron donor concentration was observed for TMPD, azulene and for low loadings of TPA and DMA. The gradients of these graphs, k_{TMPD} , k_{AZ} , k_{TPA} and k_{DMA} are summarised in Table 5.10 as a function of the oxidation potential of the electron donor and the free energy of electron transfer.

Electron Donor	Oxidation Potential / V (vs SCE)	$\Delta G / \text{kJ mol}^{-1}$	Rate of electron transfer # / $\text{g mol}^{-1} \text{s}^{-1}$
TMPD (ACN)	0.32	-74.3	1.4×10^9
DMA (ACN)	0.53	-54.0	1.5×10^{10}
Azulene (HEX)	0.71	-36.7	1.3×10^{10}
Azulene (sublimed)			1.3×10^{10}
TPA (ACN)	0.92	-16.4	4.6×10^8
TPA (HEX)			2.7×10^8
Naphthalene (HEX)	1.54	43.4	no electron transfer

Table 5.10:- Electron donor oxidation potentials, free energy for electron transfer and the rate constants for electron transfer, between the electron donors and the anthracene radical cation. Where # is taken from the plot of \bar{k} vs electron donor concentration

The rate of electron transfer quenching is seen to increase as a function of electron donor concentration, but the absolute rate e.g. k_{TMPD} does not correlate with the electron donor oxidation potential.

The rate of electron transfer in solution is governed by two components; the rate of diffusion of the molecules to one another and then the rate of electron transfer in the encounter pair. The rate of diffusion in solution has been shown to be :-

$$k_{\text{DIFF}} = 4\pi N \rho_{\text{AB}} D 10^3 \quad (5.12)$$

where N is Avogadro's number, ρ_{AB} is the reaction radius between molecules A and B, and D is the relative diffusion constant.

The diffusion coefficients can be written as :-

$$D_A = \frac{RT}{6\pi\eta r_A N} \quad (5.13)$$

where R is the gas constant, T is the absolute temperature, η is the solvent viscosity and r_A is radius of molecule A.

Assuming that $\rho_{AB} = 2r_A = 2r_B$ and $D = 2D_A$ and substituting equation 5.13 into 5.12 gives :-

$$k_{diff} = \frac{8RT}{3\eta} 10^3 \quad (5.14)$$

Thus subject to the assumptions made above, the rate of diffusion of the molecules in solution is independent of their identities. The rate of electron transfer on surfaces again will be governed by the rate of diffusion and the rate of electron transfer in the encounter pair. On silica gel the rates of diffusion of different molecules cannot be assumed to be equal due to differing strengths of adsorption to the surface and if the rate limiting step is diffusion a range of different rates will be observed. Anthracene radical cation decay in the presence of an electron donor on silica gel is not likely to be exclusively governed by the value of ΔG for the electron transfer process. A log plot of k_{TPD} , k_{TPA} , k_{AZ} and k_{DMA} versus ΔG for electron transfer (expressed in eV) reveals what appears to be a Marcus type inverted region (Figure 5.42). However with so few samples at larger- ΔG values this trend cannot be confirmed. On the basis of the evidence presented above the rate limiting step is most likely to be diffusion of the electron donor molecules to the anthracene radical cation, with the rate of electron transfer within the encounter pair being relatively fast. Another related explanation could be that there are a distribution of sites of differing accessibility which inflict steric restrictions on the encounter pair, making the observed rates due to the ease with which the anthracene and electron donor can interact in a favourable orientation.

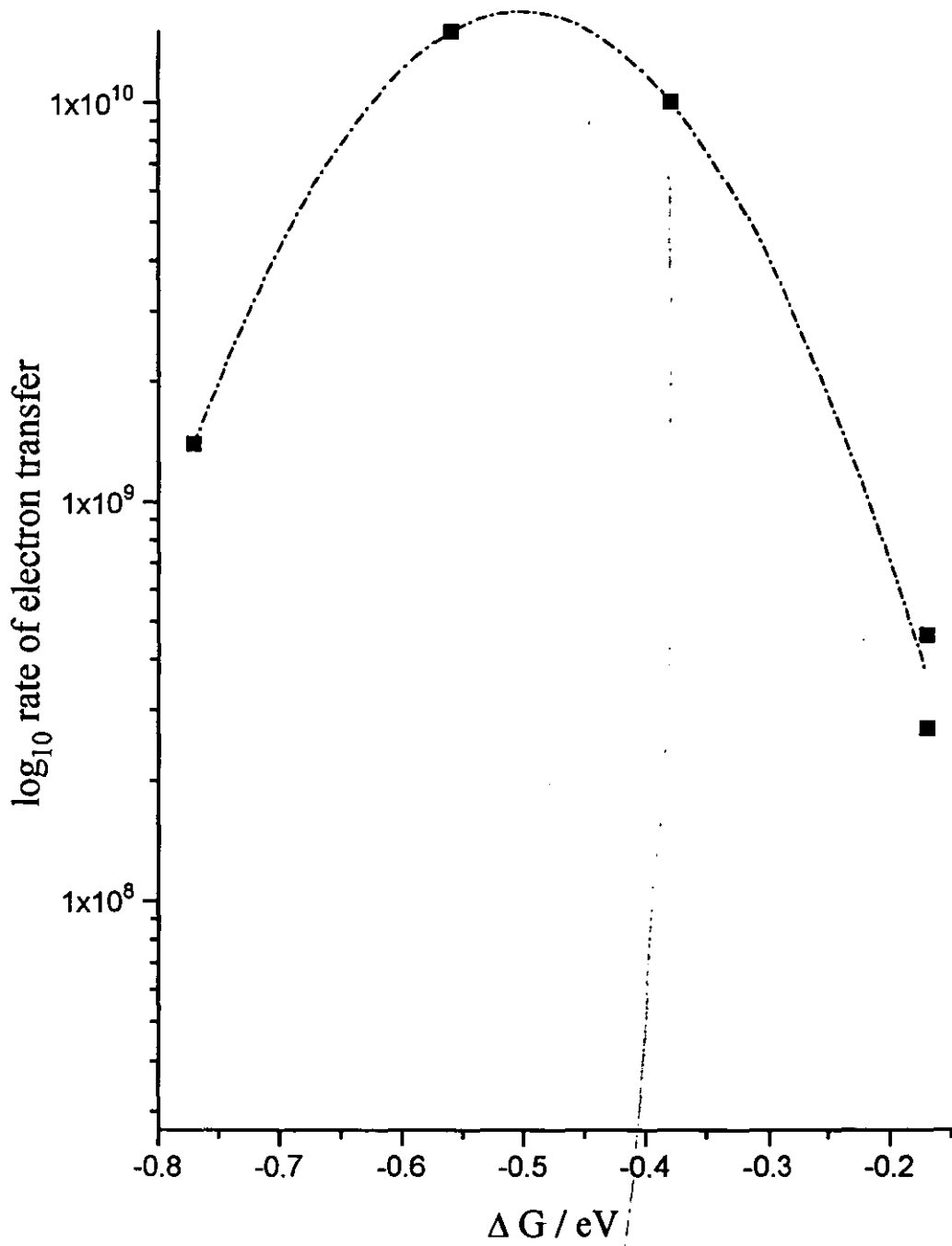
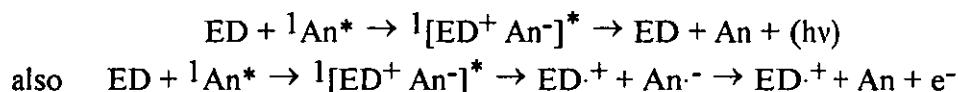


Figure 5.42 : \log_{10} of the rate of electron transfer from various electron donors to the anthracene radical cation plotted versus ΔG in eV, revealing a Marcus type inverted region.

5.3.1. Exciplex Emission Behaviour.

Transient emission spectra reveal the formation of exciplexes between the anthracene excited singlet state and the electron donors; TPA, DMA and azulene. Eremenko et al have reported exciplex formation (at 510 nm) between N,N-diethylaniline and the excited singlet of anthracene adsorbed on aerosil⁶⁴ (a non-porous silica gel). Quenching of the anthracene fluorescence was observed and exciplex formation was shown to be dynamic. Time-resolved studies of the anthracene / N,N-diethylaniline system revealed that as the anthracene singlet fluorescence intensity decreased the exciplex intensity increased. The concentration of N,N-diethylaniline used in these⁶⁴ experiments was a great deal higher than those used in the work discussed in this thesis. An anthracene surface coverage of 0.06% and 10-100% of N,N-diethylaniline were used as compared with the 0 to 5% coverage used in the work described in this thesis. In the case of TPA, the quenching of the anthracene excited singlet state by TPA is readily observed in the fluorescence spectra. The decay of the exciplex (denoted by square brackets []) could be via one of two pathways shown below :-



The anthracene electron donor exciplex may decay by exciplex emission to give the ground state molecules. Alternatively dissociation of the exciplex forming the electron donor radical cation and anthracene radical anion may occur. At high loadings DMA and TPA radical cations are formed rapidly in high yield and not via dynamic electron transfer with the anthracene radical cation. This suggests that a fairly large amount of the exciplex decays to give the amine radical cation and the anthracene anion radical, the absorption of which is obscured beneath the radical cation absorption¹³². This mechanism explains the rapid production of the amine radical cation at higher loadings.

5.3.2. 2,3-didecyloxyanthracene (2,3-DDA) and triphenylamine (TPA).

The effect of changing the nature of the electron accepting radical cation on the rate of electron transfer was also briefly studied. The transient difference spectrum of 2,3-DDA coadsorbed with TPA is shown in Figure 5.43 and its characteristics will be discussed in more detail in section 6.3. Only three different

concentrations of TPA were studied due to time restrictions. The decay of the substituted anthracene radical cation at 725 nm was fitted using the dispersive kinetic model. Table 5.11 shows the results (\bar{k} , its standard deviation (sd) and γ) of the dispersive kinetic model fits, obtained for an approximately constant 2,3-DDA concentration of $2.5 \mu\text{mol g}^{-1}$.

TPA conc. / $\mu\text{mol g}^{-1}$	\bar{k} / s^{-1}	sd	γ
1.44	231	19	3.0
3.11	523	86	2.9
5.65	1858	240	2.1

Table 5.11:- Mean rate constant (\bar{k}), standard deviation (sd) and distribution width (γ) for the electron transfer between TPA and the 2,3-didecyloxyanthracene radical cation.

\bar{k} increases with increasing TPA concentration and is shown in Figure 5.44 plotted along with the data obtained for unsubstituted anthracene for comparison. Clearly the rates obtained for the electron transfer from TPA to the 2,3-didecyloxyanthracene and the unsubstituted anthracene radical cation are comparable since both sets of data lie on the same straight line (Figure 5.44). This again suggests that the rate of electron transfer is not solely dependent on the difference in the acceptor and donor electrode potentials.

5.3.3. Electron Donors studied but not included in the above discussions.

Aniline and naphthalene were also employed as possible electron donors for electron transfer to the anthracene radical cation. The transient spectra of aniline and naphthalene coadsorbed with anthracene are shown in Figures 5.45a and 5.45b respectively. Clearly naphthalene (Figure 5.45b) did not undergo electron transfer to the radical cation, as one would expect from its oxidation potential. Aniline did electron transfer to the anthracene radical cation, but time restrictions did not allow a sufficient range of concentrations to be studied for a quenching constant to be obtained.

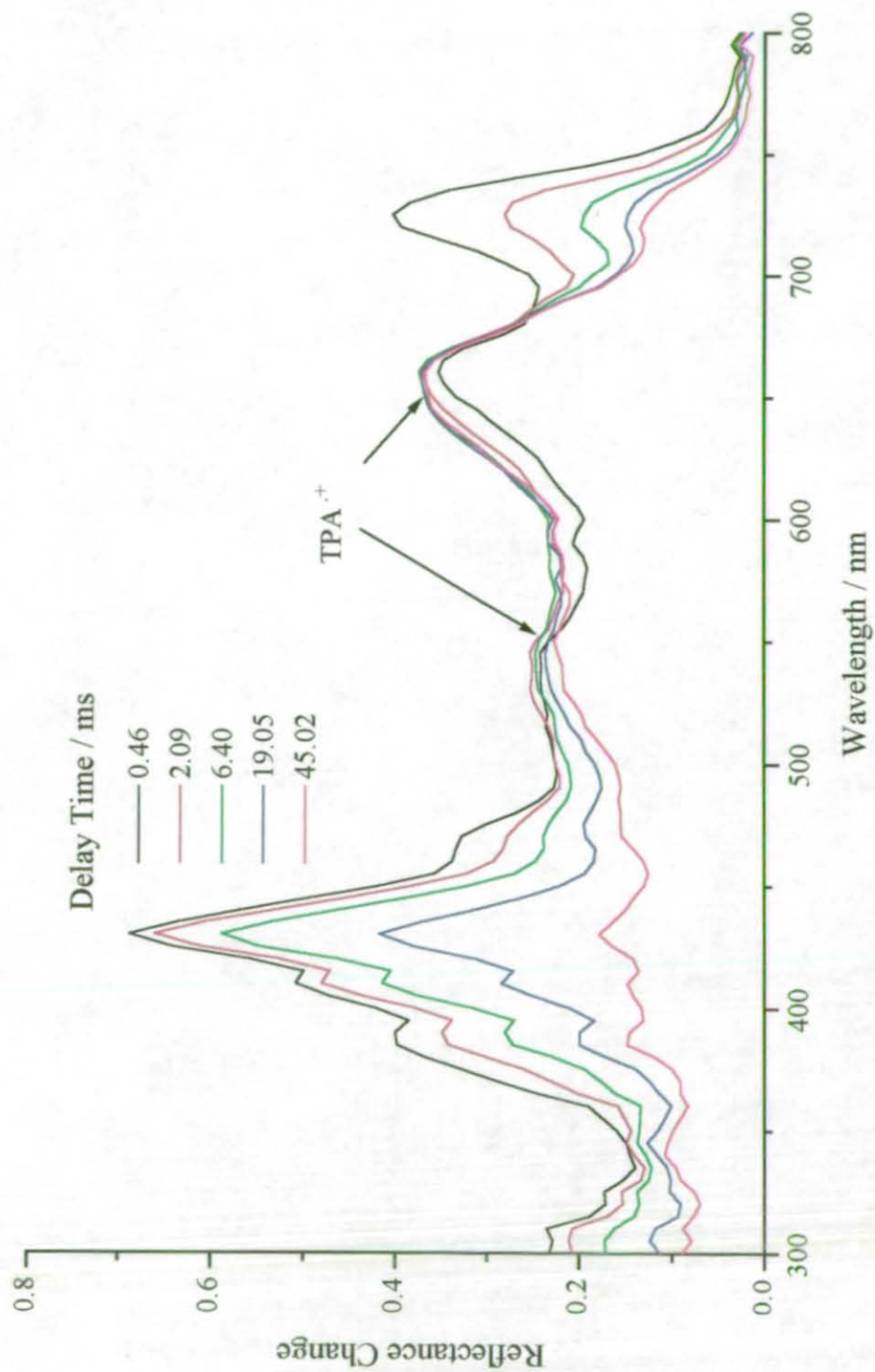


Figure 5.43 : Time-resolved transient difference absorption spectrum of 2,3-didecyloxy-anthracene coadsorbed with TPA on silica following laser excitation at 355 nm.

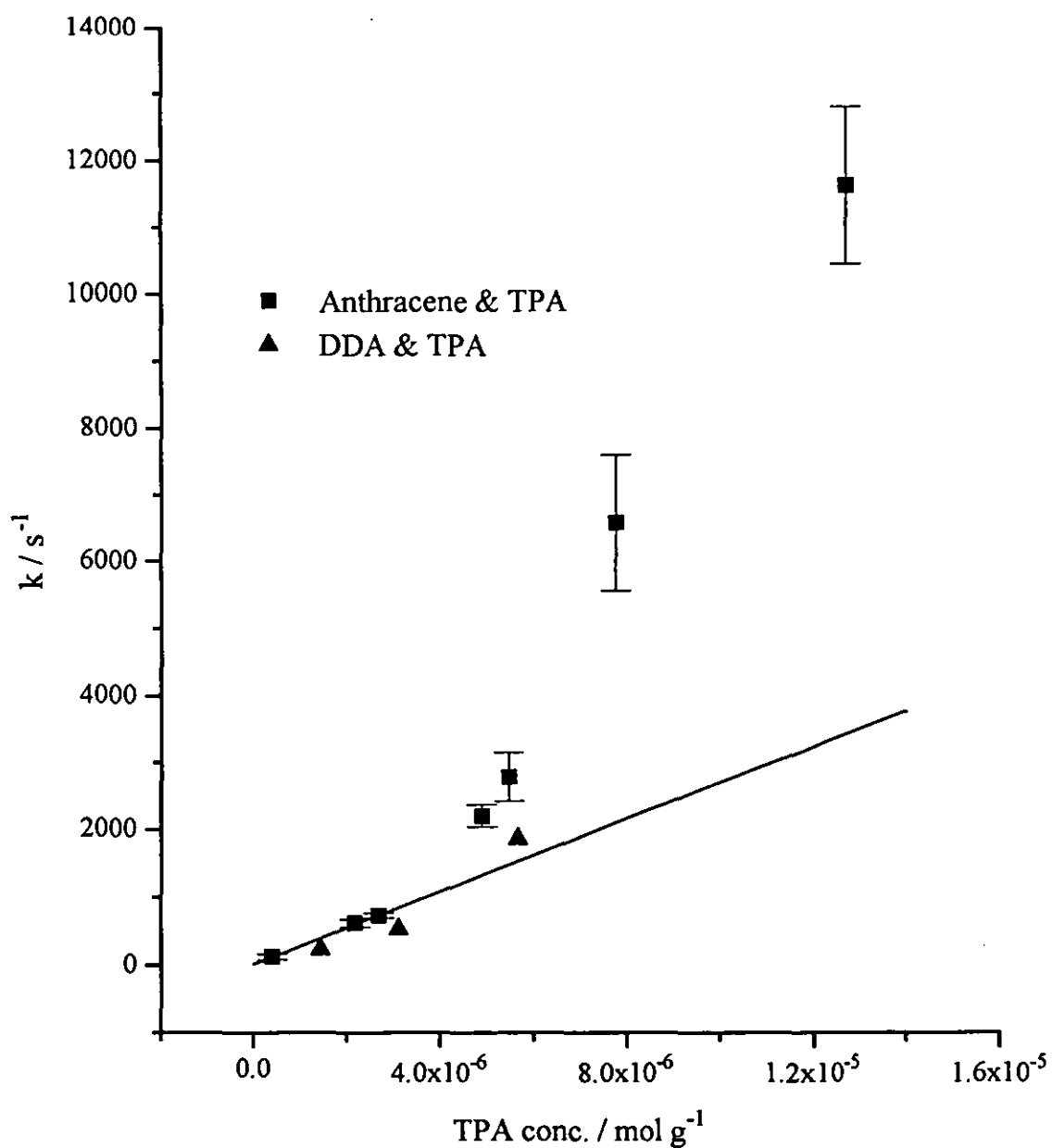


Figure 5.44 : The average rate constant \bar{k} obtained from the dispersive kinetic analysis for the rate of decay of the 2,3-didecyloxyanthracene radical cation at 725 nm plotted versus TPA concentration, along with the data obtained for unsubstituted anthracene.

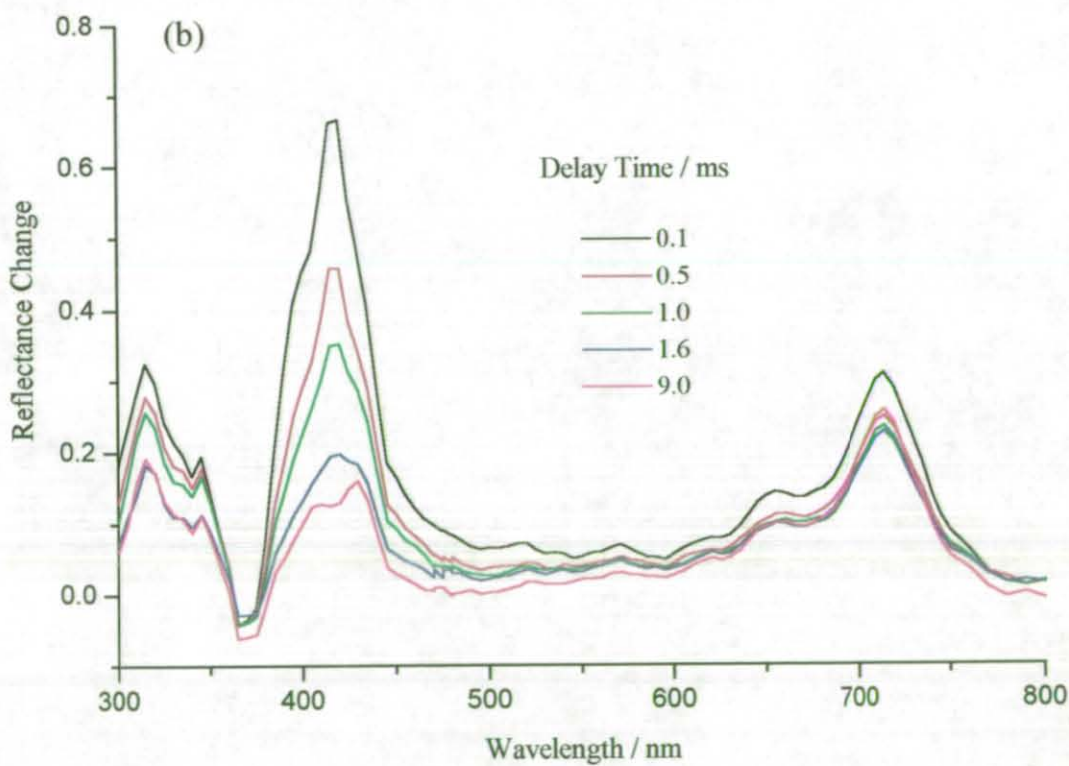
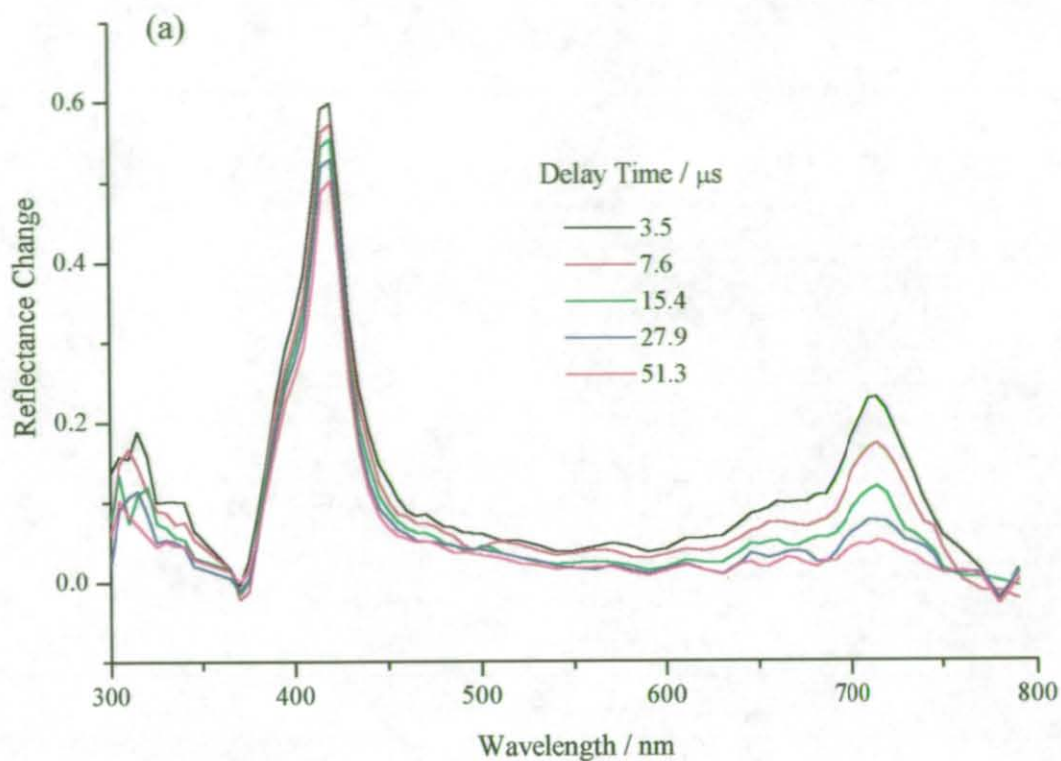


Figure 5.45 : Time-resolved transient difference absorption spectra of anthracene coadsorbed with (a) aniline and (b) naphthalene on silica gel following laser excitation at 355 nm.

5.3.4. Conclusions.

If no electron donor is present in the anthracene / silica system then electron-radical combination is the dominant decay mechanism. The coadsorption of an electron donor (with a sufficiently low oxidation potential) with anthracene causes an increase in the rate of decay of the anthracene radical cation. In these systems, it appears that the rate of diffusion of the electron donor to the anthracene radical cation and subsequent favourable interaction is the rate limiting step, with the rate of electron transfer being relatively fast. This also seems to be the case when comparing the rate of electron transfer between TPA and the 2,3-didecyloxyanthracene radical cation with the rate of electron transfer from TPA to the unsubstituted anthracene radical cation. These rates of electron transfer appear to be approximately the same, as expected if diffusion of the TPA is the rate determining step.

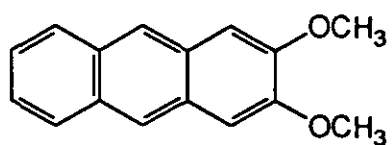
Chapter 6
Anthracene derivatives

6. Anthracene derivatives.

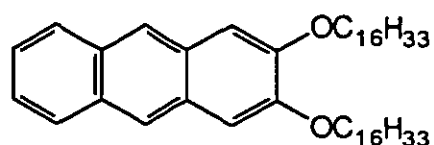
A selection of symmetrically disubstituted alkoxyanthracene derivatives adsorbed on silica gel have been briefly studied. These derivatives differ in the positions of the substituent groups, and the length of the alkyl chains. These were kindly supplied by Dr. Bouas-Laurent, of the University of Bordeaux, and were synthesised according to the methods given in references^{143,144}. In addition, 9-cyanoanthracene was also studied adsorbed on silica gel. The structures of these anthracene derivatives are shown overleaf in Figure 6.1. The samples were prepared according to preparation method B in section 3.1., i.e. by forced adsorption from evaporation of solvent. The solvent used in all these sample preparations was n-hexane.

6.1. Ground state absorption spectra.

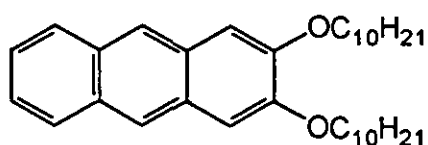
The ground state absorption spectra of the 2,3-dialkoxy derivatives adsorbed on silica gel are shown in Figures 6.2a-c expressed as remission function versus wavelength, and compared with a similar loading of unsubstituted anthracene on silica gel (Figure 6.2d). The spectra of the dialkoxy derivatives show considerably less structure than the spectrum of anthracene at a similar concentration, in contrast to observations in solution where the spectra are well structured. This lack of structure on surface adsorption could be due to one or two effects. Firstly, greater aggregation of the derivatives as a consequence of their long hydrocarbon tails would lead to the observed loss of structure, since aggregation effects for unsubstituted anthracene leads to a loss of structure in the spectrum (see Figure 5.3 in section 5.1.1.). Alternatively, greater overlap with the fluorescence emission spectra and higher fluorescence quantum yields in some cases over unsubstituted anthracene may be responsible for the observed loss of resolution. In fact, reliable ground state absorption spectra of 2,6-didecyloxyanthracene (2,6-DDA), 1,5-didecyloxyanthracene (1,5-DDA), 9,10-didecyloxyanthracene (9,10-DDA) and 9-cyanoanthracene could not be obtained due to their high fluorescence yields.



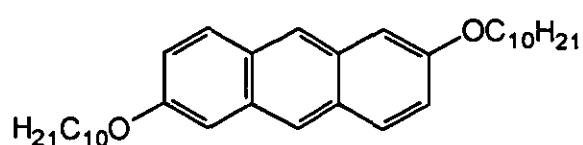
2,3-dimethoxyanthracene



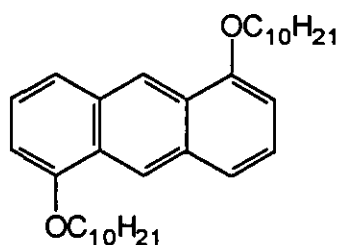
2,3-dihexadecyloxyanthracene



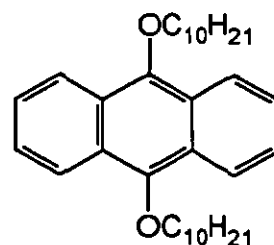
2,3-didecyloxyanthracene



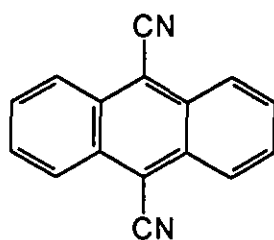
2,6-didecyloxyanthracene



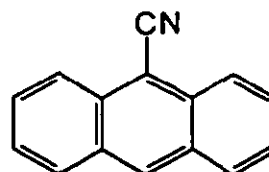
1,5-didecyloxyanthracene



9,10-didecyloxyanthracene



9,10-dicyanoanthracene



9-cyanoanthracene

Figure 6.1 : Structures of anthracene derivatives adsorbed onto silica gel.

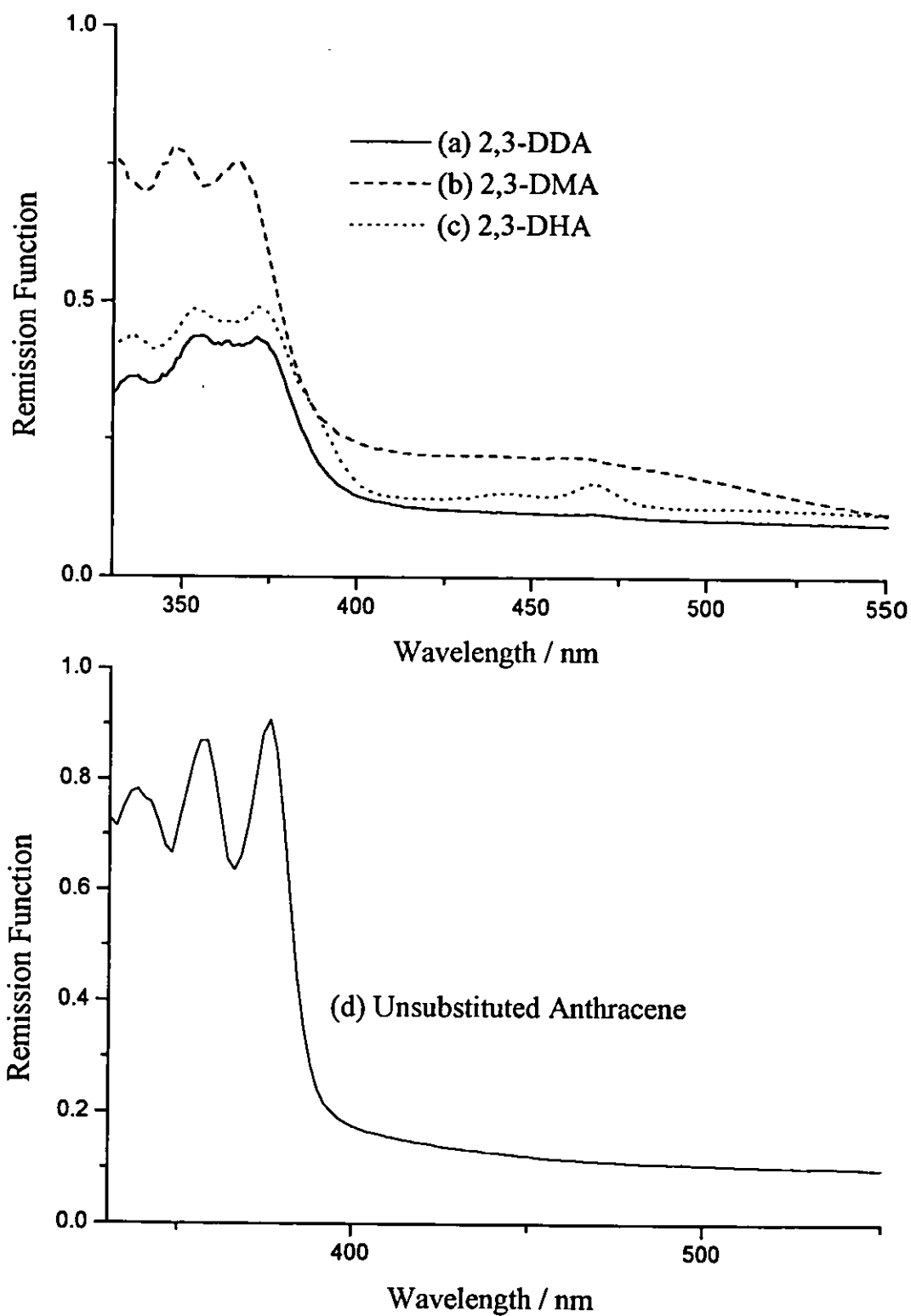


Figure 6.2 : Ground state diffuse reflectance absorption spectra of (a) 2,3-DDA, (b) 2,3-DMA, (c) 2,3-DHA and (d) unsubstituted anthracene adsorbed on silica gel plotted as remission function versus wavelength.

6.2. Fluorescence emission spectra.

The loss of spectral structure described in the previous section is also observed in the fluorescence emission spectra of the adsorbed dialkoxy substituted anthracenes. The spectra were recorded following excitation at 350 nm. Here again there may be two possible reasons for the loss of structure. Aggregation of the dialkoxy derivatives would depress the overall emission intensity if the aggregates are non-emissive, and re-absorption of the emitted light (fluorescence) by the aggregates would have a profound effect on the shapes of the emission spectra. In addition, self-absorption and re-emission effects which are clearly seen with unsubstituted anthracene adsorbed on silica gel (section 5.1.2) can also act to change both the relative peak intensities and the observed spectral resolution as a complex function of surface concentration. Figures 6.3a-f show the fluorescence emission spectra of the substituted anthracenes.

6.3. Transient Absorption Spectra.

All transient difference spectra were recorded following laser excitation at 355 nm. In contrast to the case of unsubstituted anthracene, none of the dialkoxy derivatives show delayed fluorescence arising from triplet-triplet annihilation (section 5.1.3.1a). For the derivatives with significant triplet quantum yields, this indicates that surface mobility for the dialkoxy derivatives is severely restricted. The triplet and fluorescence yields of these anthracene derivatives have been measured in solution¹⁴⁴⁻¹⁴⁶ and are shown below in Table 6.1.

Anthracene Derivative	Fluorescence Yield	Triplet Yield
anthracene ¹⁴⁵	0.3	0.71
9-cyanoanthracene ¹⁴⁶	0.93	0.04
2,3-DMA ¹⁴⁴	0.19	0.75
2,3-DDA ¹⁴⁴	0.19	0.72
2,6-DDA ¹⁴⁴	1.0	0
1,5-DDA ¹⁴⁴	0.28	0.77
9,10-DDA ¹⁴⁴	0.86	0.14

Table 6.1 :- Fluorescence and triplet quantum yields of various anthracenes

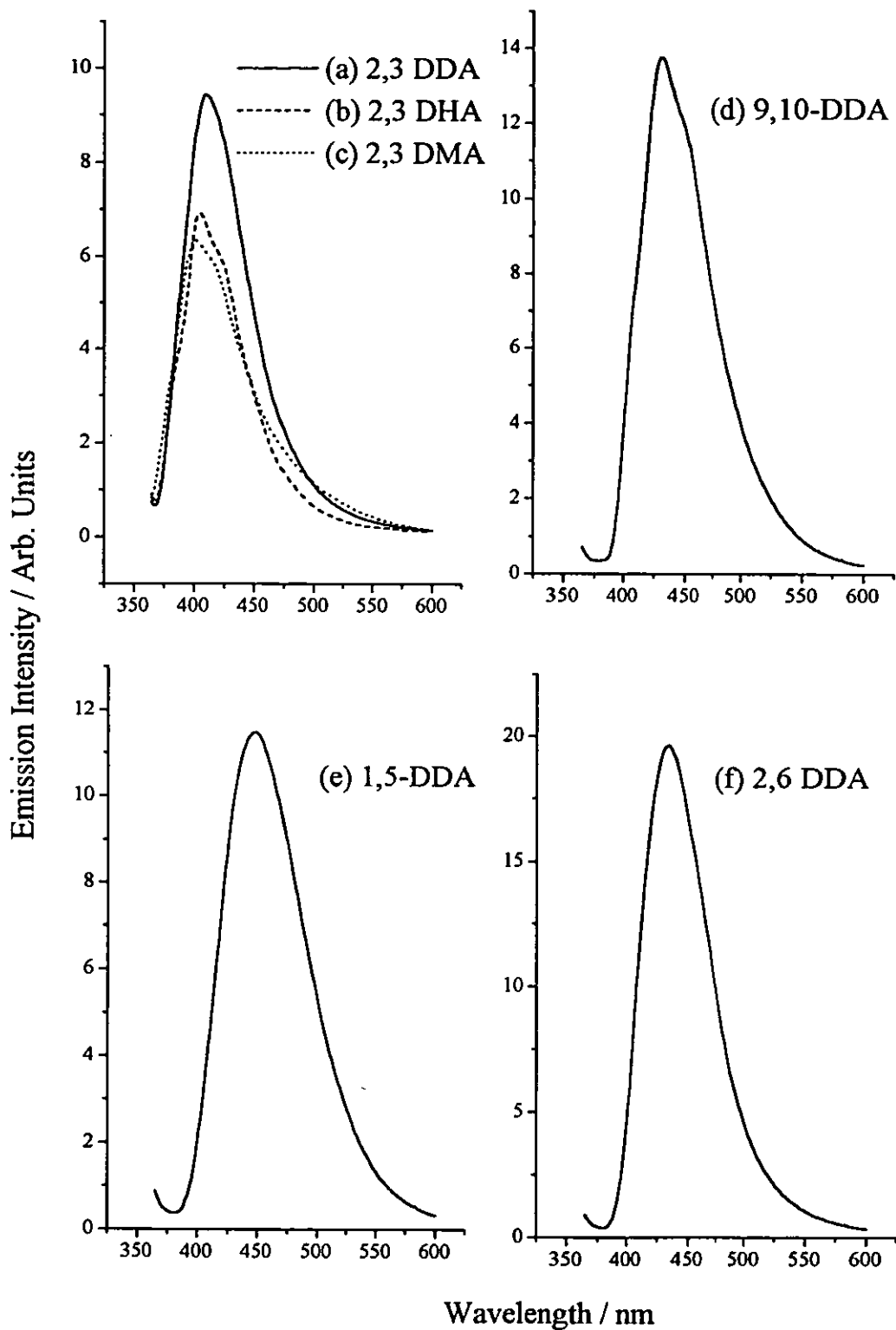


Figure 6.3 : Fluorescence emission spectra of (a) 2,3-DDA, (b) 2,3-DHA, (c) 2,3-DMA, (d) 9,10-DDA, (e) 1,5-DDA, (f) 2,6-DDA adsorbed on silica gel following excitation at 350 nm.

2,3-dimethoxyanthracene (2,3-DMA), 2,3-didecyloxyanthracene (2,3-DDA) and 2,3-dihexadecyloxyanthracene (2,3-DHA).

The transient difference spectra obtained following laser excitation at 355 nm of 2,3-DDA, 2,3-DMA and 2,3-DHA adsorbed on silica gel are shown in Figures 6.4a, 6.4b, and 6.4c, respectively. The characteristic triplet-triplet absorption peak of anthracene is observed along with the anthracene radical cation peak. However, both of these show a slight red shift of about 10 nm relative to unsubstituted anthracene, the triplet to 430 nm and the radical to 725 nm. An additional two peaks are present either side of the anthracene triplet-triplet absorption peak, and are assigned as also arising from the radical cation. They are assigned as such on the grounds of their kinetic behaviour on the coadsorption of TPA to the system, which was shown in section 5.2.3 to undergo efficient electron transfer to the unsubstituted anthracene radical cation. The transient difference spectrum of 2,3-DDA coadsorbed with TPA on silica gel following laser excitation at 355 nm is shown in Figure 6.5. This clearly shows the rise of the TPA radical cation peak at 650 nm and the decay of the 2,3-DDA radical cation peaks at 390, 470 and 725 nm. The two peaks around 390 and 470 nm decay with the same kinetics as the radical peak at 725 nm and consequently are assigned as arising from the radical cation. The triplet lifetime appears unaffected by the presence of the TPA, as is the case for unsubstituted anthracene. Hence the radical cation absorption peaks at 390 and 470 nm are red shifted by a much larger amount, as compared with their positions in unsubstituted anthracene, than the triplet-triplet absorption peak and the radical cation peak at 730 nm, being shifted by some 50 nm as compared with only about 10 nm. Comparisons of the transient difference spectra below 400 nm are not very reliable due to complications arising from the absorption of the anthracene ground state. Increasing the length of the hydrocarbon tail from methoxy to hexadecyloxy has little effect on the transient absorption spectra.

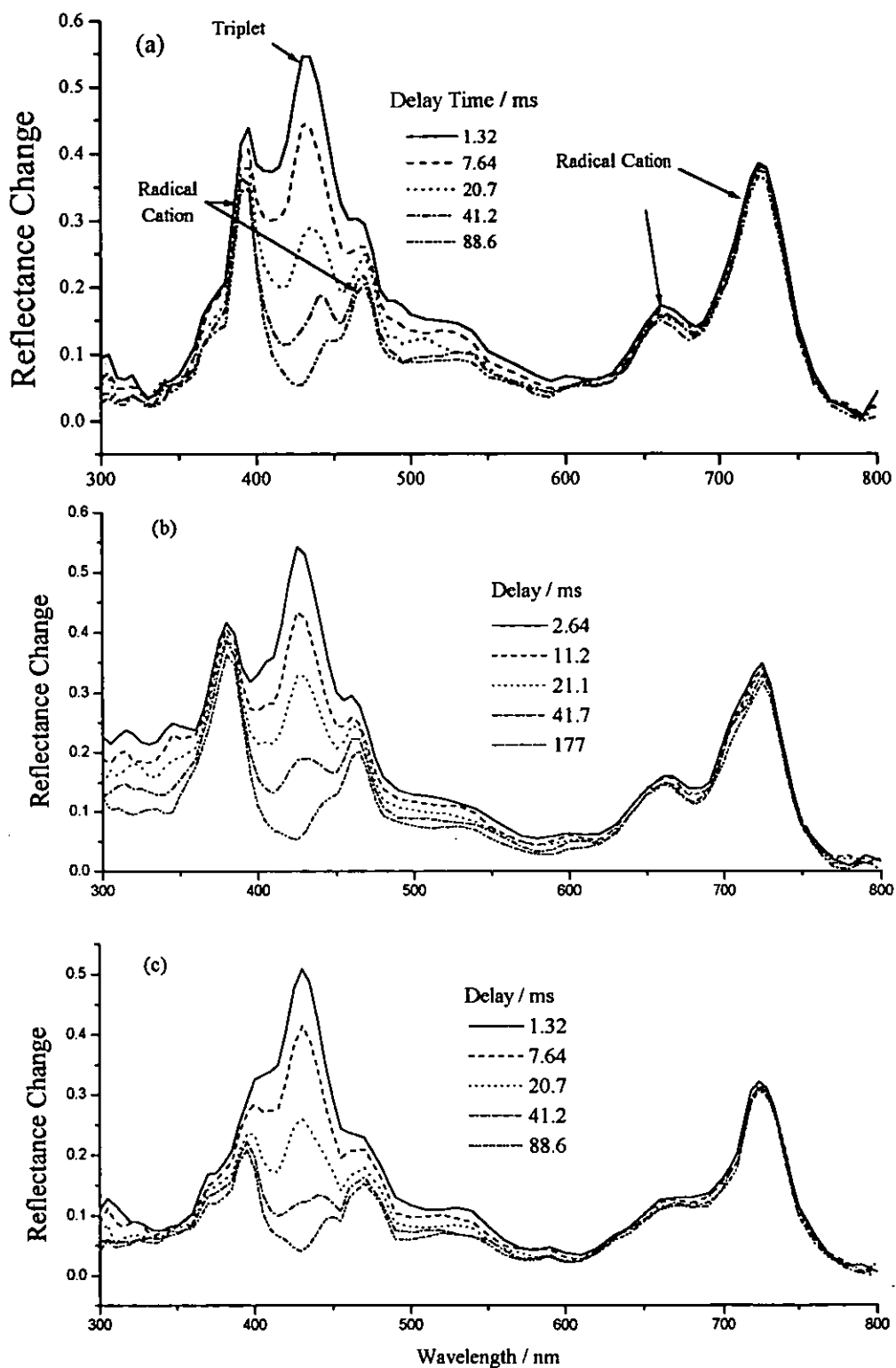


Figure 6.4 : Time-resolved transient difference absorption spectrum showing reflectance change $(R_0 - R_t)/R_0$ of (a) 2,3-DDA, (b) 2,3-DMA and (c) 2,3-DHA adsorbed on silica gel following laser excitation at 355 nm.

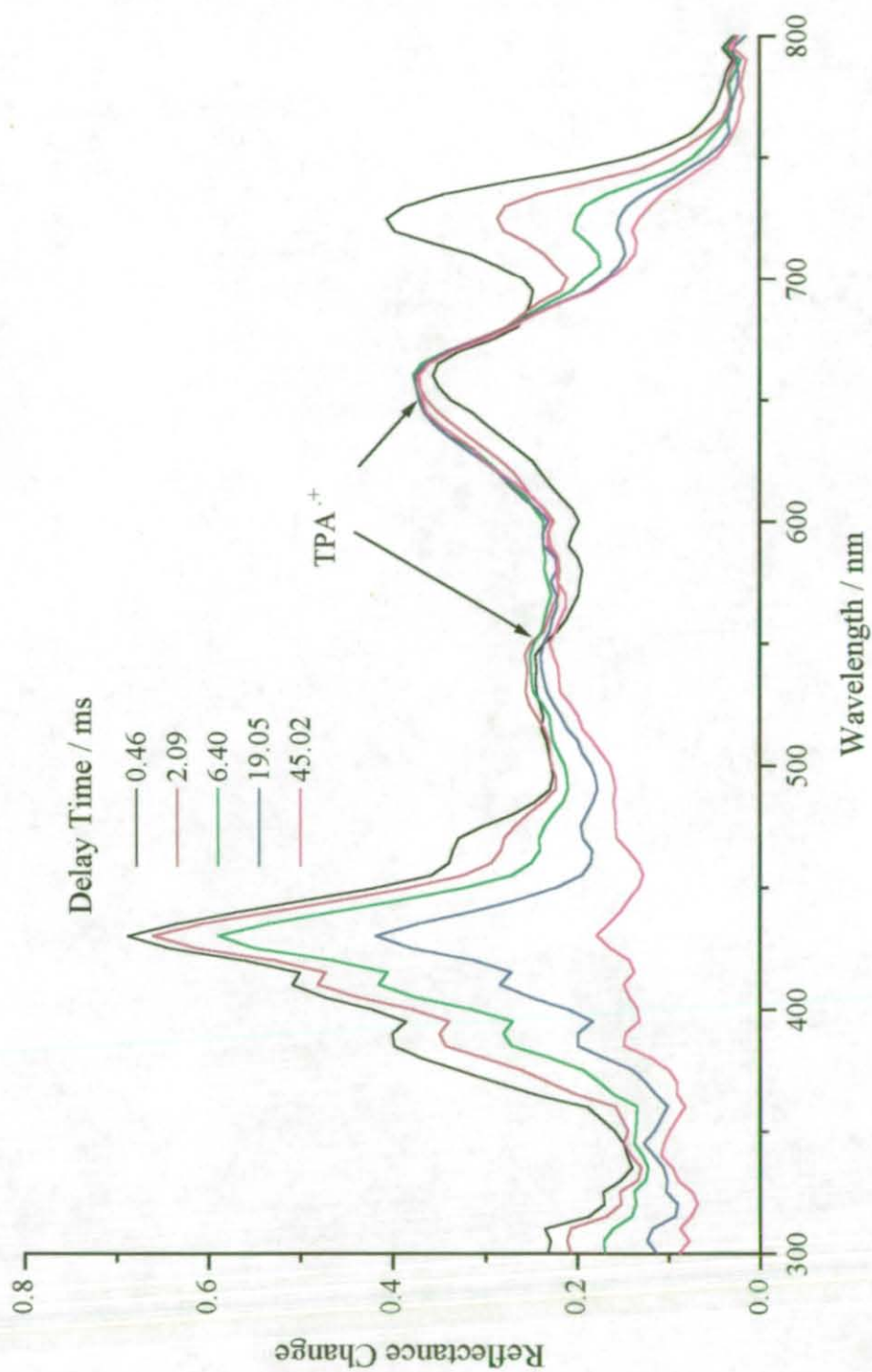


Figure 6.5 : Time-resolved transient absorption spectrum of 2,3-DDA coadsorbed with TPA on silica gel following laser excitation at 355 nm.

As mentioned previously, the dialkoxy derivatives do not show any delayed fluorescence, indicating there is little or no diffusion of the derivatives on the silica gel surface. This evidence of immobility is reinforced by the fact that increasing the 2,3-DDA concentration on silica gel from 0.6 to 2.1 $\mu\text{mol g}^{-1}$ does not cause an increase in the rate of decay of the triplet state. Unsubstituted anthracene is able to diffuse freely across the silica surface and the rate of decay of the triplet is greatly dependent on the anthracene loading (section 5.1.3.1a.). Figures 6.6a and 6.6b illustrate the dependence of the triplet lifetime on sample loading for a) unsubstituted anthracene and b) 2,3-didecyloxyanthracene.

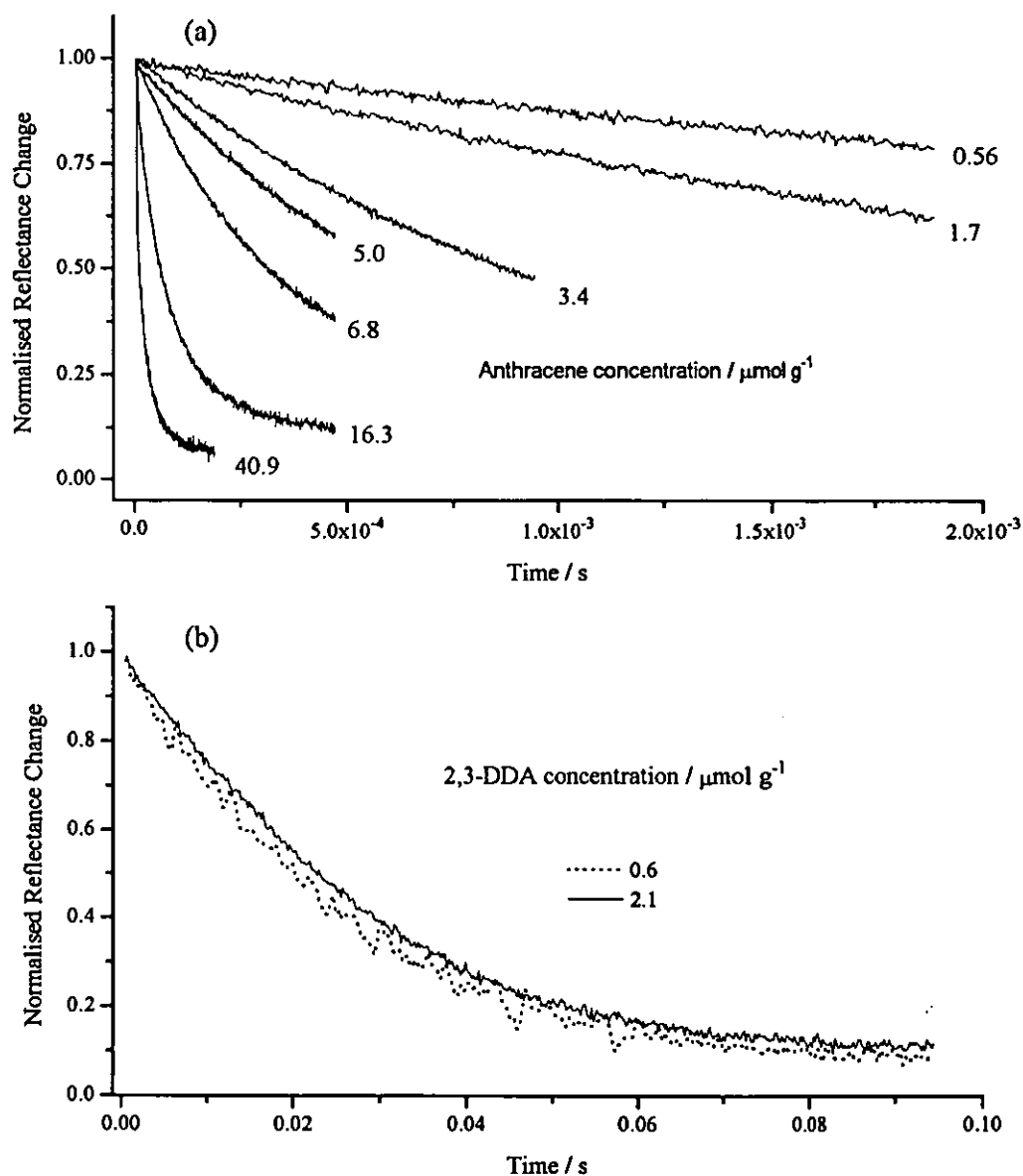


Figure 6.6 : Normalised triplet decay kinetics at 420 nm as a function of (a) unsubstituted anthracene concentration and (b) 2,3-DDA concentration on silica gel.

2,6-didecyloxyanthracene

The transient difference spectrum of the 2,6-DDA derivative adsorbed on silica gel, shown in Figure 6.7, is very similar to that of unsubstituted anthracene. The triplet yield is much lower than that of the unsubstituted anthracene, but there is clearly a small peak due to triplet-triplet absorption at 430 nm and peaks assigned as the radical cation are found at 345, 440 and 750 nm. The whole spectrum appears somewhat red shifted as compared with the spectrum of unsubstituted anthracene, where the triplet and radical cation peaks are found at 420 nm, and 320, 420, and 715 nm respectively.

1,5-didecyloxyanthracene and 9,10-didecyloxyanthracene

The transient difference spectra of these derivatives adsorbed on silica gel are very different from that of unsubstituted anthracene. The transient difference spectrum of 1,5-DDA adsorbed on silica gel is shown in Figure 6.8. The triplet-triplet absorption peaking around 430 nm decays to leave a very different radical cation spectrum from those seen with unsubstituted anthracene and the 2,3 and 2,6 dialkoxy derivatives. The features remaining following the decay of the triplet state are peaks found at 320 nm and 410 nm, and a very broad band peaking around 580 nm. The transient difference spectrum of 9,10-DDA reveals similar spectral characteristics to that of the 1,5-DDA, and is shown in Figure 6.9. A very small amount of triplet is observed at 425 nm, as expected from the relatively low triplet quantum yield found in solution (0.14 as compared with 0.77 for the 1,5 derivative) and the longer lived transient peaks are found at 310 nm, 425 nm and again a very broad band peaking at approximately 570 nm. In order to assign the origin of the broad band around 570 nm found in 1,5-DDA and 9,10-DDA, TPA was added to the system to act as an electron donor. 9,10-DDA was chosen for these experiments due to its low triplet yield, and was coadsorbed with TPA onto silica gel. The transient difference spectrum obtained is shown in Figure 6.10. This clearly shows that the decay of the 310 and 425 nm peaks is accompanied by the rise of the TPA radical cation in the region of 610 to 700 nm. The decay of the broad band observed with just 9,10-DDA which peaks at 570 nm is not obvious here, but its apparent absence can be explained by the fact that the TPA radical cation has a peak at around 550 nm. Consequently the rise of the TPA radical cation obscures the decay of the broad band resulting in a region (550 to 610 nm) where the reflectance change remains approximately constant at the delays monitored. To confirm these observations

azulene was also coadsorbed with 9,10-DDA on silica gel and the resulting transient difference spectrum is shown in Figure 6.11. The whole spectrum, including the broad band around 570 nm, has an increased rate of decay on coadsorption of azulene. These experiments provide compelling evidence that the broad band at 570 nm observed from the 1,5 and 9,10-DDA derivatives, along with the peaks at 310 and 425 nm, are characteristic of the radical cation of these derivatives.

9-cyanoanthracene

The transient difference spectrum of 9-cyanoanthracene following laser excitation at 355 nm is shown in Figure 6.12. As anticipated from the solution triplet quantum yield, very little or no triplet is observed. The three peaks observed at 350, 440 and 780 nm have been assigned as being due to the radical cation following experiments with coadsorbed TPA, similar to those described in the previous section for 9,10-DDA. The coadsorption of TPA with 9-cyanoanthracene causes an increase in the rate of decay of all three of the peaks previously observed and the concomitant rise of the TPA radical cation at 550 and 650 nm. This is shown in Figure 6.13.

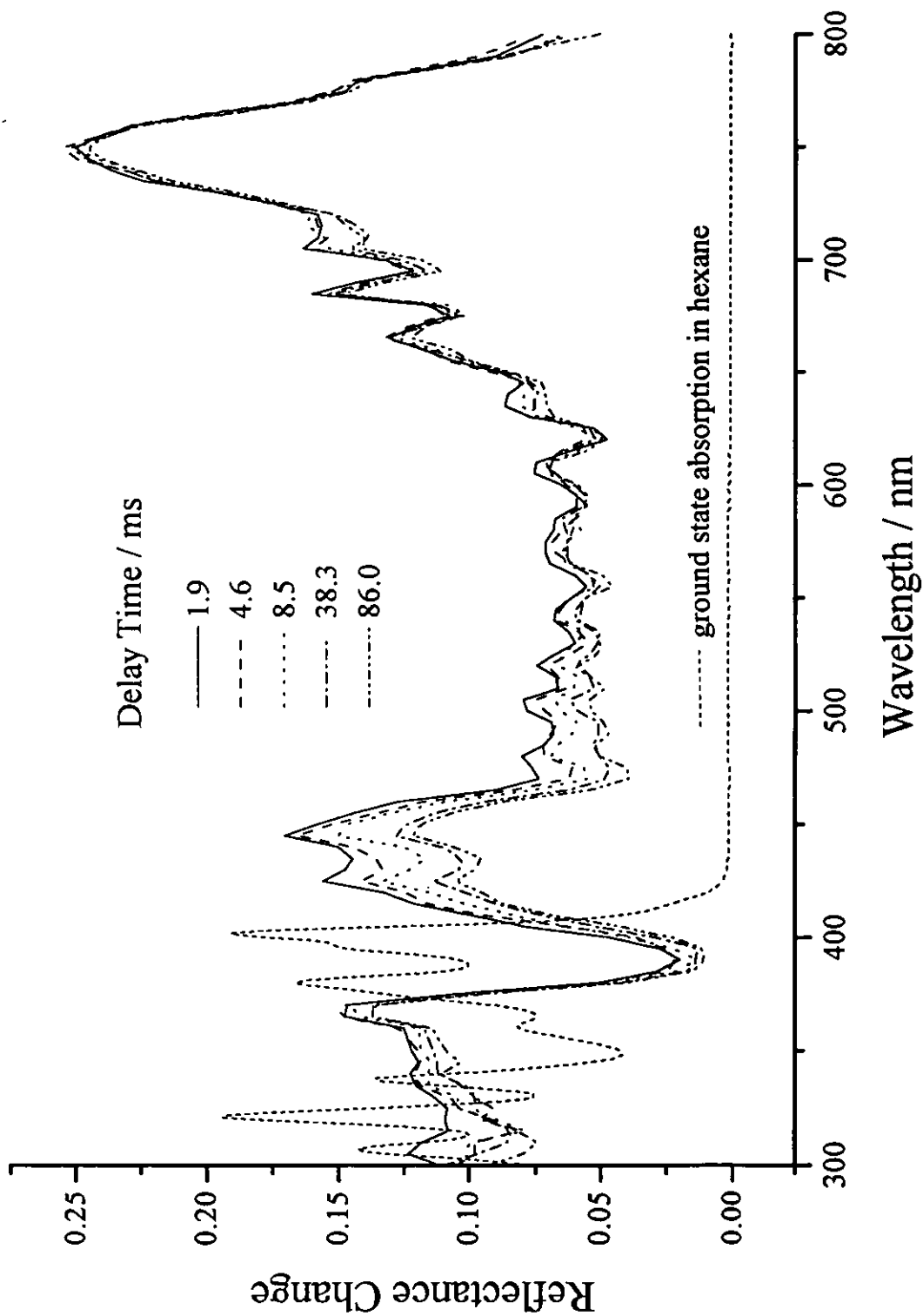


Figure 6.7 : Time-resolved transient difference spectrum showing reflectance change $(R_0-R_t)/R_0$ of 2,6-DDA adsorbed on silica gel following laser excitation at 355 nm. The ground state absorption spectrum in solution is shown for comparison.

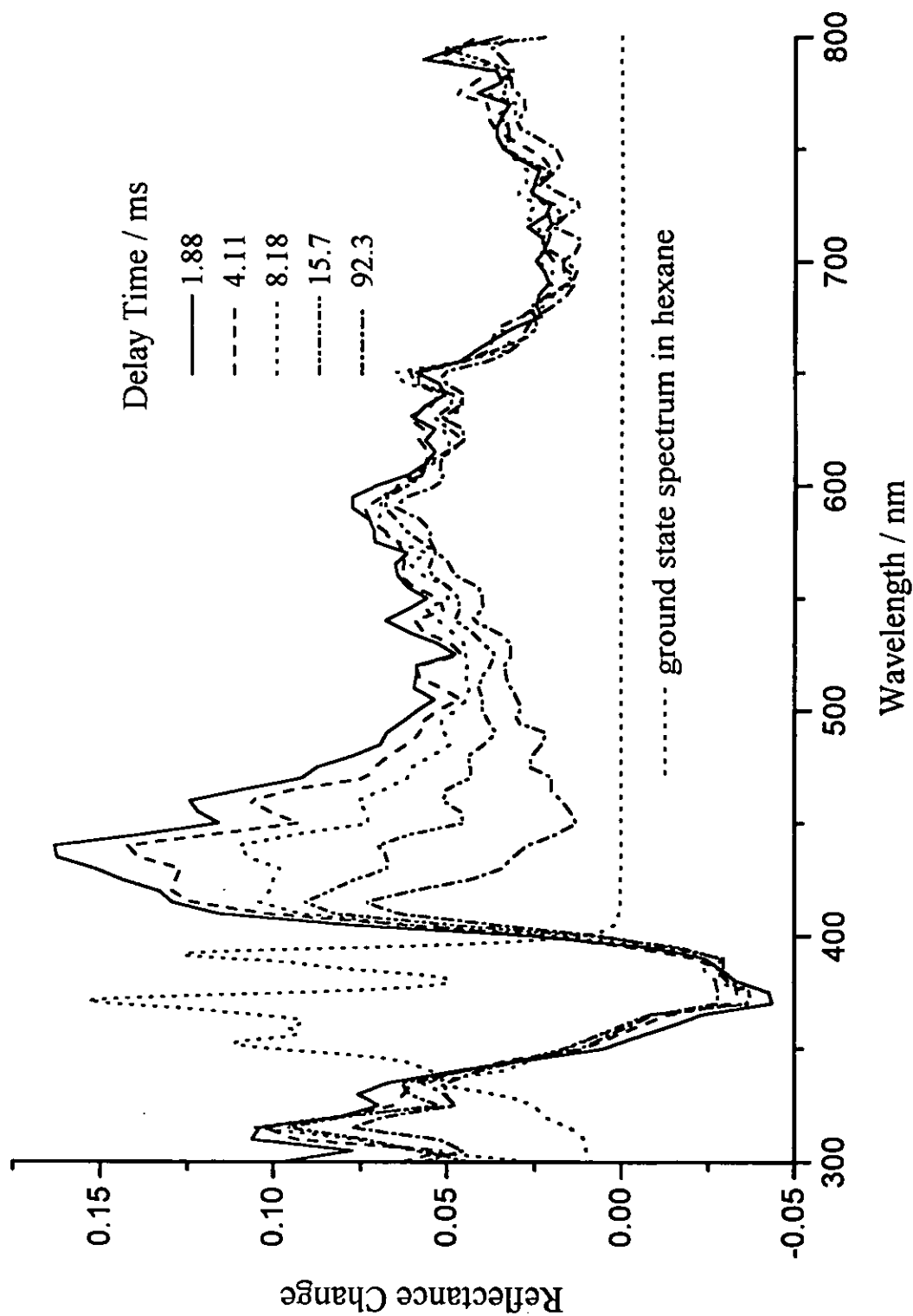


Figure 6.8 : Time-resolved transient difference spectrum showing reflectance change $(R_0 - R_t)/R_0$ of 1,5-DDA adsorbed on silica gel following laser excitation at 355 nm. The ground state absorption spectrum in solution is shown for comparison.

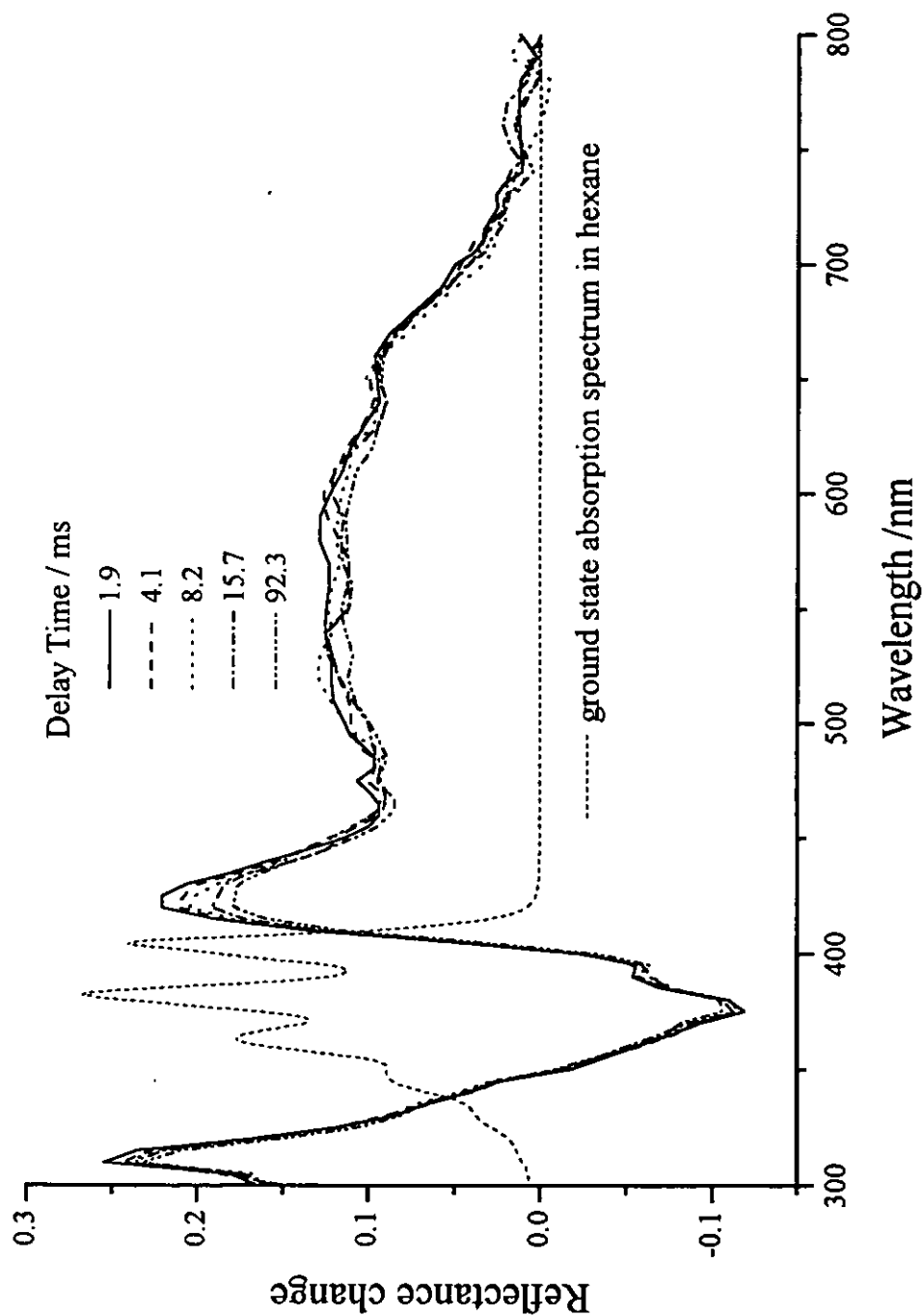


Figure 6.9 : Time-resolved transient difference spectrum showing reflectance change $(R_0 - R_t)/R_0$ of 9,10-DDA adsorbed on silica gel following laser excitation at 355 nm. The ground state absorption spectrum in solution is shown for comparison.

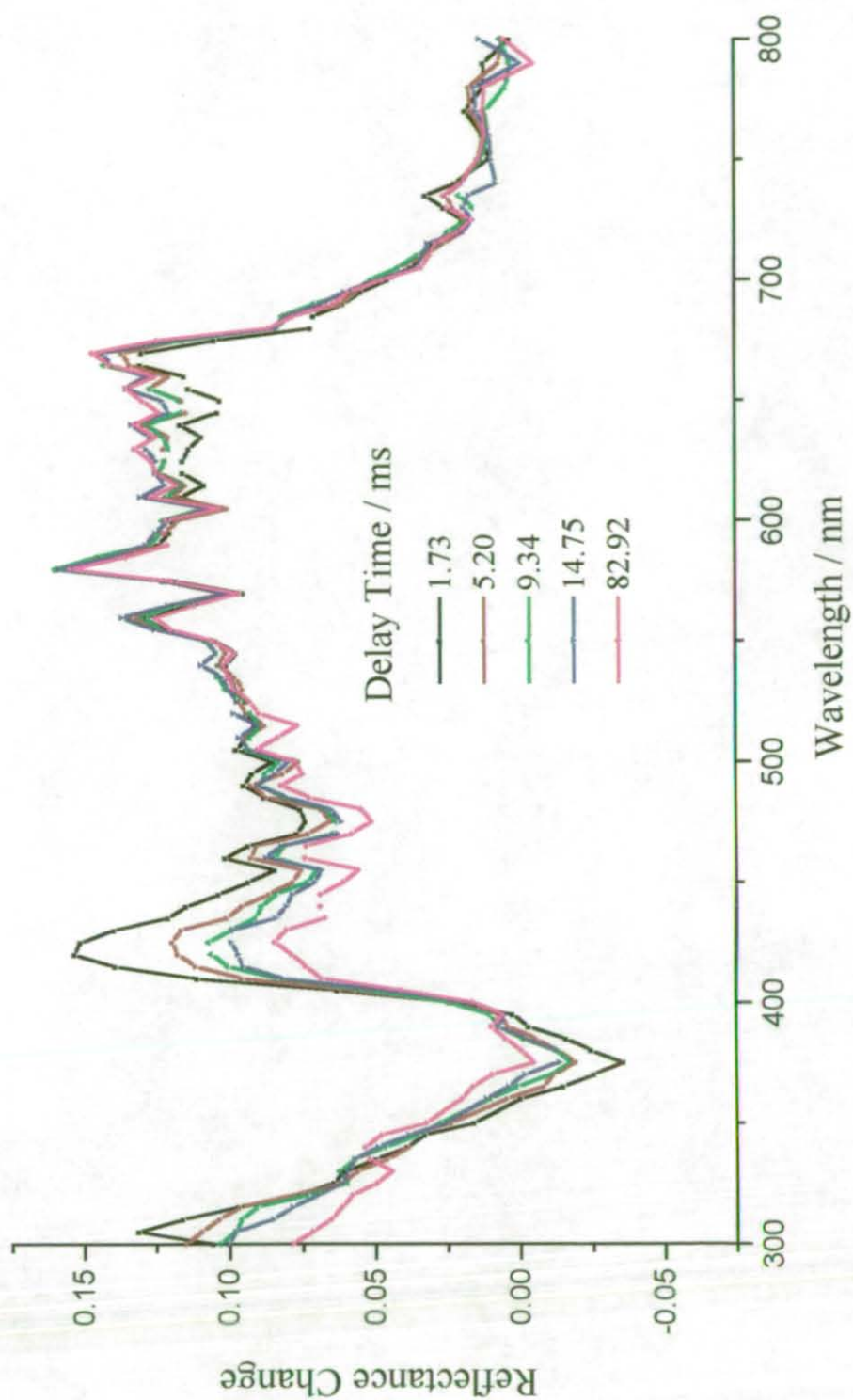


Figure 6.10 : Time resolved transient difference spectrum showing reflectance change $(R_0 - R_t)/R_0$ of 9,10-DDA coadsorbed with TPA on silica gel following laser excitation at 355nm.

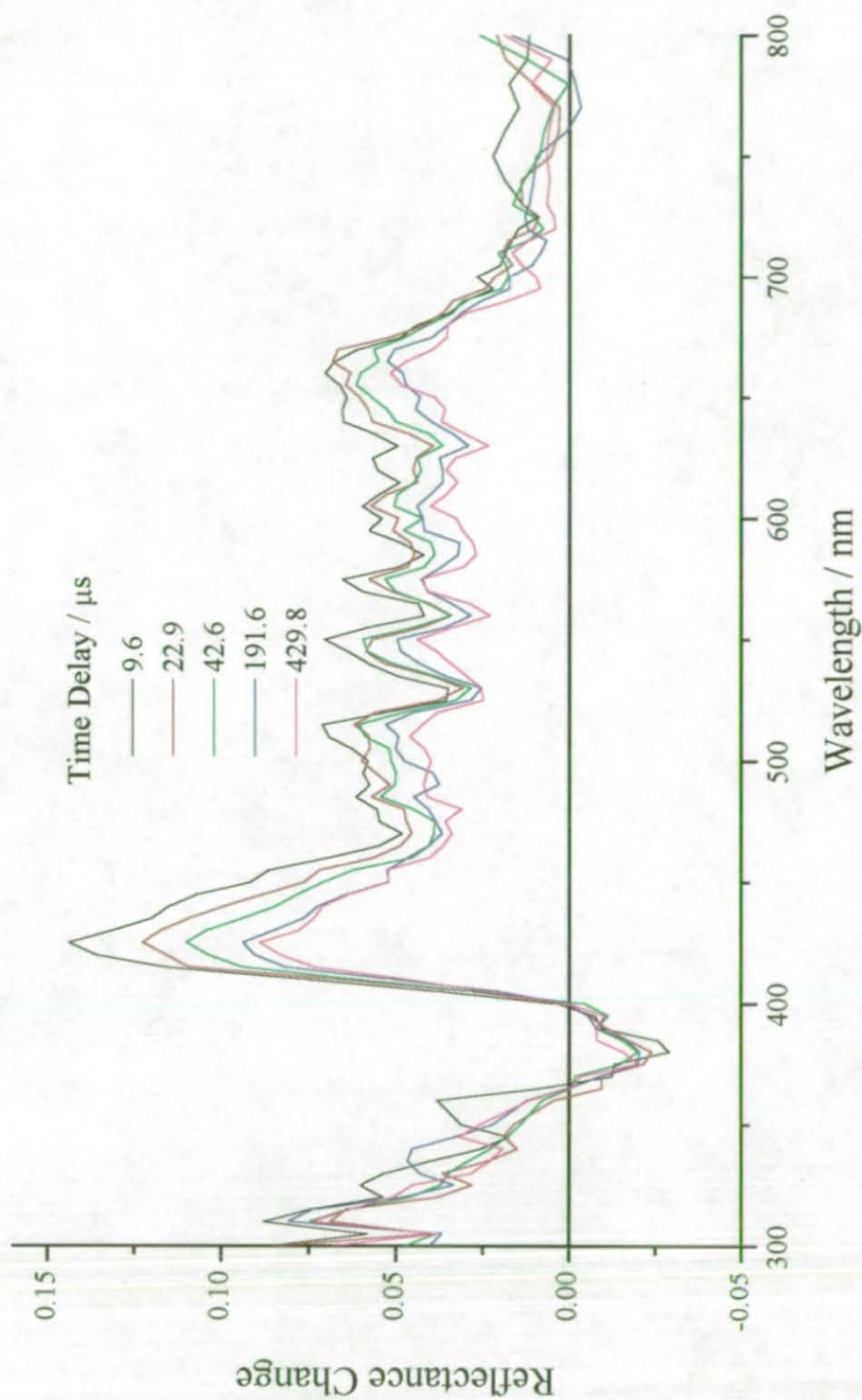


Figure 6.11 : Time resolved transient difference spectrum showing reflectance change $(R_0 - R_t)/R_0$ of 9,10-DDA coadsorbed with azulene on silica gel following laser excitation at 355nm.

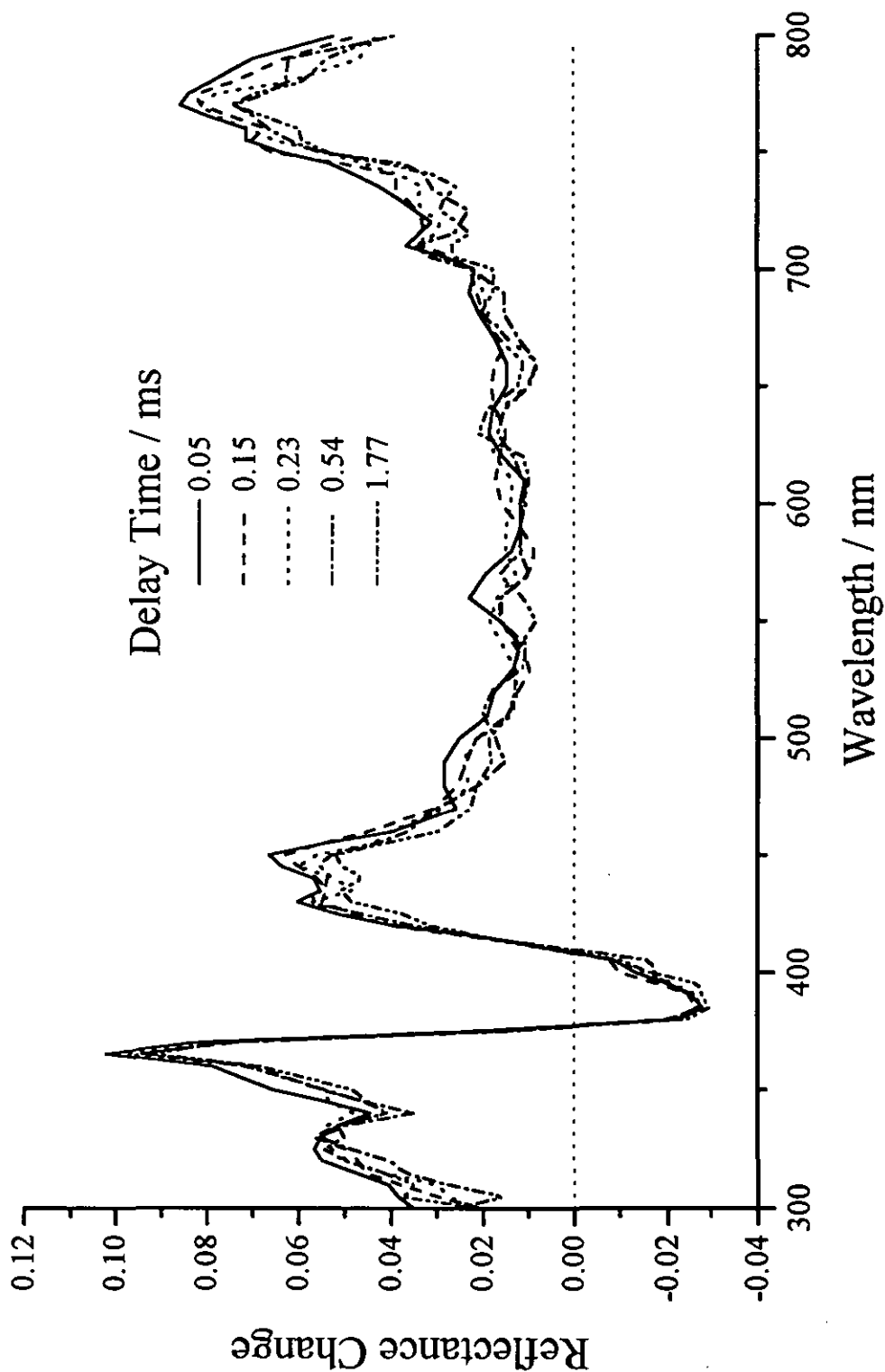


Figure 6.12 : Time-resolved transient difference spectrum showing reflectance change $(R_0 - R_t)/R_0$ of 9-cyanoanthracene adsorbed on silica gel following laser excitation at 355 nm.

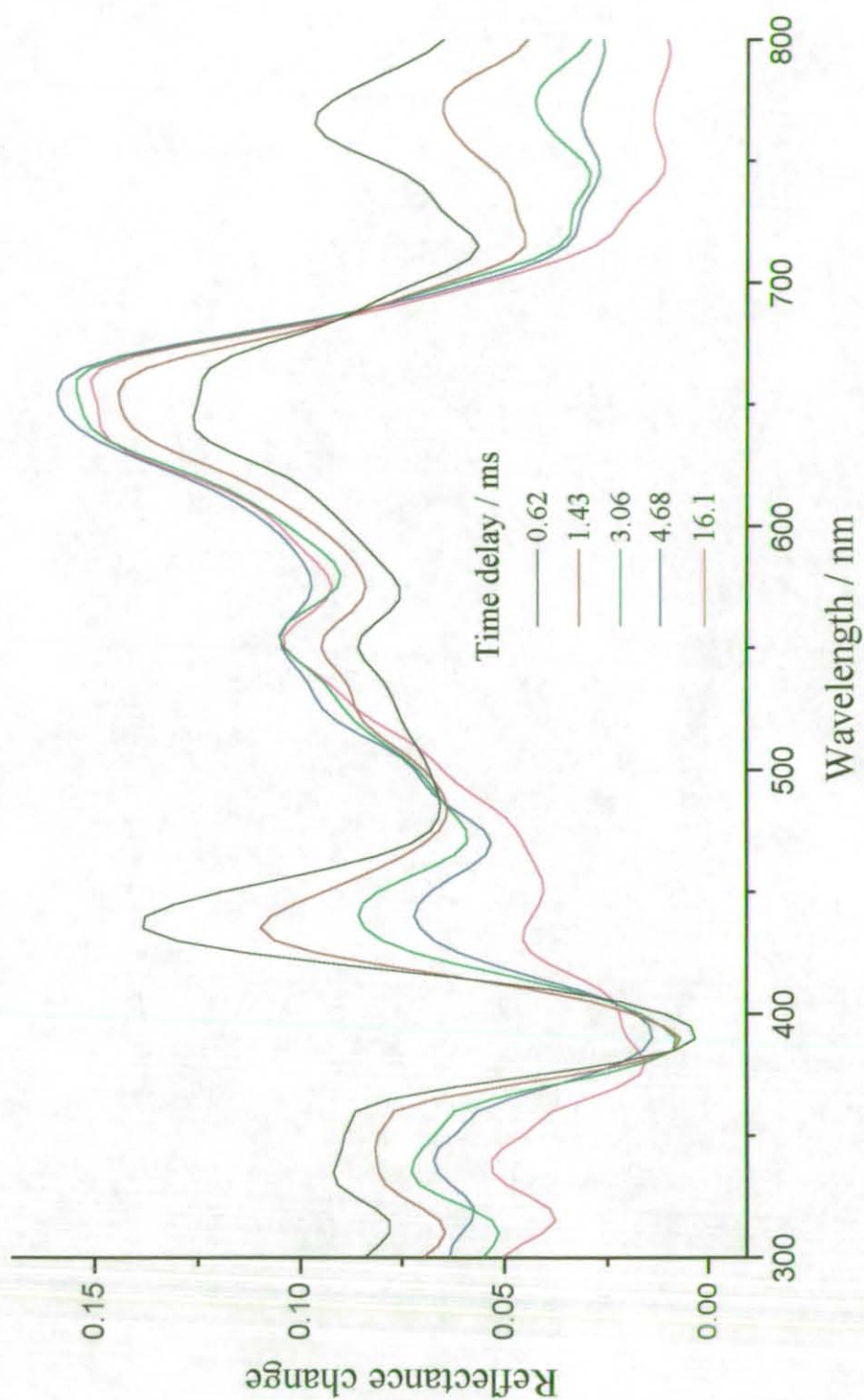


Figure 6.13 : Time-resolved transient difference spectrum showing reflectance change $(R_0 - R_t)/R_0$ of 9-cyanoanthracene coadsorbed with TPA on silica gel following laser excitation at 355 nm.

6.4. Transient Emission Spectra.

The transient emission spectra were recorded following laser excitation at 355 nm. The spectra were collected 85 ns after the laser pulse, to eliminate interference from prompt fluorescence. The integration time employed was 100 ns.

The transient emission spectra of the 2,3 derivatives are spectrally similar to the transient emission spectra of unsubstituted anthracene. The time-resolved transient emission of 2,3-DDA is shown in Figure 6.14. The spectra appear a little broader than those of unsubstituted anthracene and are slightly red shifted (see section 5.1.4 for the unsubstituted anthracene spectra). The peak assigned as the excimer emission in unsubstituted anthracene is shifted from 450 nm to 470 nm, and the emission peak previously assigned as that of protonated anthracene (section 5.1.4) is shifted from 530 nm to 560 nm. The 9,10 and 1,5 derivatives also reveal the presence of both the excimer and protonated anthracene emission peaks. Figures 6.15 and 6.16 show the time-resolved transient emission spectra of 9,10-DDA and 1,5-DDA respectively. The emission from the protonated anthracene is not observed for the 2,6-DDA derivative, shown in Figure 6.17. Inspection of the relative peak intensities of the excimer and protonated emission peaks in Figures 6.15 to 6.18 shows that the ratio of excimer emission to protonated emission increases in the series 2,3 - 9,10 - 1,5 - 2,6. Owing to the difficulties in comparing the absolute emission intensities, it is not clear at this stage whether this series reflects an increase in excimer formation or a decrease in the amount of protonated anthracene formation.

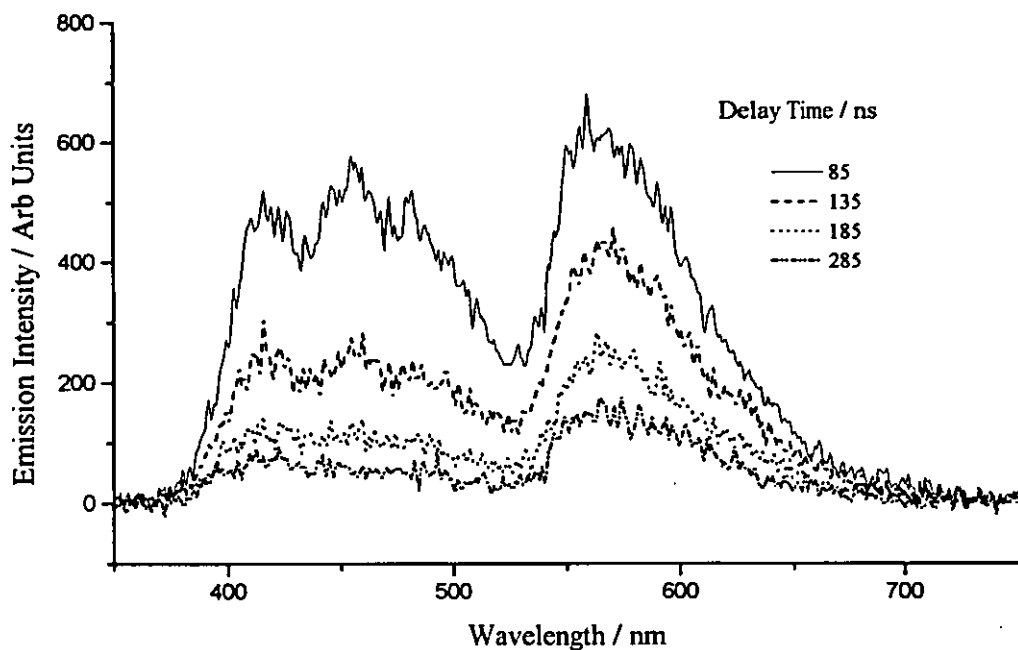


Figure 6.14 : Time resolved transient emission spectrum 2,3-DDA on silica gel following laser excitation at 355nm. Pulse energy 15 mJ cm^{-2} , gate width 100ns.

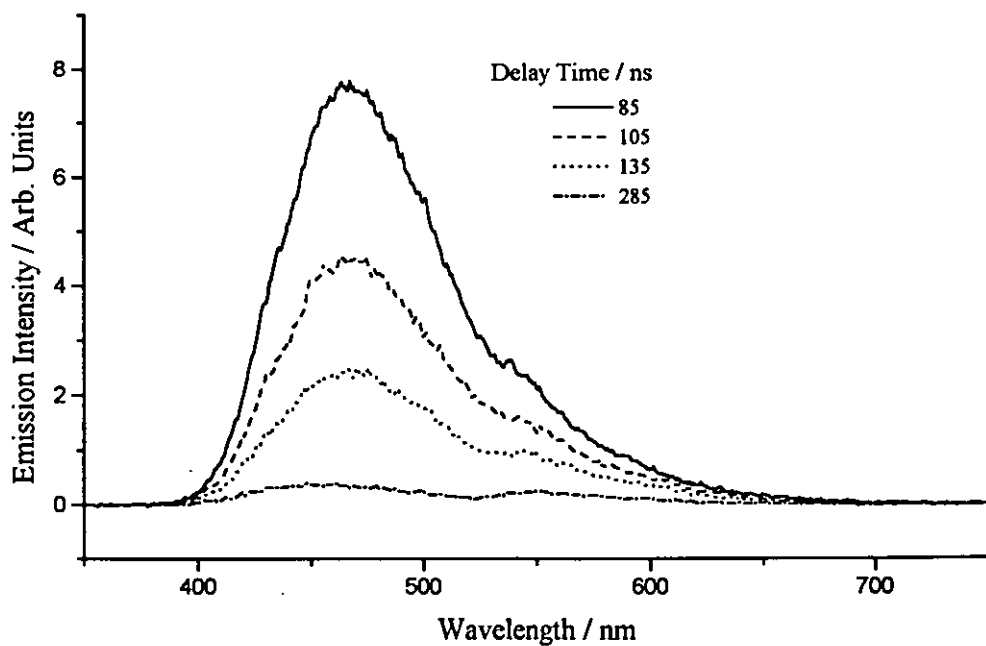


Figure 6.15 : Time resolved transient emission spectrum 1,5-DDA on silica gel following laser excitation at 355nm. Pulse energy 15 mJ cm^{-2} , gate width 100ns.

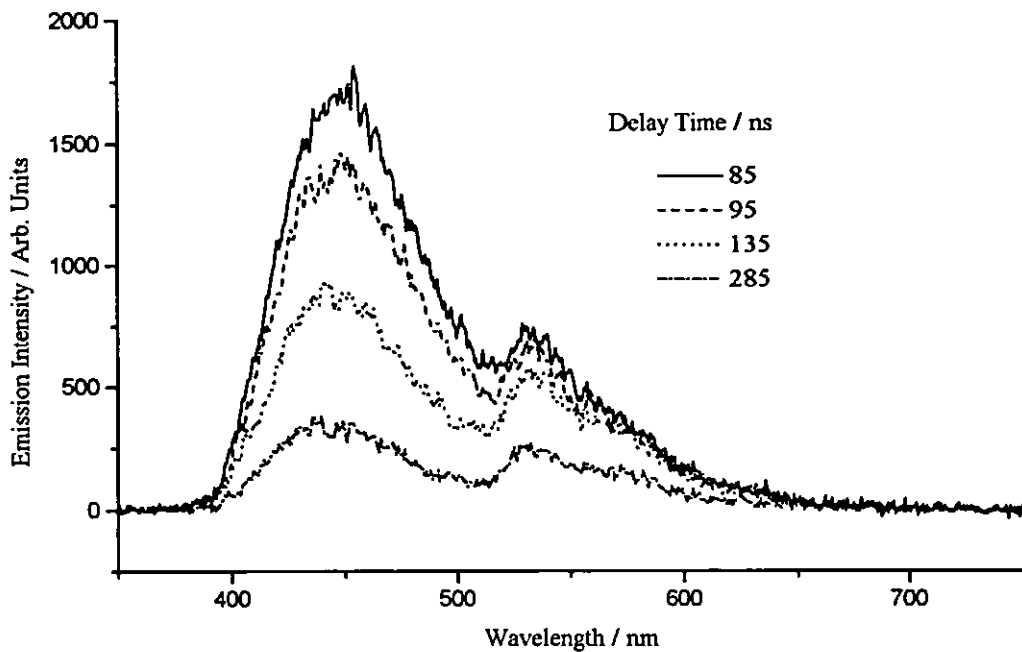


Figure 6.16 : Time resolved transient emission spectrum 9,10-DDA on silica gel following laser excitation at 355nm. Pulse energy 15 mJ cm^{-2} , gate width 100ns.

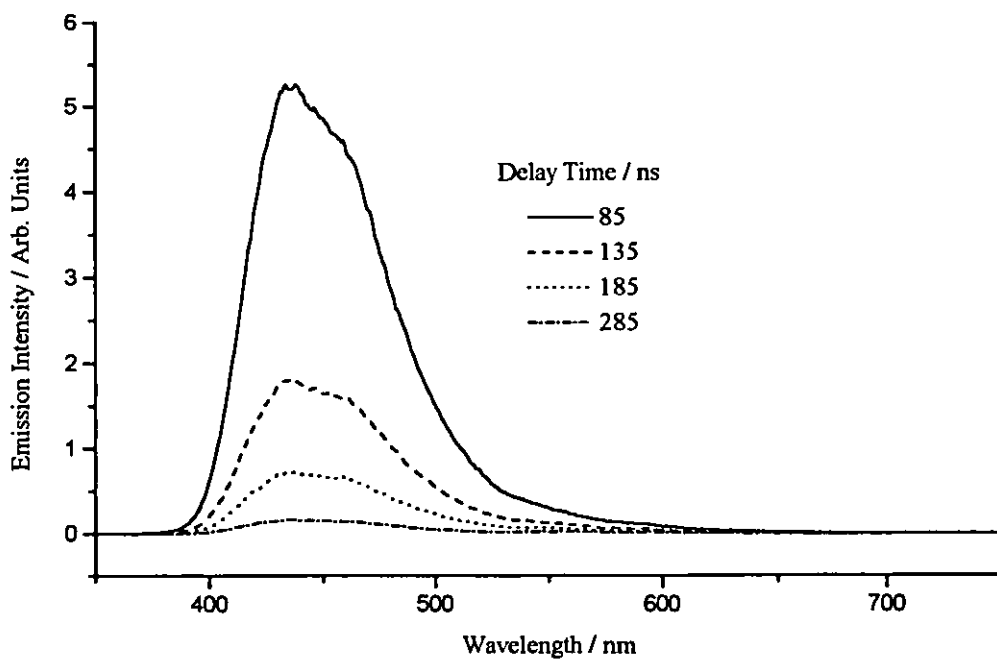


Figure 6.17 : Time resolved transient emission spectrum 2,6-DDA on silica gel following laser excitation at 355nm. Pulse energy 15 mJ cm^{-2} , gate width 100ns.

6.5. Conclusions.

On the grounds of the absence of delayed fluorescence, the dialkoxy derivatives appear tightly bound to the silica gel surface and diffusion is severely restricted. The transient difference spectra of the anthracene derivatives reveal similarities between the spectral shapes of the 2,3-dialkoxyanthracenes, 2,6-didecyloxyanthracene and 9-cyanoanthracene with that of unsubstituted anthracene on silica gel. The transient spectra of the 9,10 and 1,5-didecyloxyanthracenes are similar to one another, but significantly different from unsubstituted anthracene. The spectra observed for the radical cations of the anthracene derivative are summarised in Figure 6.19, clearly showing the marked differences in the spectra of the 9,10 and 1,5-didecyloxyanthracenes. The relative amount of triplet-triplet absorption observed for the various derivatives adsorbed on silica gel are in broad agreement with the triplet quantum yields recorded in solution.

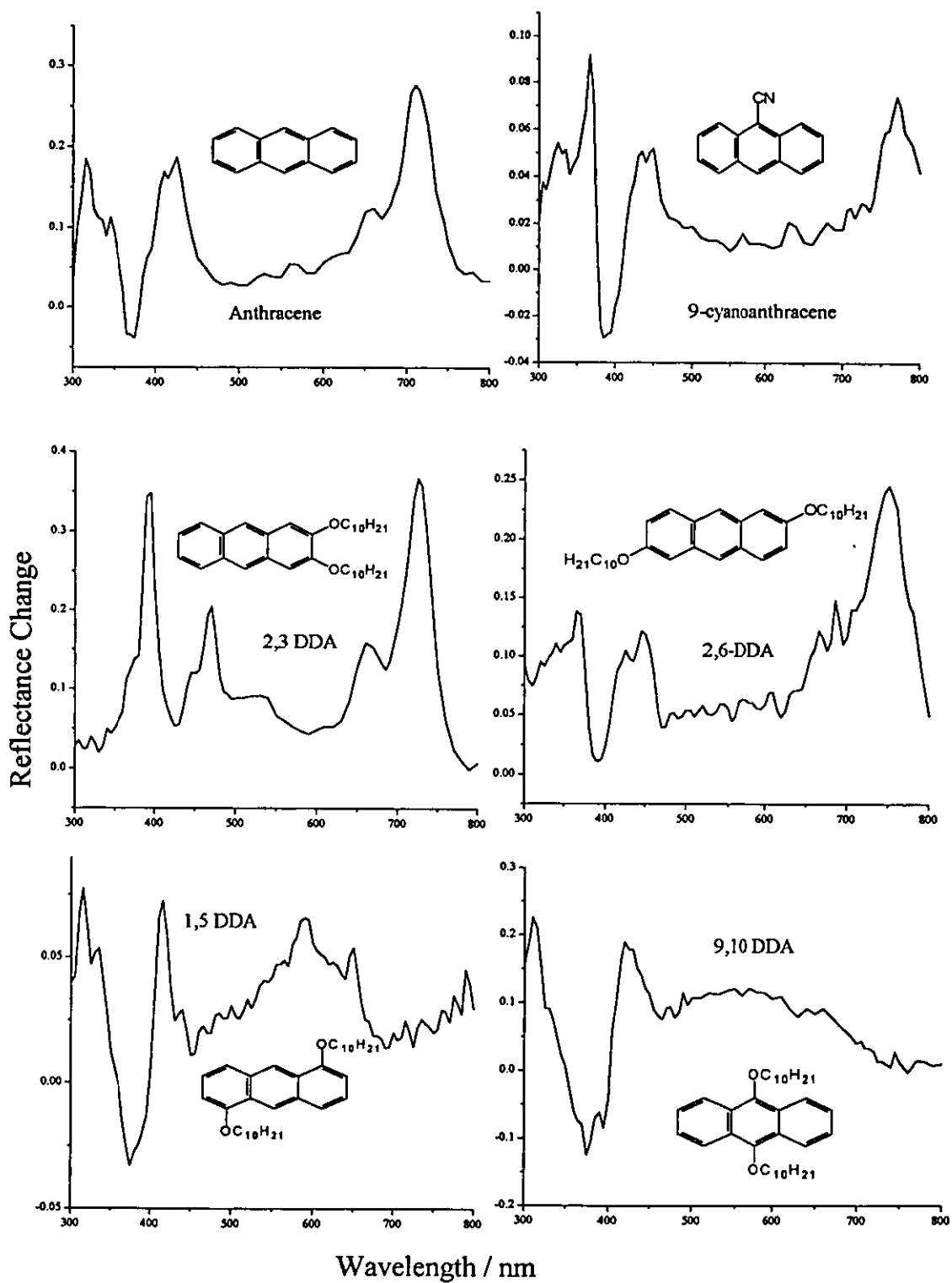


Figure 6.18 : Radical cation spectra of anthracene and its derivatives

Chapter 7

Conclusions and Further Work

7. Conclusions and Suggestions for Further Work.

Preferential adsorption sites exist on the surface of silica gel. This is illustrated by the formation of aggregates of anthracene at low loadings corresponding to a coverage of only a few percent of a monolayer. Evidence of aggregate formation was observed in both the absorption and fluorescence emission spectra. The fluorescence emission spectra are distorted by absorption by both the ground state and by aggregates. The characteristic anthracene triplet-triplet absorption and radical cation absorption spectra are both observed following laser excitation at 355 nm. Time-resolved transient emission spectra reveal the formation of excimers and protonated anthracene. The mobility of anthracene on the silica gel surface is illustrated by the presence of delayed fluorescence arising from triplet-triplet annihilation. The two-dimensional and fractal analysis of the decay of the delayed fluorescence displays the presence of two different regions for the adsorption of anthracene molecules. The different domains on porous silica gel are suggested to be due to adsorption within the pores and interconnecting channels, and adsorption over the outer, "flatter" surface. If no electron donor is present in the anthracene / silica system then electron-radical combination is the dominant decay mechanism regenerating the ground state. The radical cation at low loadings decays predominantly by geminate recombination and can be fitted by a geminate recombination model at early times.

Triplet-triplet energy transfer from anthracene to azulene was complicated by triplet-triplet annihilation between anthracenes, and consequently no rate of energy transfer could be determined.

The coadsorption of an electron donor (with a sufficiently low oxidation potential) with anthracene on silica gel causes an increase in the rate of decay of the anthracene radical cation. The decay of anthracene radical cation in the presence of electron donors can be well described by the dispersive kinetic model of Albery. The rate of electron transfer does not show a linear dependence on the free energy for the electron transfer reaction. The observed Marcus type inverted region needs further investigation, and as yet no conclusions can be drawn due to the small number of compounds studied with a high- ΔG for electron transfer (ΔG_{ET}). One would not expect molecules on surfaces to diffuse at the same rates. Therefore the differences in the rates of electron transfer for the different electron donors could be due to their different rates of diffusion across the surface. The evidence suggests that the rate of diffusion of the electron donor to the anthracene radical cation is the rate limiting step, with the rate of electron transfer being relatively fast if the interaction is favourable. This is reinforced by

the fact that the electron transfer from TPA to the 2,3-didecyloxyanthracene radical cation proceeds at the same rate as from TPA to the unsubstituted anthracene radical cation where clearly ΔG_{ET} will be different. The rates of electron transfer in both the TPA with anthracene and TPA with 2,3-didecyloxyanthracene appear to lie on the same straight line, as expected if diffusion of the TPA is the rate determining step. Preliminary experiments adsorbing azulene and anthracene from the gas phase reveal the same rates (to within experimental error) for electron transfer from azulene to the anthracene radical cation in both the samples adsorbed from solution and from the vapour phase. This suggests that the observed rates are not mediated by residual solvent on the silica gel following adsorption from solution.

On the grounds of the absence of delayed fluorescence, the dialkoxy derivatives appear tightly bound to the silica gel surface and diffusion is severely restricted. The transient difference spectra of the anthracene derivatives reveal similarities between the spectral shapes of the 2,3-dialkoxyanthracenes, 2,6-didecyloxyanthracene and 9-cyanoanthracene with that of unsubstituted anthracene on silica gel. The transient spectra of the 9,10 and 1,5-didecyloxyanthracenes are similar to one another, but significantly different from unsubstituted anthracene. The relative amount of triplet-triplet absorption observed for the various derivatives adsorbed on silica gel are in broad agreement with the triplet quantum yields recorded in solution.

Some Suggestions for Further Work

Preliminary studies that I have carried out investigating the effect of pore size on the rate of decay of the anthracene triplet and radical cation adsorbed on a range of silica gels (listed in the materials section) with differing pore sizes has revealed an apparent increase in the rate of decay of both the triplet and radical cation with decreasing pore size. Further work needs to be done to confirm this and to determine the reasons for this behaviour. Also investigation of the rate of electron transfer from the electron donors to the anthracene radical cation as a function of pore size could help to clarify the role of diffusion.

Sublimation of anthracene with the other electron donors (TPA, TMPD and DMA) should be carried out to confirm that the rates of electron transfer in these cases are not unduly influenced by any residual solvent left on the silica gel surface.

A concentration dependence study of the absorption and emission spectra of the alkoxyderivatives needs to be carried out in order to see whether the long hydrocarbon chains have an effect on the aggregation properties of the alkoxyderivatives

It is worth noting that triplet-triplet energy transfer between 2,3-DDA and azulene should not be complicated by either the radical cation decay or triplet-triplet annihilation which may be a good system for studying triplet-triplet energy transfer.

Further investigations into rates of electron transfer as a function of electron donor identity need to be carried out to confirm or refute the existence of a Marcus inverted region in the electron transfer between an electron donor and the anthracene radical cation.

Chapter 8

References

8. References

- 1 Huber, J.P.; Mahaney, M. *Chem. Phys. Lett.* 1975, **30**, 410.
- 2 Hui, M.H.; de Mayo, P.; Suau, R.; Ware, W.R. *Chem. Phys. Lett.* 1975, **31**, 257.
- 3 Beer, M.; Longuet-Higgins, H.C. *J. Chem. Phys.* 1955, **23**, 1390.
- 4 Visnawath, G.; Kasha, M. *J. Chem. Phys.* 1956, **24**, 574.
- 5 Sidman, J.W.; McClure, D.S. *J. Chem. Phys.* 1956, **24**, 757.
- 6 Dexter, D.L. *J. Chem. Phys.* 1953, **21**, 836.
- 7 Forster, T. *Faraday Discuss. Chem. Soc.* 1959, **27**, 7.
- 8 Rehm, D.; Weller, A. *Z. Phys. Chem. (NF)* 1970, **69**, 183.
- 9 Porter, G., *Proc. Roy. Soc. Lond. A*, 1950, **200**, 284.
- 10 Kessler, R.W.; Wilkinson, F. *J. Chem. Soc., Faraday Trans. 1*, 1981, **77**, 309.
- 11 Hawkes, J.; Latimer, I. "*Lasers : Theory and Practice*" Prentice-Hall international Series in Optoelectronics, first edition, Prentice Hall, (Hemel Hempstead), 1995.
- 12 Beesley, M.J. "*Lasers and Their Applications*", first edition, Taylor and Francis Ltd., (London), 1971.
- 13 Gilbert, A.; Baggott, J. "*Essentials of Molecular Photochemistry*", first edition, Blackwell Scientific Publications, (Oxford) pg. 131-139 (1991)
- 14 Fleming, G.R.; "*Chemical Applications of Ultrafast Spectroscopy*", Oxford University Press (1986)
- 15 Wendlandt, W.W.; Hecht, H.G. "*Reflectance Spectroscopy*", Chemical Analysis Monograph No. 21, Wiley Interscience, (New York), pg. 1 (1966)
- 16 Kortum, G. "*Reflectance Spectroscopy*", Springer-Verlag, (Berlin), pg. 4 (1969)
- 17 Kortum, G.; Oelkrug, D. *Z. Naturforsch.*, 1964, **19a**, 28.
- 18 Ramamurthy, V. "*Surface Photochemistry*", Ed. Anpo, M., Wiley, Chichester, 1996.

-
- 19 Thomas, J.K. *J. Phys. Chem.* 1987, **91**, 267.
 - 20 Thomas, J.K. *Chem. Rev.* 1993, **93**, 301.
 - 21 Kamat, P.V. *Chem. Rev.* 1993, **93**, 267.
 - 22 Pohle, W. *J. Chem. Soc. Faraday Trans. 1*, 1982, **78**, 2101.
 - 23 Basila, M. *J. Chem. Phys.* 1961, **35**, 1151.
 - 24 Snyder, L.R. *J. Phys. Chem.* 1963, **67**, 2622.
 - 25 Iler, R.K.; "The Chemistry of Silica Solubility, Polymerisation, Colloid and Surface Properties and Biochemistry", Wiley, New York, 1979.
 - 26 Van der Voort, P.; Gillis-D'Hamers, I.; Vrancken, K.C.; Vansant, E.F. *J. Chem. Soc. Faraday Trans.* 1991, **87**, 3899.
 - 27 De Boer, J.H.; Vleeskins, J.M. *Proc. K. Ned. Akad. Wet., Ser. B*, 1958, **61**, 85.
 - 28 Sindorf, D.W.; Maciel, G.E. *J. Am. Chem. Soc.* 1983, **105**, 1487.
 - 29 Mayo, P. *Pure Appl. Chem.* 1982, **54**, 1623.
 - 30 Wang, H.; Harris, J.M. *J. Phys. Chem.* 1995, **99**, 16999.
 - 31 Pankasem, S.; Thomas, J.K. *J. Phys. Chem.* 1991, **95**, 7385.
 - 32 Dabestani, R.; Ellis, K.J.; Sigman, M.E. *J. Photochem. Photobiol. A: Chem.* 1995, **86**, 231.
 - 33 Bjarneson, D.W.; Peterson, N.O. *J. Am. Chem. Soc.* 1990, **112**, 988.
 - 34 Beck, G.; Thomas, J.K. *Chem. Phys. Lett.* 1983, **94**, 553.
 - 35 Bauer, R.K.; de Mayo, P.; Natarajan, L.V.; Ware, W.R. *Can. J. Chem.* 1984, **62**, 1279.
 - 36 Bauer, R.K.; Borenstein, R.; de Mayo, P.; Okada, K.; Rafalska, M.; Ware, W.R.; Wu, K.C. *J. Am. Chem. Soc.* 1982, **104**, 4635.
 - 37 Eremenko, A.M.; Smirnova, N.P.; Samchuk, S.A.; Chujko, A.A. *Colloids and Surfaces*, 1992, **63**, 83.

-
- 38 Bykovskaya, L.A.; Kulikov, S.G.; Eremenko, A.M.; Yankovich, V.N. *Opt. Spektrosk.* 1988, **64**, 320.
- 39 Leermakers, P.A.; Thomas, H.T.; Weis, L.D.; James, F.C. *J. Am. Chem. Soc.* 1966, **88**, 5075.
- 40 Hara, K.; de Mayo, P.; Ware, W.R.; Weedon, A.C.; Wong, G.S.K.; Wu, K.C. *Chem. Phys. Lett.* 1980, **69**, 105.
- 41 Bauer, R.K.; de Mayo, P.; Okada, K.; Ware, W.R.; Wu, K.C. *J. Phys. Chem.* 1983, **87**, 460.
- 42 Fujii, T.; Ishii, A.; Satozono, H.; Suzuki, S.; Takusagawa, N.; Anpo, M. *J. Photochem. Photobiol. A: Chem.* 1994, **84**, 283.
- 43 Fujii, T.; Ishii, A.; Takusagawa, N.; Yamashita, H.; Anpo, M. *J. Photochem. Photobiol. A: Chem.* 1995, **86**, 219.
- 44 Lochmuller, C.H.; Colborn, A.S.; Hunnicutt, M.L.; Harris, J.M. *J. Am. Chem. Soc.* 1984, **106**, 4077.
- 45 Avnir, D.; Busse, R.; Ottolenghi, M.; Wellner, E.; Zachariasse, K.A. *J. Phys. Chem.* 1985, **89**, 3521.
- 46 Hayashi, Y.; Kawada, Y.; Ichimura, K. *Langmuir* 1995, **11**, 2077.
- 47 Iu, K-K.; Thomas, J.K. *Langmuir* 1990, **6**, 471.
- 48 Mao, Y.; Iu, K-K.; Thomas, J.K. *Langmuir* 1994, **10**, 709.
- 49 Leheny, A.R.; Turro, N.J.; Drake, J.M. *J. Phys. Chem.* 1992, **96**, 8498.
- 50 Oelkrug, D.; Uhl, S.; Wilkinson, F.; Willsher, C.J. *J. Phys. Chem.* 1989, **93**, 4551.
- 51 Oelkrug, D.; Gregor, M.; Reich, S.J. *Photochem. Photobiol.* 1991, **54**, 539.
- 52 Gunther, R.; Oelkrug, D.; Rettig, W. *J. Phys. Chem.* 1993, **97**, 8512.
- 53 Oelkrug, D.; Krabichler, G.; Honnen, W.; Wilkinson, F.; Willsher, C.J. *J. Phys. Chem.* 1988, **92**, 3589.
- 54 Oelkrug, D.; Reich, S.; Wilkinson, F.; Leicester, P.A. *J. Phys. Chem.* 1991, **95**, 269.

-
- 55 Johnston, L.J.; Scaiano, J.C.; Shi, J-L.; Siebrand, W.; Zerbetto, F. *J. Phys. Chem.* 1991, **95**, 10018.
- 56 Turro, N.J., Gould, I.R.; Zimmt, M.B.; Cheng, C-C. *Chem. Phys. Lett.* 1985, **119**, 484.
- 57 Turro, N.J. *Pure and Appl. Chem.* 1986, **58**, 1219.
- 58 de Mayo, P.; Nakamura, A.; Tsang, P.W.K.; Wong, S.K. *J. Am. Chem. Soc.* 1982, **104**, 6824.
- 59 Turro, N.J.; Zimmt, M.B.; Gould, I.R. *J. Am. Chem. Soc.* 1985, **107**, 5826.
- 60 Wilkinson, F.; Ferreira, L.F.V. *J. of Luminescence* 1988, **40 & 41**, 704.
- 61 Kazanis, S.; Azarani, A.; Johnston, L.J. *J. Phys. Chem.* 1991, **95**, 4430.
- 62 Bourdelande, J.L.; Font, J.; Wilkinson, F.; Willsher, C. *J. Photochem. Photobiol. A: Chem.* 1994, **84**, 279.
- 63 Levin, P.P.; Katalnikov, I.V.; Ferreira, L.F.V.; Costa, S.M.B. *Chem. Phys. Lett.* 1992, **193**, 461.
- 64 Yakimova, O.I.; Eremenko, A.M.; Chuiko, A.A. *J. Mol. Struct.* 1990, **218**, 447.
- 65 Murtagh, J.; Thomas, J.K. *Chem. Phys. Lett.* 1987, **139**, 437.
- 66 Levin, P.P.; Costa, S.M.B.; Ferreira, L.F.V. *J. Photochem. Photobiol. A: Chem.* 1994, **82**, 137.
- 67 Gopidas, K.R.; Kamat, P.V. *J. Phys. Chem.* 1989, **93**, 6428.
- 68 Wilkinson, F.; Willsher, C.J. *Tetrahedron* 1987, **43**, 1197.
- 69 Wilkinson, F.; Leicester, P.A.; Ferreira, L.F.V.; Freire, V.M.M.R. *Photochem. Photobiol.* 1991, **54**, 599.
- 70 Wilkinson, F.; Worrall, D.R.; Ferreira, L.F.V. *Spectrochimica Acta* 1992, **48A**, 135.
- 71 Wilkinson, F.; McGarvey, D.J.; Worrall, D.R. *Proc. Indian Acad. Sci. (Chem. Sci.)* 1992, **104**, 739.
- 72 Bauer, R.K.; de Mayo, P.; Ware, W.R.; Wu, K.C. *J. Phys. Chem.* 1982, **86**, 3781.

-
- 73 Fujii, T.; Shimizu, E.; Suzuki, S. *J. Chem. Soc., Faraday Trans. 1*, 1988, **84**, 4387.
- 74 Mao, Y.; Thomas, J.K. *Langmuir* 1992, **8**, 2501.
- 75 Zilberstein, J.; Bromberg, A.; Berkovic G. *J. Photochem. Photobiol. A: Chem.* 1994, **77**, 69.
- 76 Suib, S.L.; Kostapapas, A. *J. Am. Chem. Soc.* 1984, **106**, 7705.
- 77 Ramamurthy, V.; Sanderson, D.R.; Eaton, D.F. *J. Phys. Chem.* 1993, **97**, 13380.
- 78 Park, J.; Kang, W-K.; Ryoo, R.; Jung, K-H.; Jang, D-J. *J. Photochem. Photobiol. A: Chem.* 1994, **80**, 333.
- 79 Hashimoto, S.; Fukazawa, N.; Fukumura, H.; Masuhara, H. *Chem. Phys. Lett.* 1994, **219**, 445
- 80 Drake, J.M.; Levitz, P.; Turro, N.J.; Nitsche, K.S.; Cassidy, K.F. *J. Phys. Chem.* 1988, **92**, 4680.
- 81 Wellner, E.; Rojanski, D.; Ottolenghi, M.; Huppert, D.; Avnir, D. *J. Am. Chem. Soc.* 1987, **109**, 575.
- 82 Xiang, B.; Kevan, L. *J. Phys. Chem.* 1994, **98**, 5120.
- 83 Xiang, B.; Kevan, L. *Langmuir* 1994, **10**, 2688.
- 84 Xiang, B.; Kevan, L. *Colloids Surf. A.* 1993, **72**, 11.
- 85 de Mayo, P.; Natarajan, L.V.; Ware, W.R. *Chem. Phys. Lett.* 1984, **107**, 187.
- 86 Pankasem, S.; Thomas, J.K. *J. Phys. Chem.* 1991, **95**, 6990.
- 87 Kelly, G.; Willsher, C.J.; Wilkinson, F.; Netto-Ferreira, J.C.; Olea, A.; Weir, D.; Johnston, L.J.; Scaiano, J.C. *Can. J. Chem.* 1990, **68**, 812.
- 88 Frederick, B.; Johnston, L.J.; de Mayo, P.; Wong, S.K. *Can. J. Chem.* 1984, **62**, 403.
- 89 Lednev, I.K.; Mathivanan, N.; Johnston, L.J. *J. Phys. Chem.* 1994, **98**, 11444.
- 90 Mao, Y.; Thomas, J.K. *J. Chem. Soc. Faraday Trans.* 1992, **88**, 3079.

-
- 91 Iu, K.K.; Thomas, J.K. *J. Phys. Chem.* 1991, **95**, 506.
- 92 Liu, X.; Thomas, J.K. *Langmuir* 1993, **9**, 727.
- 93 Liu, X.; Iu, K-K.; Thomas, J.K. *Chem. Phys. Lett.* 1993, **204**, 163.
- 94 Iu, K-K.; Liu, X.; Thomas, J.K. *J. Phys. Chem.* 1993, **97**, 8165.
- 95 Iu, K-K.; Liu, X.; Thomas, J.K. *J. Photochem. Photobiol. A: Chem.* 1994, **79**, 103.
- 96 Liu, X.; Iu, K-K.; Thomas, J.K.; He, H.; Klinowski, J. *J. Am. Chem. Soc.* 1994, **116**, 11811.
- 97 Liu, X.; Mao, Y.; Reutten, S.A.; Thomas, J.K. *Solar Energy Materials and Solar Cells* 1995, **38**, 199.
- 98 Liu, Y.S.; Ware, W.R. *J. Phys. Chem.* 1993, **97**, 5980.
- 99 Liu, Y.S.; de Mayo, P.; Ware, W.R. *J. Phys. Chem.* 1993, **97**, 5987.
- 100 Liu, Y.S.; de Mayo, P.; Ware, W.R. *J. Phys. Chem.* 1993, **97**, 5995.
- 101 Avnir, D.; Rojanski, D.; Huppert, D.; Bale, H.D.; Decai, X.; Schmidt, P.W.; Farin, D.; Seri-Levy, A. *Phys. Rev. Lett.* 1986, **56**, 2505.
- 102 Levitz, P.; Drake, J.M.; Klafter, J. "Molecular dynamics in restricted geometries". Eds. J. Klafter and J.M. Drake, p 165-195. Wiley, New York.
- 103 Pines, D.; Huppert, D.; Avnir, D. *J. Chem. Phys.* 1988, **89**, 1177.
- 104 Alexander, S.; Orbach, R. *J. Phys. Lett.* 1982, **43**, 625.
- 105 Leyfraz, F.; Stanley, H.E. *Phys. Rev. Lett.* 1983, **51**, 2048.
- 106 Wilkinson, F.; Beer, R. "Photochemical Processes in Organised Molecular Systems". Ed. K. Honda, p 377-396. Elsevier Science, 1991.
- 107 Albery, W.J.; Bartlett, P.N.; Wilde, C.P.; Darwent, J.R. *J. Am. Chem. Soc.* 1985, **107**, 1854.
- 108 Krasnansky, R.; Koike, K.; Thomas, J.K. *J. Phys. Chem.* 1990, **94**, 4521.
- 109 Mao, Y.; Thomas, J.K. *J. Phys. Chem.* 1995, **99**, 2048.

-
- 110 Krasnansky, R.; Thomas, J.K. *J. Photochem. Photobiol. A: Chem.* 1991, **57**, 81.
- 111 Samuel, J.; Ottolenghi, M.; Avnir, D. *J. Phys. Chem.* 1992, **96**, 6398.
- 112 Wilkinson, F.; Worrall D.R. *Proc. Indian Acad. Sci. (Chem. Sci.)* 1992, **104**, 287.
- 113 Bryukhanov, V.V.; Ketsle, G.A.; Regir, K.F.; Runov, V.K.; Smagulov, Zh.K. *Opt. Spektrosk.* 1988, **66**, 933.
- 114 Mao, Y.; Breen, N.E.; Thomas, J.K. *J. Phys. Chem.* 1995, **99**, 9909.
- 115 Levin, P.P.; Ferreira, L.F.V.; Costa, S.M.B. *Chem. Phys. Lett.* 1990, **173**, 277.
- 116 Levin, P.P.; Costa, S.M.B.; Ferreira, L.F.V. *J. Phys. Chem.* 1995, **99**, 1267.
- 117 Miyasaka, H.; Kotani, S.; Itaya, A. *J. Phys. Chem.* 1995, **99**, 5757.
- 118 Lin, T.; Kan, H.K.A. *J. Opt. Soc. Am.* 1970, **60**, 1252.
- 119 Kessler, R.W.; Krabichler, G.; Uhl, S.; Oelkrug, D.; Hagan, W.P.; Hyslop, J.; Wilkinson, F. *Optica. Acta.* 1983, **30**, 1090.
- 120 Oelkrug, D.; Honnen, W.; Wilkinson, F.; Willsher, C.J. *J. Chem. Soc. Faraday Trans. 2* 1987, **83**, 2081.
- 121 Hite, P.; Krasnansky, R.; Thomas, J.K. *J. Phys. Chem.* 1986, **90**, 5795.
- 122 Saltiel, J.; Marchand, G.R.; Smothers, W.K.; Stout, S.A.; Charlton, J.L. *J. Am. Chem. Soc.* 1981, **103**, 7159.
- 123 Kopelman, R. *J. Stat. Phys.* 1985, **42**, 185.
- 124 Kopelman, R. *Science* 1988, **241**, 1620.
- 125 Kopelman, R.; Prasad, J.; Parus, S.J. "Molecular Dynamics in restricted Geometries". Eds. J. Klafter and J.M. Drake p 145-164. Wiley, New York.
- 126 Debye, P.; Edwards, J.O. *J. Chem. Phys.* 1952, **20**, 236.
- 127 Era, K.; Shinonoya, S.; Washizawa, Y.; Ohmatsu, H. *J. Phys. Chem. Solids* 1968, **29**, 1843.
- 128 Tachiya, M.; Mozumder, A. *Chem. Phys. Lett.* 1975, **34**, 77.

-
- 129 Abell, G.C.; Mozumder, A. *J. Chem. Phys.* 1972, **56**, 4079.
- 130 Wang, Z.; Weininger, S.J.; McGimpsey, W.G. *J. Phys. Chem.* 1993, **97**, 374.
- 131 Shida, T.; Iwata, S. *J. Am. Chem. Soc.* 1973, **95**, 3473.
- 132 Shida, T.; "Physical Sciences Data 34, Electronic Absorption Spectra of Radical Ions". Elsevier Science, Amsterdam, 1988.
- 133 Liu, A.; Sauer, M.C.; Loffredo, D.M.; Trifunac, A.D. *J. Photochem. Photobiol. A: Chem.* 1992, **647**, 197.
- 134 Szczepanski, J.; Vala, M.; Talbi, D.; Parisel, O.; Ellinger, Y. *J. Chem. Phys.* 1993, **98**, 4494.
- 135 Murov, S.L.; Carmichael, I.; Hug, G.L. "Handbook of Photochemistry" second edition, Marcel Dekker, New York, 1993. Table 10a-3. Data taken from:-
Levin, R.D.; Lias, S.G. NSRDS-NBS 1982, 71, 634. (National Bureau of Standards, Washington, DC)
Lias, S.G.; Bartmess, J.E.; Liebman, J.F.; Holmes, J.L.; Levin, R.D.; Mallard, W.G. *J. Phys. Chem. Ref. Data* 17: 861, 1988.
Lias, S.G.; Bartmess, J.E.; Liebman, J.F.; Holmes, J.L.; Levin, R.D.; Mallard, W.G. *NIST Positive Ion Energetics Database: Ver. 1.1* National Institute of Standards and Technology, Gaithersburg, MD, 1990.
- 136 Jardon, P.; Gautron, R. *J. Chim. Phys. Phys.-Chim. Biol.* 1985, **82**, 353.
- 137 Dempster, D.N.; Morrow, T.; Quinn, M.F. *J. Photochem.* 1974, **2**, 329.
- 138 Hoshino, M.; Seki, H.; Imamura, M.; Yamamoto, S. *Chem. Phys. Lett.* 1984, **104**, 369
- 139 Murov, S.L.; Carmichael, I.; Hug, G.L. "Handbook of Photochemistry" second edition, Marcel Dekker, New York, 1993. Table 10b-1 and 10b-2. Data taken from:-
Siegerman, H. "Technique of Electroorganic Synthesis". (Techniques of Chemistry, Vol. 5, Part II), Ed. N.L. Weinberg. p 667-1056. John Wiley, New York, 1975.
Zweig, A.; Lancaster, J.E.; Neglia, M.T.; Jura, W.H. *J. Am. Chem. Soc.* 1964, **86**, 4130.
Pysh, E.S.; Yang, N.C. *J. Am. Chem. Soc.* 1963, **85**, 2124.
- 140 Wilkinson, F.; Worrall, D.R.; Williams, S.L. *J. Phys. Chem.* 1995, **99**, 6689.

-
- 141 Gorman, A.A.; Hamblett, I.; Harrison, R.J. *J. Am. Chem. Soc.* 1984, **106**, 6952.
- 142 Weller, A. *Pure Appl. Chem.* 1968, **16**, 115.
- 143 Brotin, T.; Utermohlen, R.; Fages, F.; Bouas-Laurent, H.; Desvergne, J-P. *J. Chem. Soc., Chem. Comm.* 1991, 416.
- 144 Brotin, T.; Desvergne, J.-P.; Fages, F.; Utermohlen, R.; Bonneau, R.; Bouas-Laurent, H. *Photochem. Photobiol.* 1992, **55**, 349.
- 145 Wilkinson, F.; McGarvey, D.J.; Olea, A.F. *J. Am. Chem. Soc.* 1993, **115**, 12144.
- 146 Van der Donckt, E.; Barthels, M.R.; Delestinne, A. *J. Photochem.* 1973, **1**, 429.

